JAERI-M
92-124

JAERI TANDEM, LINAC & V.D.G.

ANNUAL REPORT

1991

April 1, 1991 — March 31, 1992

September 1992

Department of Physics

日　本　原　子　力　研　究　所
Japan Atomic Energy Research Institute

JAERI TANDEM, LINAC & V.D.G.

Annual Report

1991

April 1, 1991 - March 31, 1992

Department of Physics

Tokai Research Establishment

Japan Atomic Energy Research Institute

Tokai-mura, Naka-gun, Ibaraki-ken

This annual report describes research activities which have been performed with the JAERI tandem accelerator, the electron linear accelerator and the Van de Graaff accelerator from April 1, 1991 to March 31, 1992. Summary reports of 44 papers, and list of publications, personnel and cooperative researches with universities are contained.

Editors : Mitsuhiko Ishii
Chiaki Kobayashi
Akira Iwamoto
Yukio Kazumata
Hiroshi Maeta
Fujiyasu Nomura

原研タンデム，リニアック，バンデグラフ加速器
1991年度年次報告

日本原子力研究所東海研究所
物理部

　本年次報告は，原研タンデム，リニアック及びバンデグラフ加速器で，1991年4月1日から1992年3月31日までの間に東海研で行われた研究活動をとりまとめたものである。
　1）加速器運転と開発研究　2）原子分子物理，固体物理及び材料の放射線効果　3）核化学　4）軽イオン核物理　5）重イオン核物理の5部門にまたがる44編の研究報告，公表された文献，関与した職員及び大学等との協力研究のリストを収録している。

PREFACE

This report covers research and development activities during the period April 1, 1991 until March 31, 1992 at the accelerator facilities of JAERI, Tokai : the 20UD tandem accelerator, the 2 MeV V.d.G. accelerator and the 200 MeV electron linear accelerator.

During this period, the tandem accelerator, principal of the three, has been operated over 4,300 hours and has supplied stable beams to experiments in the fields of : (1) Atomic Physics, Solid State Physics and Radiation Effects in Materials, (2) Nuclear Chemistry, (3) Light Ion Nuclear Physics, and (4) Heavy Ion Nuclear Physics. Fifty three experimental programs have been carried out by the JAERI staff and collaborators from universities and national laboratories.

The JAERI superconducting booster continues under construction. A new building for the booster was completed and helium refrigerators were installed there. Sixteen superconducting resonators have been checked on RF performance and have been assembled in the cryostats. The other resonators are waiting for electrochemical polishing and RF-power test. It will take one more year to finish the construction and the tandem-booster will supply first beams in the middle of 1993.

The third workshop on instrumentation for the tandem-booster was held on February 27 - 28, 1992 at JAERI, Tokai. About seventy participants including thirty four from the universities talked about current topics on nuclear physics and its interdisciplinary applications. Activities of the workshop will be reported in another issue.

Mitsuhiko Ishii
Director
Department of Physics

Contents

I   ACCELERATOR OPERATION AND DEVELOPMENT

1.1 Tandem Accelerator Operation

Tandem Accelerator Group

Department of physics, JAERI

Accelerator operation

The scheduled operation for experiments was performed through the past one year containing two short periods for the scheduled maintenance. The following are summary of the operation from April 1,1991 to March 31,1992. In this period, about 10% of operation days were cut for the building extension works for the tandem booster. The accelerator running time was 4314.2 hours.

1) Time distribution by terminal voltage

>16 MV	28 days	15.1 %		11-12 MV	5 days	2.7 %
15-16	89	47.8		10-11	7	3.8
14-15	26	13.4		9-10	4	2.2
13-14	14	7.5		8- 9	3	1.6
12-13	10	5.4		< 8	1	0.5

2) Time distribution by projectile

H	16 days	8.6 %		S	14 days	7.5 %
D	4	2.2		Cl	8	4.3
Li	4	2.2		Fe	10	5.4
B	1	0.5		Ni	24	12.9
C	13	7.0		Cu	5	2.7
N	1	0.5		Ge	17	9.1
O	33	17.2		Br	6	3.2
F	2	1.0		I	2	1.0
Si	22	11.8		Au	4	2.2
P	1	0.5				

3) Time distribution by activity

Operation for research		187 days
Atomic and solid state physics		(26 days)
Radiation effects in materials		(19)

Nuclear chemistry	(39)
Nuclear physics	(75)
Fast neutron physics	(6)
Radiation chemistry	(2)
Detector development	(5)
Accelerator development	(0)
Voltage conditioning	7
Operation training	4
Scheduled maintenance (2 tank openings)	73
Unexpected repair(Tandem, 1 tank opening)	16
Unexpected repair(Experimental equipment)	3
Scheduled operation suspension for the building extension	18
Holidays and vacation	58

Troubles that interrupted the experimental schedule

      1) Failure in the communication system of the upper dead section

      2) Failure in the switching magnet power supply due to the deterioration of the large chemical condensers

Improvement and development

    New control computer system that utilizes parallel processing method is under development. The basic software and main part of hardware were almost completed. A part of tests has been started.

    The construction of the tandem booster is well under way as has been scheduled. The building has completed and the installation of main part of the linac and the helium cooling systems have been started. This item will be reported later paragraph.

1.2 Status of JAERI Linac

Katsuo MASHIKO, Tokio SHOJI, Nobuhiro ISHIZAKI,
Hidekazu TAYAMA, Hiroshi YOSHIKAWA* and Hideaki YOKOMIZO*

Departments of Physics,
*Office of Synchrotron Radiation Facility Project

1. Operation

The linac was operated both for internal and external user groups with repetition rates of 1-150pps for 826.7 hours from April 1, 1991 to March 31, 1992. A summary of the linac operating conditions is shown in Table 1 for each experimental program. The linac was stopped for the installation works for three months.

The group of the Office of Synchrotron Radiation Facility Projects set up the experimental apparatuses for high energy positron emission and acceleration at the Tc beam transport line from July 24 to August 31, 1991. The apparatuses consisted of a positron converter, a focussing magnet, a 3m accelerating structure, a 90° bending magnet, a Faraday cup and high power wave guides. The replacement work of the exhaust fan (250m^3/min) was done for the ventilation in the linac target room February 1 to March 31, 1992.

Research Program	Time (h)	Ratio (%)	Energy (MeV)	Rate (pps)	Length (ns)	Current (µA)
Neutron Radiography (Time of Flight Method)	160.5	19.4	120	150	25	12
Slow Positron Experiment (Emission of Monoenergetic Positron)	266.0	32.1	100	50	1000	10
First Positron Experiment	116.2	14.1	~100	~25	1000	10
JSR Injection	206.2	24.9	~150	0.5~1	1~1000	<1
Tuning and Test Operation	60.0	7.3	100~180	50~150	1000	~30
Other Experiment (RI Produce)	17.8	2.2	100~120	50	1000	10
Total	826.7	100.0				

Interval of the linac shut down : Jun 24 ~ Jul 31, 1991 and Feb 1 ~ Mar 31, 1992

Table 1 Machine Time and Output Beam for Research Program in 1991

2. Maintenance

The maintenance work for the linac was carried out while the linac was

stopped. Main items for the maintenance works are the following:

(1) Replacement of high voltage cables used for the vacuum system of accelerating structures.

The accelerating structures is equipped with ten units of vacuum ion pumps along its beam line.

The high voltage cables (7C2V) at the downstream of electron beam have often been sustained dielectric breakdown due to the gamma-ray radiation. The 25-30m long cables of ten units were all replaced.

(2) Rearrangement of the cables for the input and output at the control desk.

The pulse shape monitors at the control desk are those monitoring the pulse shapes of electron beam, microwave input and output, klystron voltage and current, and various trigger pulse systems. These are connected with hardwire to the pulse modulator, pulse transformer and accelerating structures. To check the noise level in those cables, noise amplitudes were measured carefully for each monitoring system. The noise levels in the monitor signal lines were reduced by 20-26dB by improving earth point and separating the monitor cable of pulse modulator from the control desk.

(3) Replacement of high power klystrons, thyratrons and a focussing coil for the #5 klystron.

The #2 and #4 klystrons were replaced after 8,000 and 4,100 hour operation, respectively, because of the long aging time necessary and poor emission, although those were not totally damaged. The focussing coil for the #5 klystron was replaced due to the dielectric breakdown caused by the water leakage in the cooling channel. Three thyratrons were replaced after 4-7 year operation which were also not completely broken down.

(4) Improvement.

The grid pulser and its computer controlled circuit were installed and now in operation for the new electron gun (cathode Y-796), which was replaced last year. The electron beam of 0.3A with the 1ns pulse width was obtained. The

Grid Pulse Voltage	
Pulse Width 0.5~1 μs	0~200 V
Pulse Width 10~50 ns	0~160 V
Pulse Width 1 ns	0~ 90 V
Grid Bias Voltage	0~100 V
Heater Voltage	0~ 10 V

Table 2 Output Voltage of Grid Pulser

schematic diagram is shown in Fig.1. The measured characteristics is given in Table 2.

In this circuit, the AC on-off signal, the filament voltage setup, the bias voltage and grid voltage are controlled through a microcomputer PC-98. The input signals are first converted from electrical to optical signals
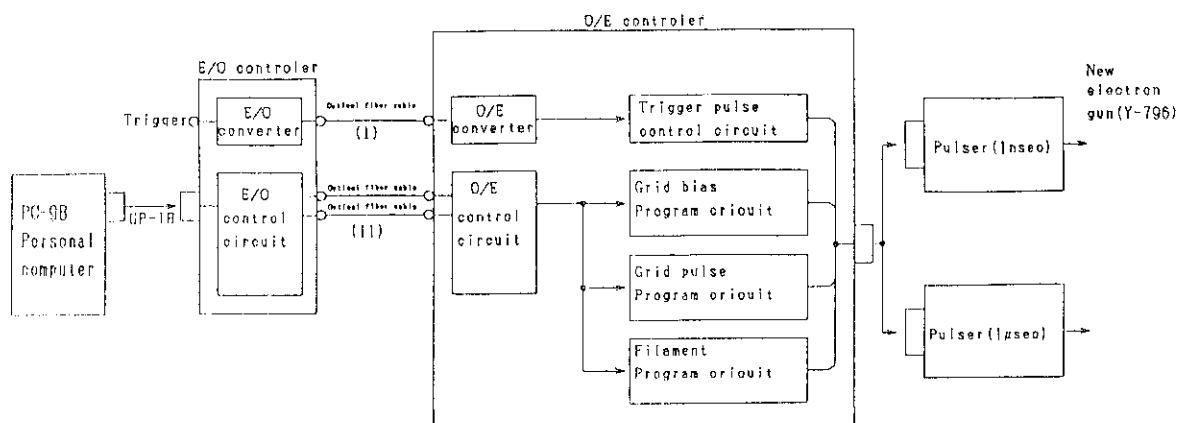
Fig.1 Block diagram of grid pulser used for new electron gun control circuit

with the E/O converters in the controller and then sent to the grid pulser power supply in the accelerator room through 12 units of fiber cables. The grid pulsers are standardized to the two units (a) and (b). The (a) unit generates pulse widths from 10ns to μs with several steps. On the other hand, the (b) unit supplies only 1ns single short pulse. Photo 1 shows the 1ns beam pulse shape which was measured with an amorphous monitor at the TL beam lineat the energy of 130MeV. The characteristics of new gun is shown in Fig.2.
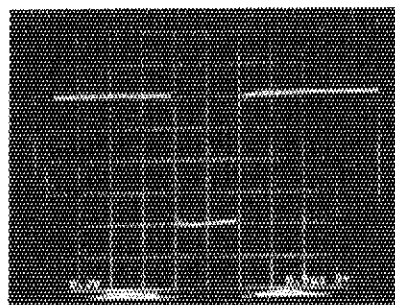
Output beam
of new gun anode
x: 0.5μsec/cm
y: 0.2   V/cm
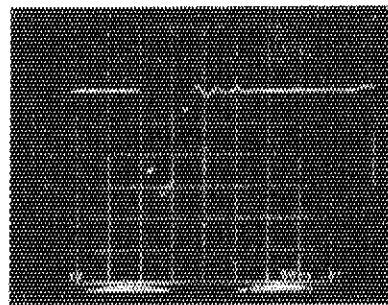
Output beam
of new gun anode
x: 50nsec/cm
y: 1   V/cm
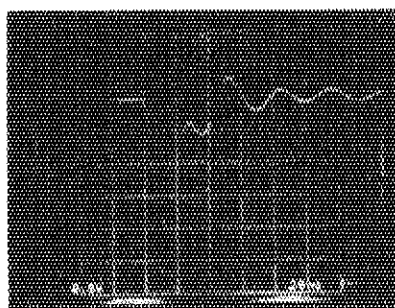
Output beam
of new gun anode
x: 20nsec/cm
y: 0.5 V/cm
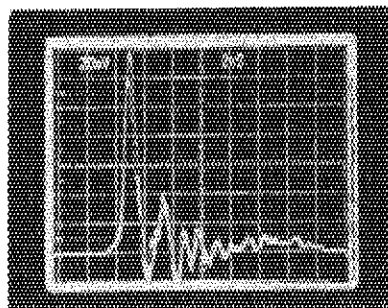
Acceration beam
Energy:130MeV
x: 2nsec/cm
y: 20 mV/cm

photo-1   Output beam current of new electron gun

Y－796 CUT-OFF BIAS

Y－796 EMISSION CURRENT
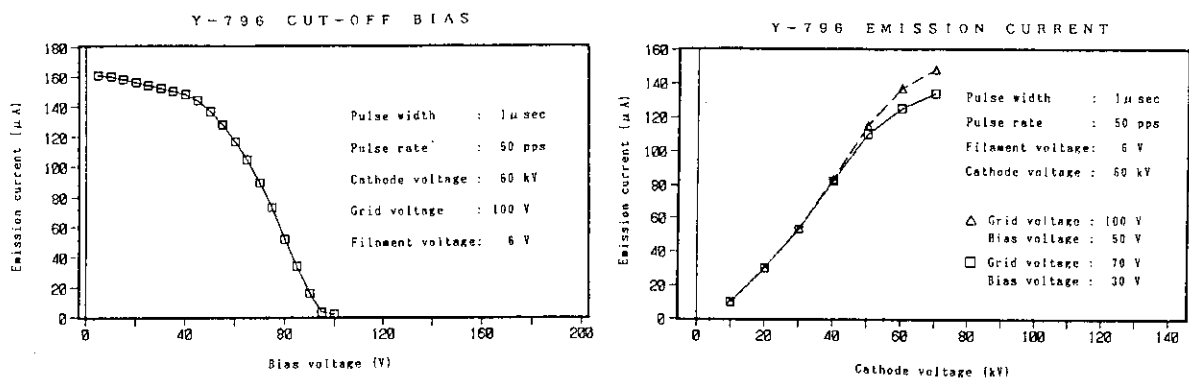
Fig.2 Characteristics of New Gun (Y-796)

3. The subjects on the linac operation

Improvement of the peak current with 1ns operation is desirable. For this purpose, it is necessary to develop a high power and low impedance pulser with the width of 1ns and peak voltage of 200V.

After nearly 20 years operation of the linac, it becomes difficult to maintain the water quality in the pipings of cooling system. Replacements of the old cables are needed under the safety consideration because of the dielectric breakdown and radio-activities caused by the long irradiation in the vicinity of the neutron target and γ-ray target room.

1.3 Superconducting Booster

Booster Project Group

Department of Physics, JAERI

1. Introduction

The project of our superconducting tandem-booster was at the final stage in fabrication of the linac units and in construction of the building in the fiscal year of 1991.

Four of ten linac units of the booster built earlier were assembled after accomplishing final surface treatments and off-line performance tests with the sixteen superconducting quarterwave resonators. The building construction was mostly completed in February 1992. Promptly, two cold boxes and their compressors of the refrigerating system were brought in and their installation started. In March, we brought various components into the new booster building, starting with the four linac units. The rest six linac units were delivered from the manufacturer, Mitsubishi Electric Corp. Kobe works, after two years long fabrication of the twenty-four resonators. Two 260 MHz quarter wave resonators for a bunching unit were also built well, delivered and given a final surface treatment and off-line performance tests. (Their cryostat comes in April 1992.) A beam energy analyzing magnet, three booster control units and quadrupole magnets in the linac were also delivered.

2. Linac units

With the former four linac units, assembling work including surface treatments and performance tests of the resonators started at the end of the last fiscal year. At the beginning, we tried performance tests with four resonators at a time after they were completely assembled in their cryostat. It resulted in finding some problems with a couple of resonators and the next units were assembled after individual performance tests in a testing cryostat. The result is described in the next section.

The latter six units including 24 resonators were built without any big problems in industries. The rest six out of nine quadrupole doublet lenses to be put in the linac were fabricated.

3. Off-line resonator performance

The result of performance tests of 16 resonators at 4.2K was shown in Fig. 1. The resonator performances well satisfied our design value of 5 MV/m at an rf input power of 4 watts. Low field Q values were about 1×10^9. The Q values were lower than expected but the highest field levels were very high. The average of 4 watts input accelerating field levels was about 6.5 MV/m.
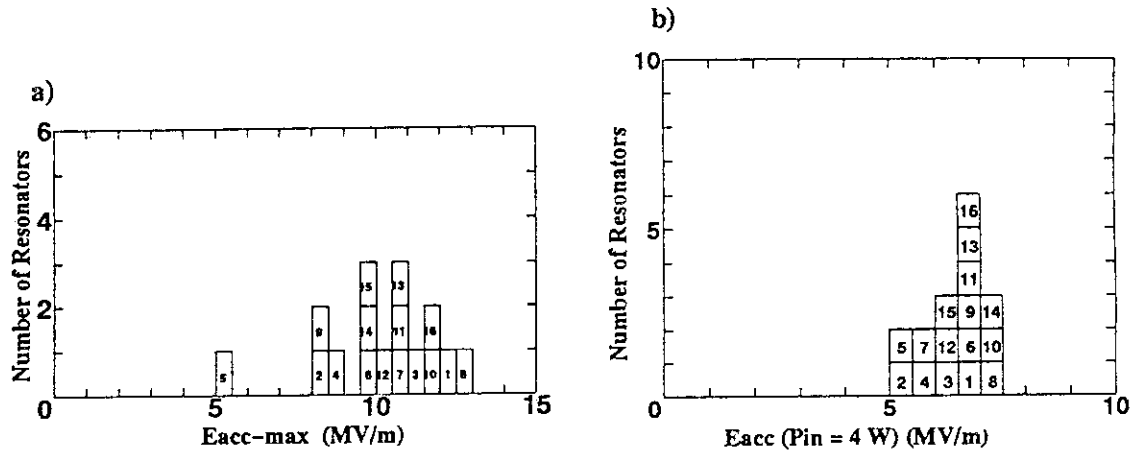
Fig. 1. Distributions of the maximum accelerating field levels(left) and the 4 watts input accelerating field levels(right) obtained with the resonators for the former 4 linac units.

4. Q-degradation due to slow cooling

In recent years, some laboratories reported degradation of Q in thermal cycles with their superconducting cavities(0.5 or 1.5 GHz) made of high RRR(residual resistance ratio) niobium. It is believed so far to be due to a precipitation of hydrogen onto the niobium surface at the saturating temperature. Since the matter is also of great importance to us, we repeated a lot of thermal cycles with our resonators.

A result obtained with our severl resonators is as follows; The Q degradation occured after a long lapse in a temperature zone between 130K and 100K. The degradation depended on the lapse of time. In the heaviest case, Q was degraded to an order of 1×10^8 or accelerating field levels at 4 watts rf input were turned down to 2 MV/m, after a lapse of overnight in the dangerous zone. The degradation was fully recovered by worming up to the room temperature and fast cool-down. To avoid a severe degradation, resonators must be cooled down at a rate of more than 20 K/h in the dangerous zone. We made experiments with sample materials and real resonators, attempting to eliminate the hydrogen precipitation. We, however, have not found any good result, yet.

Therefore, only way to avoid this problem in the booster system is to cool resonators as fast as possible across the dangerous temperature zone by manipulating refrigerators and liquid flow valves.

5. 260 MHz resonators for sub-buncher

Two 260 MHz quarter wave resonators made of niobium and copper were satisfactorily built, having a check of frequency shift due to cool-down. The optimum beam velocity for the resonators were 10 % of the light velocity. The structure is quite the same as the 130 MHz resonators for the linac except the size.

As soon as they were delivered, we made their surface treatments and tested them in a testing cryostat. One resonator had low field Q values of about 2×10^8, the highest field level of 8.8 MV/m and the accelerating field level of 6 MV/m at an rf input power of 4 watts. The Q values reduced to half by cooling down across the critical temperature of 9.2K in the presence of external magnetic field of 0.05 mT. The 4 watts input accelerating field level was 5 MV/m in that case. Therefore, the resonators have a performance good enough even without a magnetic shield(a field level of 2 MV/m is required for the sub-buncher).

6. Refrigerating system

The design of the system including plumbing to the building was finished in the early part of 1991. The cold boxes were fabricated by

Sulzer and imported to Japan in January 1992. The compressors were fabricated by a domestic industry. Application forms of the system installation were submitted to the prefectual government in January 1992 and was accepted soon. The installation started in Feburary. The refrigerators part is completed by Japan Oxigen CO., LTD. in April. The liquid transfer lines are installed later by Mitsubishi Electric Corp.

7. Booster building

The construction started off at the end of 1991 with digging the ground. Heavy walls were formed up in the middle of 1991. The buiding construction work was finished in February, 1992, except completion of plumbing for some equipments. The formal completion was scheduled in April.

8. Safety design

Various aspects of safety were considered in designing the booster facility. A safety design against the following items was refered to a laboratory committee and accepted; earth quakes, power failures, fires, exposures to radiation and incidences by oxigen deficiency.

9. Future plans

The installation and performance tests of the refrigerating system with the booster units will be finished by October, 1992. After that, it will take several months to accomplish surface treatments and reassembling of 24 resonators of latter 6 linac units. In the mean time, beam line components and rf control components will be installed. A completion enough for a beam test will be coming in 1993.

Staff of the project

The members who contributed to the work in the fiscal year of 1991 were as follows;C. Kobayashi, S. Takeuchi, T. Ishii, H. Ikezoe, M. Shibata, T. Yoshida, Y. Sugiyama, S. Kanazawa, M. Watanabe, S. Kikuchi, K. Horie, S. Kanda, Y. Tsukihashi, S. Abe, I. Ohuchi, S. Hanashima, S. Ichikawa, M. Ohshima, K. Ideno, Y. Tomita, Y. Yamanouchi, N. Ishizaki and H. Tayama. Engineering work section(Kosaku-ka) was in cooperation for the fabrication of the booster units.

II ATOMIC PHYSICS, SOLID STATE PHYSICS AND RADIATION EFFECTS IN MATERIALS

2.1 Binary Encounter Electrons Observed at 0° in Collisions of 4 MeV/amu F⁹⁺ with He

Masao SATAKA, Makoto IMAI, Yasunori YAMAZAKI[*],

Ken-ichiro KOMAKI[*], Kiyoshi KAWATSURA[**], Yasuyuki KANAI[***] and

Hiroyuki TAWARA[****]

Department of Physics, JAERI, [*]College of Arts and Sciences,

University of Tokyo, [**]Faculty of Engineering and Design,

Kyoto Institute of Technology, [***]The Institute of Physical

and Chemical Research(RIKEN), [****]National Institute for

Fusion Science

The binary encounter electron peak is a prominent feature in electron spectra originating from collisions between fast charged particles and atoms[1]. The peak is a result of close collisions between the projectile and a target electron. If collision takes place between a fully stripped ion with charge $Z_p e$ and energy E_p and a free electron at rest, the electron energy at zero degree with respect to the ion beam direction (180° in the projectile frame) is $E_b = 4(m/M)E_p$ where m and M are the electron mass and projectile mass, respectively. The binary electron production cross section for this simple case is

$$\sigma = const \times Z_p^2 e^4/E_b^2,$$

which shows a Z_p^2 dependence. The fact that the collisions involve only "quasifree" electrons which possess an initial momentum distribution due to their orbital motion around the target nucleus influences the binary encounter electron peak in two ways. The momentum distribution of the active electron gives rise to broadening of the binary encounter electron peak and the quasifree nature of the electron results in a small shift of the peak energies lower than E_b.[2]

The dependence of the binary encounter peak on the projectile charge states for partially stripped ions was investigated by Richard et al.[3] for fluorine ions with energies of 1 and 1.5 MeV/amu and charge from 3 to 9(fully stripped). They observed that for the partially stripped ions the cross section increased for decreasing charge state, a dependence which is in strong contrast to the behavior for fully stripped ions, where the cross section is proportional to the charge states to the second power. This

"surprising" charge-state dependence of the binary encounter production cross section has been treated in several theoretical papers by applying various models for electron scattering on ions.[4] In this dependence, outer screening thought to be important.

We have measured the binary encounter peaks for 0° electrons in collisions between 2 MeV/amu Si^{q+} and He.[5] As earlier measurement of Richard et al[3], we have found that the binary-encounter electron production increased for decreasing charge state. We have also found that the peak value of binary peaks were systematically shifted with increasing the charge states from expected value E_b. In the present work, measurements have been performed of zero-degree binary encounter electron spectra in collisions between 4 MeV/amu F^{q+} and He. In order to study the charge state dependence of binary electron production to impact energy, we have increased the projectile energy higher than that of measurement of Richard et al[3].

The experimental apparatus have already been described recently[6] so that only a brief outline is given here. The electron spectra were obtained by a tandem type electron spectrometer with two 45° parallel-plate electrostatic analyzer. The beam (76 MeV F^{5+} beam) was delivered by JAERI tandem accelerator. A post stripper facility provided ions with charge states 7, 8 and 9, which were magnetically separated and directed through a target cell containing helium with a pressure of about 10^{-3} Torr. Finally the beam was collected into a biased Faraday cup. Electron spectra were recorded in multiscaler mode and normalized to integrated beam intensity.

The binary encounter electron spectra were measured for F^{q+} (q=5, 7, 8 and 9) in the electron energy region between 5 and 12 keV. The peak height of the binary encounter spectra was derived from the spectra after background spectra obtained without gas in the target cell were subtracted. Figure 1 shows the ratios of the height of the peak for F^{q+} (q=5,7 and 8) to that of F^{9+} with the results measured by Richard et al.[3] for 1 and 1.5 MeV/amu. The ratios of the peak height calculated by the CTMC method by Schultz and Olson[7] are also shown. An enhancement of the peak height with increasing the number of projectile electron is seen in the figure. It is also found that the enhancement in 4 MeV/amu F^{q+} collisions is smaller than in lower energy collisions. In high incident energy region, the ratios may approach to unity, implying the Z^2 scaling is valid. The ratios derived from the present experiment is in good agreement with the theoretical values of Schultz and Olson[7] within the experimental error. The ratios from Richard

et al.[3] at lower projectile energies also agrees well with the theoretical values. The CTMC method explaines fairly well the behavior of binary peak with projectile charge states as well as projectile energies.

We are in progress to study the projectile charge state dependence of binary peak by heavier projectile than F^{q+}, such as Si^{q+}, S^{q+}, Ni^{q+}, Au^{q+}.

References

1) N.Stolterfoht: *Structure and Collisions of Ions and Atoms*, Ed. I.A.Sellin (Springer-Verlag, Berlin,1978) p.155.

2) D.H.Lee, P.Richard, T.J.M.Zouros, J.M.Sanders, J.L.Shinpaugh and H.Hidmi: Phys. Rev. A14,(1990)4816.

3) P.Richard, D.H.Lee, T.J.M.Zouros, J.M.Sanders and J.L.Shinpaugh: J.Phys.. B23,(1990)L213.

4) for example, K.Taulbjerg: J. Phys. B24,(1990)L762 and references there in.

5) P.Hvelplund, H.Tawara, K.Komaki, Y.Yamazaki, K.Kuroki, H.Watanabe, K.Kawatsura, M.Sataka, M.Imai, Y.Kanai, T.Kambara and Y.Awaya: J. Phys. Soc. Jpn, 60,(1991)3675.

6) M.Sataka, K.Kawatsura, H.Naramoto, Y.Nakai, Y.Yamazaki, K.Komaki, Y.Kanai, T.Kambara, Y.Awaya, J.E.Hansen, I.Kádár and N.Stolterfoht: Phys. Rev. A44,(1991)7290.

7) D.R.Schultz and R.E.Olson: J. Phys. B24,(1991)3409.
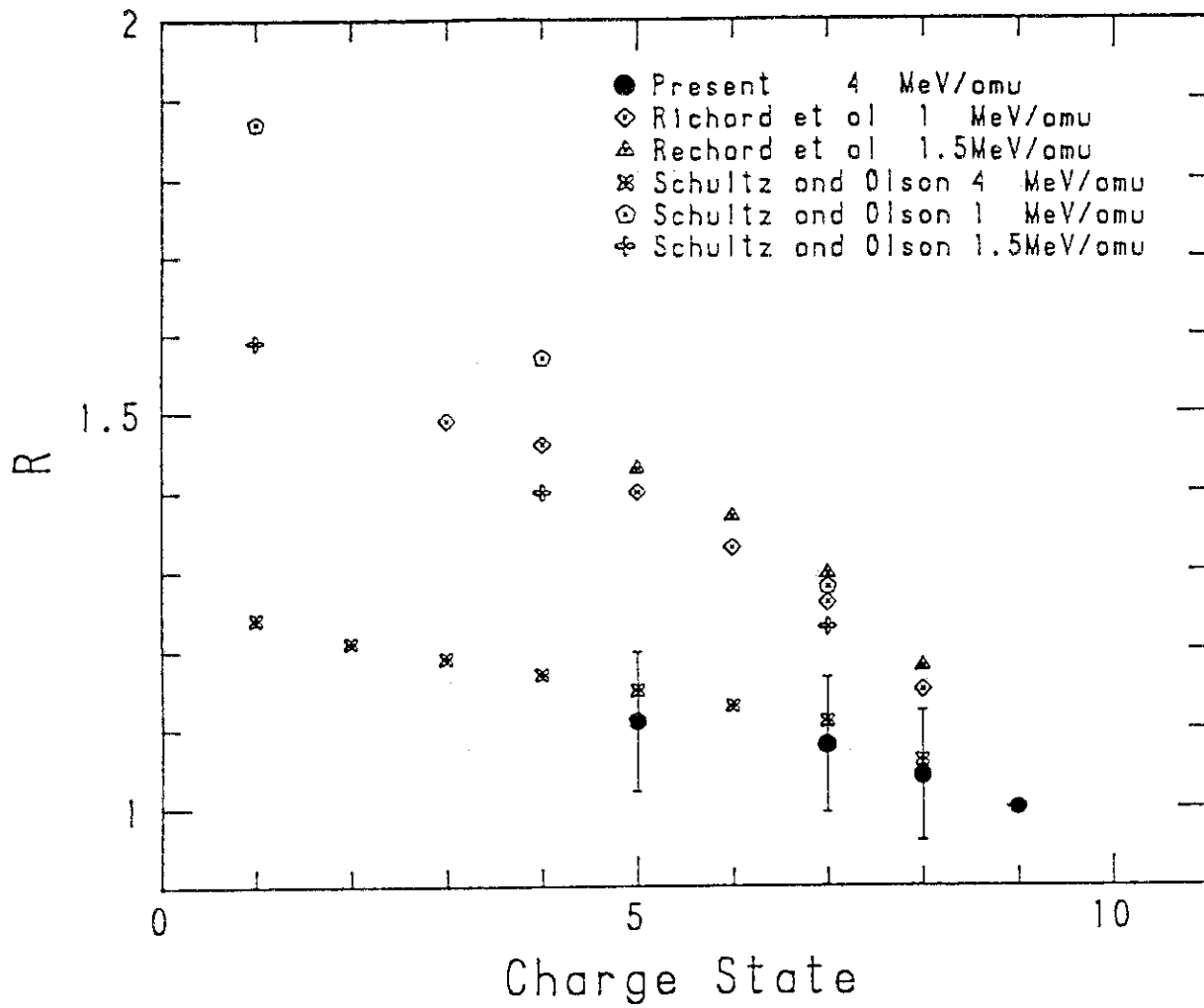
Fig.1 Ratios of the height of the binary encounter peak for F^{q+} to that of F^{9+} on He.

2.2 Charge Distribution of Neon Recoil Ions by Carbon Ions Impact in Coincidence with Projectile Final Charges

Makoto IMAI and Masao SATAKA

Department of Physics, JAERI

Introduction

The production of highly charged recoil ions in energetic-ion-atom collisions has been a stimulus problem since the pioneering work by Cocke[1]. It is known that there exists three production channels of recoil ions, plus one post-collisional process that increases the recoil ion charge states — (i) pure ionization, in which the projectile directly strikes off target electron(s) while its charge state remains unchanged, (ii) loss and ionization, where the projectile loses its electron(s) while the target atom is ionized, (iii) transfer ionization, in which the projectile captures target electron(s) into its bound states and the target may emit another electron(s) to the continuum. Additionally, provided the target results in an autoionizing state formed through inner shell vacancy production or multiple electron capture, it may autoionize and its charge state become increased. Coincidence measurements between projectile final charge states and recoil ions are needed to distinguish these three production channels. Recently it became clear from such measurements[2] that the production channels (ii) and (iii) form entirely different distributions of recoil target charge states from that of (i). More experimental and theoretical efforts are now being made, including investigations of charge multiplication via autoionizations after the collision.

We have improved our experimental apparatus at the 2MV VdG Accelerator Facility utilizing position-sensitive particle detector and multi-parameters data aquision system, and measured charge states of recoil ions produced in 100keV/amu carbon - neon collisions in coincidence with projectile final charge states.

Experiment

The present experiment was performed using 100keV/amu C^+ ions provided with the 2MV VdG accelerator. As illustrated in figure 1, the projectile beam was analyzed by its charge state and energy with 90° analyzing magnet and collides with target Ne atom, filled in the gas target cell. Neon recoil ions were extracted by an electric field through time-of-flight (TOF) drift tube and detected with a channeltron electron multiplier (CEM), while the projectile ions were detected with a position-sensitive solid-state detector (PSD) after separated by an electrostatic deflector. Charge states of the recoil ions were

identified by the TOF technique, whose outputs were recorded into two-parameters data aquision system with information on projectile final charge states in LIST-mode. Target gas pressure was kept constant automatically and was measured using the MKS spinning-rotor absolute pressure gauge. To confirm the single collision condition, we used the growth method varying the target gas pressure from 1×10^{-4} to 5×10^{-3} Torr. The effective length of the target gas cell was 80.1mm and the whole vacuum chambers downstream the 20° bending magnet were kept below 5×10^{-7} Torr during the experiment. The extraction voltage of the TOF drift tube was 3kV, which provides us with equal detection efficiency of CEM for different charge states. The PSD was covered by a square slit of 44.5×5.5mm, where, in the present case, four neighboring charge states can be detected simultaneously. When PSD is used as a projectile detector, we meet a serious problem that we have to limit the number of particles going into the PSD below 1000 counts per second. We have a special beam-reducing equipment consisted of two sets of cupper meshes upstream the 20° bending magnet, whose containing chamber is used as a stripper gas cell when we want to change the projectile initial charge state.

Results

The typical coincidence rate – the number of recoil ions to that of projectiles – was 0.135% for the present case. A typical two-dimensional plot of the number of coincident events against the projectile final charge states and the flight time of the recoil ions is shown in figure 2. We can see coincident events for four different projectile final charge states and two or three recoil ion charge states, 0 to 3 and 1 to 3, respectively, there. Relative shifts of the flight time for each projectile final charge state observed here come from delay of stop pulses. It takes some hundreds nanoseconds for electron-hole pairs induced inside the PSD to move from where they are created to the collector electrode, which causes delay to the stop pulse corresponding to the projectile's incident position.

Though the statistics is still poor, the fraction of the coincident events which resultd from electron capture or loss to the projectile to all the coincidence events is drastically high compared with that for familiar non-coincident measurements, especially for the cases where highly ionized ions were produced. This result shows that projectile electron capture or loss processes have great significance for producing recoil ions and that the higher the recoil charge state is, the more significant these processes become.
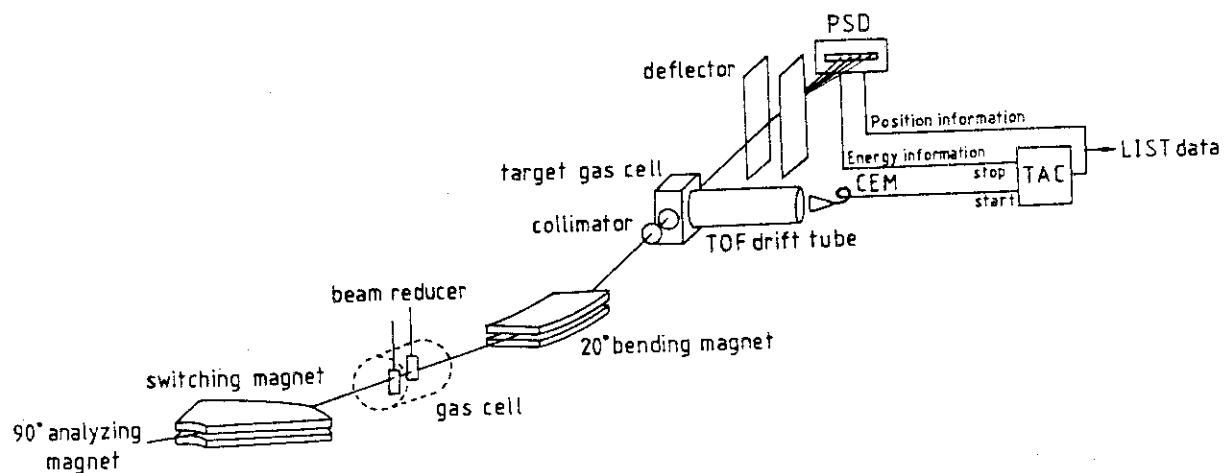
Fig.1   Schematic of the apparatus.
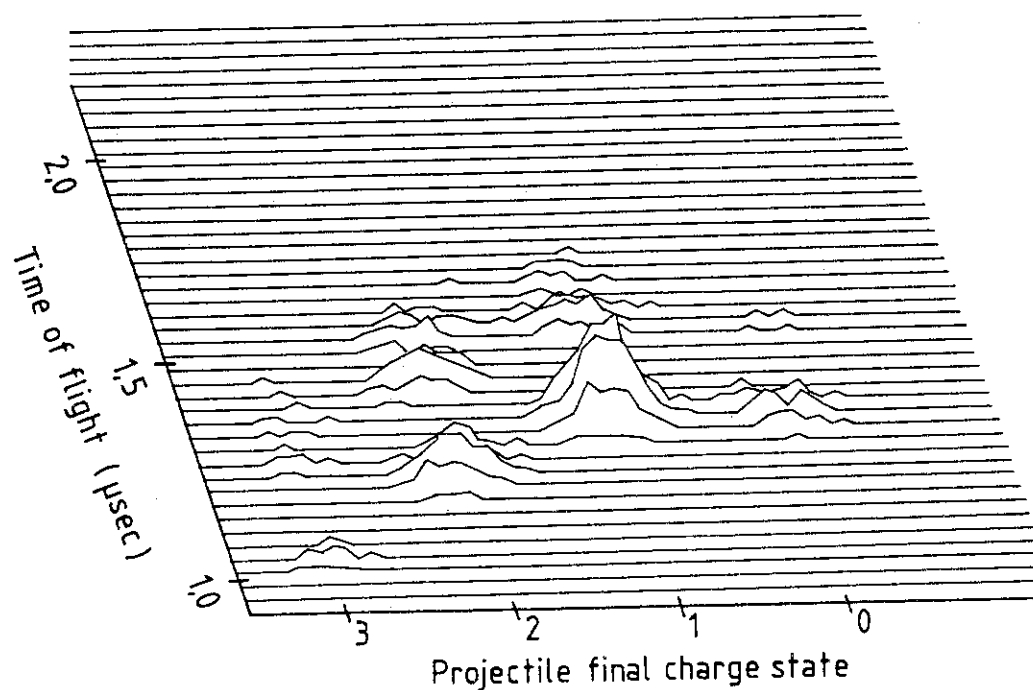
Fig.2   Two-dimensional plot of coincident events for 100keV/amu C$^+$ - Ne collisons.

References

1) C.L.Cocke: Phys. Rev. A20 (1987) 749.

2) For example; J.L.Shinpaugh, J.M.Sanders, J.M.Hall, D.H.Lee, H.Schmidt-Böcking, T.N.Tipping, T.J.M.Zouros and P.Richard: Phys. Rev. A45 (1992) 2922.

2.3 Cascade Damage in Gold by High Energy
Self-ion Irradiation

Yurugi KANZAKI, Naoto SEKIMURA* and Shiori ISHINO

Department of Nuclear Engineering, University of Tokyo,
*Nuclear Engineering Research Laboratory, University of
Tokyo

1.Introduction

The concentrated production of displacement damage in a cascade produced by a high energy PKA (primary knock-on atom) can directly form defect clusters and modify existing clusters[1]. In analyzing the effect of collision cascades, we have been monitoring the behavior of vacancy clusters produced by collision cascades, and it is necessary to perform thin foil experiment[2-4]. Gold has been mainly selected as the specimen because of its high interstitial mobility. In Au thin foil, interstitials released from cascade zone are expected to escape quickly to annihilate at surfaces or at existing vacancy clusters. Therefore, only vacancy clusters are considered to be formed.

The structure of cascade damage produced by high energy particles is dependent on PKA energy, and it is pointed out that the PKA energy spectrum analysis of cascade formation is necessary when experimental results from various irradiation means are compared[5,6]. Ion irradiation is advantageous to do such an analysis because it is easy to change ion energy, which is considered as PKA energy. So, we have studied cascade damage in gold under 400keV Xe ion irradiation[7].

In the present study, the defect clusters in gold irradiated with 197MeV Au ions at room temperature were observed to examine the difference in cascade damage structure according to the PKA energy. The goal of our study is to predict the cascade damage produced by 14MeV neutrons by means of the PKA energy spectrum analysis of cascade formation.

2.Experimental

Thin foils of 99.99% pure gold and of 25μm in thickness were thinned by electro-polishing for TEM observation and sandwiched between two sheets of copper mesh of 3mm in diameter. Then they were annealed in a high vacuum for one hour at 973K. These specimens were irradiated with 197MeV Au ions up to 4.7×10^{17} and 4.7×10^{18} ions/m^2 at room temperature using a

tandem accelerator at JEARI, Tokai. Ion flux was about 1.5×10^{14} ions/m^2/sec at the beginning of irradiation.

The defect structures in irradiated Au foils were observed using a 200kV TEM and the size distributions of defect clusters were derived. Defect cluster sizes were measured in their diameters of dark field microscope images.

3.Results and discussion

Defect clusters were formed and accumulated in Au foils irradiated with 197MeV Au ions at room temperature. Observed defect clusters were considered to be vacancy clusters formed from cascades. The range of 197MeV Au ions in gold is about 7.5μm[8], so all of the injected ions were considered to penetrate the specimens where TEM observations were performed.

Fig.1 shows the size distributions of defect clusters irradiated with 197MeV Au ions at room temperature up to 4.7×10^{17} and 4.7×10^{18} ions/m^2. It seems that the fraction of small clusters of 1nm in diameter increases with ion fluence. Similar tendency was observed in Au foils irradiated with 400keV Xe ions at room temperature[7]. Further irradiation makes defect cluster density higher, and the regions where defect clusters have not been formed are divided into smaller regions. Therefore, newly formed clusters may have higher fraction of small clusters for higher ion fluence.

Fig.2 shows the PKA energy spectrum in gold for the irradiation with
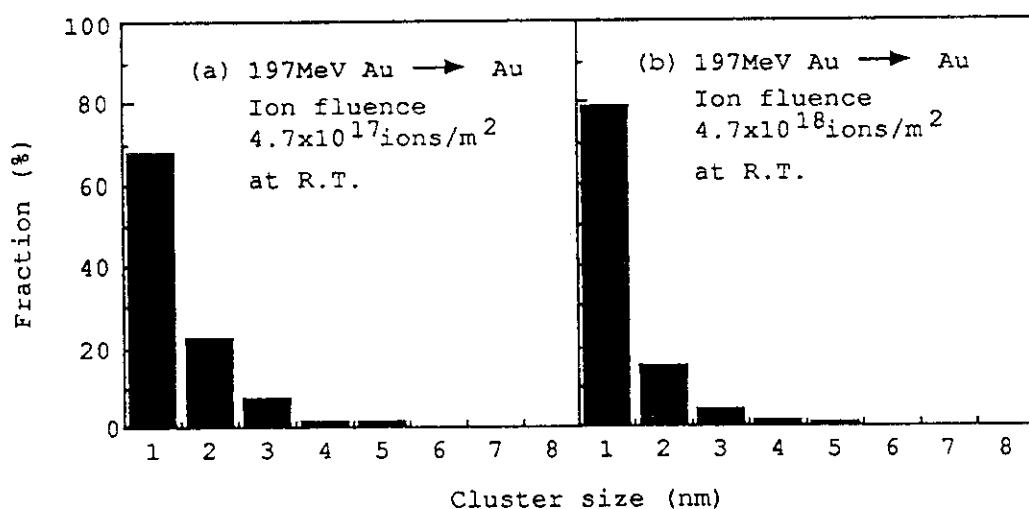
Fig.1 Size distributions of defect clusters in Au foils irradiated with 197MeV Au ions up to (a)4.7×10^{17}ions/m^2 and (b)4.7×10^{18}ions/m^2 at R.T.
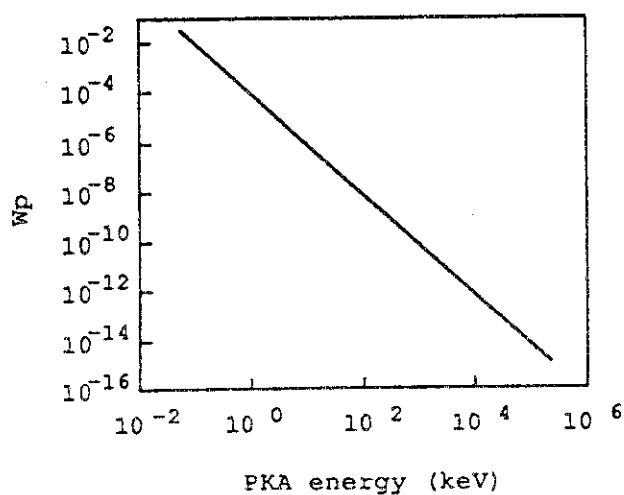
Fig.2 PKA energy spectrum in gold
for the irradiation with 197MeV Au
ions (thin foil case)

197MeV Au ions described from
Rutherford scattering[9]. Slight
fraction of the PKAs have high
energy to form cascade damages, but
considerable fraction of them have
low energy only to make Frenkel
pairs. Many migrating single
interstitial atoms (SIA) exist
compared with cascades, and vacancy
clusters produced by cascades absorb
SIAs and are considered to be
reduced in their sizes.

High energy PKAs are
considered to form plural cascades,
namely sub-cascades. The threshold
PKA energy above which plural sub-
cascades can be formed is called a
sub-cascade energy[10], which is about 13keV for gold[11]. Terefore, a size
of one cascade has its upper limit, and unless coalescence of defect
clusters do not occur, defect cluster size also has its upper limit. The
maximum size of observed defect clusters is almost the same as that of
400keV Xe ion irradiation, shown in fig.3[7].
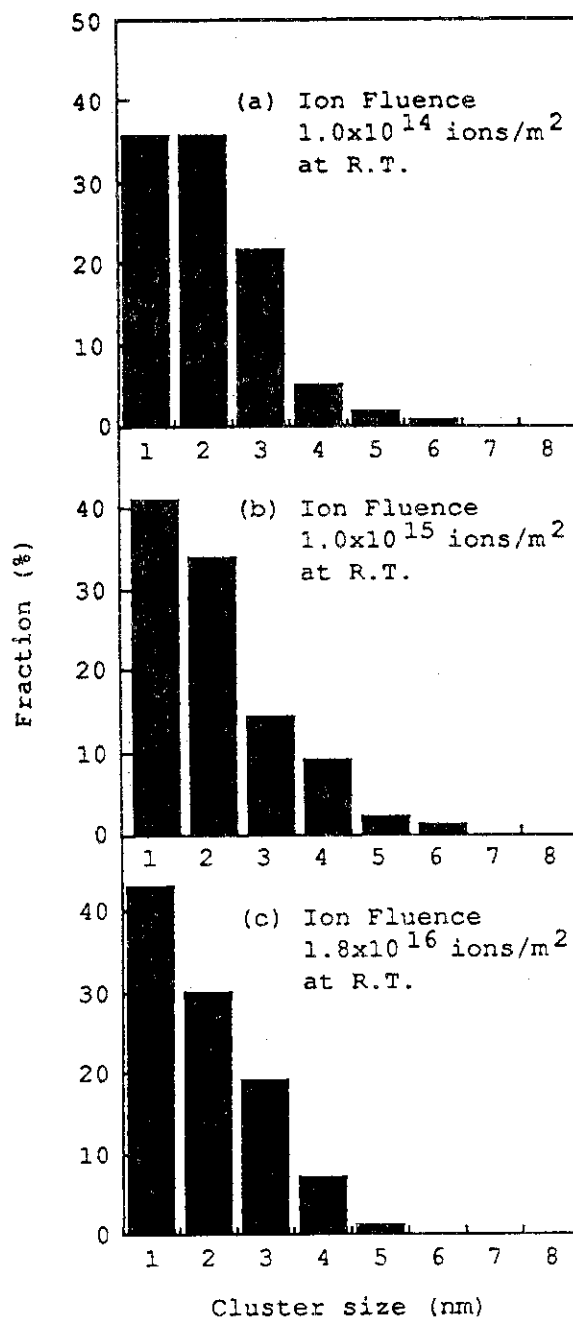
Fig.3 Size distributions of defect
clusters in Au foils irradiated
with 400keV Xe ions at R.T.

Assuming the thickness of the specimens to be the same, defect cluster density of Au foil irradiated up to 4.7×10^{18} ions/m^2 is 1.2 times higher than that irradiated up to 4.7×10^{17} ions/m^2. Defect cluster density is too high to derive information on sub-cascade structure in both cases.

4.Future work

Injected ions loose their energy while they are passing in materials. Therefore, PKA energy spectrum varies with the depth from the surface. We will make an experiment to examine the difference in cascade damage structure according to PKA energy, where PKA energy spectrum will be changed in a controlled manner by putting Au foils in proper thickness in front of Au foil specimens.

Lower fluence irradiation is necessary to analyze the sub-cascade structure, and more detailed analysis of cascade structure will be required.

References

1) S. Ishino, T. Muroga and N. Sekimura: Nucl. Eng. & Des./Fusion 2 (1985) 3.

2) M. Kiritani: Mater. Sci. Forum 15-18 (1987) 1023.

3) M. Kiritani, T. Yoshiie and S. Kojima: J. Nucl. Mater. 141-143 (1986) 625.

4) M. Kiritani: J. Nucl. Mater. 137 (1986) 261.

5) S. Ishino and N. Sekimura: Ann. Chim. Fr. 16 (1991) pp.341-350.

6) M. Kiritani: J. Nucl. Mater. 179-181 (1991) pp.81-86.

7) Y. Kanzaki, N. Sekimura and S. Ishino: to be published in the Proceedings (ICFRM-5), J. Nucl. Mater.

8) U. Littmark and J. F. Ziegler: Handbook of Range Distributions for Energetic Ions in all Elements

9) D. S. Billington and J. H. Crawford Jr.: Radiation Damage in Solids (Princeton Univ. Press, 1961)

10) T. Muroga, K. Kitajima and S. Ishino: J. Nucl. Mater. 133&134 (1985) 378.

11) M. Kiritani, T. Yoshiie, S. Kojima and Y. Satoh: Radiat. Eff. and Defects in Solids 113 (1990) pp.75-96

2.4 Dependence of Irradiation Damage on Specimen Thickness in Ion-irradiated Nickel

Akihiro IWASE, Tadao IWATA and Takeshi NIHIRA[*]

Department of Physics, JAERI, [*]Faculty of Engineering, Ibaraki University

In the previous papers, we showed that the electron excitation by high energy ions caused the radiation annealing in FCC metals with a strong electron-phonon interaction[1-4]. This effect has been observed as an anomalous reduction of stage-I recovery in Ni and Pt[1,2], a decrease of the defect production cross section in Ni[3] and so on. The above results were, however, obtained in the thin foil specimens about 0.2μm thick. In this report, we show that the radiation annealing by electron excitation can be observed independently of the specimen thickness.

In the present experiment, three nickel specimens 0.24μm, 0.65μm and 1.5μm thick were irradiated with 120 MeV Cl ions at <10 K. During irradiation, the electrical resistivity change $\Delta\rho$ was measured as a function of ion fluence. After irradiation, an annealing experiment was performed up to 300 K to get a defect recovery spectrum.

Figure 1 shows the resistivity change rate $d(\Delta\rho)/d\Phi$ on a log plot as a function of ion fluence Φ. The experimental $d(\Delta\rho)/d\Phi$ curves are the same for three specimens. The value of the defect production cross section, which can be obtained from the initial value of $d(\Delta\rho)/d\Phi$, is much smaller than expected from the atomic displacement by elastic collisions. As can be seen in Fig. 2, the anomalous reduction of stage-I recovery is observed in every specimen. From the experimental result we conclude that the radiation annealing by electron excitation occurs in nickel independently of the specimen thickness.

References

1) A. Iwase, S. Sasaki, T. Iwata and T. Nihira, Phys. Rev. Lett. 58, (1987) 2450.

2) A. Iwase, T. Iwata, T. Nihira and S. Sasaki, Mater. Sci. Forum (1992) in press.

3) A. Iwase, S. Sasaki, T. Iwata and T. Nihira, J. Nucl. Mater. 155-157, (1988) 1188.

4) A. Iwase, T. Iwata, S. Sasaki and T. Nihira, J. Phys. Soc. Jpn. 59, (1990) 1451.
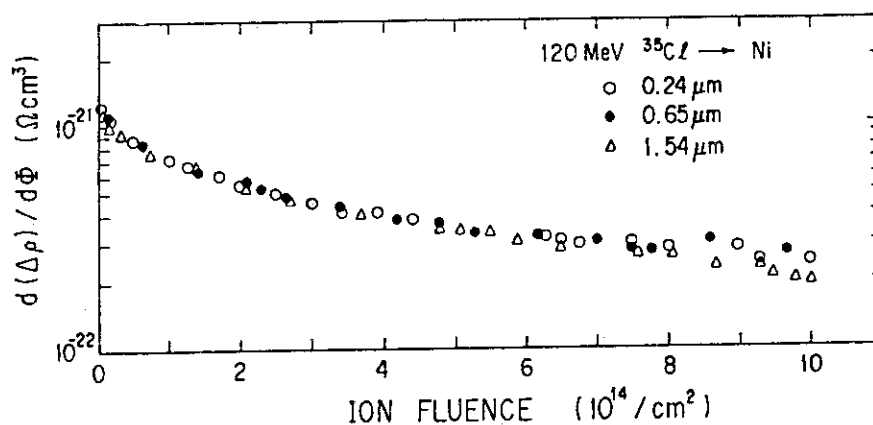
Fig. 1
Electrical resistivity change rate d(Δρ)/dΦ as a function of ion fluence in nickel irradiated with 120 MeV Cl ions.
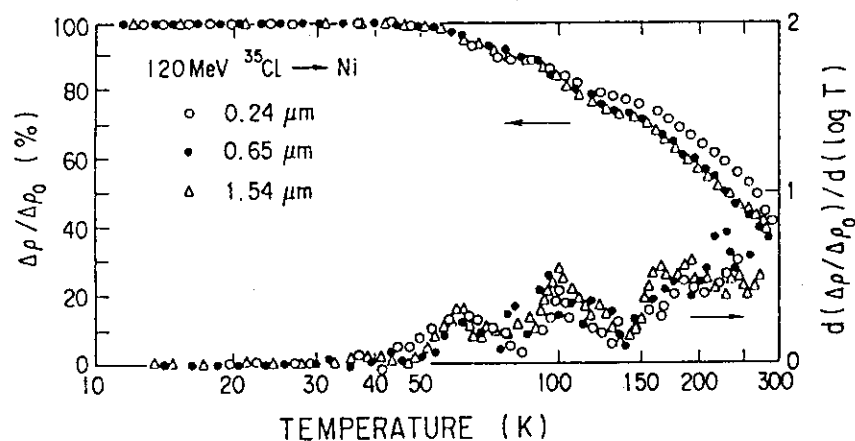
Fig. 2
Recovery curves of electrical resistivity and their temperature derivatives in nickel irradiated with 120 MeV Cl ions.

2.5 Positron Reemission Microscope using Intense Slow Positron Beam from an Electron Linac

Saburo TAKAMURA, Yasuo ITO*, Masafumi HIROSE*,

Ikuzo KANAZAWA** and Sohei OKADA***

Tokai Research Establishment, JAERI, *Research Center for Nuclear Science and Technology, The University of Tokyo, **Faculty of Education, Tokyo Gakugei University, ***Takasaki Radiation Chemistry Establishment, JAERI

1. Introduction

The positron reemission microscope is a unique way of observing subsurface defects and imaging overlying atoms. Using the positron beam from a radioactive source, the positron reemission microscope was constructed by House and Rich[1] and Brandes et al.[2] The positron beam used by them was produced by moderating positrons from a radioactive source. The exposure time for imaging required over 10-30 hours since the intensity of the positron beam was weak. So, it is important for the positron reemission microscope to use the intense positron beam produced by using an electron Linac. Here, we report the result that the intense slow positron beam produced by using an electron Linac is focused on a tungsten(W) foil and the image of reemitted positrons is produced using the proto-type of the positron reemission microscope.

2. Experimental procedures

The positron beam in our experiment was produced using the 100 MeV electron Linac. The pulse electron beam irradiated a tantalum target. The conversion from electrons to positrons was made by the target. Fast positrons were moderated through a W plate with 25 μm thick which was set in the vacuum chamber. Slow positrons were transported through the vacuum tube. The beam tube was bent twice. The intensity of the slow positron beam was about 2×10^7 e$^+$/s. The size of the beam before electrostatic accceleration in the magnetic field was about 10 mm. At the end point of the beam tube, the electrostatic lenses were installed in the magnetic field and the acceleration of the positron beam was performed using parallel grid electrodes. The beam was focused on the W foil. The beam profile was measured by a

microchannel plate assembly (MCP). The diameter of the beam spot was about 3 mm. We used the brightness-enhanced positron beam in our first experiment but the intensity of the positron beam was so weak that the direct beam was used without performing the brightness enhancement in the present work. The experiments of the transmitted positron reemission microscopy were done using the focussed positron beam. The focussed beam accelerated to 4 keV were incident to the W foil.

The lens electrodes are shown in Fig.1. The lenses are of the symmetrical three electrodes and the lenses have symmetry with respect to the midplane of the central electrode. The electrode aperture diameter was 2 mm, the interelectrode spacing was 2 mm and the thickness of the electrode was 1 mm. The end electrodes were at ground potential. The distance between the W foil and the objective lens was about 2 mm and the distance between the lens electrodes and the MCP was 60 mm. The MCP had a phosphor screen anode which generated a spot of light for incident particles. The spot was detected by a camera and recorded by an image analysis system.

The W (100) foil was 2000 A thick. The foil overlying the W mesh was mounted on the stainless steel holder having 7 mm diameter opening and the holder was installed on the samle manipulator. The mesh period was 250 μm.

3. Experimental results and discussion

The implantation profile of positrons is calculated with the following function[3].

$$P(z, E) = 2z \exp(-(z/z_0)^2)/z_0^2$$

where $z_0 = 450E^{1.6}/\rho$, ρ is the density of the foil, and E is the incident positron energy. It estimates that the implanted positrons do not directly reach at the opposite surface of the foil with the thickness of 2000 A. The positrons implanted into the one side of the foil thermalize and diffuse to the other side of the foil, and reemit with a energy by the negative of positron work function. The probability of transmitted positrons is given by

$$J = \int_0^{2000} P(z, E) \exp(-(2000-z)/L) dz$$

where L is the diffusion length in the W foil. The values of J for the accelerating voltage of 4kV are 0.05 and 0.16 for L= 600 and 1000 A, respectively. The transmitted positrons are reemitted in a narrow cone centered along the normal direction of the surface and the reemission positrons have the energy spectrum of a small energy width.

Positrons reemitted from the other side of the W foil were magnified by objective lens. The voltage was put on the W foil and the accelerating voltage between the foil and the objective lens was 2 kV. The image of the mesh placed behind the W foil was formed by ajusting the voltage of the center electrode. The magnetic beam deflectors were installed around the lenses to distinguish between heavy positive particles as protons and positrons since the present experiment was performed in a vacuum of 10^{-6} Torr and the heavy particles were considered to be accompanied. The image could be moved by a pair of deflection coils. Therefore, the image is considered to be formed by the positron beam. The picture displays the shadows of the mesh which is shown in Fig.2. The magnification was determined from the distance between the wires in the W mesh and the image distance on the detector, and was 10. The exposure time for imaging in the figure was 3 sec. In summary, we have observed the image of positrons reemitted from the 2000 A W foil by the positron reemission microscope using the intense positron beam produced from an electron Linac. The image was obtained only in 3 sec. The magnification was 10 at the present state. To generate the positron beam with high intensity and to improve the lens system of the microscope is in progress.

References

1) J.V.House and A.Rich: Phys.Rev.Lett. 61 (1988) 488.
2) G.R.Brandes, K.F.Canter and A.P.Mills,Jr.: Phys.Rev.Lett. 61 (1988) 492.
3) S.Valkaelahti and R.M.Nieminen: Appl.Phys. A35 (1984) 51.
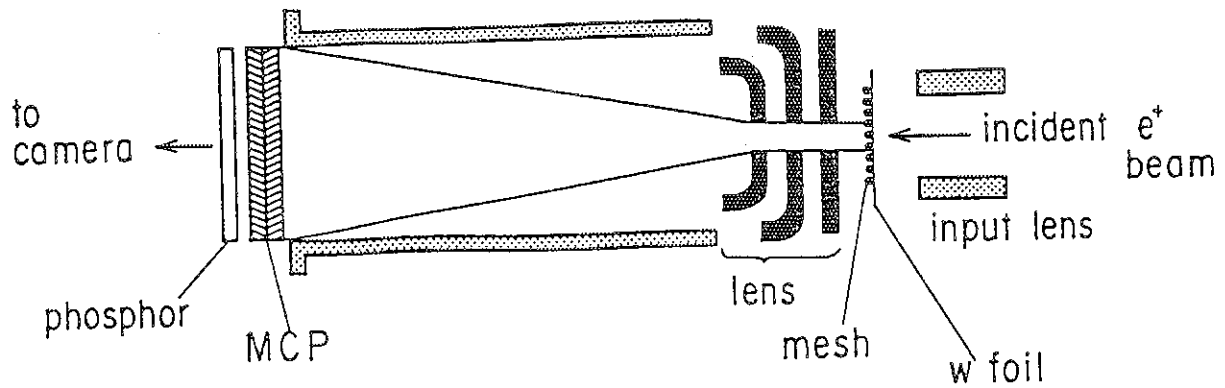
Fig. 1 Schematic of lens configuration and detector. The slow positron beam produced using an electron Linac was accelerated to 4 keV and focused, and was incident on the W foil. Image of reemitted positrons was formed at the detector by three electrode lens.
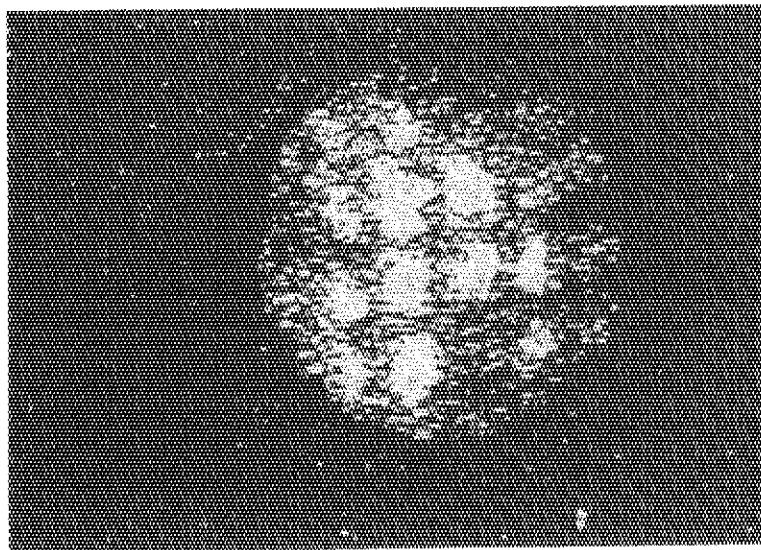
Fig. 2 Image of W mesh. The mesh period is 250 μ m and the diameter of MCP is 10 mm.

2.6 Profiling of Defects in C-ion Irradiated 316 Steel by S Parameters from Variable Energy Positron Annihilation

Takeo ARUGA, Saburo TAKAMURA[*], Masahumi HIROSE[**] and Yasuo ITOH[**]

Department of Fuels and Materials Research, [*]Department of Physics, JAERI, [**]Research Center for Nuclear Science and Technology, The University of Tokyo

More detailed information on depth profile of defects produced in the ion-irradiated solid is required in fundamental understanding on the interaction of ions with materials and radiation damage analyses. Since the first study made by Triftshäuser and Kögel[1], the variable energy positron beam techniques have been applied to depth profiling of defects introduced in metal samples by ion irradiations[2-4]. In this report are described the preliminary results of Doppler-broadening S parameters measured as a function of positron energies for the 316 stainless steel sample irradiated with 250 keV carbon ions.

The standard 316 stainless steel sample used in this study was solution annealed for 0.5 h at 1323 K in vacuum after cold rolling to 0.2 mm thick and being shaped with a size of 20x20 mm^2. The whole area of the sample was irradiated with a defocused 250 keV C-ion beam at room temperature with an ion flux of 3.9x10^{15}/m^2.s to a dose of 9.2x 10^{18}/m^2 by using a Van de Graaff accelerator. The irradiation is predicted to produce a peak displacement damage of 0.15 dpa (displacements per atom) around the depths of 250-270 nm and inject carbon atoms to about 500 appm there, by TRIM85 computer code[5].

The S parameter measurements were conducted by using an apparatus illustrated in Fig. 1, which was composed of a ^{22}Na positron source with an intensity of 1.5x10^8 Bq; a single crystal tungsten W(100) foil of 1 μm thickness which was annealed at 2273 K to remove defects and was attached closely to the source for moderating positrons; a tungsten mesh placed in front of the moderator to extract and accelerate the emitted positrons to 15 eV; solenoid coils supplying a magnetic field of 60-80 Gauss for bending the beam to eliminate high energy positron background; an accelerating system supplying 0 to 8 kV above the ground potential

between accelerating terminal flanges placed between focusing Helmholtz coils and 0 to −8 kV between the specimen and the ground. A high purity germanium detector of energy resolution capability of 1.1 keV at 511 keV is used with a multi-channel energy analyzing system for measuring annihilation gamma spectra. The beam profile was monitored by microchannel plate assembly with a phosphorescent plate. The diameter of the beam spot at the sample position was about 3 mm with the typical beam intensity of 3×10^4/s.

The S parameters of annihilation radiation spectra around 511 keV for monoenergetic positrons incident on the sample were obtained as a ratio of a count in 11 channels corresponding to 3.6 (i.e., ±1.8) keV around the peak to the total counts in 80 channels corresponing to 35 (±17.5) keV around the peak. The total count around the peak for each energy of positron was accumulated to $(4.9 - 5.3) \times 10^5$ in 1800 s. The parameters were measured as a function of positron energies from 15 eV to 16 keV at maximum. The positron with energy of 16 keV is predicted to have an average stopping range as deep as 420 nm, which is larger by 1.5 times than the projected range of 250 keV C-ions in the sample.

Figure 2 shows the positron energy dependence of S parameters measured for the solution annealed sample of 316 stainless steel and a fitted curve of S parameter obtained by using a best fit diffusion length of 51.5 nm for thermalized positrons. The S parameter decreases monotonically with an increase of the positron energy and shows a saturation tendency above 10 keV for the annealed sample. Figure 3 shows positron energy dependencies of S parameters for the sample after the irradiation with 250 keV C-ions and after annealing for 0.5 h at 423, 573, 723 and 823 K. The S parameters increase after the C-ion irradiation for positron energies above 2 keV and the increase over those before irradiation peaks at about 10 keV, which is easily seen in Fig. 4. Since the average range of 10 keV positrons is about 200 nm in the steel, the vacancy type defects seem to be peaked at smaller depths than the peak of ion-radiation damages.

From the decrease of S parameter after the anneal at 573 K as compared with those after the irradiation, it is evident that the remarkable recovery of the defects takes place after the 573 K anneal. It is seen that defects produced by the C-ion irradiation almost anneal out after the anneal at 823 K, since S parameters after the 823 K anneal

agree with those before the irradiation. It is noted that S parameters after the irradiation have large differences from those before irradiation even for the highest positron energy of 16 keV, which implies that the radiation produced defect would exist far beyond the ion range probably through displacements by sequential atom collisions.

References

1) W. Triftshäuser and G. Kögel : Phys. Rev. Lett., 48(1982) 1741.

2) S. Tanaigawa, Y. Iwase, A. Uedono and H. Sakairi : J. Nucl. Mater. 133&134 (1985) 463.

3) K. G. Lynn, D. M. Chen, B. Nielsen, R. Pareja and S. Myers : Phys. Rev. B 34 (1986) 1449.

4) A. Uedono, S. Tanigawa and H. Sakairi : J. Nucl Mater. 184 (1991) 191.

5) J. F. Ziegler, J. P. Biersack and U. Littmark :"The Stopping and Ranges of Ions in Solids" (Pergamon Press, 1985) Vol. 1.
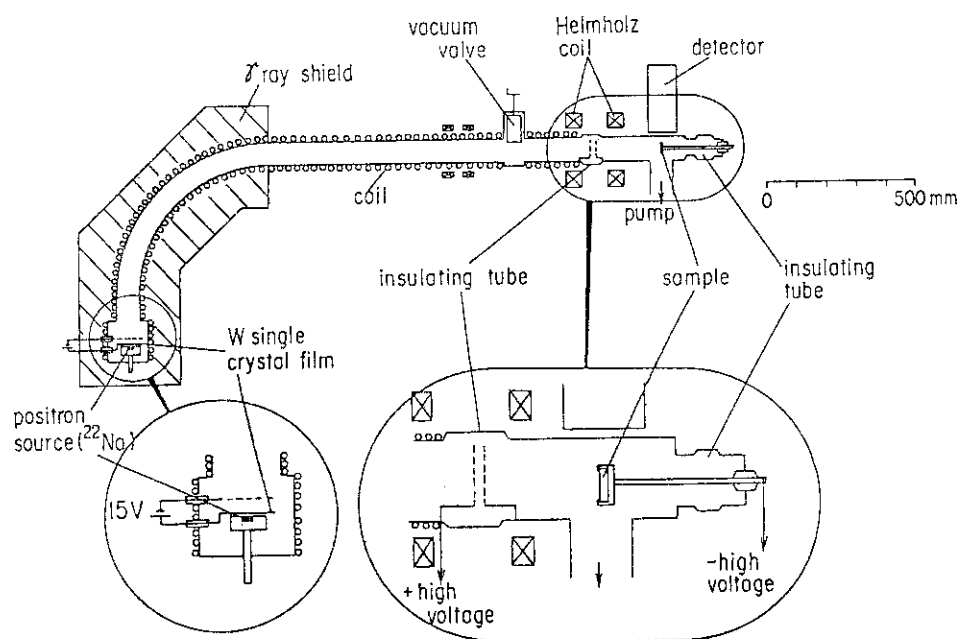
Fig. 1.   Schematic set up of positron beam system for S parameter measurement (see text).
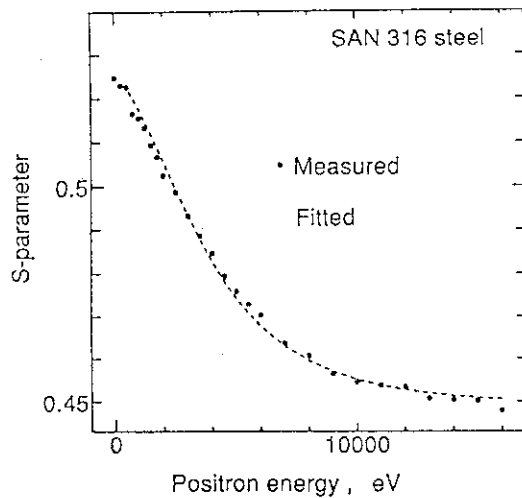
Fig. 2. Positron energy dependence of S parameters measured for solution annealed 316 stainless steel sample.
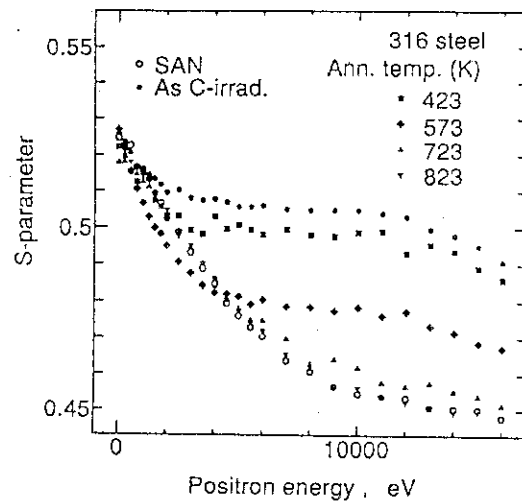
Fig. 3. Positron energy dependences of S parameters measured for 316 steel sample after C-ion irradiation and anneals at temperatures shown.
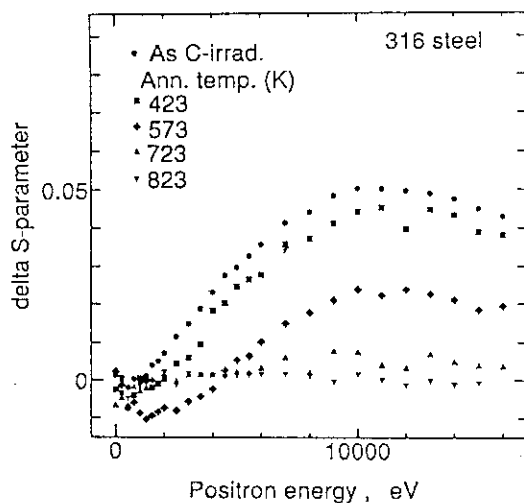
Fig. 4. Positron energy dependences of S parameter differences from those of unirradiated sample of 316 steel sample after C-ion irradiation and anneals.

2.7 X-ray Diffraction Topographic Observation of Si Single Crystals Irradiated with Energetic Heavy Ions (8)

Hiroshi TOMIMITSU and Vittaya AMORNKITBAMRUNG[*]

Department of Physics, JAERI.
[*] On leave from Department of Physics, Faculty of Science, Khon Kaen University, Thailand.

1.Introduction

The ion-implantation into the solid materials is used not only in doping the semiconductor device industry but also in studying the radiation effects in solid, especially in Si single crystal wafers which is very perfect in crystal structure.

There are many observations, results and conclusions about radiation effects with rather lower energies (1 to 2 MeV) through the conventional X-ray diffraction topography (XDT)[1]. One of the present authors(H.T.) has already reported the following results[2] through the XDT-observation of Si single crystals irradiated with various kinds of ions of rather higher energies (around 100 to 200 MeV) compared with previous authors;

(1) Macroscopic deformation was often observed all over the specimen.

(2) Very heavily strained lattice was observed at the boundaries between the irradiated- and non-irradiated areas, with black-white contrasts.

(3) Clear and beautiful interference fringes were observed within the irradiated area of the specimen crystal.

(4) On the other hand, in the same area, characteristic damage-contrasts were observed with other reflection.

The appearence- and disappearence-rule of the interference fringes were quite different from the conclusion of the observation and analysis reported by Bonse, Hart and Schwuttke[1].

The present work is mainly concerned with the difference between the effects of heavy ion-irradiations on Si single crystals during short-time and long-time with the same current at the JAERI Tandem accelerator.

2.Experimentals

120 MeV 0^{7+} ions were irradiated into two Si single crystal wafers, both being of (001) surface and of 0.5mm thickness. One was irradiated

during short period(0.25hr, dose per unit area of $3.6 \times 10^{13}/cm^2$), the other during longer period (20hrs, dose per unit area of $4.1 \times 10^{15}/cm^2$), the current being nearly the same, around 500nA, for both cases.

In the XDT-observation by conventional Lang camera, the sample crystal with the (001) surface was set so as to be rotated around the [110] axis. The X-ray generator was operated with 45kV and 25mA with Mo target, the effective focus size being 1mm in diameter. ILFORD L4 type nuclear emulsion plates of $50\mu m$ thickness were used for every topograph.

3.Results and Discussion

The XDT images of sample with short time irradiation are shown in Figs.1.(a) was taken with 440 reflection, in which only the lattice strains at the boundaries between the irradiated- and non-irradiated areas are observed with black-white contrast. Fig.1(b) was taken with $33\bar{3}$ reflection, showing clearly the interference fringes with rather long intervals. Other characteristic images in Figs.1 will be discussed later.

2mm

(a) (b)
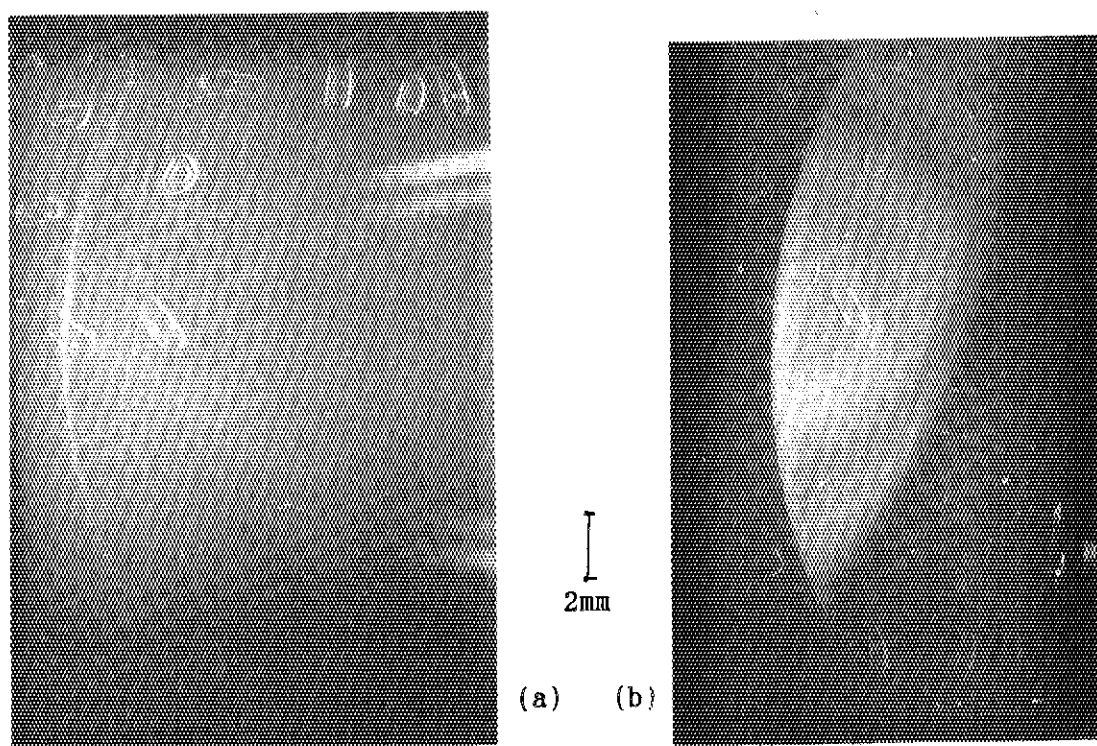
Fig.1 XDT images of the short-time irradiated specimen by 120MeV O[7+] ion. Fig.1(a) was taken with 440 reflection, while Fig.1(b) was taken with $33\bar{3}$ reflection, with rather long intervals. The irregular shaped smaller images are discussed in the text.

The XDT images of the sample with longer irradiation are shown in Figs.2. In Fig2.(a) taken with $\overline{333}$ reflection, just corresponding to Fig1(b) of short irradiated specimen, shows the interference fringes with much shorter intervals compared with short irradiation case. Fig.2(b), which was taken with $\overline{111}$ reflection, also shows the interference fringes with much longer intervals.

Furthermore, in the long-irradiation case, Fig.2(a), some special circle-shaped contrasts were very faintly observed within the irradiated area, as indicated by arrows in Fig.2(b). These contrasts seem to correspond to that reported by Schwuttke, Brack, Gardner and DeAngelis[1].

2mm

(a)   (b)
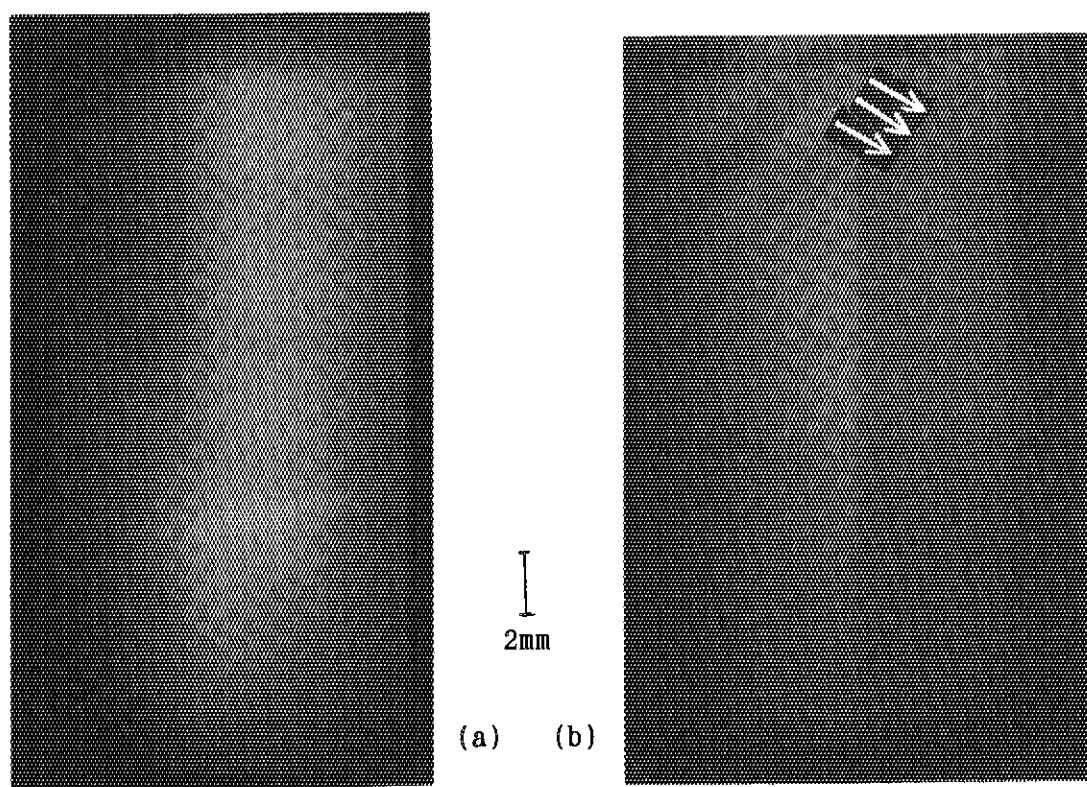
Fig.2 XDT images of the longer-time irradiated specimen by the same ion. (a) is taken with $\overline{333}$ reflection, and (b) with $\overline{111}$ reflection. Interference fringes are shown in both topographs, but the number of the fringes is much increased with higher indices (a). Several circular images are faintly seen as indicated with arrows in Fig.2(b), see text.

In both cases of irradiation time, the macroscopic deformation of the irradiated specimens was observed, i.e. the angular position of the reflection maximun in the rocking-curve slightly moved as the position of incident X-rays moved on the specimen surface, and also one could not get the total images of the specimen crystal in a topograph, but only partial images.

There are interesting images in Figs.1, which exactly correspond to the characters written on the specimen surface to record the irradiation conditions, etc., using a soft felt pen as usually. In this case, however, a special pen for transparency was used. The images show very similar contrasts as the black-white ones at the irradiation boundaries, indicating the heavily strained lattice, not a simple absorption of X= rays. Furthermore, those characteristic images were completely disappeared after the characters on the specimen surface were cleaned out by ethanol. These facts seem to show that the special ink of the transparency-pen caused the severe elastic lattice strain at the marginal part of every character.

Further investigations are now in progress.

References
1) A.R.Lang and V.F.Miuscov: Appl.Phys.Lett.7(1965)214.
   D.Simon and A.Authier: Acta Crystallogr.A24(1968)527.
   G.H.Schwuttke, K.Brack, E.E.Gardner and H.M.DeAngelis: Radiation Effects in Semiconductors (Plenum Press, N.Y., 1968)p.406.
   U.Bonse, M.Hart and G.H.Schwuttke: Phys.Status Solidi 33(1968)361.
   U.Bonse and M.Hart: ibid.33(1968)351.
2) H.Tomimitsu: Jpn.J.Appl.Phys. 22(1983)L674.
   H.Tomimitsu: from "JAERI TANDEM, LINAC & V.D.G. Annual report 1982" to bid.1987.

2.8 X-ray Diffraction from Carbon Ion-irradiated Diamond (III)

Katsuji HARUNA, Lu BANG*, Hiroshi MAETA*, Fumihisa ONO**, Yoshiharu IWASE, Toshimitu IWASAWA and Kazutoshi OHASHI

Faculty of Engineering, Tamagawa University, *Department of Physics, JAERI, **College of Liberal Arts and Sciences, Okayama University

1. Introduction

Diamond based semiconductor devices may turn out to be of great techno-logical importance due to the outstanding physical properties, such as high thermal conductivity, good thermal and chemical stability . It is very strong for radioactive rays and fits to the electron devices in the high temperature region owing to the wide energy gap. So,it is very important to study the ion irradiation effects on diamond. Ion implantation is a prime candidate technique for doping, but the issues of annealing radiation damage, avoiding graphitiza-tion, and driving implanted species into substitution sites have not been com-pletely resolved.

In order to resolve these processes, the damage due to self-implantation with 100 MeV C ions was studied by means of x-ray diffraction measurements of lattice parameters and diffraction profiles. We reported in previous paper[1] a increase of the lattice parameters and a remarkable increase of integrated inten-sities of x-ray diffraction profiles on a synthetic diamond single crystal after the ion-irradiations. Futhermore, we have reported the radiation effects of the diamond irradiated by 100 MeV C ion and 3 MeV electron so as to make the defects in diamond clear[2]. In this work, we report the result on measure-ment of the diffuse scattering.

2. Experimental Procedures

The synthetic diamond single crystals used in this experiment were pur-chased from Sumitomo Denko Co.Ltd. The specimens were a type lb crystals

which were colored yellow and contain 80 ppm of nitrogen. The crystal size was 3.5 x 3.5x 0.3 mm³ with the surfaces parallel to a (100) crystallographic plane. The specimens were irradiated with 100 MeV C^{+6} ion up to the fluences of 3.5 x10^{15} ions/cm² at about liquid nitrogen temperature using TANDEM Accelerator. After the irradiation, the specimens were warmed up to room temperature. The specimens were also irradiated at 60 °C with 3 MeV electrons to the fluences of 1 x 10^{19} e/cm².

Measurements of lattice parameters have been made at room temperature by using the X-ray Bond method in which two counters were placed symmetrically. In the present experiment the 400 reflection was observed, for which $2\theta= 160.01$. By using a fine slit of 0.2 mm in width, the Bragg reflections were measured at room temperature.

In measurement of diffuse scattering, we use the four-circl diffractometer combined with CuK rotating cathode as X-ray source and monochromatize the X-ray by Si (111) surface monochromator to select $CuK\alpha_1$ radiation.

3. Results and Discussion

We measured the diffuse scattering on 400 and 311 Bragg reflection surfaces. Figure 1 shows the results of measurement on the diffuse scattering intensity around the 400 Bragg reflection surface. We measured the diffuse scattering for h and k direction keeping l plane constant. It's results were showed in Fig.1-(a). Scattering intensity diffuses asimmetricaly as reciprocal lattice point. Fig.1-(b) and (c) show the results which were measured in the same way as in (a) keeping h and k constant, respectively. Figure 2 illustrates a shematic drawing of these resuls in reciprocal lattice space. From this, we know that the diffuse intensities exist in parallel to reciprocal lattice vector and points to an origin direction. These results suggest the existance of the interstitial type dislocation loop on (100) plane and precipitation. We could not find these phenomena in the specimen irradiated by electrons. This is due to the difference of defect concentration of which is one tenth of that by ion irradiation. We have so far showed the results as follows. With self ion irradiation of 48keV C ions the center of the irradiated region became amorphous at fluences of 4 x 10^{16}ions/cm² [2]. In present work with the 100 MeV C^{+6} ion up to the fluences of 3.5 x10^{15} ions/cm², the projected range was 102μm. So, the damage was considered to be widely distributed . The integrated intensities of the 400 diffraction profiles after the irradiations did change with fluence, extremely, after the ion irradiation. We measured the full width at half

maximum (FWHM) of the diffraction profiles for the irradiated and nonirradiated diamond specimens. It can be seen that after the electron irradiation FWHM of profiles did not change. The increases of the lattice parameter and unbroadening of profiles for the electron irradiated diamonds are presumed to be due to the formation of a point like defect and growth of defect clusters into dislocation loops. It is thought that the interstitial in diamond is mobile well below room temperature and the vacancy becomes mobile at 500 °C [3]. Most of the radiation damage are present as interstitial dislocation loops and vacancies. The increase of integrated intensities is due to the extinction effects which are associated with the point like defects and dislocation loops introduced by the ion irradiations. This fact is confirmed by the results after the electron irradiation.

A more detailed analysis of the present results and a further experimental study are currently in progress.

References

[1] H. Maeta, K. Haruna, K. Ohashi, T. Koike and F. Ono ; JAERI Tandem, Linac & V.d.G. annual report 1989. p 65–68.

[2] H. Maeta, K. Haruna, K. Ohashi, T. Koike and F. Ono ; JAERI Tandem, Linac & V.d.G. annual report 1990. p 44–47.

[3] S. Gorbatkin, R. Zuhr, J. Roth and H. Naramoto ; to be published.

Fig.1 Diffuse intensity of ion irradiated diamond

    (a) around 400 reflection on the k–h plane

    (b) around 400 reflection on the l–h plane

    (c) around 400 reflection on the l–k plane
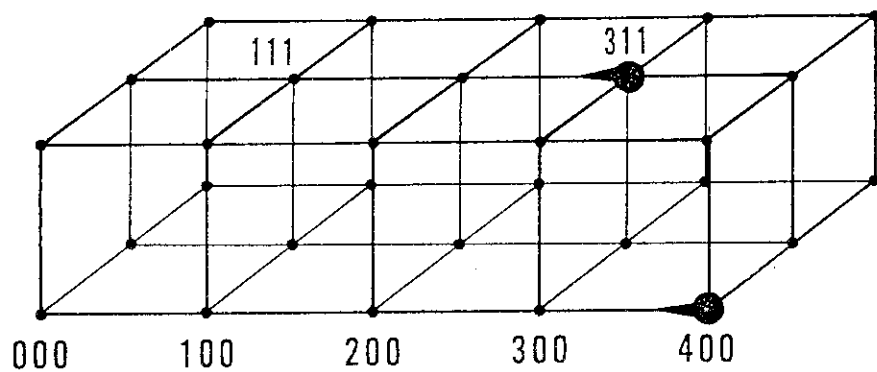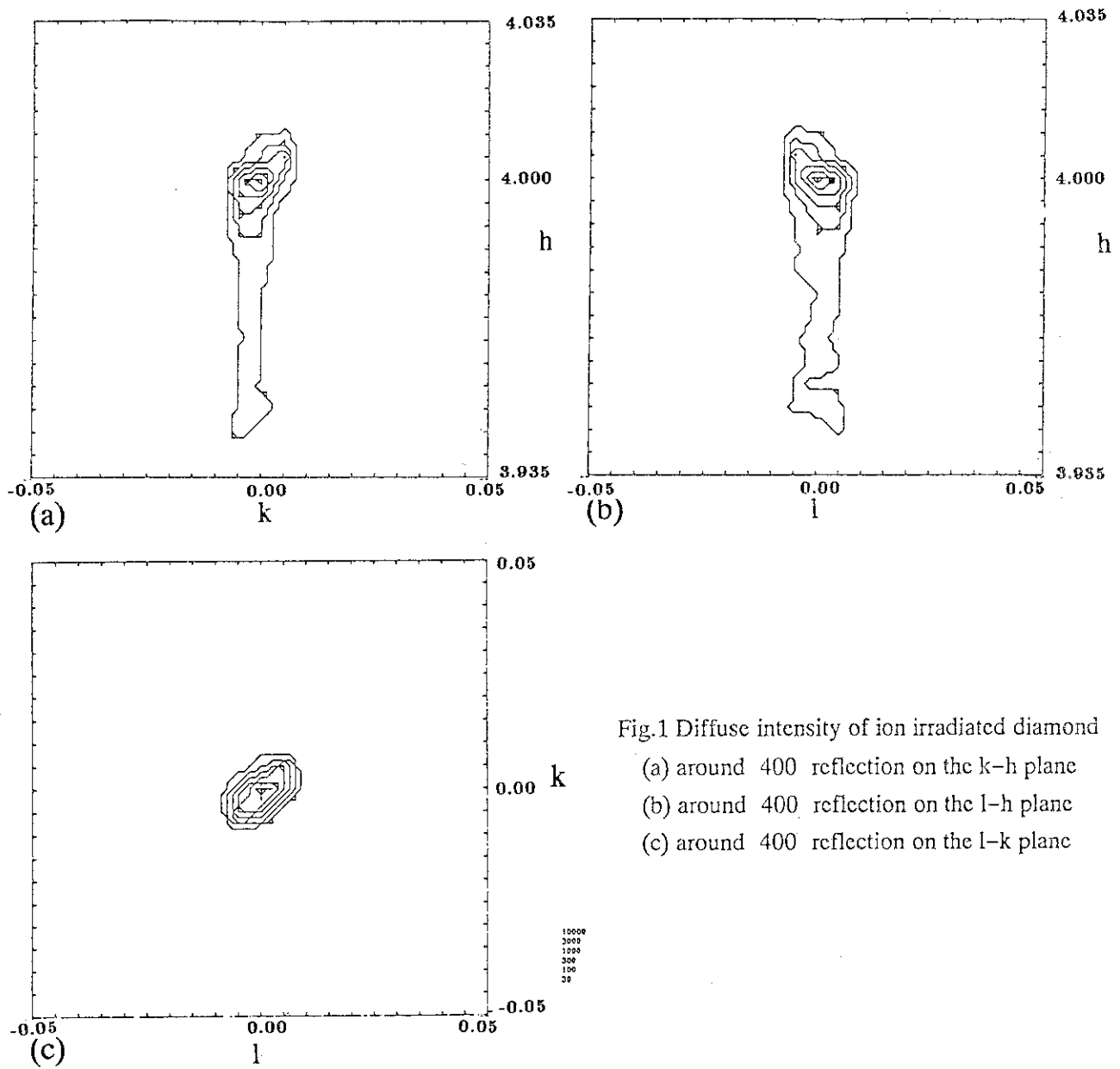
Fig.2 Schematic drawing of diffuse scattering in ion irradiated diamond

2.9 Ion Irradiation Effects of High Tc Superconducting Materials (I)

Yukio KAZUMATA and Satoru OKAYASU

Department of Physics, JAERI

In high Tc superconducting materials, radiation-induced defects are generally classified into two types; columnar defects and point-like defects including clustered defects. Whether an irreversibility line will be changed or not by point-like defects in high Tc superconducting materials is a controversial problem currently. Civale et al[1] emphasis that no change of the line is observed by point-like defects from the proton irradiation. On the contrary, systematic changes are reported in oxygen deficient YBCO[2] and in a partial substitution of various metal ions for Cu ions in YBCO[3]. Oxygen deficiency and impurity substitution are considered to be a kind of point defects. In this reason, reexamination for the change of the irreversibility line is made in this paper for O^{+7} and He^+ ion irradiation.

Thin films of YBCO were irradiated by 120 MeV O^{+7} and 1 MeV He^+ ions. Point-like defects are expected to be produced by these ion irradiation from calculation[4].

In Fig.1 temperature dependence of magnetization are shown for an
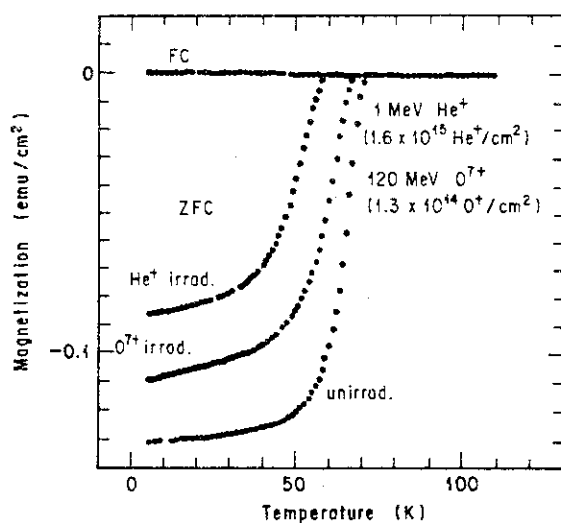
Fig.1 Temperature dependencies of magnetizations for three specimens, unirradiated, 120 MeV O^{+7} ions and 1 MeV He^+ irradiations, respectively. The irradiation doses are shown in Fig.

unirradiated specimen and two irradiated specimens for doses of 1.3×10^{14} ions/cm^2 O^{+7} ions and of 1.6×10^{15} ions/cm^2 He$^+$ ions,respectively. In this Fig.,the measurements were done at 10 gauss field and the ordinate shows magnetization normalized by the area of the films. Zero field cooling magnetizations show temperature dependence and these values are reduced by the irradiations, but field cooling magnetizations show nearly zero value. The transition temperature 71.3 K before the irradiation decreases to 68.8 K and 60.0 K for O^{+7} and He$^+$ irradiations, respectively.

Critical current densities are usually calculated by the assumption of Bean's model from the measurements of hysteresis loop. In this assumption the current density is proportional to ΔM, which means difference of magnetization between increasing and decreasing magnetic fields. ΔMs after the irradiations decrease to 0.7 and 0.4 times of the value before irradiation for O^{+7} and He$^+$ irradiations, respectively. The temperature dependencies of the ΔMs are well fitted by exponential functions as shown in Fig.2.
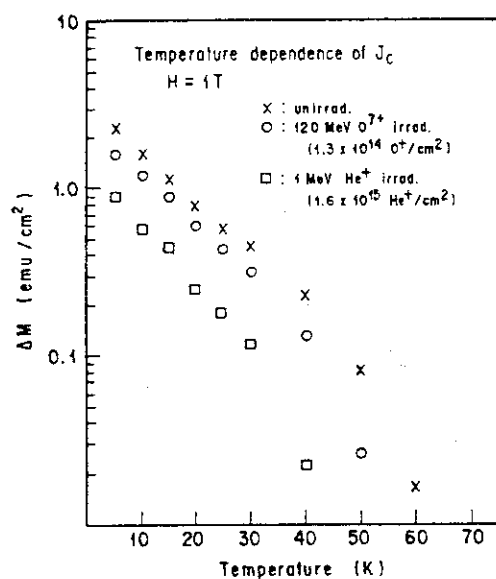
Fig.2. Temperature dependencies of ΔMs for the three specimens.

Irreversibility lines for the three specimens are shown in Fig.3. These lines are determined from the reversible magnetic fields in the hysteresis loops at the temperatures measured.The following equation is derived from the theory based on flux creep model[4],

$$H = a(1 - T_{irr}/T_c)^n \ , \ n=3/2$$

Y.Xu and M. Suenaga[2] reported that the irreversibility lines in $YBa_2(Cu_{0.98}M_{0.02})_3O_7$, where Cu ions are substituted for various metal ions M, shift parallel to that of non substituted material. Vanacken et al[3] also show that no change of the exponent of the above equation, but the coefficient a decreases systematically with the deficiency of oxygen ions in the range of oxygen contents of 7 - 6.6 in YBCO. They find that the decrease of the critical current density is proportional to the decrease of a. As pointed out above, Civale et al show no change of the line by point defects. As shown in Fig.3, however, our results indicate the change of the irreversibility line by point-like defects produced by the irradiations. The change is observed not only in the coefficient a, but also in the exponent n. This result stimulates the accumulation of experiments necessarily and also the further study of physical interpretation of the irreversibility line.
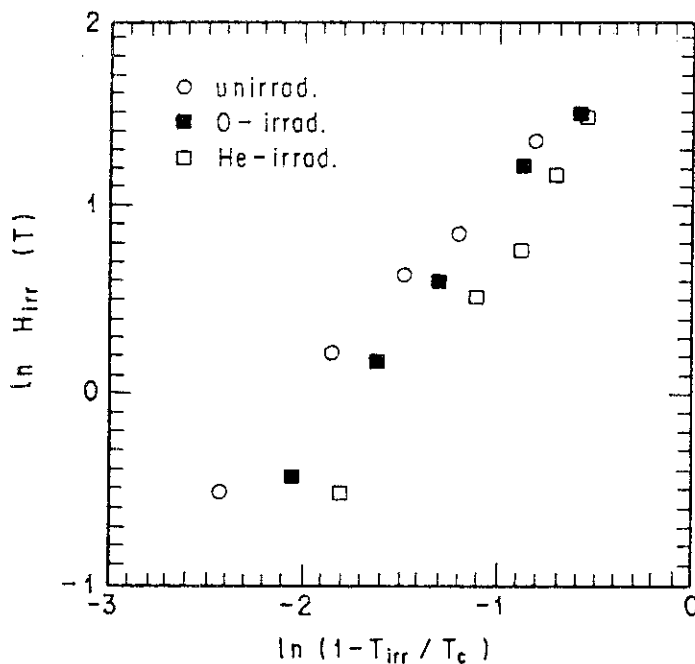
Fig.3. Irreversibility lines for the three specimens.

The activation energies of magnetic flux are obtained from the measurements of the time dependent relaxation of the magnetization. Time dependencies of magnetizations were measured under a magnetic field of 5 kgauss after reaching stable setting temperatures between 5 and 60 K. As shown in Fig.4, the activation energies after the 0^{+7} irradiation
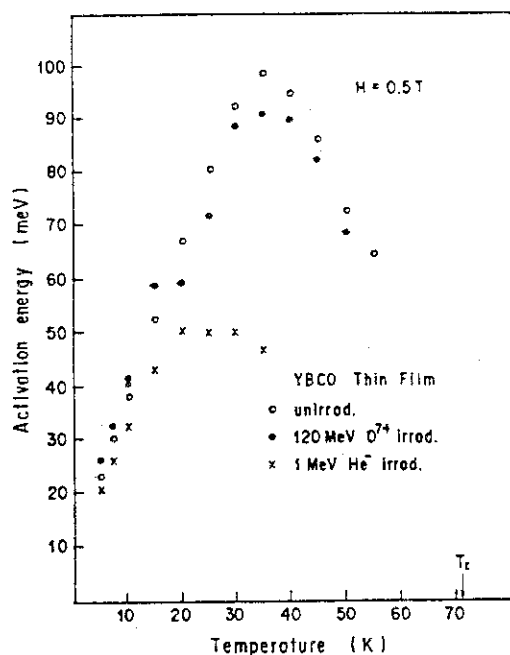
Fig.4. Activation energies obtained from time dependencies of magnetizations.

are not different from those before irradiation, but the energies after He$^+$ irradiation remarkably decrease above 15 K. This result of He$^+$ irradiation is parallel to the reduction of the current density with the irradiation.

Further details will be published soon.

References

1)L.Civale,A.D.Markwick,M.W.McElfrsh,T.K.Worthington.A.P.Malozemoff,
 F.H.Holtzberg,J.R.Thompson and M.A.Kirk: Phys. Rev. Lett. 65(1990)1164
2)Y.Xu and M.Suenaga : Phys. Rev.B43(1991)5516
3)J.Vanacken,E.Osqigul,C.Van Haesendonck and Y.Bruynseraede:
 NATO Advanced Study Institute (Greece) (1991), Private Commun.
4)T.Aruga,K.Nakata and S.Takamura: Nucl. Instrum & Method B33(1988)748

2.10 Effect of He Ion Irradiation on Activation Energy in YBa$_2$Cu$_3$O$_y$ Films

Norito ISHIKAWA, Akihiro IWASE, Tadao IWATA, Ryozo YOSHIZAKI[*], and Osamu MICHIKAMI[**]

Department of Physics, JAERI, [*]Institute of Applied Physics, University of Tsukuba, [**]NTT Interdisciplinary Research Laboratories.

In this study, we measured R-T curves (temperature dependence of resistance) for YBa$_2$Cu$_3$O$_y$ over the temperature region around T$_c$ (superconducting transition temperature) before and after the ion irradiation. We observed increase of normal-state resistance together with decrease of T$_c$ due to He ion irradiation. As a next step of the study, we measured R-T curves under the magnetic field of 2 tesla before and after the irradiation. We assumed thermally activated process of flux line[1] at the temperature just above T$_{c0}$ (endpoint of superconducting transition). Then, decrease of effective activation energy was observed when increasing ion fluence.

The thin film (Sample-1) was prepared on MgO by rf magnetron sputtering and post-annealing at 914 °C. The thickness of the film was about 3 um. T$_{c0}$ before the irradiation was about 79K. ^{4}He ion with the energy of 1.0 MeV was irradiated to the film. The film was set on a sample holder, so that the surface of the substrate was perpendicular to both the beam line and the magnetic field direction. The irradiation temperature was fixed at 100K, and the measurement of resistance was performed in the temperature region below 100K. We could probe the properties of the film before and after the irradiation without taking the film out from the chamber. This in-situ measurement guarantees the credibility of the data.

Fig.1 shows the R-T curves for the sample before and after the irradiation. As can be seen from the figure, He ion irradiation increased normal-state resistance. T$_c$ shifted to lower temperature as ion fluence increased. These results were consistent with the results of R-T curves measured for the irradiated Bi system[2] and the Y system[3].

It has already been reported that the superconducting transition width broadens when R-T curves are measured under the magnetic field[4]. Fig.2 and

Fig.3 show R-T curves under the fields of 0, 2, and 3 tesla for the sample before and after the irradiation, respectively. A shoulder at around the midpoint of the transition appeared when magnetic field was applied. We assumed that thermally activated process of flux lines is the origin of the non-zero resistance in the temperature region below the shoulder. This assumption can be justified by the following two reasons. The first reason is that the Arrhenius plots of the data at the temperature just above T_{c0} can be regarded as a straight line[5]. (See Fig.4) This means the relation between temperature and resistance can be expressed as the following activation process; $R = R_0 \exp(-U_{eff} / k_B T)$, where R_0 is the coefficient, U_{eff} is the effective activation energy, and k_B is the Boltzmann constant. The second reason is the appearance of a shoulder. The shoulder appears only when the field-direction is perpendicular to the current-direction[6]. Therefore, the shoulder can be regarded as an evidence of (effective) movement of flux lines caused by Lorentz force, which can be the origin of the nonzero resistance below the shoulder.

Based on this recognition, we assumed the movement of flux lines assisted by thermal process. In Fig.5, the estimated U_{eff} was plotted as a function of ion fluence. U_{eff} decreased as increasing ion fluence. The result for the Y-Ba-Cu-O film (Sample-2) with different T_c ($T_c \approx 71K$) was plotted in the same figure. Qualitatively, the results for the two samples show the same tendency, but the magnitude of U_{eff} differed by the factor of about 2. We could not specify the origin of this difference. Nevertheless, the magnitude of U_{eff} seems to be related with the value of T_c. This hypothesis can be supported by Fig.6, which shows that both U_{eff} and T_c were decreased by the He ion irradiation. This figure suggests that U_{eff} value scales with the value of T_c. The data obtained for the Eu-Ba-Cu-O system (Sample-3 :as-sputtered film with the thickness of about 0.3μm), which has identical structure with the Y-Ba-Cu-O system, were plotted in the same figure.

References

1) Y.Yeshurun and A.P.Malozemoff, Phys. Rev. Lett. 60 (1988) 2202.

2) T.Hoshiya, S.Takamura, T.Aruga, M.Kobiyama, S.Miura, Y.Kubo, and N.Shohata, Jpn. J. Appl. Phys. 29 (1990) L2026.

3) B.Roas, B.Hensel, G.Saemann-Ischenko, and L.Schultz, Appl. Phys. Lett. 54 (1989) 1051.

4) See for example "PHYSICAL PROPERTIES OF HIGH TEMPERATURE

SUPERCONDUCTORS I" edited by D.M.Ginsberg (World Scientific, Singapore,

1989) p.102.

5)T.T.M.Palstra, B.Batlogg, L.F.Schneemeyer, and J.V.Waszczak, Phys. Rev.

Lett. 61 (1988) 1662.

6)J.N.Li, K.Kadowaki, M.J.V.Menken, A.A.Menovsky, and J.J.M.Franse, Physica

C 161 (1989) 313.
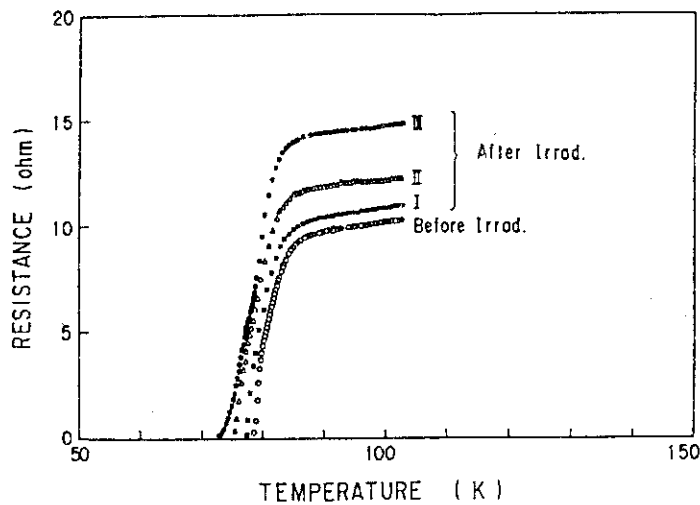
Fig.1 R-T curves for the
Y-Ba-Cu-O system before
and after the irradiation.
I : $5.5*10^{13} cm^{-2}$,
II : $2.0*10^{14} cm^{-2}$
III : $5.6*10^{14} cm^{-2}$
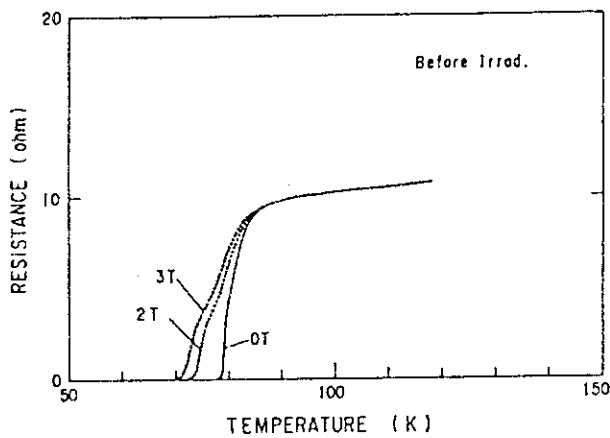
Fig.2 R-T curves under magnetic
field for the sample before irradi-
ation.
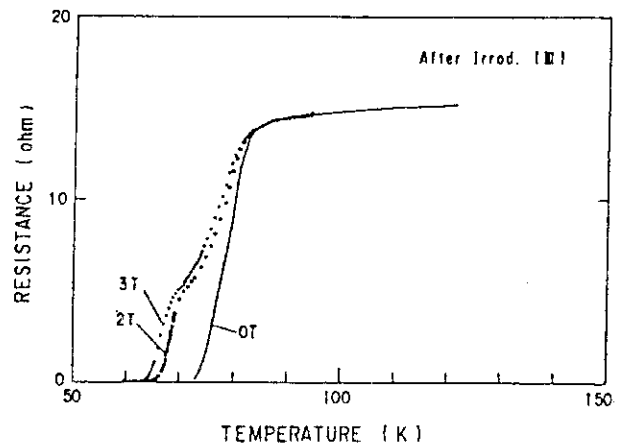
Fig.3 R-T curves under magnetic
field for the sample after irradi-
ation.
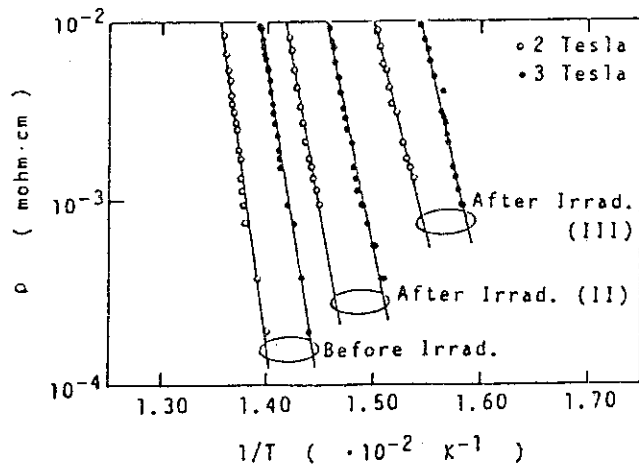
Fig.4 Arrhenius plots of resistivity before and after the irradiation for a magnetic field of 2T and 3T.
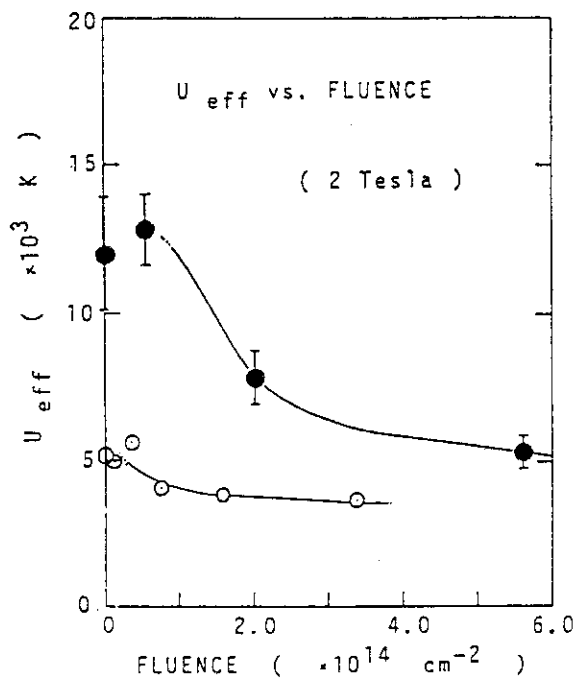
Fig.5 The dependence of effective activation energy on the ion fluence for Sample-1 (●) and Sample-2 (○).
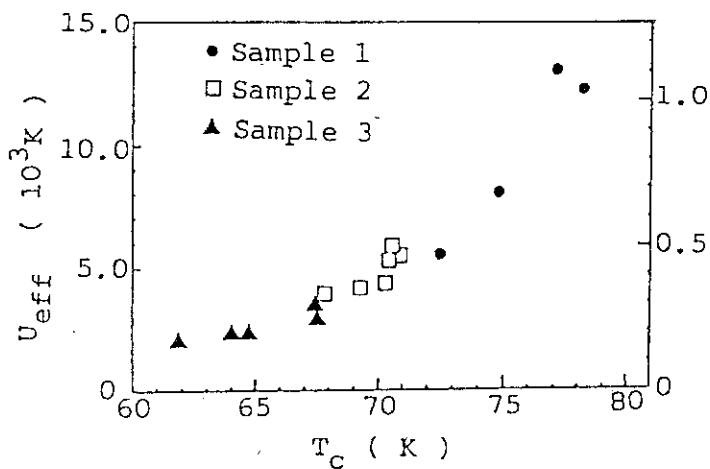
Fig.6 The effective activation energy plotted against T_c for Sample -1, -2, and -3. The values before and after irradiation are plotted in the same figure. This figure suggests U_{eff} scales with T_c.

2.11 180MeV Cu^{+11} Irradiation on $Bi_2Sr_2CaCu_2O_8$ Superconductor

Hiroaki KUMAKURA, Bernard CHENEVIER, Hitoshi Kitaguchi, Shozo IKEDA, Kazumasa TOGANO, Satoru OKAYASU[*] and Yukio KAZUMATA[*]

National Research Institute for Metals, [*]Japan Atomic Energy Research Institute

Introduction

Irradiation is one of the useful methods to introduce flux pinning centers in superconductors. Irradiation of electrons, neutrons or ions seems to be effective to introduce pinning centers and to increase J_c values in oxide superconductors. In addition to the increase of J_c values, so-called irreversibility field should be improved for the practical application. However, it was not clear, especially for Bi-based oxide, whether the irreversibility line in B-T plane moves or not by the irradiation. Recently, Weber et al. showed that by the neutron irradiation this irreversibility line shifted to higher fields for $Bi_2Sr_2CaCu_2O_8$ (2212)[1]. From a practical point of view, ion irradiation is more advantageous than the neutron irradiation because an ion irradiated material is much less radio-active than a neutron irradiated material. In this experiment, we have carried out high energy Cu^{11+} irradiation on the grain-oriented 2212 tapes. Observation of defects introduced by the irradiation and measurement of superconducting properties were carried out.

Experiments

Samples were polycrystalline $Bi_2Sr_2CaCu_2O_8$ (2212)/Ag tapes prepared by doctor blade method[2]. The 2212 layers have highly grain-oriented microstructure with c-axis perpendicular to the tape surface. 180MeV Cu^{11+} irradiation was carried out on the 2212 layers with different fluence using Tandem accelerator. Direction of the incident beam was perpendicular to the tape surface(i.e., parallel to the c-axis of 2212). Irradiation was done at 100K and fluence was changed from 10^{10} to 10^{12} ions/cm^2. The projected range of the Cu^{11+} in 2212 was calculated by the method reported by Aruga et al.[3] and we obtained 16.4μm which was larger than the thickness of 2212 layers. Therefore, almost all ions penetrated the 2212 layers.

Transition temperature T_c was measured by a four probe resistive method. Transport J_c was also measured by the resistive method in magnetic fields of 6-12T at 4.2K and in zero field at 77K. D.C. magnetization was measured in magnetic fields up to 5T at various temperatures using SQUID magnetometer(Quantum Design). For the magnetization measurement, the samples were cut into small pieces of $3\times3mm^2$ and they were piled up. Magnetic field was applied parallel to the c-axis(perpendicular to the sample surface).

Defects introduced by the irradiation were observed using a 400kV transmission electron microscope(TEM) for fluence of 6.7×10^{11} ions/cm^2.

Results and Discussion

T_c is almost constant up to fluence of 5×10^{10} ions/cm^2, and then decreases for larger fluence. Transition width increases with increasing fluence. The fluence where the T_c begins to decrease is much smaller than that for the neutron irradiation. This difference between Cu^{11+} irradiation and neutron irradiation primarily comes from the difference of scattering process.

Enhancement of transport J_c was obtained for the fluence up to 3×10^{11} ions/cm^2. This J_c increase is due to the introduction of pinning centers by the irradiation. Above 3×10^{11} ions/cm^2, however, transport J_c decreases rapidly with increasing fluence. This rapid decrease in transport J_c is due to the damage at weak couplings such as grain boundaries, because the hysteresis in D.C. magnetization for the fluence above 3×10^{11} ions/cm^2 is larger than that of the non-irradiated sample as will be mentioned later. Transport J_c in zero mangetic field at 77K, on the other hand, shows no increase by the irradiation. J_c in zero field at 77K was almost constant up to 1×10^{11} A/cm^2 and then rapidly decreased with increasing fluence. This no increase in transport J_c by the irradiation can be understood from the fact that the transport J_c of the polycrystalline oxide at zero magnetic field is primarily dominated by the coupling of grains.

Effect of irradiation on the hysteresis of magnetization ΔM is shown in Fig. 1, where ΔM at 25K was plotted as a function of magnetic field for fluence of 1.0×10^{11} and 6.7×10^{11} ions/cm^2. ΔM was enhanced by the ion irradiation. Especially the enhancement of ΔM in high magnetic field region is very large. This indicates that strong pinning centers were
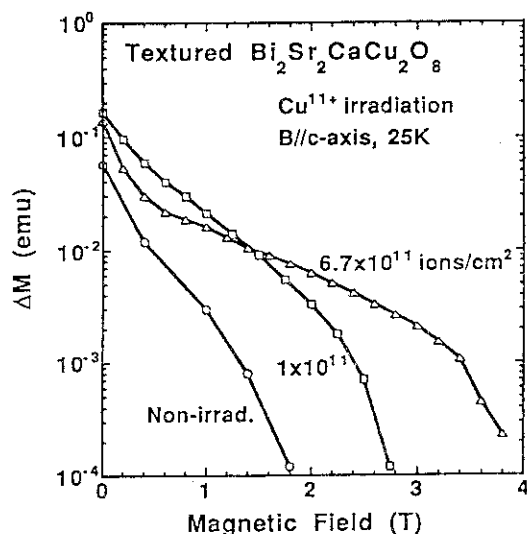
Fig. 1 Effect of irradiation
on ΔM vs magnetic field
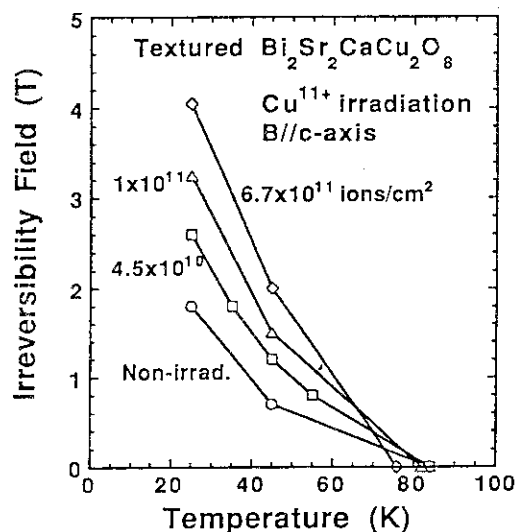
Fig. 2 Fluence dependence of
irreversibility field

introduced by ion irradation. Similar enhancement in ΔM was also observed
at higher temperatures.

It is difficult to deduce J_c from ΔM for our polycrystalline samples
because both the intragrain J_c and intergrain J_c contribute to ΔM.
However, as the intergrain J_c (transport J_c) decreases by the irradiation
for the fluence larger than 3×10^{11} ions/cm^2 as mentioned above, we can
conclude that the enhancement of ΔM by the irradiation with fluence of
6.7×10^{11} ions/cm^2 comes from the increase of the intragrain J_c, and the
actual increase of intragrain J_c by the irradiation should be larger than
the increase of ΔM for this fluence.

Irreversibility fields were defined as the fields where ΔM vanished in M-B
curves. Figure 2 shows irreversibility field as a function of temperature
for several fluences. Irreversibility field increases with increasing
fluence. For the fluence of 6.7×10^{11} ions/cm^2 T_c decreases by 9K,
however, irreversibility field still increases and enhancement larger than
factor two is obtained. The result indicate that ion irradiation is
effective to introduce defects acting as strong pinning centers, and
hence, to move irreversibility line to higher fields.

TEM image taken with electron beam parallel to the c-axis is given in Fig.
3(a). Modulated structure along b-axis is clearly observed. The
projection of the crystal defects perpendicular to the ion beam direction
consists of disks of highly damaged material with diameters ranging
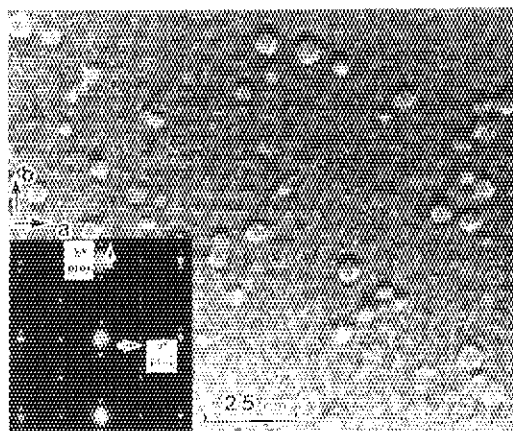
Fig. 3(a) TEM image with
electron beam parallel to c-axis.
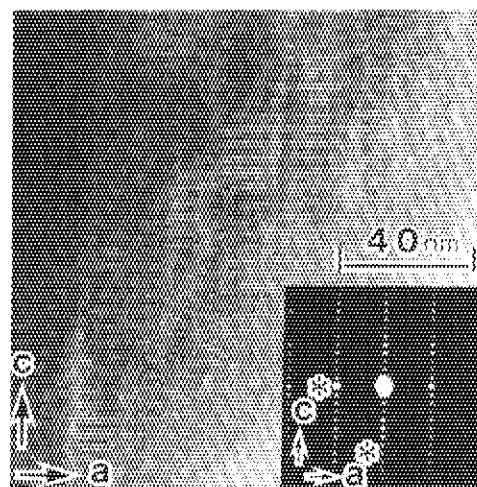
Fig. 3(b) TEM image with electron
beam parallel to b-axis.

between 2 and 8nm. TEM image taken with electron beam parallel to the b-axis is shown in Fig. 3(b). Bright stripes, parallel to the c-axis, can be oberved. Stripes have a width greater than 5nm and they are longer than 90nm. High resolution TEM image indicates that the stripes were composed of amorphous or highly damaged materials. Since, in all the investigated microcrystal, the bright stripes are parallel to the ion beam direction, they likely image the tracks of the damages produced by the Cu ions. Similar defects of cylindrical columns are also reported by L. Civale et al. for 580MeV Sn^{30+} irradiated $YBa_2Cu_3O_7$ crystals[4]. These defects act as strong pinning centers and J_c enhancement is obtained when a magnetic field is parallel to the columnar defects.

References

1) H.W. Weber, H.P. Wiesinger, W. Kritscha, F.M. Sauerzopf, G.W. Crabtree, J.Z. Liu, Y.C. Chang and P.Z. Jiang, in Proc. LT-19 Satellite Conf., Cambridge, Edited by E. Evetts, (Adam Hilger, Bristol, 1990) p.103.

2) J. Kase, T. Morimoto, K. Togano, H. Kumakura, D.R. Dietderich, and H. Maeda, IEEE Trans. Magn. 27, 1254(1991).

3) T. Aruga, K. Nakata and S. Takamura, Nucl. Instrum. & Method B33(1988)748.

4) L. Civale, A.D. Marwick, T.K. Worthington, M.A. Kirk, J.R. Thompson, L. Krusin-Elbaum, Y. Sun, J.R. Clem and F. Holtzberg, Phys. Rev. Lett. 67, 648(1991).

2.12 Irradiation Behavior of Tritium-breeding Ceramics

Hisayuki MATSUI, Mikio HORIKI, Manabu HOSHINO,

Kenji NODA*, Yoshinobu ISHII*, Tetsuya NAKAZAWA*

and Hitoshi WATANABE*

Department of Nuclear Engineering, Nagoya University,

*Division of Material Development, JAERI

Introduction

During the operation of the fusion reactor, various irradiation defects will be induced in ceramic breeder materials, due to bombardment of high energy neutrons up to 14 MeV, tritons (2.7 MeV) and helium ions (2.1 MeV) produced by Li(n,)H reactions. Therefore, it is important to study how irradiation-induced defects influence the physical properties of those materials.

In a decade, we investigated the radiation damage of Li_2O single crystals. Among a variety of Li compounds, Li_4SiO_4 is a hopeful candidate for the breeder materials of D-T fusion device. Al-doped Li_4SiO_4 is also developed to improve the tritium release. In that material, the tritium release is considerer to be increased, because of an introduction of litium vacancies. In the present study, pure and Al-doped Li_4SiO_4 ($Li_{3.7}Al_{0.1}SiO_4$) were irradiated with 120 MeV oxygen and 60 MeV Li ions. Ionic conductivity and Raman spectra were preliminarily studied in order to obtain the information of radiation defects in those materials. The main aim of the study was to obtain knowledge of irradiation damage on those materials, from which we could evaluate the change of transport phenomena concerning Li atoms, and, thus, tritium diffusion as well. The information concerning irradiation induced defect structure will allow us a fruitful discussion on the mechanism of matter transport.

Experiments

Pure and Al-doped lithium orthosilicates (hereafter, we denote "pure" as Li_4SiO_4 and "Al-doped" as $Li_{3.7}Al_{0.1}SiO_4$) were synthesized in powder form by the methanol process developed by Vollath et al. After pressing the powder at hydrostatic pressure of 1.6×10^2 MPa, sintered pellets were obtained by heating at 1353 K for 5 h in air. The pellet was cut out into

thin disk (8 mm in diameter and about 0.4 mm in thickness).

The ionic conductivity was measured in an irradiation vacuum chamber attached to a tandem accelerator. The specimens were irradiated at ambient temperatures with high energy ions. Before and after the irradiation, the ion conductivity was measured by the two terminal AC method using the HP 41 94A Impedance Analyzer. A ful-automatic data collection system was used and a set of data of the ionic conductivity (converted from the resistance) were compiled in a microcomputer. Details of the experimental procedures were reported before.

In the Raman measurement, we irradiated the specimens in another chamber. The Raman spectra were measured at room temperature with JASCO NR1100 Specrometer operated at 200 mW using the 488 nm Ar laser for the excitation source.

Results and Discussion

1. Ionic Conductivity of "Pure" and "Al-doped" Specimens

Ionic conductivity (σ) of "pure" and "Al-doped" lithium orthosilicates are somewhat different. The conductivity of Li_4SiO_4 increased with ion fluence in the temperature range of 413 and 613 K. Whereas $Li_{3.7}Al_{0.1}SiO_4$ showed a slight increase with the fluence in the temperature range between 373 and 413 K, and no fluence dependence was observed between 443 and 503 K.

During irradiation, Li ions are displaced and a number of Li-ion interstitials and vacancies are introduced. Such Li-ion defects increase the ionic ocnductivity. However, the Li-interstitials should be migrate and/or aggregate more easily than the vacancies. Therefore, the Li vacancies are thought to contribute predominantly to the increase of the Li-ion diffusivity and the ion conductivity of Li_4SiO_4.

On the contrary, a large number of Li vacancies are introduced in the $Li_{3.7}Al_{0.1}SiO_4$, because of Al doping. In this material, some of solute atoms (Al) at the Li-ion sites are also displaced. This results in a change of Li vacancies in order to maintain the electroneutrality. In this process, a part of Li interstitials may be consumed by a mutual annihilation with the Li vacancies. On the other hand, the surviving interstitials may also aggregate into clusters. Thus, the Li vacancies are also considered to be predominant defects in the Al-doped Li_4SiO_4.

2. Raman Specrum

Raman spectum was measured at room temperature after ion irradiation. The Raman spectra of irradiated Li_4SiO_4 were shown in Fig. 1 for 3.21 x 10^{19} and 1.09 x 10^{20} O-ions/m^2, together with non-irradiated one. Dominant peak appears at around 830 cm^{-1}. There seems at least three peaks in that peak, 806, 830 and 890 cm^{-1}. The intensity ratio of the peak at 806 to 830 cm^{-1} was changed with fluence. However, the intensity ratio of the peak at 890 to 830 cm^{-1} did not change with fluence. At the highest fluence (1.09 x 10^{20} ion/cm^2) , new peaks at about 1360 and 1600 cm^{-1} were observed.

Li_4SiO_4 has a monoclinic crystal structure and contains isolated SiO_4 tetrahedra being connected to LiO_n polyhedra. Therefore, the peaks at around 830 cm^{-1} could be attributed to a stretching mode of the Si-O vibration being analogous to the Raman spectra due to Si-O bond in Li_2O-SiO_2 glass. Displacement of oxygen ion due to irradiation should lead to the change of the vibration mode of surviving Si-O bonds in the SiO_4 tetradedra. Therefore, the change of the intensity ratio of the peak above mentioned could be attributed to the displacement of oxygen during irradiation. By the irradiation, a number of the Si-O bonds may decrease and results in the change of the vibration mode of the Si-O bonds.

The new peaks at about 1360 and 1600 cm^{-1} in higher fluence could not be clearly assigned to specific atomic bond. However they seemed to be attributed to a certain atomic bond relating to the silicon and oxygen atom displaced by irradiation.

The Raman peak at around 830 cm^{-1} was also observed in $Li_{3.7}Al_{0.1}SiO_4$, as shown in Fig. 2 (806, 830 and 870 cm^{-1}). No fluence dependence was observed between the intensity ratio of each peak. In addition, no clear peak at around 1360 and 1600 cm^{-1} was found in this materials. The doped Al, which has three electrons to bind the oxygen atoms, seems to lead to a higher binding strength between Al and O ion in comparison with that between Li and O ions. Therefore, oxygen in $Li_{3.7}Al_{0.1}SiO_4$ might not be displaced so easily. This fact implies that the formation of SiO_4 tetrahedra with an O vacancy is difficult in this compound. Thus, the resistance of $Li_{3.7}Al_{0.1}SiO_4$ to the irradiation seems to be higher than that of Li_4SiO_4. Recovery behavior of the Raman spectra was also examined and the recovery was completed at about 573 K.
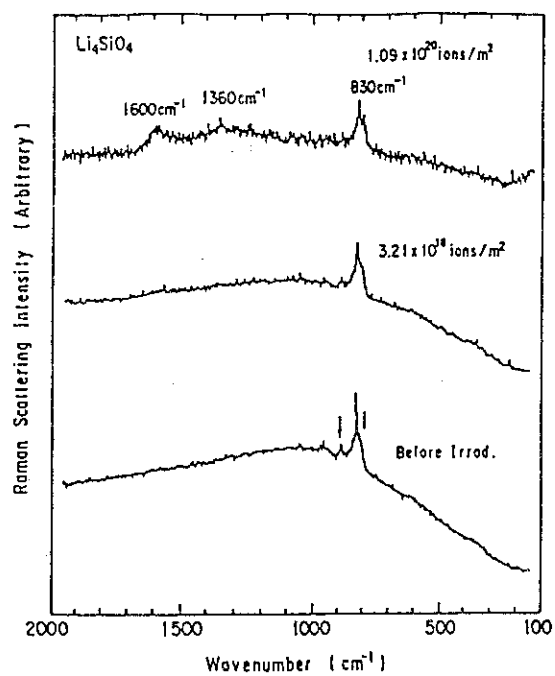
Fig.1 Raman Spectra (Li₄SiO₄)
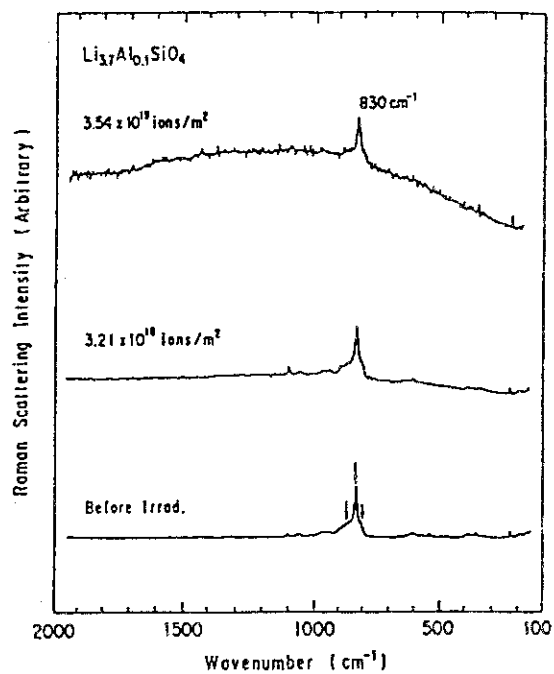
Fig.2 Raman Spectra (Li₃.₇Al₀.₁SiO₄)

2.13 Electrical and Structural Properties of Li-ion Irradiation β-LiAl

Kazuo KURIYAMA, Hiromi TAKAHASHI, Chiaki YOSHIIE,

Yukio KAZUMATA*, Hiroyuki SUGAI**

College of Engineering and Research Center of Ion Beam Technology, Hosei University, *Department of Physics, JAERI, **Department of Radioisotopes, JAERI

LiAl alloy is an useful material for solid-blankets of nuclear fusion[1]. Electrical conductivity of β-LiAl below room temperature has been reported.[2-4] The important feature of the conduction mechanism for β-LiAl is governed by positive carriers (holes)[5,6] in the valence band. The electrical conductivity based on these holes is affected considerably by the defect structure[7] in β-LiAl (about 48 -56 at.% Li). The defect structure at room temperature consists of two types of defects: vacancies in the lithium sublattice (V_{Li}), and lithium anti-structure atoms in the aluminum sublattices (Li_{Al}). The purpose of the present work is (i) to measure the electrical resistivity of β-LiAl before and after heavy ion irradiation and (ii) to survey the modification of Li vacancies in Li-ion irradiated β-LiAl.

Samples were prepared by a resistance furnace melting of 99.9 % lithium and 99.999 % aluminum. The details of sample preparation have been previously described.[8,9] Ion irradiations were performed by a tandem accelerator at JAERI. 60 MeV - $^7Li^{3+}$, 65 MeV - C^{4+} and 70 MeV - S^{7+} ions were used in this study. The irradiation condition is shown in Table 1.

The electrical resistivity measurements were carried out at room temperature using Van der Pauw technique[10]. In order to evaluate the depth profiles of electrical properties, a few μm of the irradiated surface of sample were removed for each measurement. In the previous estimation[11] for the depth dependence of resistance, we used the following equation;

$$\Delta R_s(t) = R_s(irra.(t)) - R_s(unirra.(t))$$

$$= [\rho(irra.(t)) - \rho(unirra.(t))] / t,$$

where, ρ(unirra.) and ρ(irra.) are a resistivity before and after the irradiations, respectively. However, it was observed that $\Delta R_s(t)$ values estimated in this method diverge with decreasing sample thickness (t). In the present study, the variation of the resistivity ($\Delta\rho(t)$) after the irradiation was normalized by the resistivity (ρ_b) before the irradiation. The improved equation is as follows;

$$\Delta\rho(t) / \rho_b = [\rho(irra.(t)) - \rho(unirra.(t))] / \rho_b.$$

Since this measurement is destructive method, we assume that the resistance in each depth is constant before the irradiation. Figure 1 shows the typical depth profiles of resistivity before the irradiation. This indicates that the values measured are constant in depth within experimental error.

Figure 2 shows the depth profiles of $\Delta\rho / \rho_b$ after the irradiation. The depth profile of $\Delta\rho / \rho_b$ does not show the remarkable variation, in particular, near the projection rage (see Table 1). Since the radiation damage may be annealed out at room temperature, it is necessary to measure the resistivity under as-irradiated condition at low temperature such as liquid helium temperature.

References

1) J.R. Powell, F. T. Miles, A. Aronson and W.E.Winsche: BNL-18236, Brookhaven National Laboratory(1973).

2) K.Kuriyama, T.Kamijoh, and T.Nozaki: Phys. Rev. B22(1980)470; K.Kuriyama, S.Yamada, T.Nozaki, and T.Kamijoh: Phys. Rev. B24(1981)6158.

3) T.Asai, M.Hiratani, and S.Kawai: Solid State Commun. 48(1983)173.

4) L.H.Hall, T.O.Brun, G.W.Crabtree, J.E.Robinson, S.Susman, and T.Tokuhiro: Solid State Commun. 48(1983)547.

5) K.Kuriyama, T.Nozaki, and T.Kamijoh: Phys. Rev. B26(1982)2235.

6) M. Yahagi: Phys. Rev. B24(1981)7401.

7) K.Kishio and J.O.Brittain: J. Phys. Chem. Solids 40(1979)993.

8) K.Kuriyama, S.Saito, and K.Iwamura: J. Phys. Chem. Solids 40(1979)457.

9) M. Yahagi, J. Crys. Growth 49(1980)396.

10) L.J.Van der Pauw: Philips Tech. Rev. 20(1958)220.

11) K.Kuriyama, N.Mineo, H.Takahashi, Y.Kazumata, and H.Sugai: JAERI Tandem, Linac and V.D.G. Annual Report 1990, P.32-35.

Table 1 Irradiation parameters of Li^{3+}, S^{7+}, S^{9+}, and C^{4+} ions.

Ions	Li^{3+}	S^{7+}	S^{9+}	C^{4+}
Energy [MeV]	60	70	150	65
Fluence [ions / cm^2]	1×10^{16}	2×10^{15}	4×10^{15}	6×10^{15}
Temperature [K]		< 140		
Projected Range [μm]	562	26.2	60.4	125.9
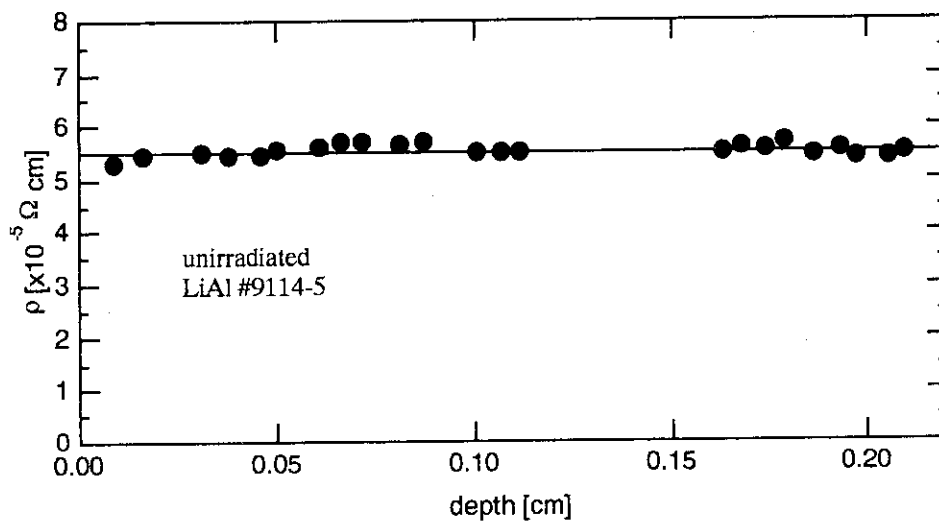
Fig. 1 The depth profile of resistivity (unirradiated β-LiAl).
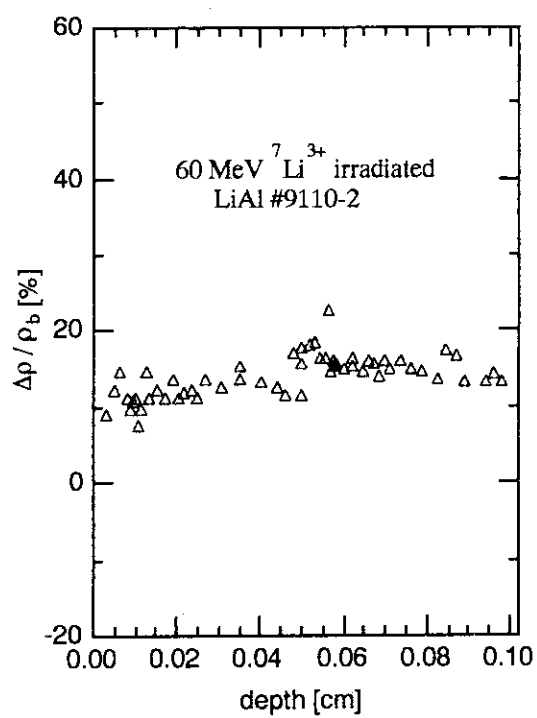
Fig. 2 (a) The depth profile of $\Delta\rho / \rho_b$

(Li-ion irradiated β-LiAl).
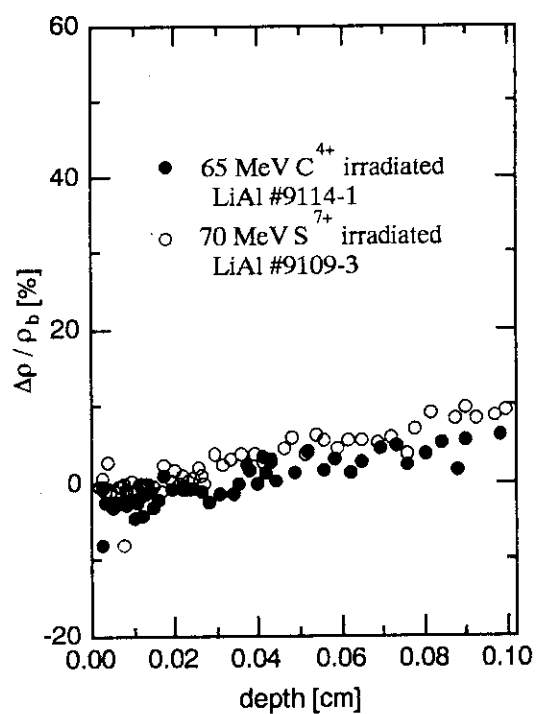
Fig. 2 (b) The depth profile of $\Delta\rho / \rho_b$

(C- and S-ion irradiated β-LiAl).

2.14 Electron Microscopic Observation of Ion-irradiated Li$_4$SiO$_4$

Kenji NODA, Tetsuya NAKAZAWA, Yoshinobu ISHII,

Kotaro KURODA*, Takashi INUZUKA*, Hiroyasu SAKA* and

Hitoshi WATANABE

Department of Fuels and Materials Research, JAERI, *Faculty

of Engineering, Nagoya University

Radiation damage induces swelling, degradation of mechanical integrity and changes of various properties of ceramic materials. Studies on the radiation damage are very important for development of radiation resistant ceramic materials for advanced nuclear energy systems including fusion reactors.

Li$_4$SiO$_4$ is a candidate of tritium breeding materials for D-T fusion reactors. In the present study, radiation damage of Li$_4$SiO$_4$ was studied by electron microscopic observation.

Li$_4$SiO$_4$ pellets were fabricated by pressing the powder synthesized with the methanol method[1] at 1.6×10^2 Pa and sintering at 1353 K for 5h in air. The pellets were cut into thin disks by a diamond cutter, and the disks were polished with emery papers. Thin foil specimens for electron microscopic observation were made using the ion-milling technique. The specimens were irradiated to 6.8×10^{19} and 8.7×10^{20} ions/m^2 at room temperature with 500 keV Ne ions. After the ion irradiation, microstructure of the specimens was observed using a 200 kV transmission electron microscope (TEM).

Fig. 1 shows electron micrographs of the Li$_4$SiO$_4$ specimen irradiated to 8.7×10^{20} ions/cm^2 with 500 KeV Ne ions and electron diffraction patterns for the observed regions. Microstructural changes due to the Ne ion irradiation could not be observed, as shown in fig. 1(a). However, during subsequent TEM observation of the specimens, amorphization of the observed region, i.e., the region irradiated with 200 kV electrons, occurred. Some void-like contrasts appeared at electron irradiation fluence of about 10^{23} electrons/m^2 (fig. 1(c)) and hallow rings indicating amorphization were observed in the the electron diffraction pattern for the above-mentioned region.

The amorphization of Li$_4$SiO$_4$ was also observed to occur by only 200

kV electron irradiation at the high fluence levels such as 9.4×10^{25} electrons/m^2 [2]. The electron fluence level at which the amorphization was induced by the electron irradiation combined with the Ne ion irradiation is much smaller than that for simple electron irradiation. Thus, it is seen that the Ne ion irradiation followed by the electron irradiation enhances the amorphization due to the subsequent electron irradiation substantially.

The void-like contrasts were also observed for the region irradiated at the high fluences with 200 kV electrons, although the size of the void-like contrasts was smaller than the case in the present study[2]. Systematic studies with combination of ion irradiation using various kinds of ions (gas ions and metallic ions) and electron irradiation will be necessary to clarify effects of implantation of gas ions such as Ne on damage microstructure.

References

1) D. Vollath and H. Wedemeyer: J. Nucl. Mater. 141-143 (1986) 334.
2) K. Noda, Y. Ishii, K. Kuroda, M. Sasaki, H. Saka and H. Watanabe, JAERI-M 90-139 (1991) p.96-98.
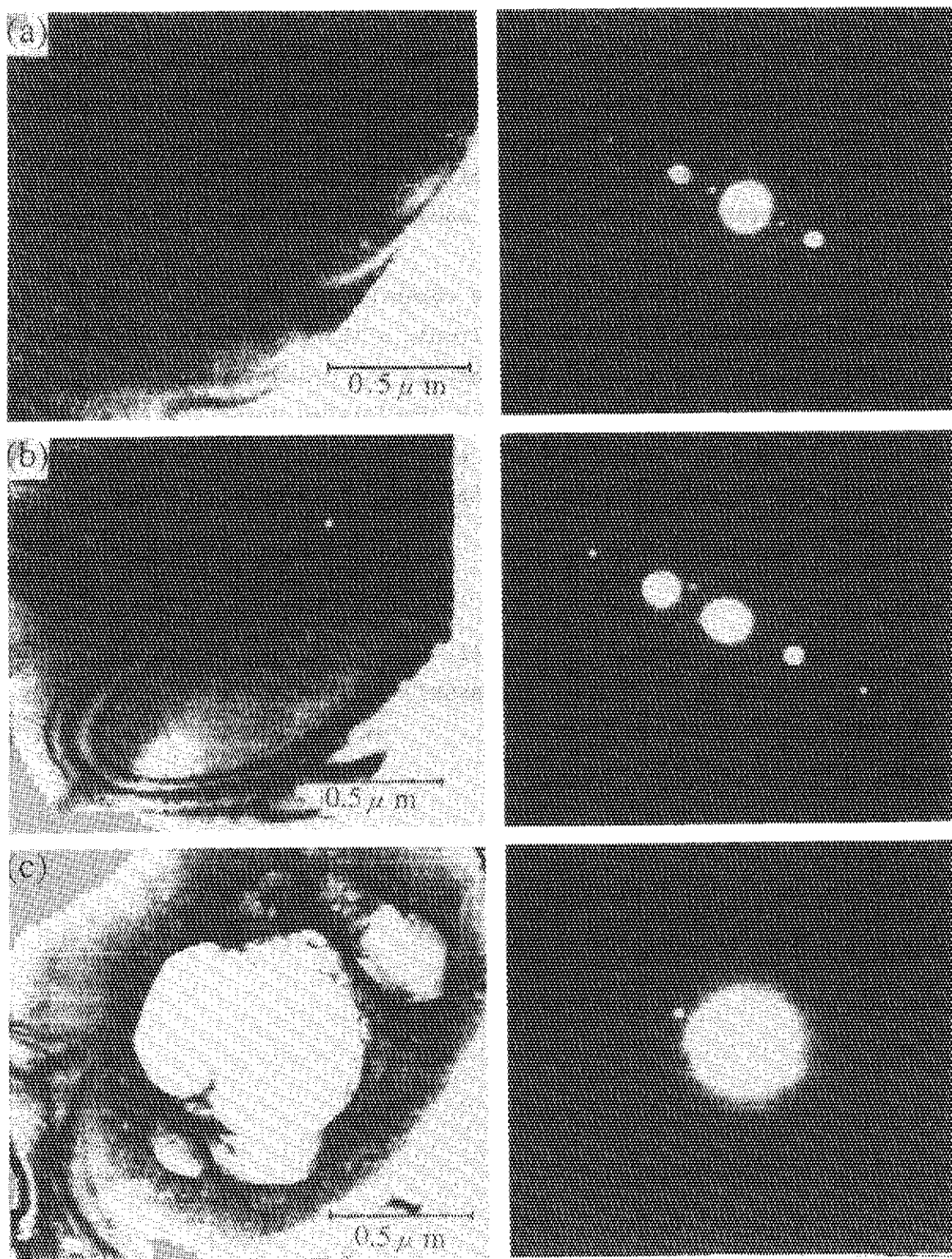
Fig.1 Electron micrographs of the Li4SiO4 specimen irradiated to 8.7×10^{20} ions/cm^2 with 500 KeV Ne ions and the electron diffraction patterns before and after subsequent 200 kV electron irradiation; (a) before electron irradiation, (b) at electron fluence of about 5×10^{22} electrons /cm^2, (c) at electron fluence of about 1×10^{23} electrons/cm^2.

2.15 A Radiation Damage Study of Pure and Al-doped Lithium Orthosilicate

Kenji NODA, Tetsuya NAKAZAWA, Yoshinobu ISHII,

Hisayuki MATSUI*, Dieter VOLLATH**, Mikio HORIKI*,

Naomi OBATA* and Hitoshi Watanabe

Department of Fuels and Materials Research, JAERI, *Faculty of Engineering, Nagoya University, ** Kernforschungszentrum Kurlsruhe GmbH, Institut fur Material und Festkorperforschung III

1. Introduction

Lithium Orthosilicate (Li_4SiO_4) is a candidate of tritium breeder material for D-T fusion reactors. Al-doped Li_4SiO_4 is an advanced tritium breeding material which was recently developed by Vollath et al.[1] . In this material, the tritium diffusivity is considered to be increased by introduction of lithium-ion vacancies due to doping Al.

During operation of fusion reactors, severe radiation damage will be introduced in the ceramic breeder materials. The radiation damage will cause thermal property changes, swelling and tritium release performance change etc. Recently, irradiation defects and radiolysis products in Li_4SiO_4 and Li_2SiO_3 irradiated with gamma-ray, electrons and neutrons were investigated[2]. In the study, colloidal lithium metals, lithium and silicon oxides etc. were found as the final products of radiolysis.

In the present study, radiation damage in Li_4SiO_4 and Al-doped Li_4SiO_4 ($Li_{3.7}Al_{0.1}SiO_4$) irradiated with oxygen ions and the thermal recovery behavior were investigated using Raman spectra measurements.

2. Experimental

Specimens were thin disks (8-9 mm in diameter, 0.4-1 mm in thickness) of Li_4SiO_4 and $Li_{3.7}Al_{0.1}SiO_4$ pellets. The specimens were irradiated at an ambient temperature with 120 MeV oxygen ions in an irradiation chamber attached to a tandem accelerator at JAERI. Raman spectra of the specimens were measured at room temperature with a JASCO NR 1100 Raman spectrometer operated at 200 mW using the 488 nm line Ar laser.

3. Results and discussion

Fig. 1 shows the Raman spectra of Li₄SiO₄ irradiated to the fluence of 3.21×10^{18} and 1.09×10^{20} ions/m² together along the spectrum of the unirradiated specimen. In the spectra of unirradiated specimens, peaks around 830 cm⁻¹ were observed as dominant peaks. These peaks consisted of at least three peaks at about 806, 830 and 890 cm⁻¹. The intensity ratio between the peak at about 806 cm⁻¹ and that at about 830 cm⁻¹ was changed with the fluence. On the other hand, the intensity ratio between the peaks at about 890 cm⁻¹ and that at about 830 cm⁻¹ was hardly changed with the fluence. At the high fluence of 1.09×10^{20} ions/cm², new peaks at 1360 and 1600 cm⁻¹ appeared in addition to the peaks around 830 cm⁻¹.

In fig. 2, the Raman spectra of Li₃.₇Al₀.₁SiO₄ irradiated to the fluence of 3.21×10^{18} and 3.54×10^{19} ions/cm² are shown together with the spectra of the unirradiated specimen. The peaks around 830 cm⁻¹ were also observed as dominant peaks for Li₃.₇Al₀.₁SiO₄, and they consisted of 806, 830 and 870 cm⁻¹. The intensity ratios between peaks at about 806 cm⁻¹ and that at about 830 cm⁻¹ and between the peaks at about 870 cm⁻¹ and that at about 830 cm⁻¹ were not virtually changed with the fluence. In addition, the peaks at about 1360 and 1600 cm⁻¹ were not clearly observed at the fluence (8.52×10^{19} ions/cm²) being similar to the fluence level at which the above-mentioned two peaks were observed for Li₄SiO₄.

The peaks around 830 cm⁻¹ can be attributed to the stretching mode of the Si-O vibration of SiO₄ tetrahedra in Li₄SiO₄ and Li₃.₇Al₀.₁SiO₄ on the analogy of the Raman spectra due to the Si-O bonds of SiO₄ tetrahedra in Li₂O-SiO₂ glasses[3]. The intensity ratio between the peak at about 806 cm⁻¹ and that at 830 cm⁻¹ for Li₄SiO₄ was changed with the fluence. The displacement of oxygen ions due to irradiation leads to change of vibration mode of surviving Si-O bonds in the SiO₄ tetrahedra of which oxygen ions were displaced. Consequently, the change of the intensity ratio mentioned above can be attributed to displacement of oxygen ions due to irradiation. Silicon atoms in SiO₄ tetrahedra are also displaced as well as the lithium and oxygen ions during irradiation. Thus, the number of the Si-O bonds may decrease in addition to the change of the vibration mode of the Si-O bonds.

The new peaks observed at about 1360 and 1600 cm⁻¹ in the high fluence regime could not be assigned to specific atomic bonds, although they seem to be attributed to some atomic bonds relating to the silicon

and oxygen atoms displaced by the irradiation.

The intensity ratios between the peaks around 830 cm^{-1} were not virtually changed with the fluence for the Raman spectra of $Li_{3.7}Al_{0.1}SiO_4$. The doped Al atom, which has three electrons to bind the oxygen atoms, seems to lead the higher binding strength between the aluminum ions and the oxygen ions in comparison with that between the lithium ions and oxygen ions. Consequently, the oxygen ions in $Li_{3.7}Al_{0.1}SiO_4$ may not be displaced so easily in contrast with the case of Li_4SiO_4. This means that the possibility of formation of SiO_4 tetrahedra having an oxygen vacancy in $Li_{3.7}Al_{0.1}SiO_4$, which causes the change of vibration mode of the Si-O bonds, is small as compared with Li_4SiO_4. Thus, it seems that the number of Si-O bonds in $Li_{3.7}Al_{0.1}SiO_4$ decreases with the fluence without the detectable intensity ratio change of the peaks mentioned above by displacement of silicon atoms due to the irradiation.

The recovery behavior of the Raman spectra of Li_4SiO_4 was examined by isochronal annealing experiments. The spectra were measured at room temperature, after the specimens were heated at each annealing temperature in the range 373 to 573 K for 30 min. Fig. 3 shows the recovery behavior of the spectra of Li_4SiO_4 irradiated to 1.09×10^{20} ions/cm^2. The intensity ratio between the peaks at about 806 cm^{-1} and that at about 830 cm^{-1} was changed by the annealing and the ratio at the annealing temperature of 573 K became close to the ratio before irradiation. Furthermore, the intensity of the peaks at 1360 and 1600 cm^{-1} was decreased by the annealing. These may imply that the recovery of the oxygen-ion vacancies in SiO_4 tetrahedra and of the Si-O bonds takes place by the migration of oxygen and silicon interstitials.

In th present study, the irradiation defects for Si-O bonds of SiO_4 tetrahedra in Li_4SiO_4 and $Li_{3.7}Al_{0.1}SiO_4$ were investigated. However, further experiments using Raman spectroscopy, electron-spin resonance (ESR) and X-ray microanalyzer etc. are necessary to clarify the irradiation defects.

References

1) D. Vollath and H. Wedemeyer, Advances in Ceramics 27 (1990) 3.
2) J.E.Tiliks, G.K.Kizane, A.A.Abramenkovs, J.J.Tiliks and V.G.Vasiljev, Fusion Eng. Des. 17 (1991) 17.

3) M. Tatsumisago, T. Minami, N. Umesaki and N. Iwamoto, Chem. Lett. (1986) 1371.
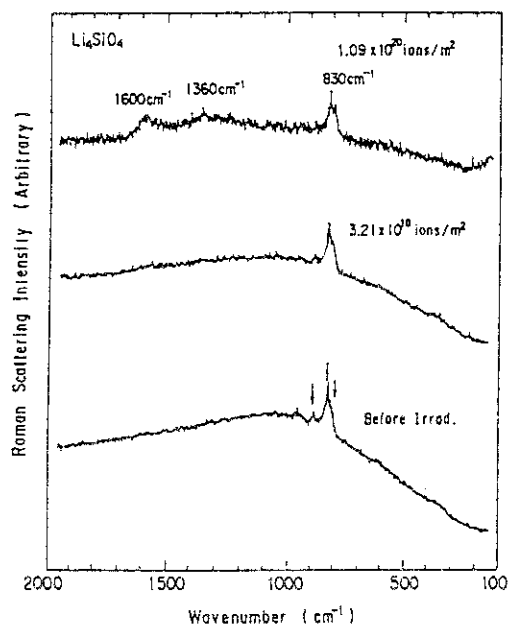
Fig.1 Raman spectra of Li4SiO4 irradiated to various fluences with 120 MeV oxygen ions.
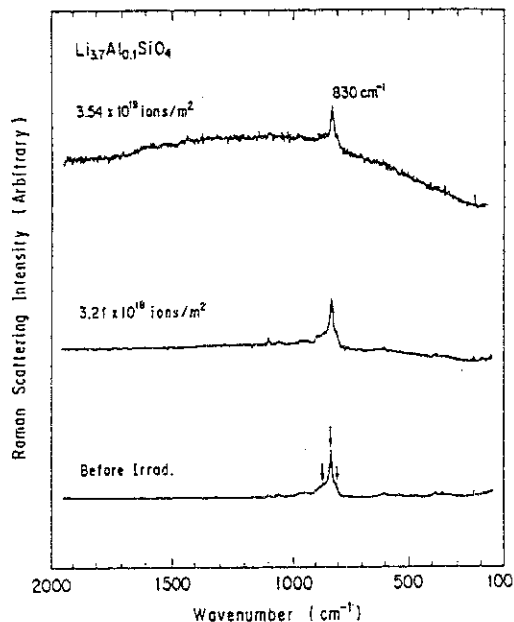
Fig.2 Raman spectra of Li3.7Al0.1SiO4 irradiated to various fluence with 120 MeV oxygen ions.
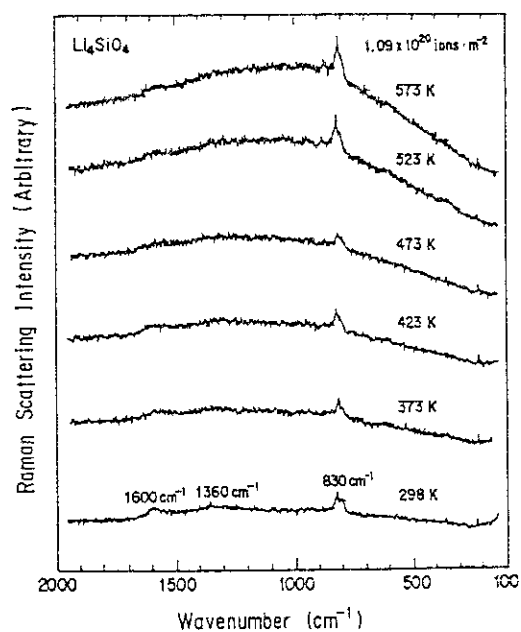
Fig.3 Recovery behavior of Raman spectra of Li4SiO4 irradiated to 1.09×10^{20} ions/m2 with 120 MeV oxygen ions in the isochronal annealing experiments.

2.16 Radiation Damage of UO_2 Irradiated with 100 MeV Iodine, Bromine and Oxygen Ions

Kimio HAYASHI, Hironobu KIKUCHI, Tetsuo SHIRATORI,
Satoru KASHIMURA[*], Mitsuo AKABORI and Kousaku FUKUDA

Department of Fuels and Materials, JAERI, [*]Nuclear Material
Control Center

1. Introduction

In the course of high burnup fuel development programs of light water reactors (LWR), special attention has recently been directed to the "rim effect". This is unexpected, significant release of fission gases (Kr and Xe) from the UO_2 matrix to small bubbles at the rim region of the fuel pellet[1,2]. The release is accompanied by a change of microstructure of the UO_2 matrix, i.e., loss of definable grain structure and an increase of porosity[1]. The microstructure change is considered to be related with radiation damage introduced by fission fragments at low temperatures around $400^\circ C$ at the rim region.

So far, radiation damage studies of nuclear fuels have been made mostly by implantation of relatively low-energy (<1MeV) ions[3]. The low-energy implantation is effective in causing radiation damage due to nuclear energy deposition. In the real fission events, however, much larger energy is deposited through electronic collision between the incident fission fragments (with energies of ca. 100MeV) and the UO_2 target.

In the present study, high-energy (100MeV) ions have been adopted for studying the high-energy deposition effect.

2. Experimental

The specimens used were sintered UO_2 discs sliced from fuel pellets for LWR fuel. The specimen discs were polished with emery papers and diamond paste, followed by drying in vacuum at $50^\circ C$ for 1 hour. The O/U ratio for the as-fabricated fuel was 2.01.

The specimens were irradiated with 100 MeV I^{7+}, Br^{7+} and O^{6+} ions using the TANDEM accelerator at JAERI. The irradiation was made at room

temperature with a water-cooled sample holder, which was kept at 20°C. Temperatures of the specimens were raised up to about 400°C at maximum by the beam heating. Depth profiles of incident ions and nuclear energy deposition are depicted in fig.1; these were calculated by using EDEP-JR87 code[4] modified from the EDEP-1 code.

After irradiation, the sample was brought to observation by optical and scanning electron microscopy. Also it was analyzed by an X-ray diffraction apparatus, Rigaku RU-200B, with a Cu-K alpha beam to determine the change of the lattice parameter of the UO_2 matrix.

3. Results and Discussion

3.1 Surface Appearance

The beam spot, white in appearance, was clearly observed by optical microscopy and even with naked eyes for Iodine (I) and Bromine (Br) irradiation; while not for Oxygen (O) irradiation.

Typical surface appearances are given in fig.2 for I- and O-irradiation. As-fabricated pores are easily observed for the un-irradiated and the O-irradiated specimens, while the pores have almost disappeared for the I-irradiated specimen. Moreover, the I-irradiated surface has become smooth, and it appears that the surface melted during irradiation.

Two interpretations are possible for the difference in the surface appearance. One is that the difference can be attributed to the difference in the total (mainly electronic) stopping power for these projectile atoms, even having the same incident energy, 100MeV. Iodine has much larger (electronic) stopping power than oxygen in this energy region. Another possibility is that the surface change is due to the surface damage relevant to the nuclear stopping power, because this component is negligible for O-implantation but not for I-implantation, as seen in fig.1.

In order to examine these two possibilities, next plans are under consideration; (i) to change the incident energy of iodine ions (e.g. 50 and 200 MeV) and (ii) to use different ion species with medium mass number (e.g. Cl or Ni).

3.2 Lattice Parameter

A prominent change was detected in the lattice parameter for I- and Br-irradiated UO_2 specimens, as illustrated in fig.3. The lattice parameter tends to saturate at a maximum ratio of ca. +0.4%. This value is significantly larger than a maximum value (ca. +0.1%) observed by Nakae et al.[5] for fission-induced lattice parameter change in their in-pile experiment. Moreover, with increasing fluence, the present data does not show the decreasing tendency after the maximum, while the decrease was observed for the reactor irradiation[5]. Interpretation of the present change is under way.

Further studies are planned as follows:

- to measure the fission-induced lattice parameter change by an in-pile experiment for the same (natured) specimens as used in the present experiment,
- to measure the depth profile of the lattice parameter change, and examine its relationship with the damage profile, and
- to quantify the lattice distortion observed for I- and Br-irradiation.

References

1) J.O.Barner, M.E.Cunningham, M.D.Freshley and D.D.Lanning: Proc. Intern. Topical Mtg. on LWR Fuel Performance (Avignion, France, April 21-24, 1991) pp.538-548.

2) R.Manzel and R.Eberle: ibid. pp.528-537.

3) e.g. Hj.Matzke: Rad. Effects 64 (1982) 3.

4) T.Aruga, K.Nakata and S.Takamura: Nucl. Instr. Meth. in Phys. Research B33 (1988) 748.

5) N.Nakae, A.Harada and T.Kirihara: J. Nucl. Mater. 71 (1978) 314.
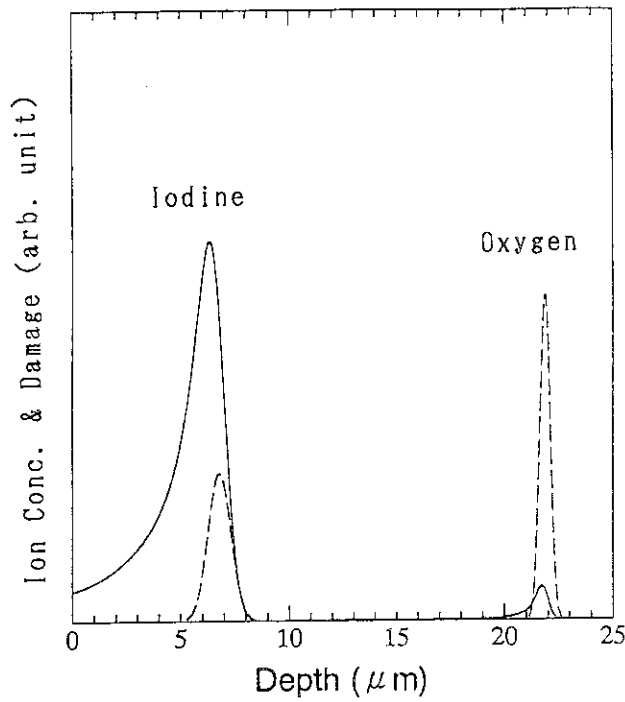
Fig.1 Depth profiles of range (dashed) and damage (solid line) calculated by EDEP-JR87 code[3].
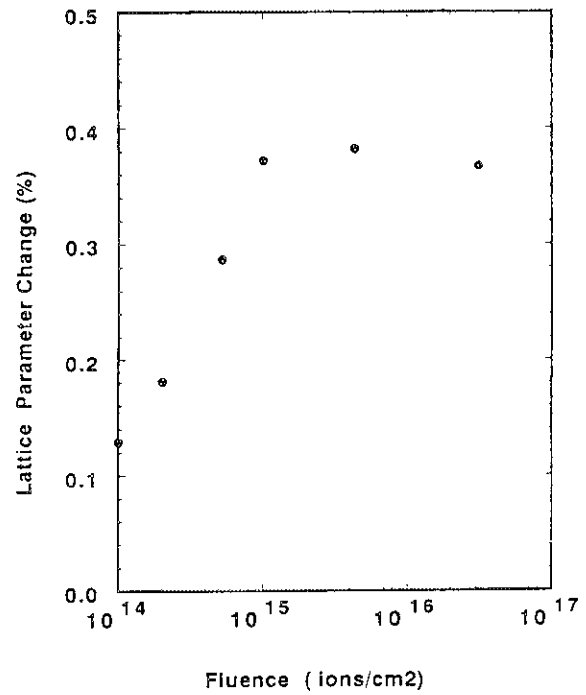
Fig.3 Lattice parameter change of UO_2 irradiated with 100 MeV Iodine.
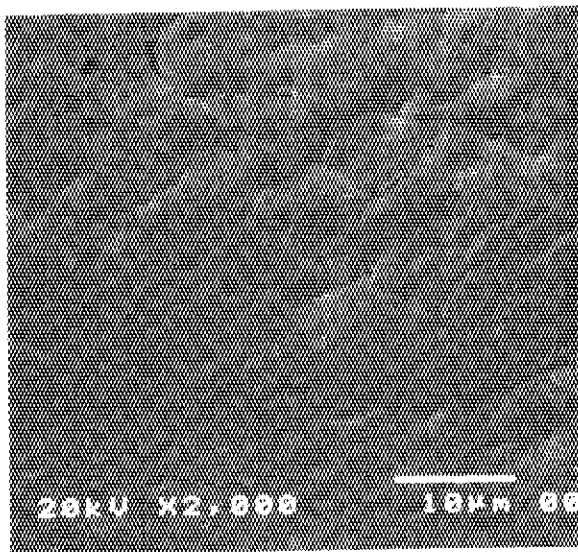
(a)
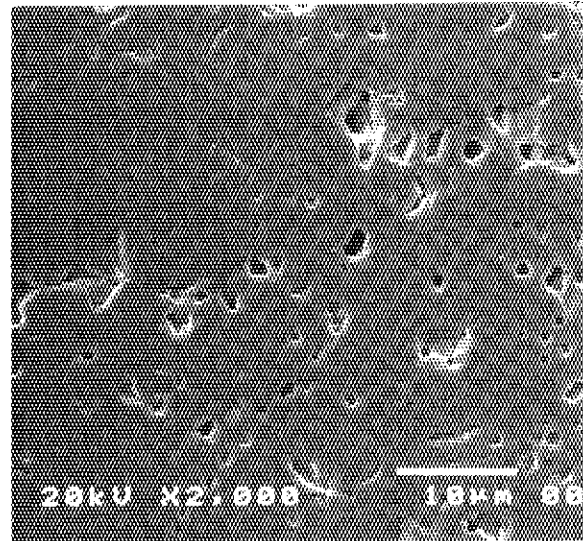
(b)

Fig.2 SEM structures of UO_2 irradiated by 100MeV Iodine (a) and Oxygen (b).

2.17 Measurements of Plasma Delay in Silicon Surface Barrier Detector

Ikuo KANNO*, Hiroshi IKEZOE†,

Satoshi KANAZAWA‡ and Itsuro KIMURA‡

Department of Reactor Engineering, JAERI, †Department of Physics, JAERI, ‡Kyoto University

Silicon surface barrier detector (SSBD) is widely used as an excellent charged particle detector. The SSBD has an excellent energy resolution, an excellent proportionality of pulse height to the kinetic energy of an incident charged particle. These features are, however, somewhat spoiled when the SSBD is employed in the measurements of heavy ions.

The deterioration of the proportionality between the output pulse height and the incident energy of heavy ion is called pulse height defect (PHD). One of the authors reported the model of dielectric plasma column, which explained the bias voltage dependence of the PHD clearly.[1]

The time retardation of output signal from the time of charged particle incidence is called plasma delay. The plasma delay depends on the mass and atomic numbers of the incident charged particle and on the applied bias voltage and the resistivity of the employed SSBD. Even the energetic alpha particle has the plasma delay of a few nano seconds. Any measurements on the time of flight of charged particles can avoid the effect of the plasma delay. The measurements of the plasma delay, however, have been reported only for a few charged particles. One of the present author reported the model of the plasma column erosion elsewhere,[2] which model explained the experimental results of the plasma delay measured by Bohne et al.[3] fairly well.

In this paper, we report the experimental results of the plasma delay of ^{16}O and ^{79}Br ions measured by the SSBDs of two different resistivities, changing the applied bias voltages.

Charged particles were accelerated by the Tandem accelerator and scattered by a gold foil of $130\mu g/cm^2$ in thickness at the center of scattering chamber. The scattered charged particles were extracted to the flight path with scattering angle of 50 degrees. On the flight path, micro channel plate detector (MCP) and SSBD were placed, with the distance between them 105.8cm.

Charged particles employed in our experiments were ^{16}O ions with 61.1MeV and

79.9MeV in energy and ^{79}Br ions with 93.6MeV and 123.1MeV in energy, after they passed the entrance window of the SSBDs. The resistivities of the employed SSBDs were 362Ωcm and 2100Ωcm, respectively. The time of flight (TOF) of each charged particle were measured by as a function of reciprocal effective electric field strength $(1/F_{eff})$.

The time delay between the electronic circuits of MCP and SSBD was obtained by subtracting the calculated TOF from the measured TOF. The zero time of the electronic circuit was determined by extrapolating the delay time to the one of the infinite electric field strength $(1/F_{eff} = 0)$. The plasma delay is obtained by subtracting the delay time from the zero time.

The plasma delays of ^{16}O ions and ^{79}Br ions measured by 362Ωcm and 2100Ωcm SSBDs are shown in Figs. 1 and 2, respectively. We can see that the plasma delays of the SSBD with higher resistivity is greater than the ones of the lower resistivity SSBD, even though the electric field strength is the same.

For comparison, the plasma delays of alpha particle, ^{40}Ar ion and ^{129}Xe ion measured by Bohne et al.[3] with the SSBD of 4700Ωcm are plotted in Fig. 3. The energies spent to produce electron-hole pairs, the plasma column lengths, and the approximate electron-hole densities of the charged particles shown in Fig. 3 are listed in Table 1. In the case of approximate electron-hole density less than 10^{-3}MeV/μm^3, the plasma delay saturates or has a peak as a function of $1/F_{eff}$. On the contrary, the plasma delay increases monotonously as the $1/F_{eff}$ increases for the charged particle with its approximate electron-hole density greater than 10^{-3}MeV/μm^3. With the experimental data of Bohne et al. and the present results, it is concluded that the behavior of plasma column does not depend on the resistivity of the SSBD employed in the measurement of the plasma delay.

* Present address : Kyoto University.

References
1) I. Kanno, J. Nucl. Sci. & Technol., **28**, 87 (1991).
2) I. Kanno, Rev. Sci. Instrum., **58**, 1926 (1987).
3) W. Bohne, W. Galster, K. Grabisch, and H. Morgenstern, Nucl. Instr. and Meth., **A240**, 145 (1985).

Table 1 Energies spent to produce electron-hole pairs E, plasma column lengths l, and approximate electron-hole densities E/l^3. The p and m in the table indicate the plasma delay has peak (or saturetes) or monotonously increases, as a function of the reciprocal field strength $1/F_{eff}$.

Particle	Energy (MeV)	$l(\mu m)$	$E/l^3 (MeV/\mu m^3)$	p/m
O-16	61.1	46.9	5.92×10^{-4}	p
Br-79	93.6	15.1	2.72×10^{-2}	m
α	8.78	57.6	4.59×10^{-5}	p
Ar-40	268	72.6	6.95×10^{-4}	p
Xe-129	166	19.7	2.31×10^{-2}	m
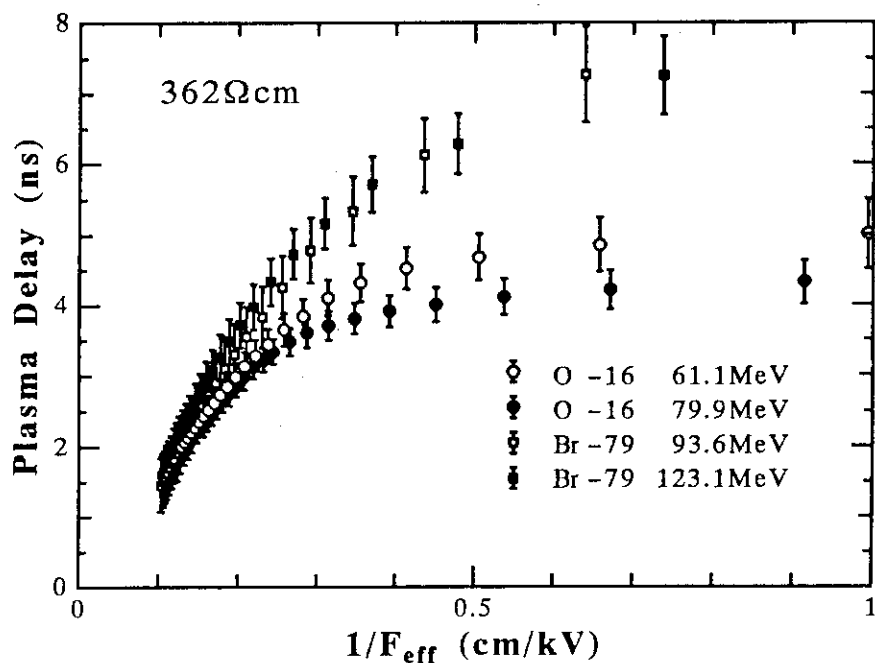
Fig. 1 Plasma delays measured by the SSBD of $362\Omega cm$ in resistivity. Incident charged particles are indicated in the figure.
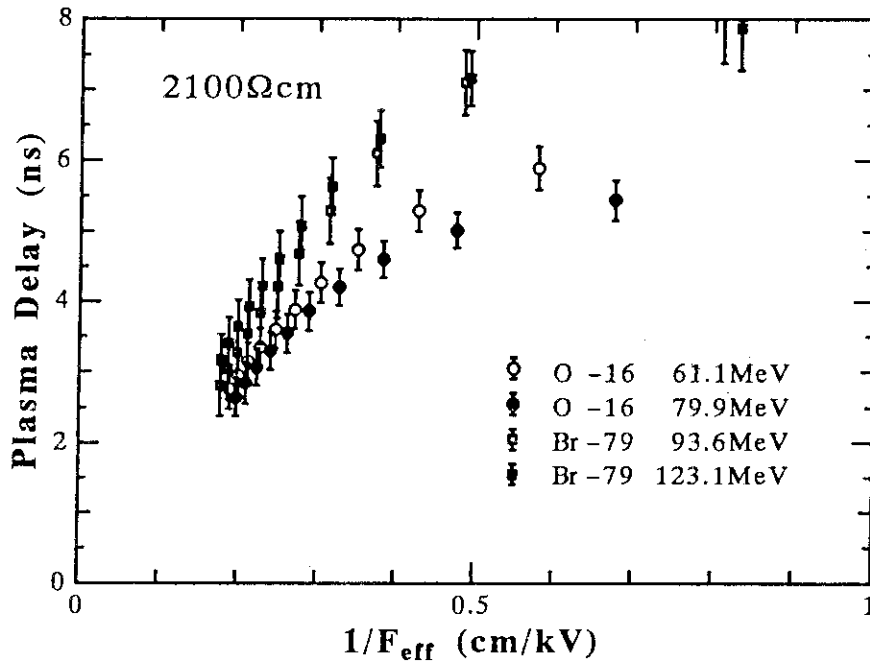
Fig. 2   The same as in Fig. 1 but measured by the SSBD of 2100Ωcm in resistivity.
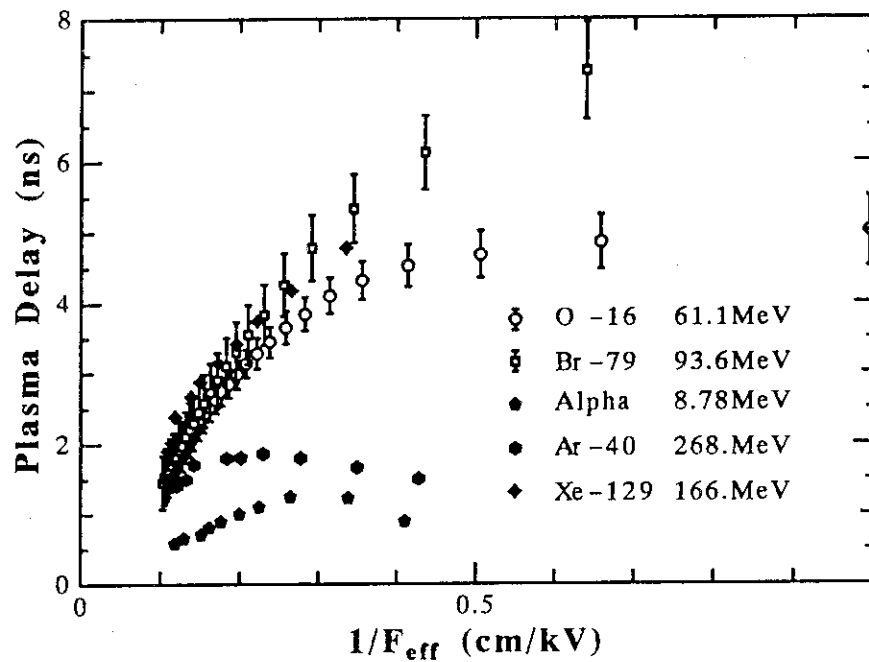
Fig. 3   Plasma delays measured by the present authors (^{16}O ion and ^{79}Br ion) with 362Ωcm SSBD and by Bohne et al. (α particle, ^{40}Ar ion and ^{129}Xe ion) with 4700Ωcm SSBD.

2.18 Mechanism and Evaluation Technique for Single Event Phenomenon of Power MOSFETs and SRAMs

Ikuo KANNO*, Hideshi YASUDA, Hiroshi TAKADA,
Toshinobu SASA, Yousuke MORITA**, Toshio HIRAO**,
Tadaaki KUROSAKI***, Sumio MATSUDA***,
Satoshi KUBOYAMA***, Takashi TAMURA***,
Yosuke SHIMANO***, Masato UESUGI***, and Tooru KANNO***

Department of Reactor Engineering, JAERI,
*Present Address : Kyoto University,
**Department of Development, JAERI,
***Parts and Material Laboratory, NASDA

A new characteristics for single event burn-out (SEB) of power MOSFETs and single event latch-up (SEL) of SRAMs have been acquired. Moreover a new characterization technique for SEB has been developed.

INTRODUCTION

1. Power MOSFETs have a possible catastrophic failure mode known as SEB for the space electronics. Several models for SEB have been proposed [1-4]. Since the other nondestructive SEB measurements have been done using only a current monitor circuit with pulse counter [5], detailed SEB mechanism has not been acquired experimentally. Newly-developed measurement system called EPICS (Energetic Particle Induced Charge Spectroscopy) enabled the direct observation of the phenomenon.

2. Since there are some discrepancy between ground test data of SEL for SRAM and on-orbit data [6,7], we examined two types of CMOS SRAM. By irradiating them with high energy heavy ion, SEL of 64k SRAM was detected. However, SEL of 256k SRAM was not found.

EPICS SYSTEM FOR THE SEB TEST

To identify the mechanism for SEB, charge collection characteristics of p-n junction should be measured. Generally, the charge collection characteristics are measured using PHA(Pulse Height Analyzer) with CSA(Charge Sensitive Amplifier). However, some modifications are required

to configure the adequate measuring system. Fig.1 shows the block diagram of the EPICS. The lowest signal level to be measured is about 0.2pC that corresponds to incidence of a 5.4MeV α particle from ^{241}Am source, and the highest level is about 50nC (C_{OSS}:100pF x V_{DS}:500V) that corresponds to possible collected charge at SEB occurrence. Therefore, dynamic range of the CSA should be more than 100dB. The CSA is also modified to prevent the destruction of DUT(Device Under Test) and the CSA itself. Fig.2 shows a schematic diagram of the CSA. The modifications were made to add R_L and C_H. The R_L is a current limiting resistor to protect DUT and C_H is a voltage holding capacitor to attenuate the voltage swing at the first stage of amplifier when SEB occurs.
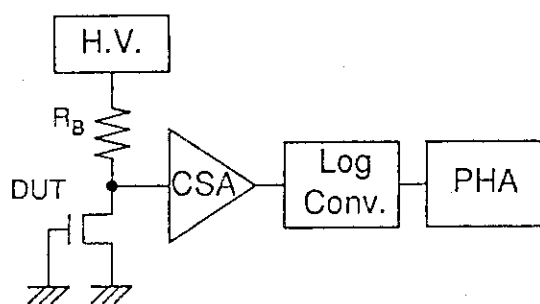
Fig.1. Block diagram of the EPICS
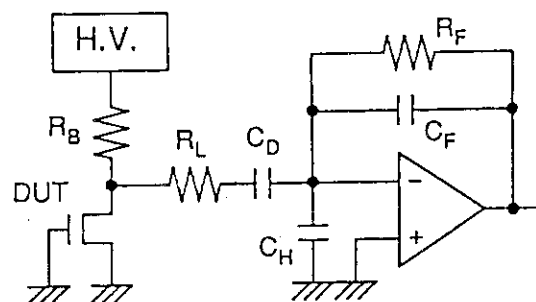
Fig.2. Schematic diagram of the CSA

EXPERIMENTS

Three types of power MOSFETs and two types of SRAMs were irradiated with heavy ions using tandem Van de Graaff accelerator facility at JAERI.

1. Power MOSFETs: The incident ions were 140MeV Si, 200MeV Ni and 133 MeV Br, and their range in Si were 52, 32 and 20um, respectively. The 1st sample power MOSFET was commercial type which had 500V of rated BV_{DS} and 12A of I_D. The 2nd sample was fabricated with the same photo mask set and process conditions without source diffusion process. Therefore, the 2nd sample has diode construction only and no parasitic transistor. The 3rd sample was also commercial type from different manufacturer which have the same maximum rating as the 1st sample. Fig.3 shows a typical structure and parasitic bipolar transistor.
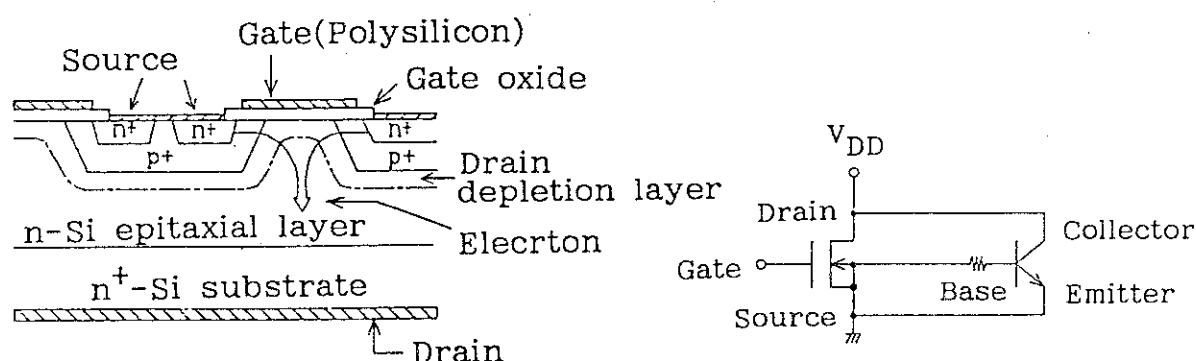
Fig.3. Typical structure of power MOSFET and parasitic transistor

2. SRAMs: The incident ions were 203MeV Ni, 101MeV Ni, 128MeV Si and 128MeV Si, and LET(Linear Energy Transfer) was adjusted by changing of the incident angle (θ) of beam exposed to DUT. Therefore, LET and measured latch-up cross section were corrected by $1/\cos\theta$ [8]. The devices irradiated were 64kbits CMOS SRAM for commercial use and 256kbits CMOS SRAM for space use. Fig.4 shows a CMOS structure and parasitic bipolar thyristor. When voltage of p-well increase caused by the penetrated heavy ion into the SRAM, the thyristor is triggered and latch-up occurs.
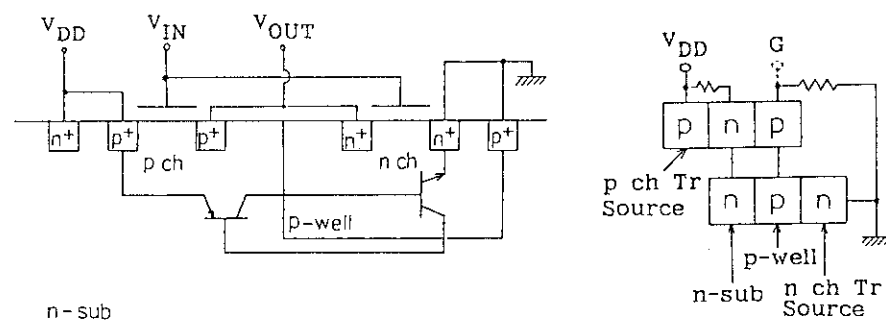
Fig.4. Typical structure of SRAM and parasitic thyristor

RESULTS AND DISCUSSION

1. Power MOSFETs: Fig.5 shows typical experimental data for the 1st sample. It is clearly observed that the collected charge is amplified by avalanche effect as V_{DS} increase. At higher V_{DS}, the collected charge reaches to the certain value and triggers SEB. Therefore, there are SEB signals only in the region larger than this value. So, we call this value as threshold charge, Q_{TH}. The Q_{TH} is attributable to device design and does not depend on incident ions. The fact was confirmed by the 3rd sample and several additional samples. Therefore, the Q_{TH} can be used as a measure of SEB hardness for power MOSFETs.

Fig.6 shows the experimental data for the 2nd sample with the same conditions as shown in Fig.5. The difference from Fig.5 is the lack of the 2nd (right side) peak. Therefore, the first peak must be from drain and p+ body junction, and the second peak for the 1st sample indicates additional amplification by the parasitic bipolar transistor. The second peak is too sharp as expected by formerly proposed model [2-4]. In the model, the voltage drop generated by the hole current along the p+ body cause the activation of the parasitic transistor. Because the value of the voltage drop depends on the position of an ion track in the p+ region, the second peak should be very broad. To explain the discrepancy, another mechanism should be proposed. The observed second peak suggests position independent charge collection mechanism. Therefore, we propose the mechanism, that the voltage drop generated by the current flow along the ion track directly make active the parasitic transistor. Because the first peak and the second peak correspond directly to the integrated base current and the emitter current respectively, the distance between the first and second peak represents the current gain of parasitic transistor. The observed distance is almost constant at all the ions and V_{DS}. This is an evidence to support the proposed mechanism.

Finally, Fig.7 shows avalanche multiplication factors as a function of LET and V_{DS} for the 3rd sample. It is found that avalanche multiplication factors increase, as LET and V_{DS} increase. This fact supports the internal field modification by generated plasma column as proposed formerly [4]. The LET and V_{DS} dependence of the avalanche multiplication factor in conjunction with Q_{TH} maybe able to give SEB prediction with fewer experimental data. Additionally, the data for Si ions at V_{DS}=300V shows that SEBs are triggered, whereas the first and second peaks are still bellow the Q_{TH}. The data suggests recoils or nuclear reactions dominantly trigger SEB, because there are some signals between the second peak and the Q_{TH} in contrast with Ni and Br ions. In this case, observed SEB cross-section is small, but required LET is also small. The data shown in reference [5] by Fe ions may be explained with this mechanism.

2. SRAMs: 256kbits SRAM has detected no latch-up in this test (up to LET 61MeV/(mg/cm^2) whose incident angle was 60°). On the other hand, 64kbits SRAM was very susceptible to the latch-up. Fig.8 shows plots of the latch-up cross section versus the effective LET for 64kbits SRAM.

According to the other data for 64kbits SRAM, the threshold LET acquired by an experiment using cyclotron was 2-19MeV/(mg/cm^2) [6], and the latch-up cross section acquired by an experiment using Cf-252 was 0.105cm^2 [7]. On the other hand, it is clearly confirmed that the threshold LET is about 9.5MeV/(mg/cm^2) and the saturation cross section is 0.24cm^2 in Fig.8.
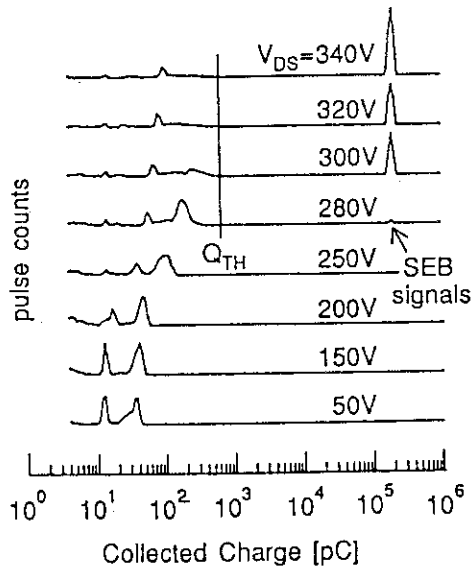
Fig.5. EPICS spectrum for the 1st sample MOSFET with 200MeV Ni
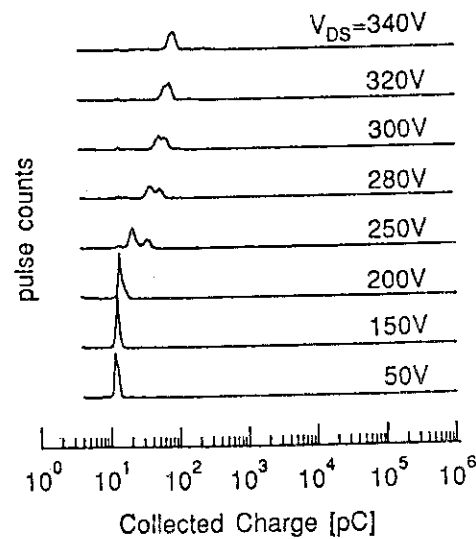
Fig.6. EPICS spectrum for the 2nd sample MOSFET with 200MeV Ni
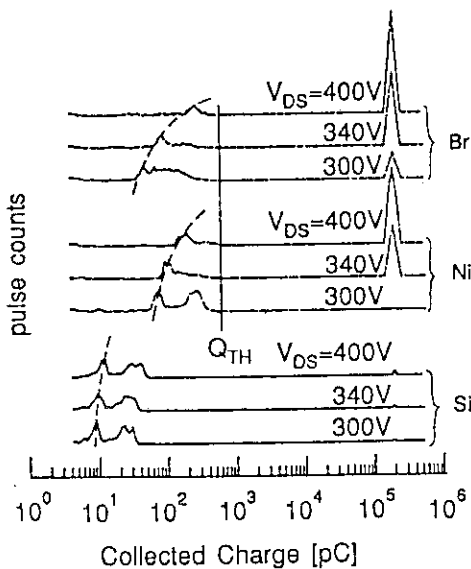
Fig.7. Multiplication factors as a function of LET and V_{DS} for MOSFET
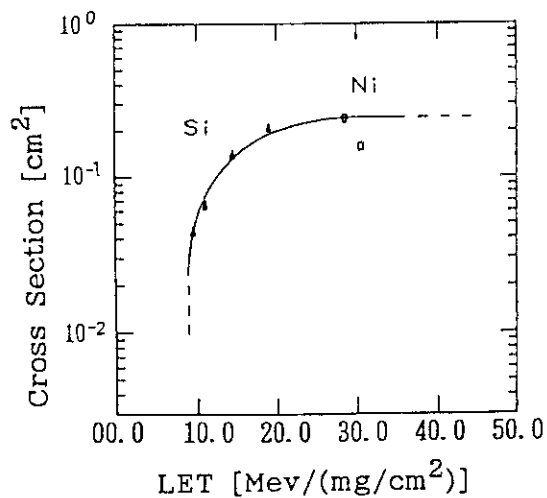
Fig.8. Plots of latch-up cross section vs. LET for 64k SRAM

CONCLUSIONS

Newly developed characterization technique of SEB for power MOSFETs with the EPICS was demonstrated. The technique can extract the Q_{TH} , which gives the SEB hardness attributable to the device design. New SEB triggering mechanism by current flow along the ion track was proposed. The LET dependence of the avalanche effect was confirmed. It was observed that recoils or nuclear reactions could trigger SEB with low LET but high energy ions.

Moreover, by irradiation with high energy ions using tandem Van de graaff, we acquired data of latch-up cross section of SRAMs in a wide range of effective LET. Continuously, we are planning to acquire the exact threshold LET by irradiation using lower incident LET.

REFERENCES

1) T.A.Fischer,"Heavy-Ion-Induced,Gate-Rupture in Power MOSFETs," IEEE Trans.Nucl.Sci., Vol.NS-34, No.6, pp.1786-1791, (1987)

2) A.E.Waskiewicz, J.W.Groninger, V.H.Strahan and D.M.Long, "Burnout of Power MOS Transistors with Heavy Ions of Californium-252, IEEE Trans.Nucl.Sci., Vol.NS-33, No.6, pp.1710-1713, (1986)

3) J.H.Hohl and K.F.Galloway,"Analytical Model for Single Event Burnout of Power MOSFETs,"IEEE Trans.Nucl.Sci., Vol.NS-34,No.6,pp.1275-1280,(1987)

4) J.H.Hohl and G.H.Johnson, "Features of the Triggering Mechanism for Single Event Burnout of Power MOSFETs," IEEE Trans.Nucl.Sci., Vol.NS-36, No.6, pp.2260-2266,(1989)

5) D.L.Oberg and J.L.Wert, "First Nondestructive Measurements of Power MOSFET Single Event Burnout Cross Sections," IEEE Trans.Nucl.Sci., Vol.NS-34, No.6, pp.1736-1741,(1987)

6) N.Shiono, Y.Sakagawa, M.Sekiguchi, K.Sato, I.Sugai, T.Hattori and Y.Hirao, "Single Event Effects in High Density CMOS SRAMs," IEEE Trans. Nucl.Sci., Vol.NS-33, No.6, pp.1632-1636,(1986)

7) T.Goka,S.Kuboyama,Y.Shimano and T.Kawanishi, "The On-orbit Measurements of Single Event Phenomena by ETS-V Spacecraft,"Proceeding of the ESA Workshop on Space Environment Analysis.,Vol.ESA WPP-23, Section 5.21,(1990)

8) F.W.Sexton, J.S.Fu, R.A.Kohler and R.Koga, "SEU Characterization of A Hardened CMOS 64K and 256K SRAM,"IEEE Trans. Nucl. Sci., Vol.NS-36, No.6, pp.2311-2317, (1989)

III   NUCLEAR CHEMISTORY

3.1 Distribution of Recoil Atoms in Ion-guide ISOL

Shin–ichi ICHIKAWA, Masumi OSHIMA[*], Toshiaki SEKINE[**],
Ichiro NISHINAKA[**†], Yuichi HATSUKAWA[**], Tsuneyasu
MORIKAWA[**#] and Hideki IIMURA

*Department of Chemistry, *Department of Physics,
**Department of Radioisotopes, JAERI*

As described in Ref.[1], we have applied an ion–guide ion method for isotope separator on–line for the study of short–lived nuclei far from the β–stability line. The extraction efficiency has been measured to be about 0.15% for the primary production coming out of the target. In order to increase the extraction efficiency of reaction products produced by heavy–ion induced reactions, we need to use heavier buffer gases as a stopping material than He. The reaction products may be partly implanted on the inner wall of the target chamber due to its high recoil energy, or be trapped there during the thermal motion. These process causes loss of the extraction efficiency. The amount of the loss, however, has not been measured so far. Because of this, we measured the distribution of radioactivity produced by a nuclear reaction in an ion–guide chamber. The data provides valuable information for the development of a laser–enhanced ion–guide ion source, which is described in Refs. [3,4].

In order to derive distribution of reaction products, we measured the distribution of the radioactivity produced inside the chamber. The schematic layout of the chamber used is shown in Fig. 1. The buffer gas of 0.2–atm He was introduced in the chamber and evacuated through a skimmer of a diameter of $\phi = 0.8$ mm by a turbo molecular pump with a pumping speed of 1800 l/s. The reaction ^{nat}Sn (^{12}C,xn) was used to produce ^{125}Ba activities. First, the total number of recoil atoms from the target was measured by collecting the recoil atoms of ^{125}Ba on an Al foil placed closely behind the target in the ion–guide chamber (not shown in the figure). It was found that 18% of the reaction products recoiled out of the target owing to its finite thickness. Secondly, Al foils were placed on the inner surface of the chamber as shown in Fig. 2. After irradiation by the carbon beam, the ^{125}Ba radioactivity collected on the foils was
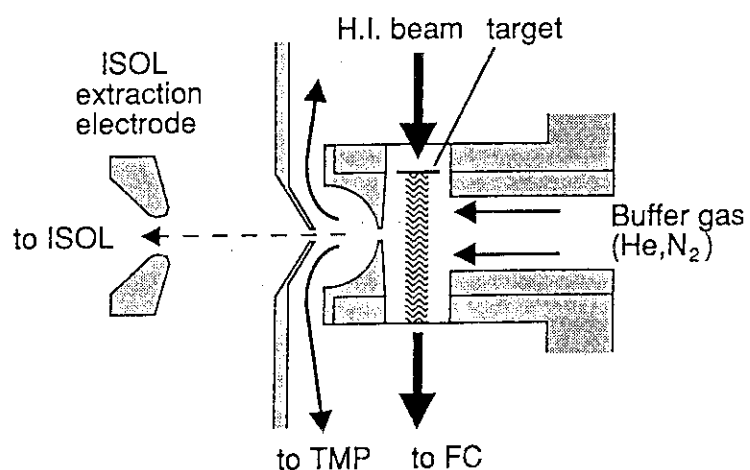
Fig. 1. Schematic layout of Ion—Guide chamber.
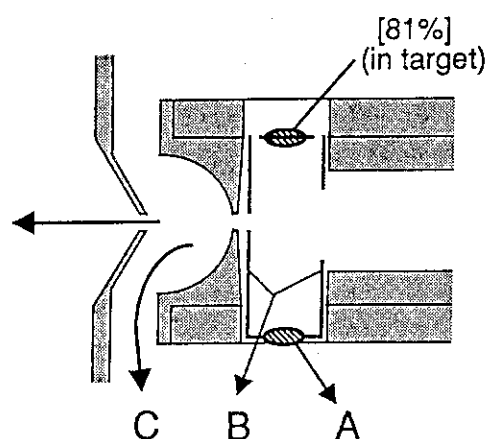
Fig. 2. Activity distribution measurement.

Table I. Distribution of [125]Ba activity for three buffer gases after irradiation of a Sn target by a carbon beam. The uncertainty for the fraction is 5%.

| buffer gas | fraction | | |
	A	B	C
He	52%	40%	8.4%
N_2	36%	27%	37%
Ar	33%	22%	45%

measured. The yield of Ba atoms which were evacuated through the skimmer was derived by subtracting the radioactivity remaining inside the chamber from the total radioactivity recoiling out of the target. The result is presented in Table I. The fraction of the radioactivity is normalized to the total number of Ba atoms recoiling out of the target. As mentioned above, the recoil energy of the reaction products should show a distribution from zero to the energy corresponding to the reaction occurring at the rear surface of the target. From a range calculation the fraction of atoms stopped in the gas was calculated to be 25%. This can be compared with the experimental value of 8.4 ± 5.0 %. This discrepancy is considered to be due to the fact that the atoms are trapped on the inner surface of the chamber during thermal motion.

In order to see the effect of buffer gas, the He buffer gas was replaced by N_2 and Ar gas of a pressure of 0.2–atm. The radioactivity distribution is given in Table I measured in the same way as for He. The fraction of atoms evacuated from the ion–guide chamber amounts to 37% and 45% for N_2 and Ar, respectively, which can be compared with the estimated value of 100% obtained in the same way as for He. Hence, the use of heavier gas has turned out to be effective for stopping the recoils and keeping a considerable amount of the atoms in the gas phase without sticking to the inner surface, until they are evacuated through the skimmer.

The present result is useful to understand the behavior of recoil atoms in the ion–guide chamber and hence to improve the ion–guide efficiency.

References

[1] S.Ichikawa et al., JAERI–M report 90–139, 119 (1990).

[2] J.Arje, J.Aystro, J.Honkanen, K.Valli, and A.Hautojarvi, Nucl. Instr. Meth. **186**, 149 (1981)

[3] M.Oshima et al., Nucl. Instr. Meth. (1992) in press.

[4] T.Sekine et al., in this volume.

3.2 Development of a Laser Ion Source: Off-line Test of Laser Resonance Ionization of Ba Atoms

T. SEKINE,[1] M. OSHIMA,[2] S. ICHIKAWA,[3] Y. HATSUKAWA,[1]
I. NISHINAKA,[1,*] T. MORIKAWA[1,†] AND H. IIMURA[3]

[1]*Department of Radioisotopes*, [2]*Department of Physics*
and [3]*Department of Chemistry, JAERI* * †

The present work aims at developing a laser ion source to be used in on-line isotope separation for very unstable nuclei possesing half-lives as short as several milliseconds. The ion source proposed by the present authors is based on an ion-guide method, as described elsewhere,[1] for rapid isotope separation. The ion-guide method, however, is not efficient partly due to neutralization of the ions in the buffer gas which thermalizes the recoiling atoms. An attractive method to increase the efficiency is to re-ionize the neutral atoms by resonant photo-ionization with lasers, as used in resonance ionization spectroscopy[2] (RIS): two or three laser beams tuned in resonance with the relevant atomic transitions are used to excite and ionize the atoms. Another important advantage of this technique is the Z-selectivity in ionization, which can be achieved by the element-dependent resonance scheme.

In the present paper, we present results on off-line resonance ionization experiments for Ba atoms.

We performed an off-line experiment using two tunable dye lasers pumped by a copper-vapor laser with a repetition rate as high as 6-9 kHz and an average output power of 30 W. The band width of the dye lasers is 0.2 cm^{-1} or 6 GHz. The Doppler broadening of the atoms of mass number A at the temerature T is given by

$$\Delta\nu/\nu = 7.16 \times 10^{-7}(T/A). \tag{1}$$

For a wave length of 600 nm the Doppler broadening for the mass number $A = 130$ is $\Delta\nu = 0.52$ GHz at room temperature. Thus the laser band width covers well the Doppler broadening

An experiment with Ba atoms was performed in an off-line chamber by three-step resonance ionization. The experimental set-up is shown in Fig.1. An atomic beam of Ba was produced from an oven heated at 1020 K. Dyes of Rhodamine 110 and Rhodamine 6G were used for RIS of Ba as previously reported in Ref.3. The dye laser beams were collimated to a diameter of 1mm at the interaction region with the atomic beam. In the vicinity of the interaction region a Ceratron device was placed to detect the ions produced. Resonance-ionization spectra were measured with a multichannel analyzer in
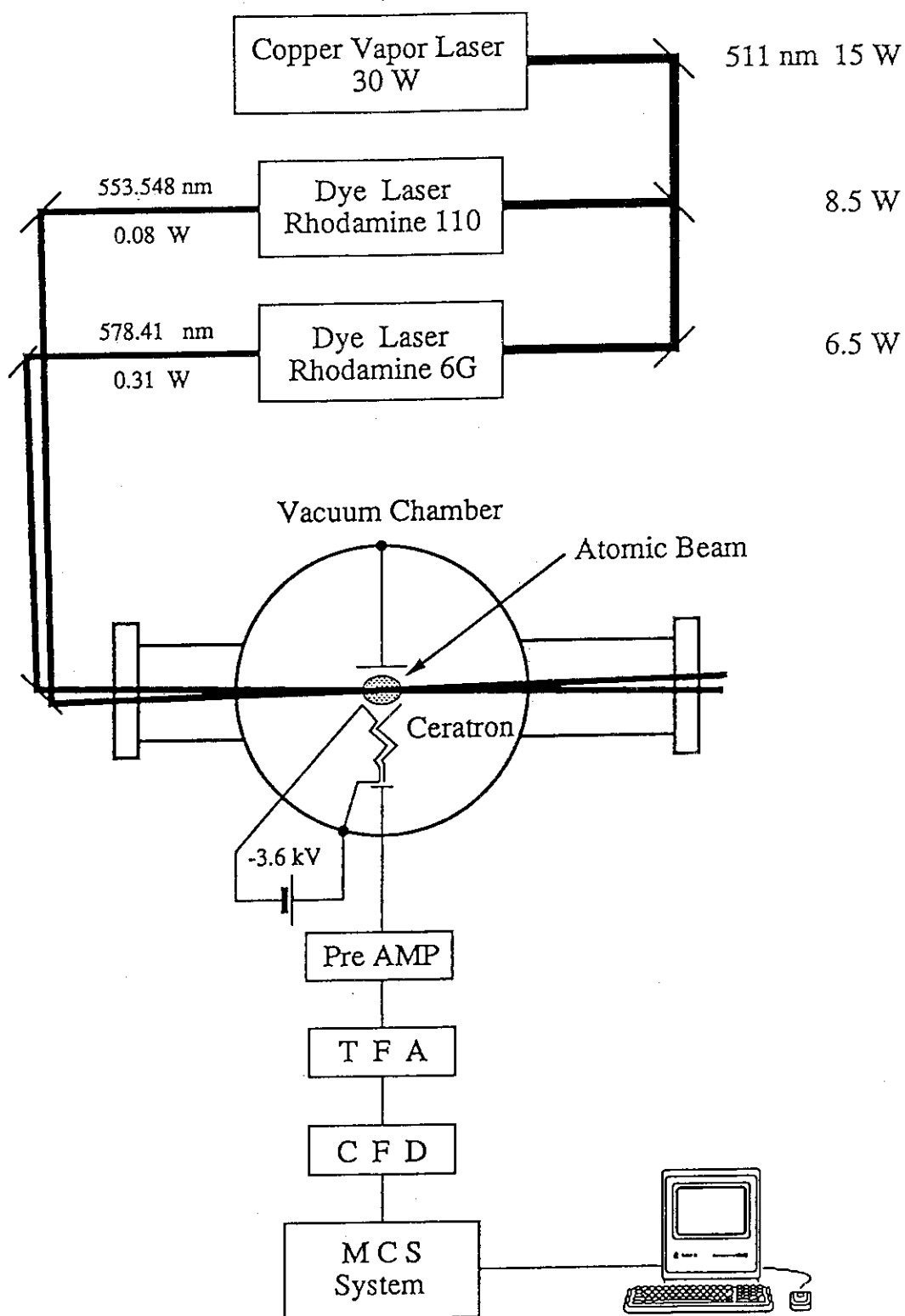
Fig. 1. Experimental setup for off—line resonance ionization spectroscopy. TFA: Timing filter amplifier; CFD: Constant fraction discriminator; MCS: Multi—channel scaling.
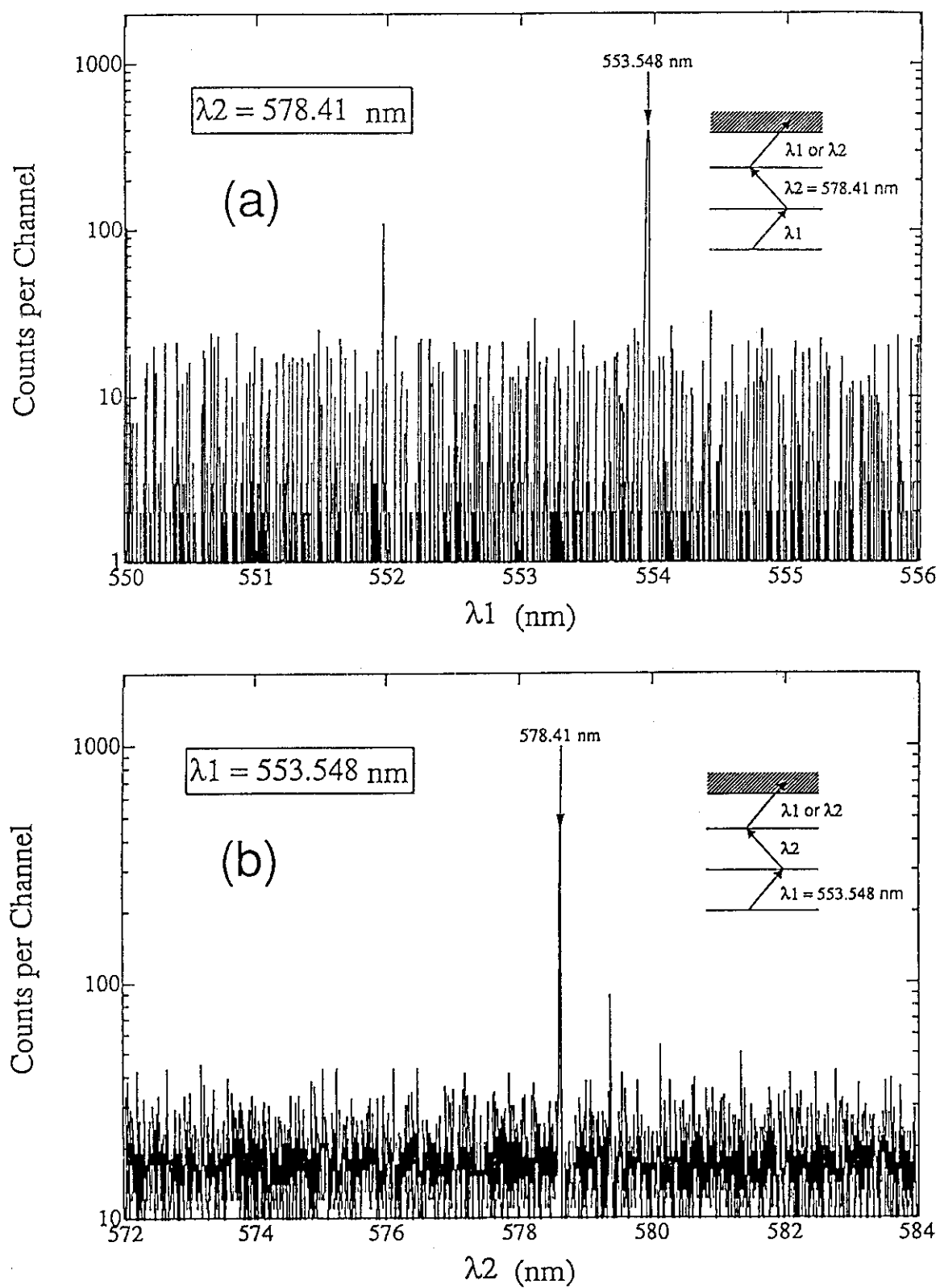
Fig. 2. Resonance ionization spectra for Ba atoms. (a) λ_1 is scanned while λ_2 is fixed to 578.410 nm. (b) λ_2 is scanned while λ_1 is fixed to 553.548 nm.

a multichannel scaling mode, while the wave length of one of the dye lasers was scannned at a constant speed and that of the other was fixed at either 553.548 or 578.410 nm. From the measurement with a laser repetition rate of 6 kHz and a dwell time of 0.1 s in multichannel scaling, clean spectra were obtained, as shown in Fig.2, proving the three-step, two-color resonance ionization for Ba atoms.

The ionization efficiency for Ba atoms was measured by three-color, two-step resonant RIS under the following conditions: the wave lengths of the dye lasers pumped by the green output ($\lambda = 510$ nm) of the copper-vapor laser, were the above resonance wave lengths. Enhancement of the last step was accomplished by adding the yellow laser beam, from the copper-vapor laser ($\lambda = 578$ nm, average power 15 W), not used for pumping the dye lasers. The schematic setup is shown in Fig.3. In order to determine the density of the atomic Ba beam, the Ba atoms were collected on a Mylar foil placed just above the laser-atom interaction region. The number of the Ba atoms on the foil was determined by neutron activation analysis. The samples were irradiated together with a standard sample of Ba under a thermal neutron flux of 4×10^{13} cm^{-2} s^{-1} in the JRR-4 reactor at JAERI. The ^{139}Ba radioactivity in each sample was measured by γ-ray spectrometry. The result gave $\rho v = 2.9 \times 10^{12}$ atoms/cm$^2 \cdot$ s; ρ being the density of Ba atoms in the interaction region and v the mean velocity of the atoms. Since the mean velocity v is expressed as

$$v = (3kT/m)^{1/2} = 4.3 \times 10^4 \text{cm/s} \tag{2}$$

at $T = 1020$ K, the Ba-atom density in the interaction region is estimated to be 6.9×10^7 atoms/cm^3. Since the diameter of the lasers was typically 1 mm, the number of atoms in the interaction region was determined to be 5.4×10^5. From this value and the ion current $I = 1 \times 10^{-11}$ A measured in the setup shown in Fig.3, the ionization efficiency per pulse was found to be 1.9%. The resulting efficiency can be compared with the calculated value of 35% obtained by using the emperical formula given in Ref.4. The fact that the experimental efficiency was lower than the calculated one might be due to a smaller effective interaction volume of the atoms and the lasers than expected.

References

1) S. Ichikawa, M. Oshima, T. Sekine, I. Nishinaka, Y. Hatsukawa, T. Morikawa and H. Iimura, in this volume.

2) G.S. Hurst and M.G. Payne, "Principles and Application of Rosonance Ionization Spectroscopy" , I. O. P. Publishing Ltd, 1988.

3) L.W. Green, R.G. Macdonald, F.C. Sopchyshyn and L.J. Bonnell, Inst. Phys. Ser. No.84, Section 3, I.O.P. Publishing Ltd, 1986, p.133.

4) H. Kramers, Phil. Mag. 44, 836 (1927).
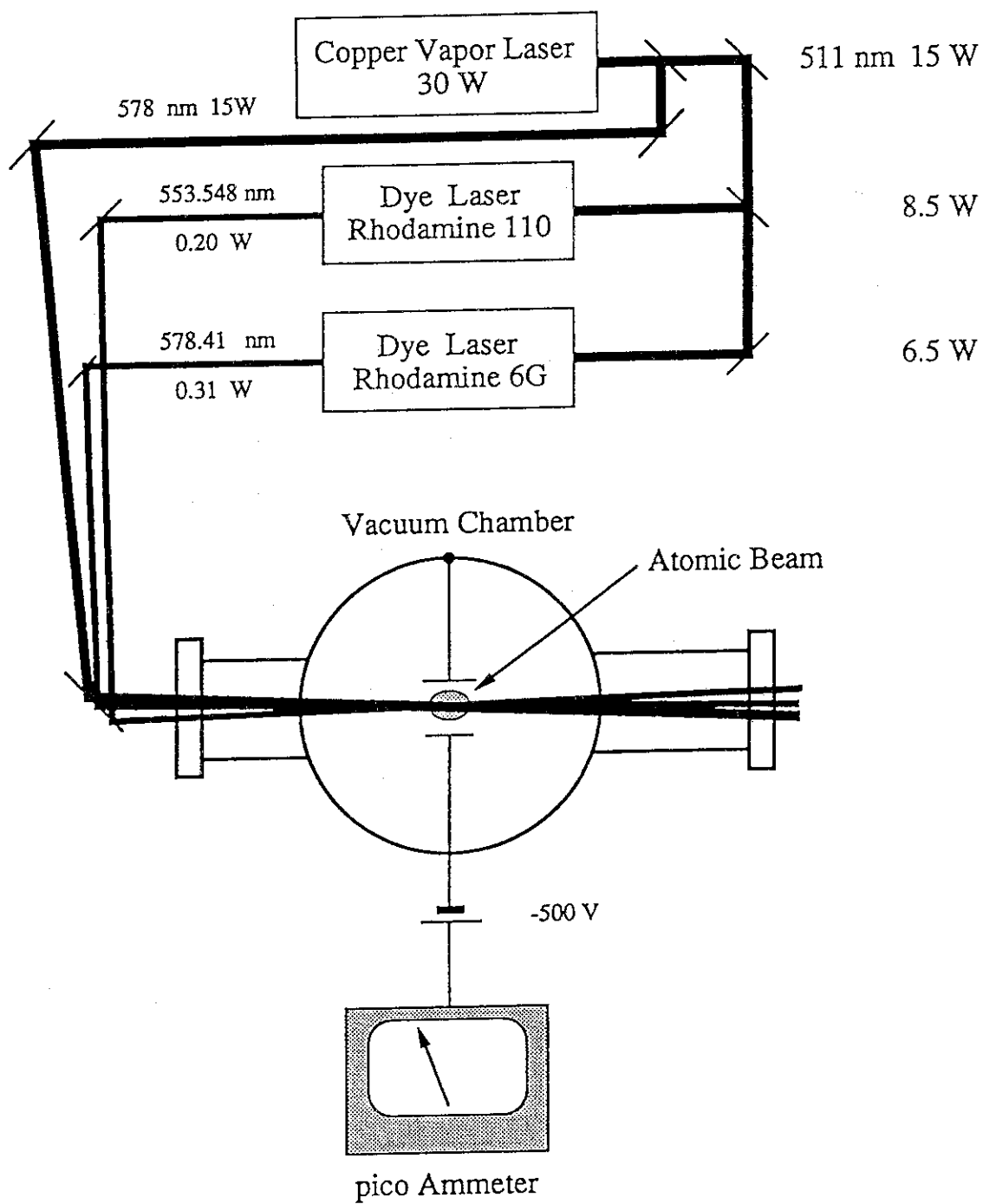
Fig. 3. Experimental setup for off—line measurement of ion intensity.

3.3 Beta-decay Study of Mass Separated ^{121,123}Ba

Akihiko OSA,§ Shin-ichi ICHIKAWA, Hideki IIMURA,
Tomohiko IKUTA,§ Akihiro TANIGUCHI,§ Hiroshi YAMAMOTO,§
Kiyoshi KAWADE,§ Toshiaki SEKINE† and Masumi OSHIMA‡

Department of Chemistry, †Department of Radioisotopes,
‡Department of Physics, JAERI, and
§Department of Nuclear Engineering, Nagoya University

INTRODUCTION

The features of low-lying states of Cs (Z=55) nuclei are clearly dependent on the neutron number N [1, 2, 3]. Information of these levels from β-decay of Ba is, however, very scarce in the neutron deficient region. In the present work, we studied β-decay of ^{121,123}Ba using the JAERI-ISOL[4].

EXPERIMENT

The experiments were performed at the tandem accelerator in JAERI, by using the reaction ^{92}Mo(^{32}S,2pn)^{121}Ba and ^{nat}Mo(^{32}S,2pxn)^{123}Ba with a 5.1 MeV/u ^{32}S beam. The thickness of natural molybdenum target was about 4.1 mg/cm^2 and one of enriched molybdenum(^{92}Mo 97.37%) target was about 3 mg/cm^2. The reaction products were ionized in a surface-ionization ion source and mass-separated. The mass-separated reaction products were implanted into an aluminum coated Mylar tape in a tape transport system and periodically transported to a measuring position, where γ-ray singles and γ-γ coincidence measurements were performed with two HPGe low-energy photon spectrometers (LEPS). Gamma-ray multi-spectra were measured with the LEPS. The decays of each γ-rays were traced by taking consecutively 16 spectra. Beta-γ delayed coincidences were observed with a plastic scintillator and the LEPS to measure half-lives of excited states. Coincidence events were recorded in list mode on a magnetic tape by means of multi-parameter system (AMS-1600) controlled by a personal computer (NEC-PC9801).

The β^+-ray maximum energies of ^{121,123}Ba were also measured. Singles β^+-ray and β^+-γ coincidence measurements were performed with the LEPS and the x-γ HPGe detector. Energy calibration of the LEPS was made up to 8 MeV with prompt γ-rays from the thermal neutron capture of ^{35}Cl(n,γ). Thermal neutrons were generated by a ^{252}Cf neutron source of 3.5 MBq.

RESULTS

Decay curves of intense γ-rays measured at the mass A=121 are shown in Fig. 1. The half-life is deduced to be 29.5±0.5 s. This value agrees with the previous one of 29.7±1.5 s [5]. The Q_{EC}-value for ^{121}Ba was determined to be 6.34±0.16 MeV. This value is consistent with the previous one derived from delayed proton study [5], as shown in Fig. 2.
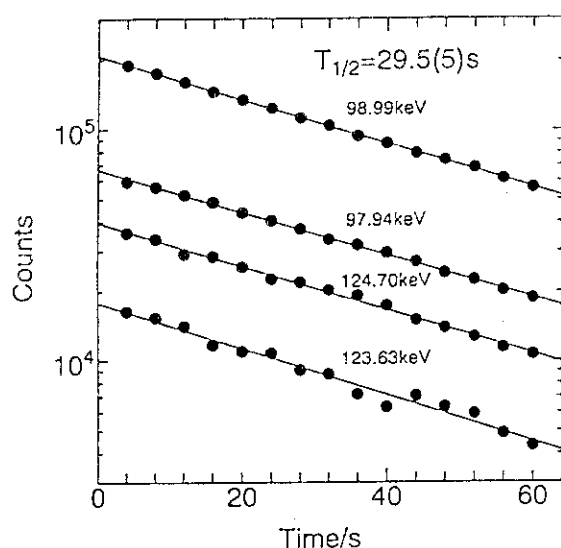
Fig. 1. Decay curves of the γ-rays of ^{121}Ba.
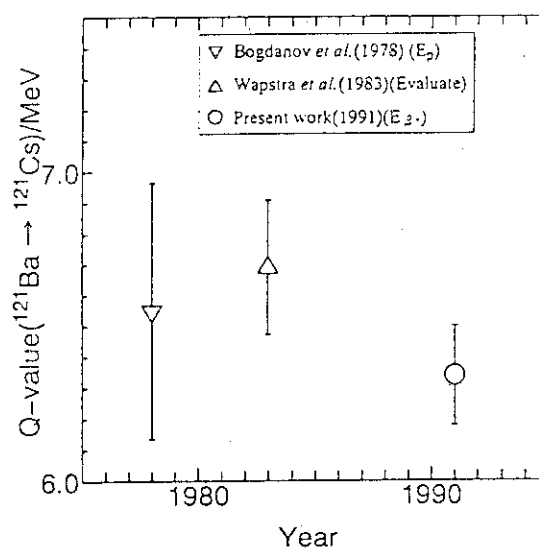
Fig. 2. Q_{EC}-value of ^{121}Ba in this work compared with previous one.

In our previous work [6, 7], partial decay scheme was proposed, but the coincidence relations were not found in this work. A decay scheme for ^{121}Ba is suggested from present experimental results, as shown in Fig. 3.

A decay scheme for ^{123}Ba was also constructed. The present results are consistent with the results reported by Marguier et al.[10]. The Q_{EC}-value for ^{123}Ba was determined to be 5.23±0.10 MeV, which was the first experimental value.

Half-lives of excited states for neutron deficient odd-mass Cs were summarized in Table 1. The spin and parity of the 99.0 keV state in ^{121}Cs were estimated as $5/2^+$ from the neighboring nuclei.
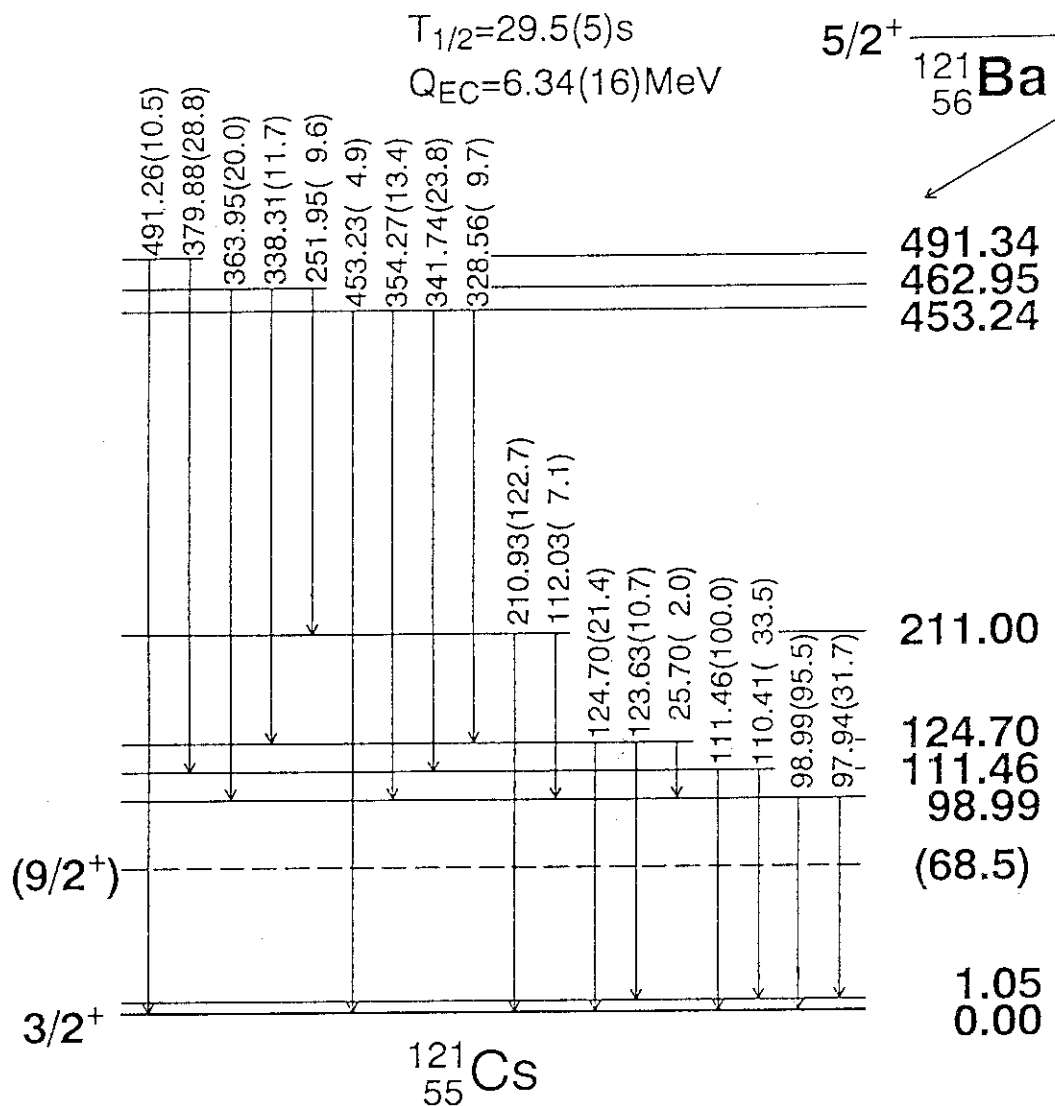
Fig. 3. Decay scheme suggested for ^{121}Ba in this work.

Table 1 Half-lives of excited states for odd-mass Cs isotopes.

Nuclide	Level energy (keV)	Spin & parity	Half-life (ns)	
			Present	Reference §
^{121}Ba	99.0	$(5/2^+)$	3.7±0.2	-
^{123}Ba	94.6	$5/2^+$	7.8±0.1	9±3
^{125}Ba	85.0	$5/2^+$	12.6±0.3	14.5±1.5

§ taken from ref. 1.

REFERENCES

[1] G.Beyer, A.Jasiński, O.Knotek, H.-G.Ortlepp, H.-U. Siebert, R.Arlt,
E.Herrmann, G.Musiol and H.Tyrroff; Nucl.Phys. A260 p.269 (1976)

[2] C.Ekström, S.Ingelman, G.Wannberg, M.Skarestad and the ISOLDE Collaboration;
Nucl.Phys. A292 p.144 (1977)

[3] U.Garg, T.P.Sjoreen and D.B.Fossan; Phy. Rev. C19 p.217 (1979)

[4] S.Ichikawa, T.Sekine, M.Ohshima, H.Iimura and Y.Nakahara,
Nucl. Instrum. Meth. B in progress.

[5] D.D.Bogdanov, A.V.Demýanov, V.A.Karnaukhov and L.A.Petrov;
Sov.J.Nucl.Phys. 21 p.123 (1975)

[6] S.Ichikawa, T.Sekine, H.Iimura, M.Oshima and N.Takahashi;
JAERI Annual Rep. (1984)

[7] Nuclear Data Sheets 64 p.323 (1991)

[8] J.Genevey, A.Gizon, G.Marguier, C.Richard-Serre, A.Knipper, P.Paris, CF.Liang,
B.Weiss, the Isolde and Isocele collaborations; Z.Phys.A 338 p.405 (1991)

[9] K.Sofia,B.N.Subba Rao,and J.E.Carwford
Phys.Rev C24(4) p.1615 (1981)

[10] G.Marguier, A.Charvert, J.Genervey, C.Richard-Serre, A.Knipper, G.Walter and
the ISOLDE Collaboration
J.Phys.G:Nucl.Phys. 7 p.101 (1981).

3.4 Measurement of β-ray Maximum Energy of ^{126}Cs with a Pair-spectrometer

Shin-ichi ICHIKAWA, Tomohiko IKUTA[***], Akihiko OSA[***], Kiyoshi KAWADE[***], Masumi OSHIMA[*], Toshiaki SEKINE[**] and Nobuo SHINOHARA

Department of Chemistry, [*]Department of Physics, [**]Department of Radioisotopes, JAERI
[***]Department of Nuclear Engineering, Nagoya University

The precise experimental data of β-decay energies(Q_β) are particularly important, because information for the masses of nuclei can be obtained. The Q_β-value of short-lived nuclei is determined from β-ray maximum energy and knowledge of the level scheme of the daughter nucleus.[1,2,3] In our previous work, a high purity germanium (HPGe) detector has been used for measurement of β^--,β^+-decay energy.[4,5] In the case of β^+-ray measurement, the measured spectrum is complicated because of summation of annihilation photons.

To suppress a summing effect of annihilation photons, we have been constructed a pair-spectrometer for measurement of Q_{EC}-values; it consists of an HPGe β-ray detector and two pairs of BaF$_2$ scintillation detectors for annihilation photons. With this system, the energy dependence of response function is studied by measuring monoenergetic positron. A Q_{EC}-value of neutron deficient ^{126}Cs nucleus is also determined after separated by means of the JAERI on-line isotope separator(JAERI-ISOL).

Figure 1 shows the detector setup, for example, at JAERI-ISOL. The HPGe detector, the same one used in our previous work, has a germanium crystal with dimension of 16 mm in diameter and 10 mm in thickness. This detector can fully stop positrons of energies up to 9 MeV. Each BaF$_2$ scintillation detector for annihilation photons has a length of 150 mm and a thickness of 60 mm. The energy resolution of each unit of the BaF$_2$ detector is about 15% for 511 keV γ-ray. The relative detection efficiency of the β^+-2γ$^\pm$ coincidence system to the singles measurements was deduced to be 2.5±0.5%.

determined directly by observing the spectrum of monoenergetic positrons in the energy range of 0.7 to 2.7 MeV. A double focusing beta-ray spectrometer at Kyoto University Research Reactor Institute(KURRI) was used to provide monoenergetic positrons from sources of ^{68}Ge-^{68}Ga and ^{34m}Cl. The source of ^{34m}Cl were produced by bremsstrahlung irradiation of sodium chloride at KURRI-LINAC. The observed response function consists of three parts in the same manner as electron; a full energy peak, the escape of bremsstrahlung photons and escape of back and side scattering of positrons from surface of detector. The observed ratio of escape of back and side scattering to the total counts shows in Fig. 2 together with the same ratio for electrons. As seen, the ratio for positrons was the same as for electrons at energies above 1.5 MeV.

The β^+-ray spectra of ^{126}Cs ($T_{1/2}$=1.6 min) free from summation were measured with this system. This isotopes was produced by bombarding a 4.1 mg/cm^2 thick Mo foil with a 5.1 MeV/u ^{32}S beam from tandem accelerator and separated with the JAERI-ISOL. The mass separated products were implanted into an aluminum coated Mylar tape and periodically transported to measuring position by a tape transport system. The decay energy of ^{126}Cs was measured by means of three-parameter β^+-$2\gamma^\pm$-γ coincidences. The β^+-ray spectra of ^{126}Cs observed with this system are shown in Fig. 3. The β^+-ray spectra free from summation were corrected with the same response function as for electron. The endpoint of the corrected β^+-ray spectrum is given by a least-squares fit to the Fermi-Kurie function. The endpoint energies of 3.81±0.04 and 3.39±0.16 MeV are deduced from the β^+-$2\gamma^\pm$ and β^+-$2\gamma^\pm$-γ coincidence spectra, respectively. The mean values of Q_{EC} for ^{126}Cs is determined to be 4.82±0.04 MeV. The accuracy of the Q_{EC}-value of ^{126}Cs has been improved.

We would like to say in the concluding that the measurement of β^+-ray maximum energy with a pair-spectrometer introduces more accurate results than a singles measurement.
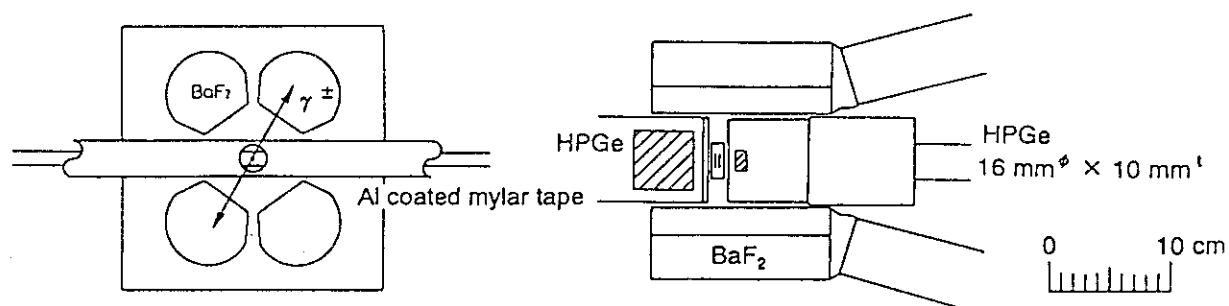
Fig. 1. Schematic view of a pair-spectrometer setup
at JAERI-ISOL.
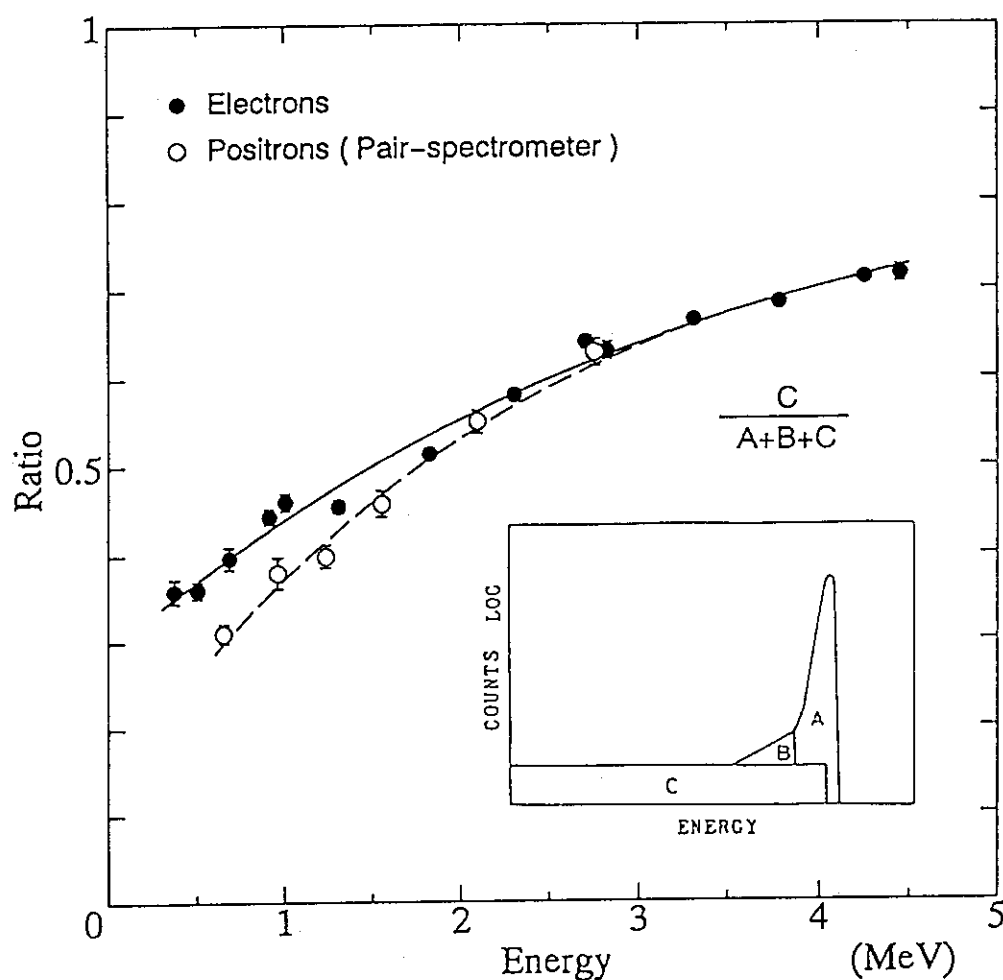
Fig. 2. The energy dependence of ratio of back and side
scattering to the total counts of response function
for electrons and positrons in coincidence with two
511 keV annihilation photons.
The inset shows a schematic diagram of a response
function utilized for an analysis.
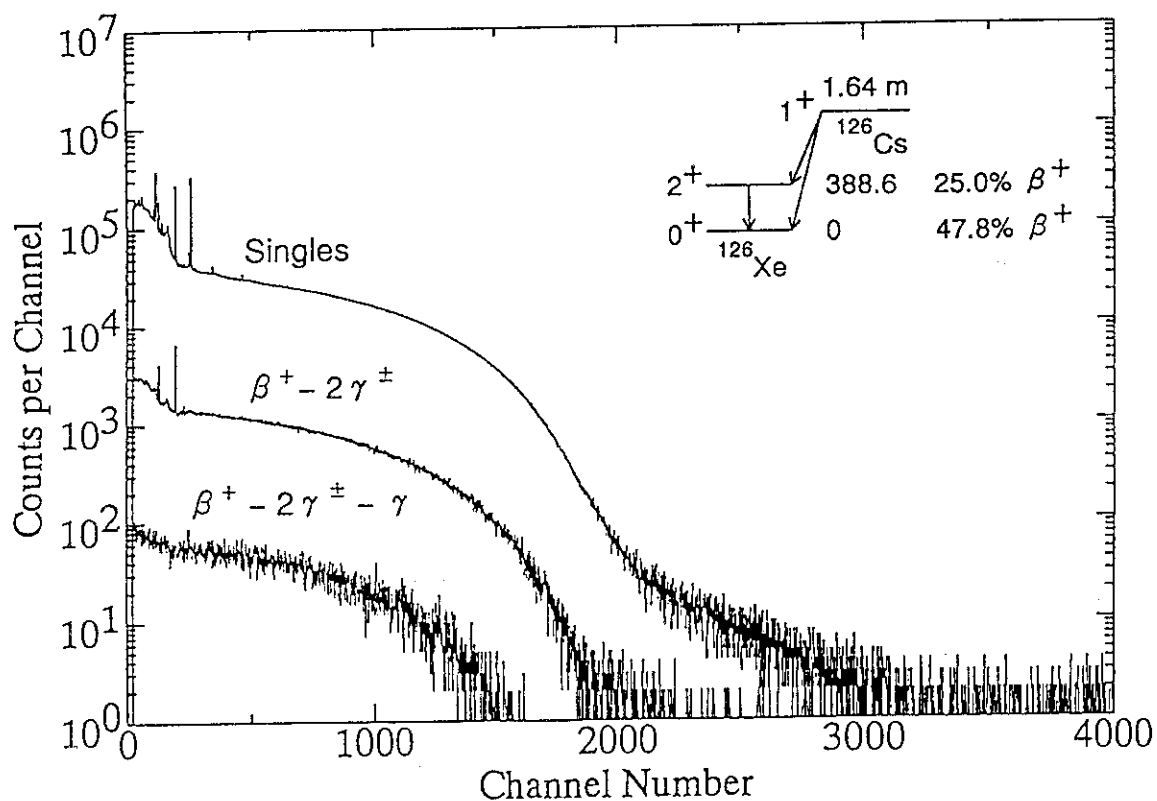
Fig. 3. β^+-ray spectra of ^{126}Cs: (singles), singles measurement, (β^+-2$\gamma^\pm$), coincidence with two 511 keV annhilation photons, (β^+-2$\gamma^\pm$-γ_{389}), additional coincidence with 389 keV γ-ray.

References

1)R.Decker, K.W.Wunsch, H.Wollnik, G.Jung, E.Koglin and G.Siegert, Nucl. Instr. Meth.**192**,261(1982).

2)D.M.Rehfield, Nucl. Instr. Meth. **157**,351(1978).

3)H.Keller, R.Kirchner, O.Klepper, E.Roeckl, D.Schardt, R.S.Simon P.Kleinheinz, C.G.Liang and P.Paris, Nucl. Instr. Meth. **A300**,67(1991).

4)H.Ukon, M.Miyachi. T.Ishii, H.Yamamoto, K.Kawade,T.Kato, Y.Kawase, K.Okano and J.Z.Ruan, in Proc. of the Int. Conf. on Nuclear Data for Science and Technology, 1988, Mito p.893.

5)A.Osa, M.Miyachi, M.Shibata, H.Yamamoto, K.Kawade, Y.Kawase J.Z.Ruan and S.Ichikawa, in Proc. Int. Symp. on Advanced Nuclear Energy Research, 1990, Mito p.731.

3.5 Production of ^{139}Ce with Lanthanum Oxide Target

Mishiroku IZUMO, Noriko SHIGETA, Kazuyuki HASHIMOTO,
Katsutoshi KOBAYASHI, Yuichi HATSUKAWA, Hiromitsu MATSUOKA
and Toshiaki SEKINE

Department of Radioisotopes, JAERI

The ^{139}Ce radioisotope ($T_{1/2} = 137.2$ d) decays by electron capture, emitting a γ-ray of 165.9 keV, and is used as a γ-ray source for efficiency calibration of Ge detectors. For production of this radioisotope, previously reported studies[1,2,3] proposed proton or deuteron bombardment of a lanthanum-metal target combined with an ion exchange or solvent extraction method for separation of ^{139}Ce.

In the present work, a possibility of using lanthanum oxide as a target material, instead of lanthanum metal was examined; lamthanum metal is not necessarily appropriate as a target material because the metal is easily oxidized in air. In view of the routine production of ^{139}Ce, comparison was made for two chemical separation methods: solvent extraction and ion exchange methods.

A 0.888-g powder of lanthanum oxide was shaped into a pellet of 15 mm in diameter and 503 mg/cm^2 in thickness under a pressure of 700 kg/cm^2. Since a lanthanum oxide pellet, produced in this way, becomes powder again on exposure to air, the lanthanum-oxide pellet mounted on an irradiation holder was kept in a helium atmosphere. The lanthanum-oxide target was bombarded with 15 MeV protons using the JAERI tandem accelerator. The average beam current during the irradiation period of 16.9 h, monitored with a Faraday cup connected to a current integrator, was 0.6 μA. The upstream side of the target was cooled with a helium-gas flow, while the downstream side was cooled with water (10 °C). After irradiation, the target was kept in a helium atmosphere. In 40 days after irradiation, the target was inspected and then subjected to chemical processsing; the target kept its shape of a pellet.

The irradiated target was divided into two parts, after being dissolved in 6N HCl. In the solvent extraction method proposed by Peppard et al.[3], as shown in Fig.1, the chemical separation was accomplished by oxidizing the cerium from Ce^{3+} to Ce^{4+} in a solution of 1M KBrO$_3$/10 M HNO$_3$. The distribution ratios of ^{139}Ce in the solvent extraction were 4.2×10^3 and 3.0×10^3. These values were in agreement with that of 4×10^3 reported by Peppard et al.[3] The chemical yield of ^{139}Ce was 96% and the lanthanum content was 0.0036%.

In the ion exchange method proposed by Mayer et al.[2], the chemical separation was accomplished by anion exchange following oxidation of the cerium from Ce^{3+} to Ce^{4+}

in a solution of 0.12M $HBrO_3$/6 M HNO_3, instead of 1M $KBrO_3$/10 M HNO_3 used in the solvent extraction method. The chemical yield of ^{139}Ce was 96% and the lanthanum content was 0.0048%.

The ^{139}Ce radioactivity produced in the target was determined to be 6.16 MBq at the end of bombardment. This value was in agreement with that of 8 MBq estimated from the systematics of the thick-target yield given by Keller et al.[4]

It was concluded that lanthanum-oxide would be used as a target material. Both the solvent-extraction and ion-exchange methods gave the same radiochemical yield of ^{139}Ce and almost the same lanthanum content in the final products. The length of time for processing was 12 h for the solvent extraction method and 48 h for the ion-exchange method. Although the ion-exchange method needs a longer time for processing, this method could be considered to be more advantageous to remote-control operation in a shielded cell.

References

1) R. D. Neirinckx, Int. J. Appl. Radiat. Isotopes, **21**, 681 (1970).

2) G. D. Mayer, T. N. Vander Walt, R. G. Bohmer and P. Andersen, Radiochim. Acta, **34**, 207 (1983).

3) D. F. Peppard, G. W. Mason and S. W. Moline, J. Inorg. Nucl. Chem. **5**, 141 (1957).

4) K. A. Keller, J. Lange and M. Münzel, "Q-values and excitation functions of nuclear reactions," Springer-Verlag, Berlin (1974).

Target preparation

Irradiation

Irradiated La metal or La₂O₃ Target
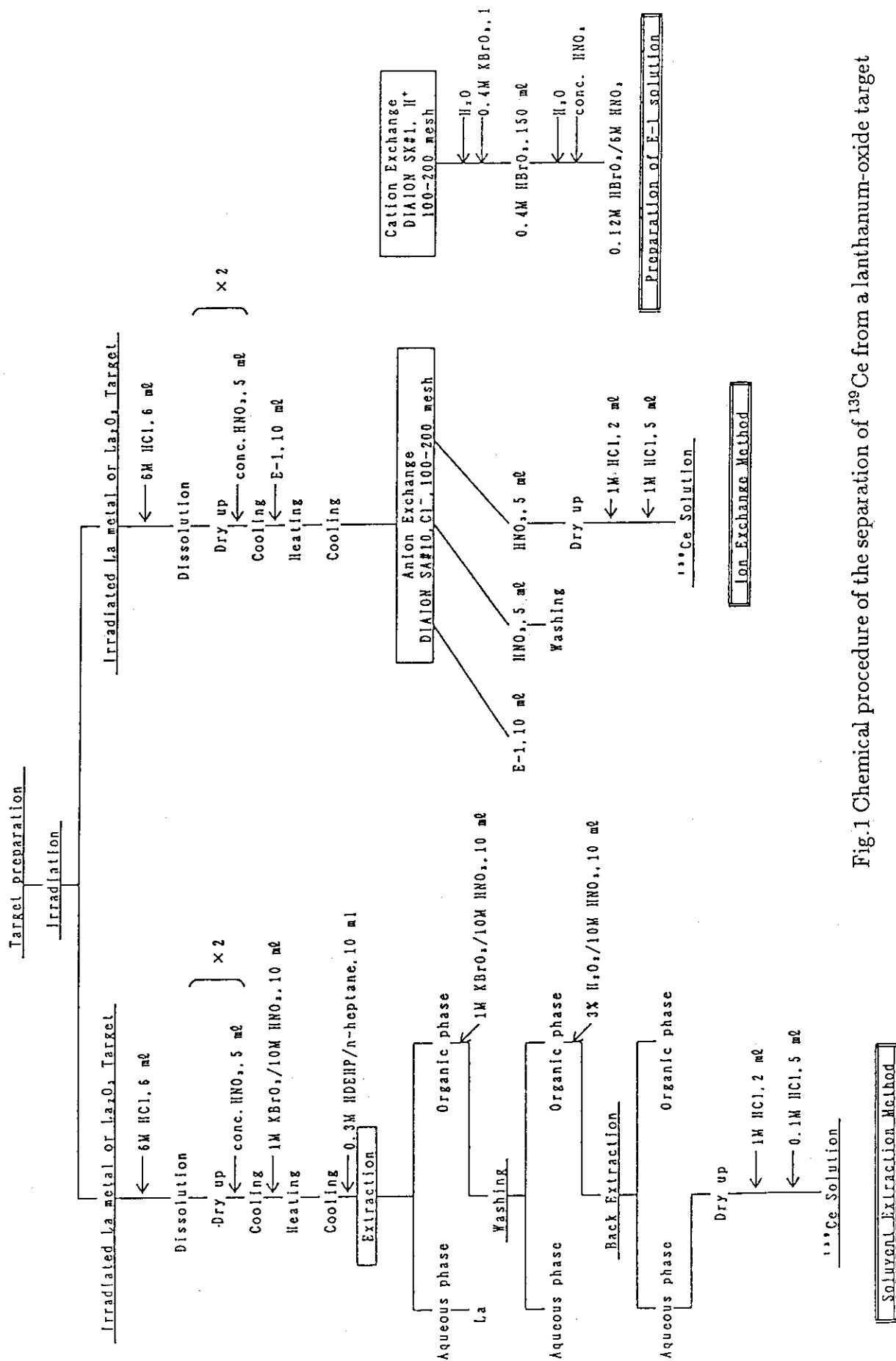
Cation Exchange
DIAION SK#1. H⁺
100~200 mesh

H₂O
0.4M KBrO₃.1

0.4M HBrO₃.150 mℓ

H₂O
conc. HNO₃

0.12M HBrO₃/6M HNO₃

Preparation of E-1 solution

×2

Irradiated La metal or La₂O₃ Target

6M HCl.6 mℓ

Dissolution

Dry up
conc.HNO₃.5 mℓ

Cooling

E-1.10 mℓ

Heating

Cooling

DIAION Anion Exchange
SA#10. Cl⁻.100~200 mesh

HNO₃.5 mℓ

HNO₃.5 mℓ

Washing

E-1.10 mℓ

Dry up

1M HCl.2 mℓ

1M HCl.5 mℓ

¹³⁹Ce Solution

Ion Exchange Method

Irradiated La metal or La₂O₃ Target

6M HCl.6 mℓ

Dissolution

Dry up
conc.HNO₃.5 mℓ

Cooling

1M KBrO₃/10M HNO₃.10 mℓ

Heating

Cooling

0.3M HDEHP/n-heptane.10 ml

×2

Extraction

Aqueous phase
La

Organic phase

1M KBrO₃/10M HNO₃.10 mℓ

Washing

Aqueous phase

Organic phase

3% H₂O₂/10M HNO₃.10 mℓ

Back Extraction

Aqueous phase

Organic phase

Dry up

1M HCl.2 mℓ

0.1M HCl.5 mℓ

¹³⁹Ce Solution

Solvent Extraction Method

Fig.1 Chemical procedure of the separation of ¹³⁹Ce from a lanthanum-oxide target

3.6 A Research for the Production of Transuranium Elements

Ichiro FUJIWARA, Seiichi SHIBATA*, Hisaaki KUDO**, Kazuaki TSUKADA***, Nobuo SHINOHARA****, Shin-ichi ICHIKAWA****, Hideki IIMURA****, Masaaki MAGARA****,

School of Economics, Otemon Gakuin University, *Institute for Nuclear Study, University of Tokyo, **Department of Chemistry, Niigata University, ***Department of Chemistry, Tokyo Metropolitan University, ****Department of Chemistry, JAERI

Transuranium isotopes produced by the heavy ion reactions have been studied by the helium-jet recoil-transport system.[1,2] As the helium-jet system is sometimes unstable in transporting the reaction products to the moving-tape system, the transport efficiency was at first measured by the $^{12}C + ^{181}Ta$ reaction. First, a tantalum foil was bombarded by ^{12}C beam, and the isotopes of ^{189m}Au (half life; 4.55 min) and ^{188}Au (8.84 min) recoiling from the target were collected on an aluminum catcher foil placed behind the target. Second, a tantalum target located within the reaction chamber of the helium-jet system was bombarded by the same beam. The reaction products were transported and collected on a catcher disk which was placed within the moving-tape system. The γ-rays of the gold isotopes collected in the two procedures were measured by a Ge detector. The transport efficiency, determined by both of the γ-ray intensities of ^{189m}Au and ^{188}Au, was in the range of 40-60 % during this experiment.

Target of ^{243}Am (200 μg/cm^2 in thickness) was bombarded by ^{12}C beam of energy 80 MeV (on the target) at intensity of 600 enA. A result of the α-ray measurement is shown in Fig. 1. The isotopes of ^{251}Md (half-life; 4.0 min), ^{250}Md (52 s) and ^{249}Md (24 s) produced by the $^{243}Am(^{12}C,4n)^{251}Md$, $^{243}Am(^{12}C,5n)^{250}Md$ and $^{243}Am(^{12}C,6n)^{249}Md$ reactions, respectively, are identified in this spectrum. The formation cross sections of these isotopes are calculated to be less than 10 nb under this experimental condition.
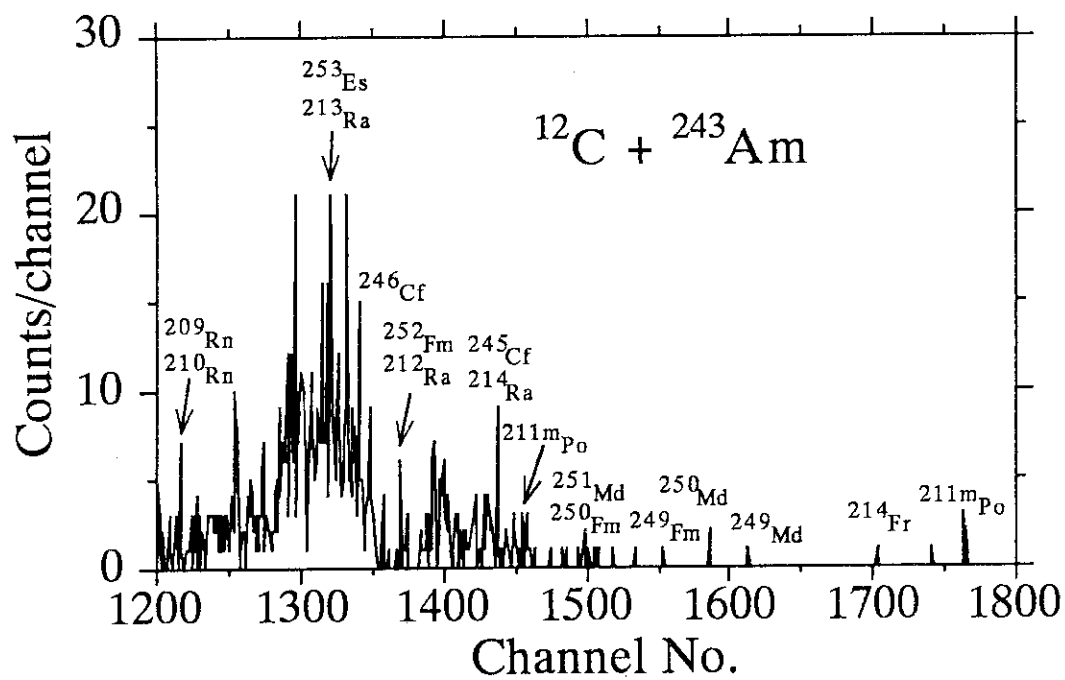
Fig. 1   Alpha-ray spectrum produced by bombardment of ^{243}Am with ^{12}C.

References

1) I. Fujiwara, et al.: JAERI-M 90-139 (1990) 123.

2) I. Fujiwara, et al.: JAERI-M 91-170 (1991) 87.

3.7 Ru Isotopic Distributions from Heavy Ion-induced Fissions of Actinides

Nobuo SHINOHARA, Shin-ichi ICHIKAWA, Masaaki MAGARA,

Kazuaki TSUKADA, Tsutomu OHTSUKI*

Department of Chemistry, JAERI

*Laboratory of Nuclear Science, Tohoku University

The isotopic yields of $^{105-111}$Ru have been measured in the ^{12}C- and ^{19}F-induced fissions of ^{235}U, ^{238}U and ^{237}Np using a fast radiochemical separation technique followed by γ-ray spectrometry,[1] where the excitation energies of the compounds are identically 58 MeV for both of the ^{12}C- and ^{19}F-systems. Figure 1 shows a result of the relative yields of the Ru isotopes produced in the ^{12}C + ^{238}U and ^{19}F + ^{238}U reactions together with the proton-induced fission of ^{238}U (19 MeV of the excitation energy). Fission or fission-like products in heavy ion-induced reactions are observed from several reaction channels like compound nucleus formation or quasi-fission (or fast fission). Especially, heavy ion-induced reactions of actinide targets make a number of fission process, like fission of compound nucleus formed by complete fusion of projectile and target, or transfer reaction followed by fission, and these reactions are complex depending on the entrance channel and on dynamic factors. The isotopic yields in the heavy-ion induced reactions (C+U and F+U) are apparently different from those in the proton-induced reaction (p+U) as seen in Fig. 1.

Fig. 1 Relative yields of the Ru isotopes produced in the systems of p, ^{12}C, ^{19}F + ^{238}U.

Reference

1) N. Shinohara, et al.: JAERI-M 91-170 (1991) pp.89-92.

3.8 Binary Scission Configuration in the Fission of Light Actinides

Tsutomu OHTSUKI, Yuichiro NAGAME*, Hiroshi IKEZOE**,
Kazuaki TSUKADA***, Masaaki MAGARA***
Ichiro NISHINAKA****, Hiromichi NAKAHARA****

Laboratory of Nuclear Science, Tohoku University
*Department of Radioisotopes, **Department of Physics,
***Department of Chemistry, JAERI, ****Department of Chemistry,
Tokyo Metropolitan University

Recent experimental results for low energy nuclear fission of heavy nuclides indicate the existence of multicomponents in the kinetic energy distribution of fission fragments.[1,2,3,9] Especially, the total kinetic energy (TKE) distributions in the fission of heavy actinides such as ^{258}Fm, ^{258}No, ^{259}Fm, ^{259}Md, ^{260}Md and ^{262}No reveal the existence of two types scission configurations for the same symmetric mass division. Such phenomena have been called bimodal fission.[1,2] In order to understand the phenomena, theoretical calculations have showed the existence of fission valleys on the potential energy surface of deformation process to scission in the heavy nuclides.[4,5,6,7,8] But a exact understanding has not been yet given. At the present stage, further investigation will be needed to understand the multi-modal structure experimentally and theoretically.

To search for modal structure in the kinetic energy distributions of light actinides, velocity and kinetic energy distributions of fragments in the proton-induced fission of ^{232}Th and ^{238}U have been measured by means of the double arm time-of-flight method. The beam of 13 MeV protons from the JAERI tandem accelerator was used for the bombardment. Details of the experimental procedures have already been given in ref.9.

The primary mass distributions of each fragment for the ^{232}Th+p and ^{238}U+p were obtained from the ratios of the velocities of the pair fragments. The mass resolution was estimated to be $\sigma(m) \sim 1.5$u. The characteristic feature of the mass distributions was typically asymmetric as expected. The TKEs of the fragment mass A=127, 129, 131 for the ^{232}Th+p, and A=126, 128, 130 for the ^{238}U+p fission are shown in fig.1(a) and fig.1(b). It is found that the shapes of the distributions change systematically and a shoulder is clearly seen in the distributions. The observed TKE distributions were analyzed, as a first approximation, by two Gaussians in the fragment mass A=127-133 for the ^{232}Th+p and A=125-131 for the ^{238}U+p fission, and the peak position and the area

of each Gaussian were obtained. Solid curves in figs.1(a) and 1(b) indicate the result of a Gaussian fit to the TKE distributions. The peak positions of the two Gaussians were 169 MeV and 185 MeV for A=128 in the ^{232}Th+p, 173 MeV and 188 MeV for A=128 in the ^{238}U+p, and the difference of the two peaks was about 16 MeV and 15 MeV, reapectively. The lower and higher TKE values decomposed by the two-Gaussian analysis are plotted in the TKE systematics in fig.2. The lower TKE values seem to be in agreement with Viola's systematics[10] well, while the higher TKE components fall on the upper side of the systematics. A dashed line can be drawn through the higher energy components of the present work and those reported by Gruzintsev et al.[11] for the fission of pre-actinide. It seems to reach to the high energy points reported for the heavy actinide[12]. It may represent the avarage total kinetic energy of fission fragments that have experienced a strongly shell-influenced path which ends up with a compact scission configurations. On the side of these lines, the two types scission configurations are drawn schematically in fig.2.

In the proton-induced fission of ^{232}Th and ^{238}U, a binary structure was observed in the velocity and the TKE distributions of fission fragments with A=126-131. From the present results, it is concluded that there are at least two kinds of scission configurations: elongated shapes probably associated with the symmetric liquid-drop path, and more compact shapes associated with the asymmetric shell-influenced path. The binary fission in the heavy actinides can be mere extention of that observed in this work for the lighter actinide.

References

1) E.K. Hulet, J.F. Wild, R.J. Dougan, R.W. Lougheed, J.H. Landrum, A.D. Dougan, M. Schädel, R.L. Hahn, P.A. Baisden, C.M. Henderson, R.J. Dupzyk, K. Sümmerer, and G.R. Bethune, Phys. Rev. Lett. **56** (1986)313.

2) E.K. Hulet, "Bimodal Fission" in Proceedings of the 50 Years with Nuclear Fission, 1989, Washington, D.C. and Gaithersburg, Maryland, editted by J.W. Behrens and A.D. Carlson(Published by American Nuclear Society, Inc., La Grande Park, Illinois 60525 USA), **Vol.2** (1989)533.

3) M.G. Itkis, V.N. Okolovich, A.Ya. Rusanov, G.N. Smirenkin, Z.Phys. A, **320** (1985)433.

4) P. Möller, J.R. Nix, and W.J. Swiatecki, Nucl. Phys. **A469** (1987)1.

5) S. Ćwiok, P.Rozmej, A. Sobiczewski and Z. Patyk, Nucl. Phys. **A491** (1989)281.

6) V.V. Pashkevich, Nucl. Phys. **A169** (1971)275.

7) J.F. Berger, M. Girod and D. Gogny, Nucl. Phys. **A428** (1984)23c.

8) U. Brosa, S. Grossmann, and A. Müller. Z. Phys. **A325** (1986)241.

9) T. Ohtsuki, Y. Nagame, H. Ikezoe, K. Tsukada, K. Sueki, and H. Nakahara, Phys. Rev. Lett. **66** (1991)17; T. Ohtsuki, Y. Nagame, H. Ikezoe, I. Kanno,

M. Magara, K. Tsukada, I. Nishinaka, T. Sekine, and H. Nakahara, JAERI-M-91-170 (1991)93.

10) V.E. Viola, K. Kwiatkowski, and M. Walker, Phys. Rev. C31 (1985)1550.

11) E.N.Gruzintsev, M.G.Itkis, Yu.V.Kotlov, V.N.Okolovich, A.Ya.Rusanov, and G.N.Smirenkin, Sov. J. Nucl. Phys., 47 (1988)765.

12) D.C.Hoffman, Nucl. Phys., A502 (1989)21c.
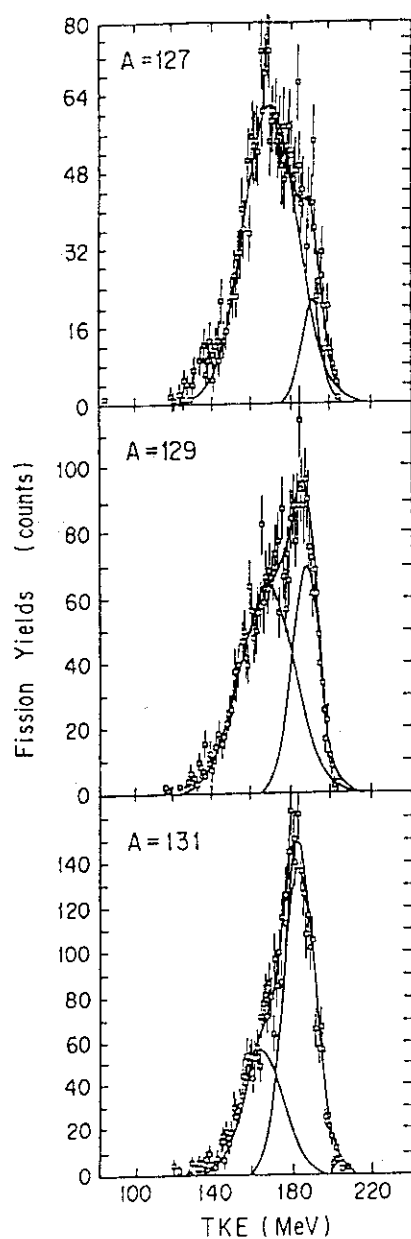
Fig.1(a) Energy distributions for the fragment mass A=127, 129, and 131 observed in the proton-induced fission of ^{232}Th. Solid curves indicate the result of a Gaussian fit to the energy distributions.
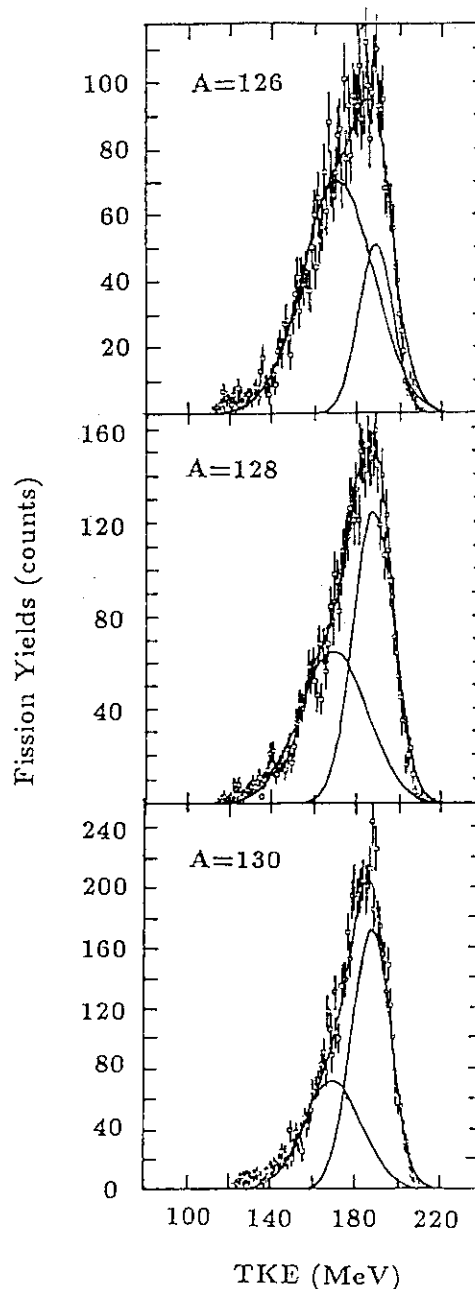
Fig.1(b) Same sa Fig.1(a), but for the fragment mass A=126, 128, and 130 observed in the proton-induced fission of ^{238}U.
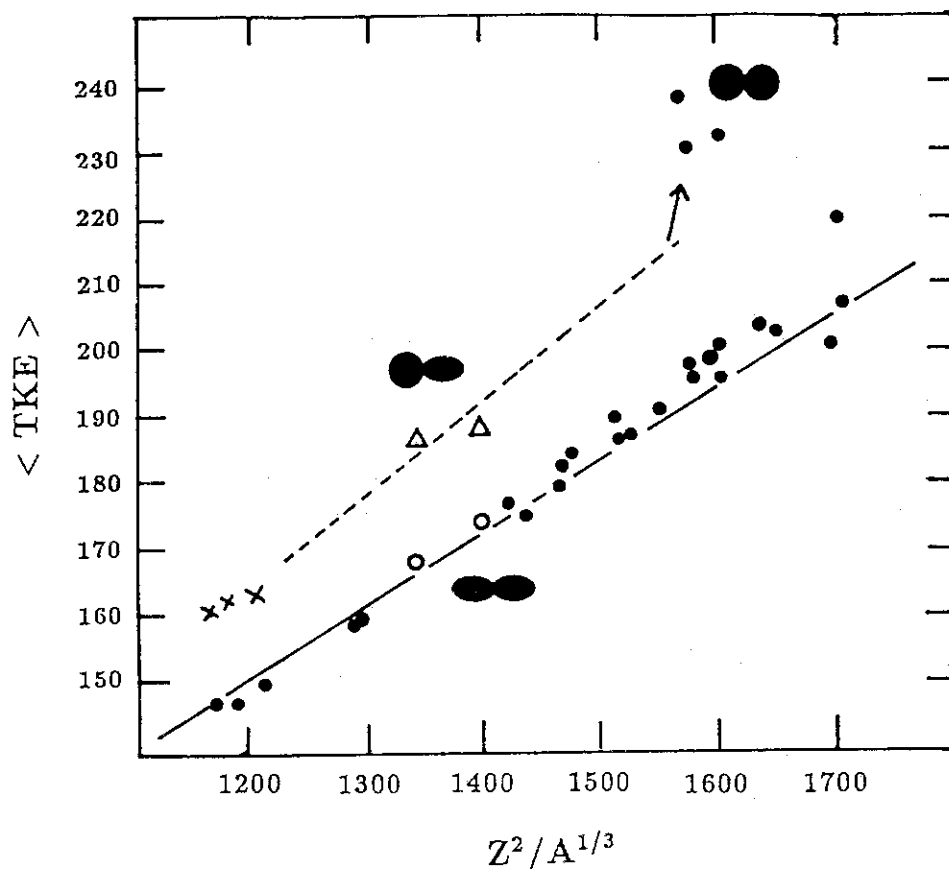
Fig.2 Systematics for the $< TKE >$ as a function of $Z^2/A^{1/3}$ taken from ref.11(Similar plot is shown in ref.12). Open symbols indicate the present results for the decomposed TKE of ^{232}Th+p and ^{238}U+p fissions. Cross symbols are the high energy components reported by Gruzintsev et al .[11] Solid line is Viola's systematics. Dashed line indicates the shell-influenced path from our results. Schematical configurations for the liquid-drop-like elongated shape and the shell-influenced compact fission shape are drawn in the figure.

3.9 Mass Distribution of Fission Fragments in Light Actinide Region

Ichiro NISHINAKA, Masashi TANIKAWA, Kazuaki TSUKADA,
Keisuke SUEKI, Hiromichi NAKAHARA, Tsutomu OHTSUKI*,
Masaaki MAGARA**, Toshiaki SEKINE***, Yuichiro NAGAME***,
and Hiroshi IKEZOE****

Department of Chemistry, Tokyo Metropolitan University,
*Laboratory of Nuclear Science, Tohoku University,
Department of Chemistry,*Department of Radioisotopes,
****Department of Physics,JAERI

Symmetry or asymmetry of mass division is the most essential feature of nuclear fission, and there have been accumulated a large number of data on mass yield distributions of fission fragments in relation to, mostly, excitation energy and atomic number of fissioning nuclides. From such data on proton induced fission of ^{232}Th, Turkevich and Niday[1] proposed a "two-mode" hypothesis which assumed the presence of two different fission barriers that independently led to symmetric and asymmetric mass division. No theory, however, has yet predicted the presence of two saddle points except for those by Pashkevich[2] and Brosa[3] who claim the presence of such saddle points in their calculated static mass surface for deformed heavy nuclei.

Recently, Hoffman et al.[4] showed experimentally that mass yield distribution is critically dependent on the neutron and proton number of the fissioning nuclide in the spontaneous fission of very heavy actinides. Hulet et al.[5] observed two kinds of kinetic energies present even for the same mass division and named such phenomena "bimodal fission". Then, Ohtsuki et al.[6] observed such bimodal phenomena in the fission of light actinides and demonstrated, in correlation with the data of excitation function studies, that there were two independent fission paths in the course of deformation of a nucleus from saddle to scission: namely, one saddle leading to symmetric mass division while the other leading to asymmetric mass division.

Presence of such fission paths is expected to be critically influenced by the shell structure of a nucleus in the course of deformation, and as Möller[7] points out, it is expected to be mainly determined by the shell structure of neutrons. Therefore, it is extremely interesting to know how mass yield distributions vary as a function of the neutron number of the fissioning nuclide. However, only a few experimental data are available on such dependence[4,8] probably due to a limited number of available target nuclides.

The aim of this work is to observe how mass division phenomena are affected by the neutron number of the fissioning nuclide in the region of light actinides. Our previous results showed that the fission of the compound nucleus ^{233}Pa(N=142) induced

by the proton bombardment of ^{232}Th revealed the existence of two fission channels[6].
In order to see the effect of neutron number, fission phenomena were observed for the
following light-heavy-ion induced reactions; ^{16}O, ^{18}O $+^{209}$Bi, compound nucleus being
^{225}Pa(N=134) and ^{227}Pa(N=136), respectively.

Experiments were carried out at the tandem accelerator facility. The ^{209}Bi metal
target (about 40 g/cm^2) evaporated onto a carbon backing foil (10 g/cm^2) was bom-
barded with a 92 MeV ^{16}O^{5+} and a 85 MeV ^{18}O^{5+} beam. The detector arrangement is
illustrated in Fig.1. Time of flight (TOF) and kinetic energies of fission fragments were
measured with two pairs of fission detecters in coincidence mode set up at θ_f=60° and
262°-261°(with respect to the beam), respectively. Each pair of fission detecters consists
of the start detecter composed of a carbon foil and a micro-channel-plate (MCP), and
the stop detecter constructed of a parallel-plate-avalanche counter (PPAC) and a SSD.

TOF and energy of the detection sys-
tems were calibrated by recoil nuclides
produced by bombarding 350 MeV
^{127}I^{25+} beam onto Ag, Sb, Ba, Al thin
targets. Two-dimensional TOF-energy
spectrum is shown in Fig.2, and the en-
ergy spectra observed by the SSD are
shown in Figs.3(a) and 3(b) for ^{16}O
and ^{18}O induced fission, respectively.
In Fig.3(b), there seems to be a com-
ponent at around the channel number
5600. Detail analysis of these data are
now in progress.
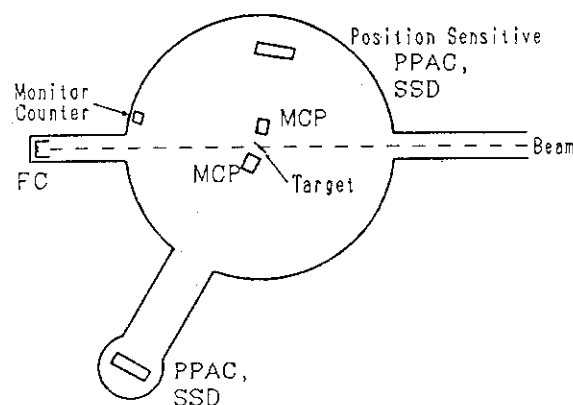
Fig.1 Schematic view of experimental
set up.

References
1) A.Turkevich, and J.B.Niday, Phy.Rev.84 (1951)52.
2) V.Pashkevich, Nucl.Phys. A169 (1971)275.
3) U. Brosa, S. Grossmann, A. Müller, Phys. Rep. 192 (1990)167.
4) D.C.Hoffman, D.M.Lee, K.E.Gregorich, M.J.Nurmia, R.B.Chadwick, K.B.Chen,
   K.R.Czerwinski, C.M.Gannett, H.L.Hall, R.A.Henderson, B.Kadkhodayan,
   S.A.Kreek, and J.D.Leyba, Phys.Rev. C41 (1990)631.
5) E.K.Hulet, J.F.Wild, R.J.Dougan, R.W.Lougheed, J.H.Landrum, A.D.Dougan,
   M.Schädel, R.L.Hahn, P.A.Baisden, C.M.Henderson, R.J.Dupzyk, K.Sümmerer,
   and G.R.Bethune, Phys.Rev.Lett. 56 (1986)313.
6) T. Ohtsuki, Y. Nagame, H. Ikezoe, K. Tsukada, K. Sueki, and H. Nakahara, Phy.Rev.
   Lett. 66 (1991)17.
7) P.Möller,Nucl.Phys. A192 (1972)529.
8) C. Wagemans, P. Schillebeeckx, and A. Deruytter, Nucl. Phys. A502 (1989)287c.
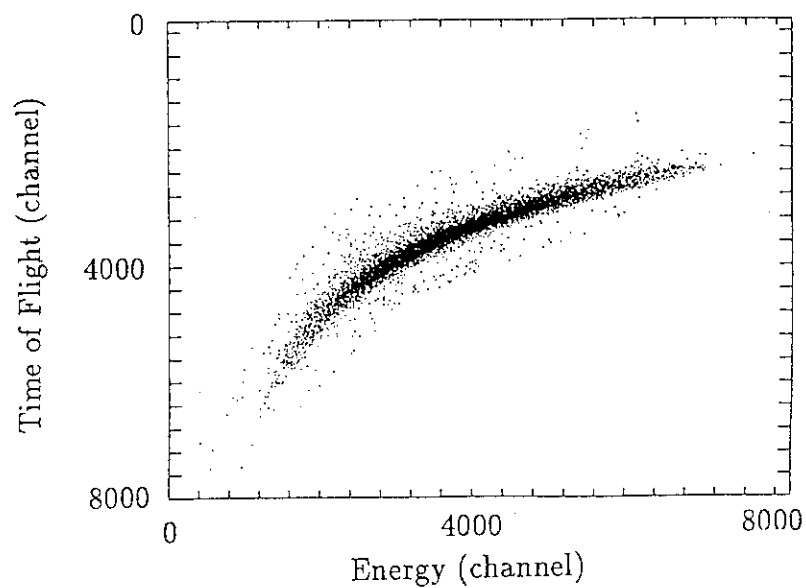
Fig.2 Time distribution as a function of fragment energy for $^{18}O+^{209}Bi$.
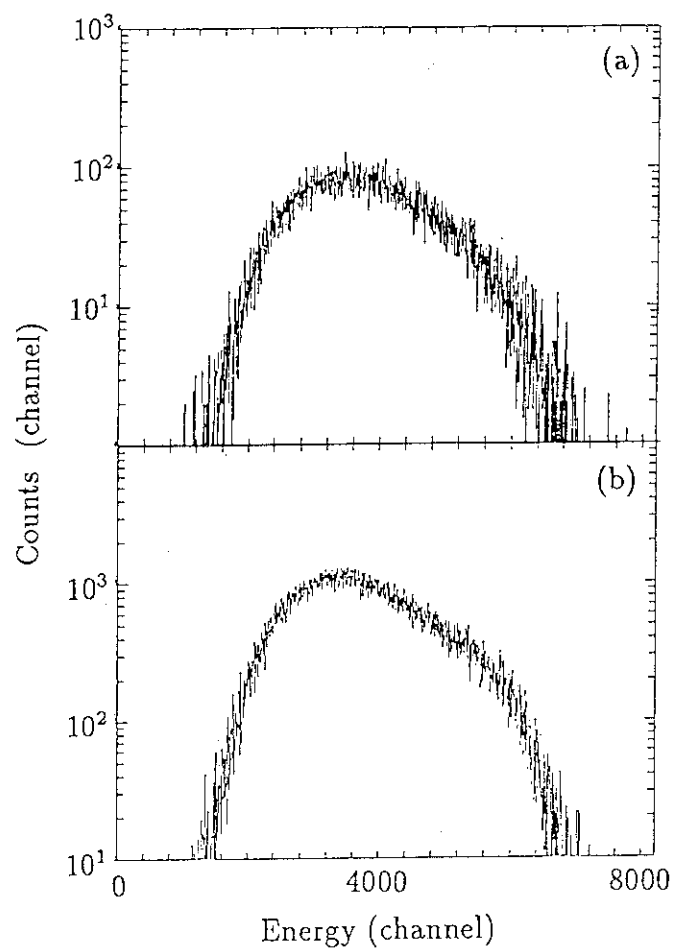
Fig.3 Energy distributions of fission fragments observed for $^{16}O+^{209}Bi$ (a) and $^{18}O+^{209}Bi$ (b).

3.10 Angular Distributions of Fission Fragments in 15 MeV Proton-induced Fission of [232]Th

Kazuaki TSUKADA, Nobuo SHINOHARA*, Keisuke SUEKI, Takayuki KOBAYASHI, Masaru TANIKAWA, Ichiro NISHINAKA, Masaaki MAGARA*, Shin-ichi ICHIKAWA*, Michio HOSHI* and Hiromich NAKAHARA

Faculty of Science, Tokyo Metropolitan University, *Department of Chemistry, JAERI

The incident energy dependence on the yields of fission fragments produced in the extremely asymmetric fission (A_H/A_L=2) have been studied by a radiochemical method[1]. It was found that the extremely asymmetric region, which is obviously different from the symmetric region, is very similar to the asymmetric region near the peak top[2]. Namely, the fission of the extremely asymmetric region, A_H/A_L=2, is dominated by the same mode as the fission near the peak top. In order to investigate the correlation between the angular anisotropy[3,4] and the fragment mass in the extremely asymmetric region, the angular distribution of fission fragment has been measured.

Angular distribution of fission fragments in 15 MeV proton-induced fission of [232]Th was measured by the recoil-catcher foil method[5]. Thicknesses of the thorium targets ranged from 300 to 500 $\mu g/cm^2$. The target and catcher foil assembly is schematically drawn in Fig.1. An aluminium catcher foil of 4.9 mg/cm^2 thick was put on the wall of a semicylindrical holder of 60mm in length and 35 mm in radius. The proton beam was collimated with a 3 mm-diameter stainless steel collimator. The proton-bombardment was performed during 3-11 h at the JAERI tandem accelerator. The beam current was about 0.8 μA. After bombardment, the aluminium catcher foil was removed from the target assembly and cut in strips of appropriate widths corresponding to some solid angles. For θ smaller than π/4, a portion of the catcher foil corresponding to the azimuthal angle of φ=0 to π was used, whereas for θ larger than π/4, only the portion corresponding to the angles φ=0 to π/2 was employed, since the energy loss of the fission fragment within the target might become appreciable for the larger φ. The strips of the aluminium catcher foil were first weighted to make correction for the error caused by imprecise cutting of the catcher foil. The cutting ambiguity was within a few percent. Then the strips were folded to the same area so that the geometrical efficiencies did not vary with samples in the direct gamma-ray spectrometry. The rare earth elements were separated from each strip by a computer-

controlled rapid ion-exchange separation system[6], and determined by γ-ray spectrometry. After the measured radioactivities were corrected for decay, genetic relationships, chemical yield, and cutting ambiguity, the relative radioactivity at the end of bombardment was obtained. The same experiments were carried out five times to obtain precise angular distributions. The relative radioactivity of a nuclide measured in each strip was normalized to a ratio to the total radioactivity of all of the strips for the nuclide. The angular distributions were measured for 17 nuclides as shown in Table 1. The angular distribution (relative radioactivity) of ^{143}Ce is shown in Fig.2. In this method, the angular distributions of asymmetric fission fragments ($A_H/A_L=1.9$) have been measured.

References   1)K.Tsukada et.al, JAERI-M 91-170 (1991) 96.

2)P.Moller and S.G.Nilsson, Phys.Lett. 31B (1970) 283.

3)R.Vandenbosch et.al, IAEA Vienna, 1965, Vol.I,p.547.

4)B.L.Cohen et.al, Phys. Rev. 98 (1955) 685.

5)H.Kudo et.al, Phys. Rev. C25 (1982) 909.

6)K.Tsukada et.al, Radiochim. Acta 51 (1990) 77.
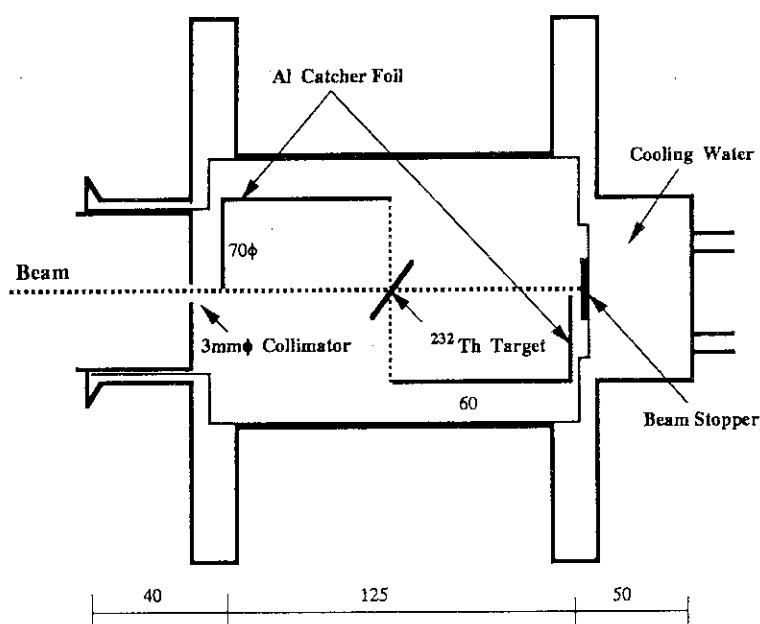
Fig.1   Target and catcher foil assembly used in the measurement of angular distributions of fission fragments in 15 MeV proton-induced fission of ^{232}Th. Dimension in mm.

Table 1 Nuclides measured in this experiment of angular distributions.

nuclide	half life	γ-ray energy	Iγ
^{88}Kr	2.84 hour	196.3 keV	26.0%
^{91}Sr	9.5 hour	555.6 keV	56.1%
^{92}Sr	2.71 hour	1383.9 keV	90.%
^{99}Mo	66.0 hour	140.5 keV	90.7%
^{105}Rh	35.36 hour	318.9 keV	19.2%
^{115g}Cd	2.23 day	336.2 keV	45.9%
^{127}Sb	3.85 day	685.7 keV	35.3%
^{132}Te	78.2 hour	228.2 keV	88.0%
^{139}Ba	1.396 hour	165.9 keV	18.8%
^{140}Ba	12.75 day	537.3 keV	24.4%
^{141}Ce	32.5 day	145.4 keV	48.4%
^{142}La	1.54 hour	641.3 keV	47.4%
^{143}Ce	33.0 hour	293.3 keV	42.8%
^{147}Nd	10.98 day	531.0 keV	13.1%
^{149}Nd	1.73 hour	114.3 keV	19.0%
		211.3 keV	25.9%
^{151}Pm	28.4 hour	340.1 keV	22.%
^{153}Sm	46.7 hour	103.0 keV	28.3%
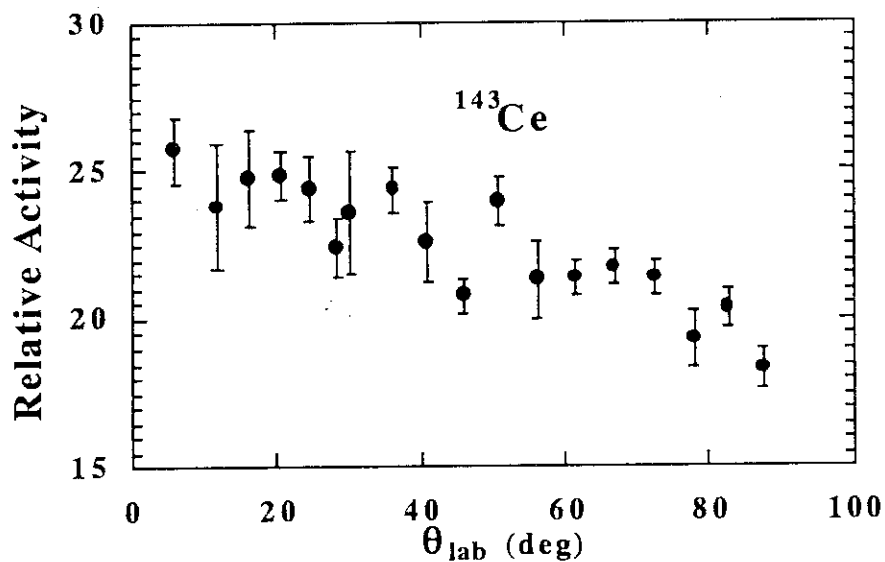
Fig.2 Angular distribution of ^{143}Ce produced in 15 MeV proton-induced fission of ^{232}Th.

3.11 Fission of the ^{238}U + p System in the Giant Dipole Resonance Region

Noriko NITANI, Takayuki YAMAGUCHI, Daisaku YANO, Naruto TAKA-
HASHI, Hiroshi BABA and Nobuo SHINOHARA*

Department of Chemistry, Faculty of Science, Osaka University, *De-
partment of Chemistry, JAERI

Fission characteristics of actinide nuclei in lower excitation energy(spontaneous and thermal neutron induced fission) are known to be different from those in the region above 20 MeV. For example, it was reported[1] that the light-mass wing of asymmetric fission mass distribution is a mirror image of the heavy-mass wing, and the width parameter, α, of Gaussian curves fitted to obseved yields increases with the excitation energy, E_x, in the ^{238}U fission induced by protons with the energies between 18 and 45 MeV. The relationship is expressed as

$$\sqrt{\alpha - 106} = 0.235(E_x - 14.0). \tag{1}$$

Equation (1) implies that the systematics holds only above 14-MeV excitation energy, therfore the lower limit of the systematics exists. Further, the FWHM of the Gaussian curve is 17.1 amu at E_x=14 MeV, and this value is fairly higher than that in thermal neutron induced fission (the FWHM is about 14 amu). This implies that the change of the characteristics rapidly occures in the region of E_x=14 MeV.

On the other hand, it is the very energy at which fission due to the giant dipole resonance, GDR, takes place[2]. One might reckon, therefore, that the difference between the fission phenomena at lower and higher excitation energies is due to the difference of excitation modes. The former is caused by the single particle excitation whereas collective is very likely to be responsible for the latter. On the other hand, one cannot disregard the possibility that the second chance fission bringe about the change of the fission phenomenon. So the charge and mass distributions of the fission fragments were measured for the ^{238}U + p system in the range of E_x = 11.7 - 20.6 MeV in order to elucidate the above mentioned conjecture.

Uranium targets were prepared by electrodeposition of UO_2 onto aluminum foils of 1.5 mg/cm^2 in thickness. The thickness of uranium was 1.5 - 2 mg/cm^2. Each target was sandwiched by two carbon foils of 22.5 mg/cm^2 in thickness to collect the fission fragments. Irradiation was carried out with proton beam from the cyclotron at Osaka University Laboratory of Nuclear Studies and the tandem Van de Graaff at Japan Atomic Energy Research Institute. The excitation energies applied in the experiments were in the range of 11.7 to 20.6 MeV.

Long and short irradiations of uranium targets were carried out; the former for 3 hours and the latter for 30 minutes in general. After the irradiation the targets were subjected to the non-destructive γ ray spectrometry. Antimony, iodine and rare earth elements were chemically separated from the target and other fission products in separate runs. The targets for chemical separation were sandwiched with thick aluminum foils in order to dissolve into acid.

Gamma-rays were measured by means of Ge detectors for the non-destructive and chemically separated samples. Measured γ-ray spectra were analyzed by the use of BOB code[3].

The detected photopeaks were assigned to relevant nuclides and their formation cross sections were determined. We deduced the most probable charge for earch mass number from measured cross sections of an isobaric multiplet. The most probable charges linearly depend on the fragment mass in the case of excitation from 21 to 25 MeV. On the other hand, the presently observed most probable charges at lower excitation energy substantially deviate from this straight line for light fragments. It is considered that the double magic shell of Z = 50 and N = 82 sets in the low energy fission; that is, a heavy fragment retains a spherical shape at the scission point because of the shell effect and the complementary light fragment sustains a large deformation to lower the potential. It follows that the light fragment carries most of internal exci- tation energy which is dissipated by emitting neutrons. It is also consistent with the broadening of the light mass wing of the mass yield distributions.

The mass distributions at E_x = 12.4 - 20.6 MeV are shown in Fig. 1. The shape of light-mass wing varies with increasing the excitation energy. The relationship of the excitation energy and the FWHM of the Gaussian curve fitted to the observed mass distribution is shown in Fig. 2. The width of heavy wing is nearly constant at all energies. On the other hand, the width of light wing monotonously increases with the excitation energy and reaches to the maximum around E_x = 17 MeV though it is equal to that of heavy wing at E_x = 12.4 MeV. Then the FWHM decreases with increase of the excitation energy and approaches to that of heavy wing at E_x = 20.6 MeV again. The different behaviors of the light and heavy wings may be due to the difference in the neutron emission.

We could not obtain the results which correlate the change of fission characteristics to the GDR. We are further planning to perform the experiment to demonstrate the transition of the fission characteristics in a more clear fashion.

References

1) S.Baba, H. Umesawa and H. Baba, Nucl. Phys.,A175(1971)177.

2) J.T. Cadwell, E. J. Dowdy, B. L. Berman, R. A. Alvarez and T. Meyer, Phys. Rev. C21(1980)1215.

3) H. Baba, T. Sekine, S. Baba and H. Okashita, JAERI Report, (1972)1227.
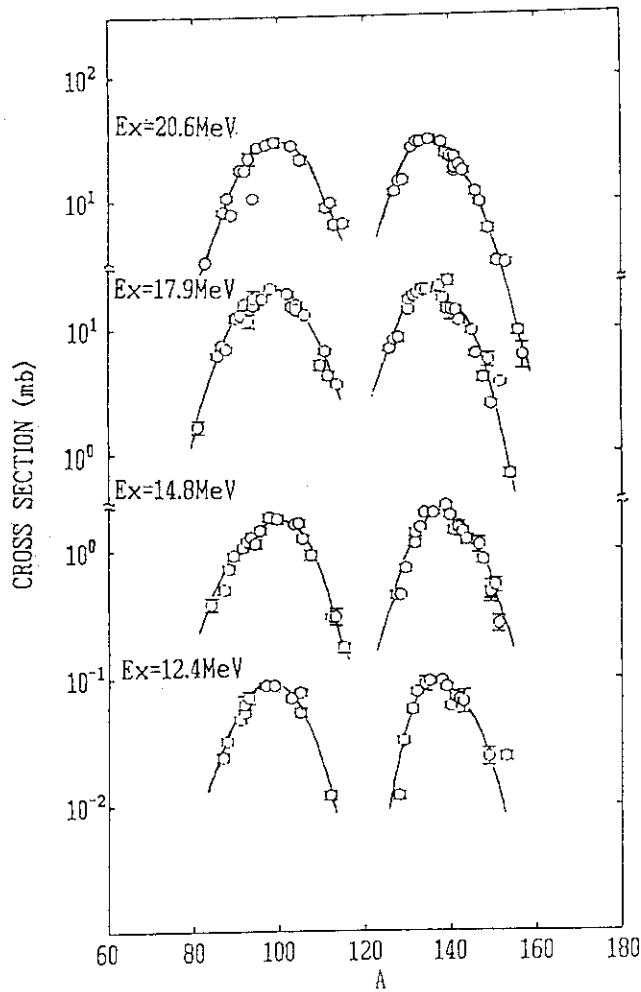
Fig. 1. Mass distribution of the ^{238}U + p system at E_x = 12.4 - 20.6 MeV
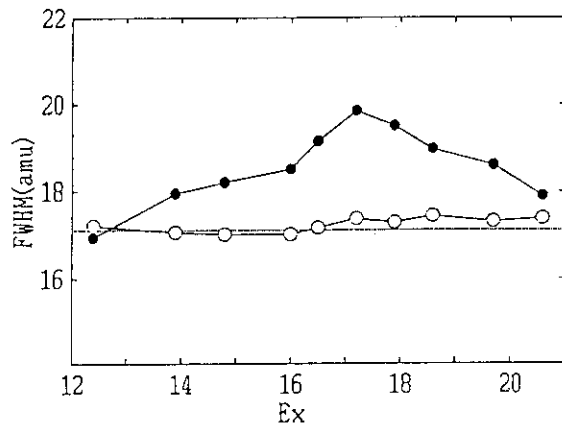
Fig. 2. The variation of the FWHM with excitation energy ●: light wing, o: heavy wing.

3.12 Effect of Gamma Ray Exposure prior to Etching of Heavy Ion Track in Polyimide

Yoshihide KOMAKI, Nirou ISHIKAWA, Katsutoshi FURUKAWA,
Shinichi OHNO and Tsutomu SAKURAI

Department of Chemistry, JAERI

Introduction

Polyimide film has been expected to contribute various fields of applications, because of the superior thermal-resistivity, size-stability and radiation-resistivity[1]. The use as a membrane microfilter has large possibility for evolution.

In the earier time, Monnin and Isabelle[2] studied "Kapton" polyimide as a track detector. In the recent time, at GSI, heavy ion track microfilters of Kapton polyimide has been studied for examining the membrane characteristic[3], and used for the hydrodynamic study[4] and for separation of the two phases of an emulsion[5].

The authors[6] have previously reported the formation of polyimide (UPIREX, UBE Industry Co.Ltd) microfilter by irradiating $^{12}C^{6+}$, $^{38}Cl^{9+}$, $^{58}Ni^{10+}$ and $^{64}Cu^{11+}$ ions and etching in a saturated solution of $KMnO_4$. The etched tracks have been found to emerge by the bombardment of the heavier ions than the Cl ion, and not by the C ion. Then, the growth of perforated holes were examined in relation to the etching rate of track. When the shape of a hole was examined from the comparison between etching rates for the track and the bulk polymer, the vertical cross section of the perforated hole in the polyimide proved to show a rather cone angle than cylindrical. In the present paper authors have examined the effect of exposure of the heavy ion irradiated polyimide film to gamma ray prior to etching in order to change the etching rates and the subsequent cone angle of the track hole.

Experimentals

The $^{58}Ni^{12+}$ ion of 200 MeV in energy and $^{107}Ag^{15+}$ ion of 250 MeV from Tandem accelerator were separately irradiated on 12.5 μ m thick and 13 mm diameter polyimide film(UPIREX, UBE Industry Co.Ltd.). Then, the films

were again irradiated by gamma-ray in a vessel of stainless steel with O2 gas of 7 kg/cm2 in pressure. This condition was selected from the experiment[7] at Takasaki establishment. The coexisting oxygen was found to promote the radiation damage during the gamma ray or the electron irradiation. The oxygen permeated into the trajectory of the heavy ion in a polymer was expected to selectively increase the local damage of track by the subsequent gamma ray exposure. Each film was exposed to doses of 1x10^{7}, 1x10^{8}, 2x10^{8} and 6x10^{8} Rads (the dose rate equals to 4.5x10^{5} R/hr) by gamma ray of ^{60}Co, respectively. After the exposure to gamma ray, the films were dipped into a 10% NaClO etching solution at 65°C. In order to examine the pore size, the gaseous transmittance of Ar was measured through the holes for a period. The diameter of hole was calculated from Knudsen's equation.

Results and Discussion

In the detection of tracks the gamma ray irradiation on polymers has been mostly studied as the influence in the high dose circumstance of radiation.[8] The authors, against this, have expected the enhancement of ratio V_t/V_g in etching rates from a point of view that the bulk film hardly increased the solubility with increasing dose of irradiation, but only the degradation in the damaged region around the trajectory of the heavy ion might selectively increase. V_t is the etching rate along the track and V_g the etching rate of the bulk polyimde[9]. Both etching rates, V_t and V_g were listed in Table 1. Strictly speaking, such a V_t is not the same as the usual V_t, but both of them equal approximately[10]. The ratio, V_t/V_g is rather smaller in polyimide than that in polyvinylidene fluoride or polyesters, which shows to be 10[2]-10[3]. The vertical cross section of the perforated hole in the polyimide proved to show a rather cone angle than cylindrical. The cone angle in the hole results in the radiation-resistivity of polyimide. In Fig. 1 the enhancement of diameters of holes in polyimide separately irradiated by the Ag and the Ni ions are shown on the exposure to ^{60}Co gamma ray of doses up to 1x10^{7}, 1x10^{8}, 2x10^{8} and 6x10^{8} Rads. Bold lines show the etching behavior for the Ni ion and fine lines for the Ag ion. In each ion irradiation the diameter enhances linearly with etching after a certain period. The period has found to be the time necessary to connect with

the holes which were etched from both sides of the film during etching. The etching rate per the length of the ion range (Vt) is calculated from the period. In Fig. 1 there are a little different slopes, but all of the values can be considered to be roughly elual. The different slopes result in the different quantity of incident ions, that is, the different number of holes. The roughly equal slope indicates the bulk polymer not to be yet considerably effected by the gamma ray radiation.

Figure 2 shows the etching time to take to the 0.07 μm diameter in polyimide irradiated by the Ag and/or the Ni ions, and the influence of the gamma ray dose on the track etching rate. Conclusively speaking, the track etching rate is larger at the irradiation by the Ag ion than by the Ni ion. The effect of the gamma ray irradiation shows to make the track etching rate 1.8 times larger at the dose of 6×10^8 Rad than that without any irradiation and considerably increases at the dose more than 2×10^8 Rads.

References

1   T. Sasuga, POLYMER. 29(1988)1562

2   M. Monnin and D.B. Isabelle, Ann.Phys.Biol.Med. 4(1970)95

3   S.L Guo, Y.H Zhao, Y.L Wang, H.H Hao, R. Brandt and P. Vater, Nucl.Tracks Radiat.Meas. 15(1988)763

4   T.C Zhu, R. Brandt, P. Vater,and J. Vetter, Nucl.Tracks Radiat.Meas. 15(1988)771

5   P. Vater, Nucl.Tracks Radiat.Meas. 15(1988)743

6   Y. Komaki, Y. Matsumoto, N. Ishikawa,and T. Sakurai, POLYMER COMMUNI-CATION,30(1989)43

7   T. Seguchi, S. Hashimoto, K. Arakawa, N. Hayakawa, Y. Watanabe,and I. Kuriyama, J.Radiat.Phys.Chem. 17(1981)195

8   H.A Khan, M.A Atta, S. Yameen, M.R Haroon,and A. Hisain Nucl.Instrum & Methods. 127(1975)105

9   R.L. Fleischer, P.B. Price, and R.M. Walker,Nuclear Tracks in Solids, principle and applications, University of California Press,Berkeley (1975)

10 Y. Komaki, Nucl.Tracks. 3(1979)33
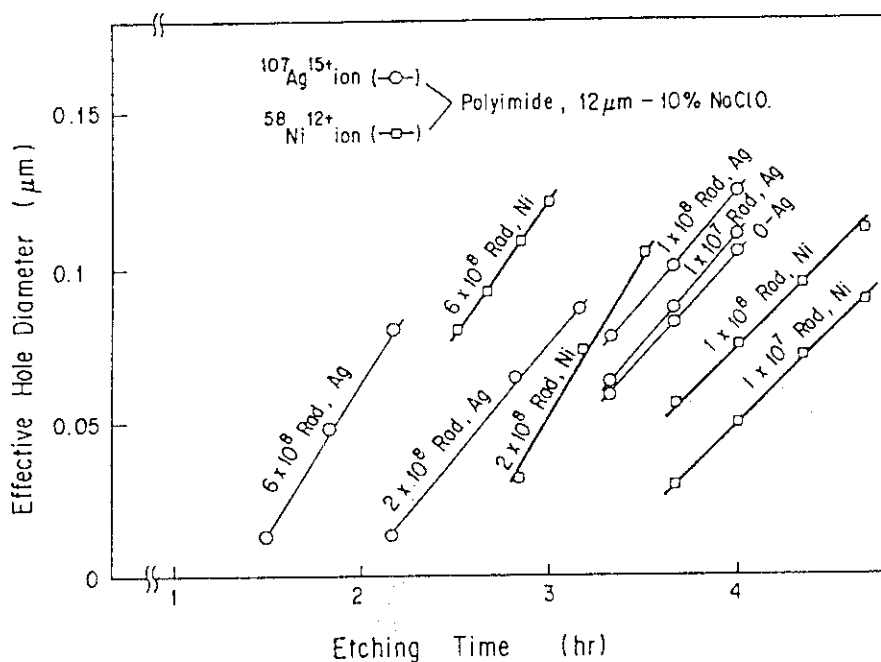
Fig. 1   Effective hole diameter in polyimide versus etching time for the $^{107}Ag^{15+}$ and $^{58}Ni^{12+}$ ions

The irradiation conditions were $^{107}Ag^{15+}$ ion at 250 MeV and $^{58}Ni^{12+}$ ion at 200 MeV, with 2nA current for about ten seconds. The hole density was $4\times10^8/cm^2$.   The etching condition was 10%NaClO solution at 65°C.
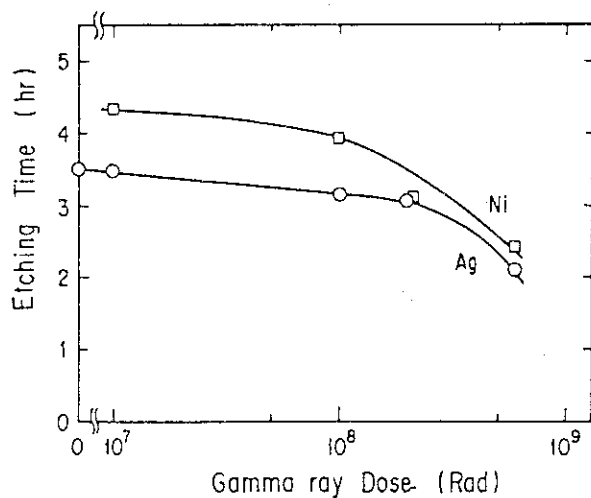
Fig. 2   Etching time taking to 0.07μ m diameter versus Gamma ray Dose

The irradiation conditions are the same as those in Fig. 1

Table 1 The etching rate along the hole (V_t) in UPIREX polyimide.

IONS	Track etching rate(μm/hr)				
	Gamma ray Dose(Rad)				
	0	1(7)	1(8)	2(8)	6(8)
Ag	2.4	2.3	2.7	2.4	4.4
Ni	—	1.9	2.2	2.4	3.8

注：1(7)は1x10⁷を示す

The irradiation conditions are : $^{107}Ag^{15+}$(250 MeV) and $^{58}Ni^{12+}$ (200 Mev).   Hole density is $4\times10^8/cm^2$.

IV LIGHT ION NUCLEAR PHYSICS

4.1 Measurements of Double Differential Charged-particle Emission Cross Sections for Reactions on ^{98}Mo and ^{nat}Si Induced by 25.6 MeV Proton

Yukinobu WATANABE*, Akira AOTO*, Hiroki HANE*, Hironori KASHIMOTO*, Yoshihide KOYAMA* Yasunao SAKAKI*, Yukinori KANDA*, Norihiko KOORI**, Yoshimaro YAMANOUTI[+], Masayoshi SUGIMOTO[+] and Satoshi CHIBA[+]

*Department of Energy Conversion Engineering, Kyushu University,
** College of General Education, The University of Tokushima,
[+]Department of Physics, JAERI

Double differential cross sections of charged particles emitted from proton-induced reactions on ^{98}Mo and ^{nat}Si have been measured at 25.6 MeV to investigate preequilibrium process. The exciton model calculation using the same parameters as those obtained from the previous analysis in 10-20 MeV region shows good agreement with the measured proton spectra for ^{98}Mo. Preliminary calculations based on the SMD-SMC model are also compared with the experimental (p,xp) and (p,xn) spectra.

Introduction

Substantial contribution from preequilibrium process is observed in continuous spectra of particles emitted with forward-peaked angular distributions in nuclear reactions induced by several tens of MeV nucleon. Systematic measurements of double differential charged-particle emission cross sections have so far been performed for proton-induced reactions in 10 to 20 MeV region at Kyushu University[1]. In the present work, the incident proton energy range is extended to 20-40 MeV using the JAERI tandem accelerator, and similar measurements of charged-particle spectra from proton-induced reactions are planned for further studies of the preequilibrium process as follows: (i) incident energy dependence of the preequilibrium component (ii) simultaneous analysis of both energy spectra of (p,p') and (p,n) reactions which are main reaction channels in the proton-induced reaction (iii) tests of the validity of several preequilibrium models through the above analyses.

In the present work, we have carried out the measurement of double differential cross sections for charged particles emitted from the proton-induced reaction on ^{98}Mo and ^{nat}Si at 25.6 MeV. The measured (p,xp) spectra are analyzed together with the (p,xn) spectra on the basis of the exciton model[2] and the SMD-SMC model[3]

Experimental Procedure

The experiment has been performed using a 25.6 MeV proton beam from the JAERI tandem accelerator. The proton beam was transported in a scattering chamber 50 cmϕ which was installed in N1 beam line. It was focused within about 2 mm ϕ on a target and its current changed in the range from about 50 nA to 300 nA, depending on the measured angle. A target of ^{98}Mo was a self-supporting metallic foil whose thickness and enrichment were 0.45 mg/cm^2 and 97.1%, respectively; a target of ^{nat}Si was also a self-supporting metallic foil of 0.2 mg/cm^2 thickness.

A charged particle detecting system consisted of a ΔE-E counter telescope of two silicon surface barrier detectors having thickness of 300 μm and 5000 μm, respectively. A defining aperture 3.0 mm in diameter was placed just in front of the ΔE detector and was located 147 mm from the target. Standard commercially available NIM modules were used as electronic equipments. Both signals of ΔE+E (the energy spectrum) and PI (the mass spectrum) from a particle identifier module (MPS-1230) were processed using the Canberra MPA/PC Multiparameter system. Energy spectra of emitted charged-particles were measured at thirteen angles of 30° to 150° in step of 10°.

Experimental results

Measured double differential proton emission cross sections for ^{98}Mo are shown for 40°, 90°, and 120° in Fig.1 as an example of the experimental data. Open and closed circles indicate the experimental data for the present measurement and the previous one[4], respectively. Both data show agreement within about 15% except the low outgoing energy region. The discrepancy at low energies is due to the difference of the threshold energy that is determined from the thickness of ΔE detector. Solid lines present the proton spectra calculated in terms of the exciton model. The details of the calculation will be mentioned in the following section. As can be seen in Fig.1, the angular distributions are peaked forward in the continuum region between 10 and 20 MeV. This result suggests that the preequilibrium process or the direct process is dominant in this energy region.

Analyses and discussion

The (p,xp) spectra for ^{98}Mo were analyzed on the basis of the one-component exciton model[2] in which isospin conservation was taken into account. The same model parameters as in our previous analysis[2] were employed and a modified version[5] of Kalbach -Mann systematics was applied to calculations of angle-dependent energy spectra. The calculated results are shown by the solid lines in Fig.1. The calculated spectra reproduce the experimental ones well in 10-20 MeV region for all angles. From the present analysis, it was
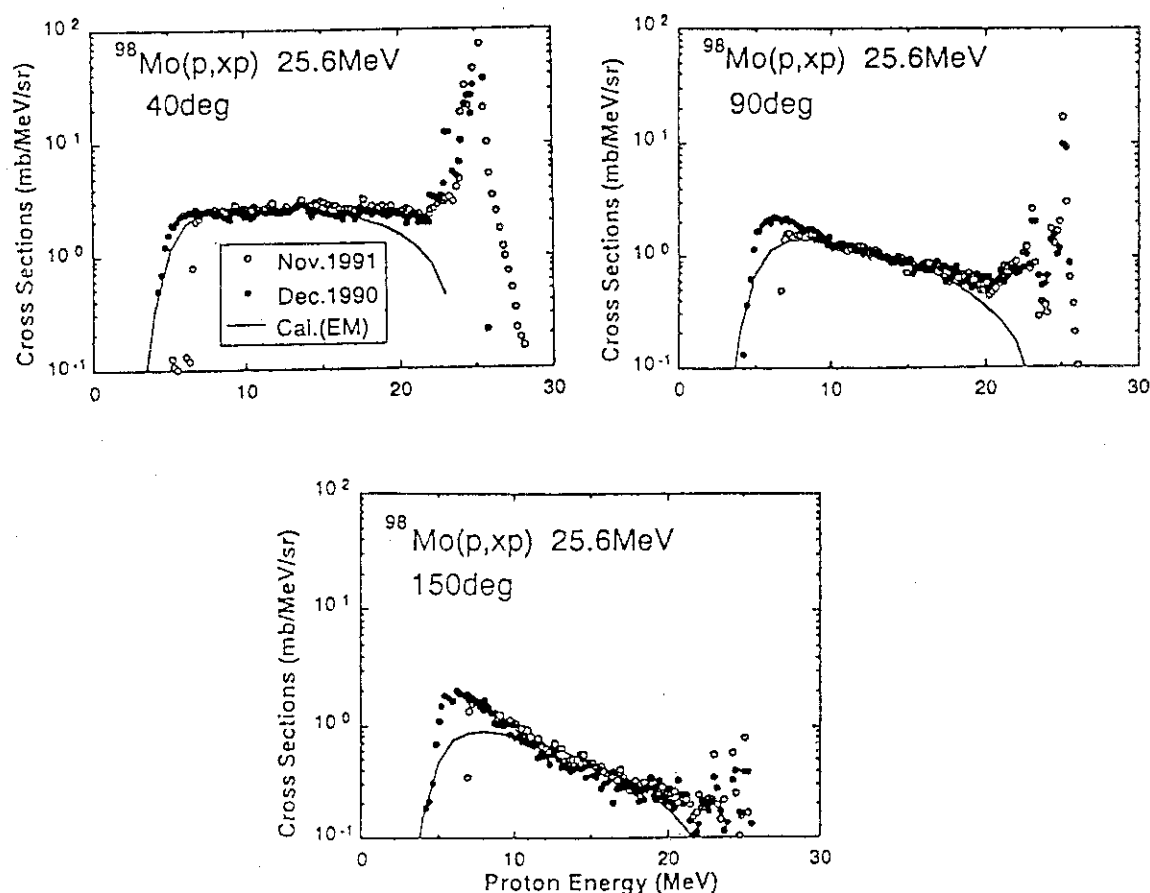
Fig.1 Measured double differential proton emission cross sections for ^{98}Mo and those on the basis of the exciton model. See in the text for details.
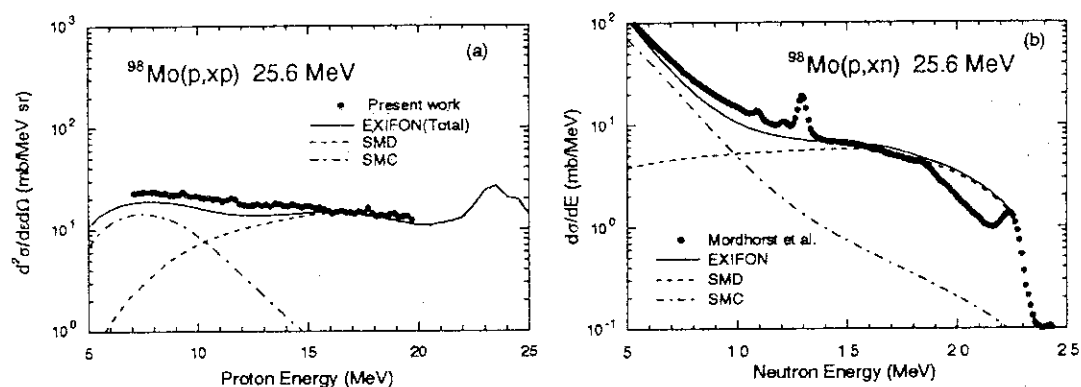
Fig.2 Comparisons of experimental energy spectra and those calculated by the SMD-SMC model for 25.6 MeV (p,xp) and (p,xn) reactions on ^{98}Mo. Dash lines and dash-dotted lines represent statistical multistep direct (SMD) component and statistical multistep compound (SMC) component, respectively.

confirmed that the adjustable parameter K-value[6] derived from the previous analysis[2] of 12-18MeV (p,xp) reactions for ^{98}Mo is applicable to those at higher incident energy.

Next we have analyzed simultaneously two dominant preequilibrium decay channels - proton and neutron channels - within the framework of the quantum-mechanical SMD-SMC model. In the calculation, a EXIFON code[3] is used and the default values set in the code are employed as the option parameters. Comparisons of the experimental (p,p') and (p,n) spectra[7] and the calculated ones are shown in Fig.2. Overall agreement is given over a whole outgoing energy range, although there is underestimation in the low outgoing energy region. The calculated bump structure at 23.5 MeV of the proton outgoing energy corresponds to overlapping peaks of inelastic scattering to 2^+ and 3^- low lying states. The present analysis is preliminary and it will be necessary to adjust some option parameters, especially the pairing energy so as to reproduce the (p,p') and (p,n) spectra consistently.

Conclusions

Double differential cross sections of charged particles emitted from proton-induced reactions on ^{98}Mo and ^{nat}Si have been measured at 25.6 MeV. The experimental (p,xp) data for ^{98}Mo were analyzed together with the (p,xn) data by the following two models: the one-component exciton model and the SMD-SMC model. As a result, the exciton model calculation using the same parameters as in the previous analysis in 10-20 MeV region showed good agreement with the (p,xp) spectra for ^{98}Mo. Furthermore, the SMD-SMC model calculation reproduced both the experimental (p,xp) and (p,xn) spectra reasonably.

In future, we intend to perform systematic measurements of double differential cross sections of charged particles emitted from proton-induced reactions over a wide mass range and at higher incident energies in order to enhance understandings of the preequilibrium process for medium-heavy nuclei and the multiparticle breakup process for light nuclei.

Finally, the authors would like to thank the members of the accelerator division of JAERI for their kind help during the experiment.

References

1) Y. Watanabe et al., *Proceedings of the XX th Int. Symp. on Nuclear Physics, Nuclear Reaction Mechanism*, Germany, Nov. 12-16, 1990, pp.151.

2) Y. Watanabe et al., Z. Phys. A **336**, 63 (1990).

3) H. Kalka, Phys. Rev. C **40**, 1619 (1989); private communication (1991).

4) Y. Watanabe et al., JAERI tandem annual report (1990).

5) I. Kumabe et al., Nucl. Scie. and Eng. **104**, 280 (1990).

6) C. Kalbach, Nucl. Phys. **A 210**, 590 (1973).

7) E. Mordhorst et al., Phys. Rev. C **34**, 103 (1986).

4.2 Measurement of the Thick-target (p,xn) Neutron Spectra from Accelerator Structural Materials at 10 MeV

Satoshi CHIBA, Kazuo HASEGAWA[*], Tokio FUKAHORI,

Masayoshi SUGIMOTO, Motoharu MIZUMOTO[*] and Hiroshi NAKASHIMA[*]

Department of Physics, JAERI, [*]Department of Reactor Engineering, JAERI

The energy and angular distributions of neutrons produced from the (p,xn) reactions with thick targets induced by 10 MeV protons were measured for several accerelator structural materials by the time-of-flight method. Distinct structures were found in the energy spectra from C and Al targets where the isobaric analog state resonances play an important role. For heavier targets, the distributions were found to be fairly smooth. γ-ray activities from the irradiated targets were also measured.

Introduction

The problem of radioactive wastes produced from nuclear power plants is one of the biggest concerns in the nuclear energy system. In JAERI, a high intensity proton LINAC ETA (1.5 GeV, 10 mA) is being planned as an engineering test to incinerate the transuranium wastes by spallation and subsequent fission reactions. As a mock-up test of the injector of ETA, a smaller version (BTA, 10 MeV, 10 mA) is currently under detailed design[1]. The BTA and ETA will be constructed in Tokai site of JAERI. Therefore, the shielding of these ultra-high powered LINACs is an important problem. On the contrary, the data, especially those of (p,xn) neutron spectra which should be used for shielding calculations, are not well established in the low energy region. In this experiment, neutron energy and angular distributions produced from the thick target (p,xn) reactions at incident proton energy of 10MeV were measured for several structural materials of linear accelerators. γ-ray activities from the irradiated targets were also measured to obtain information useful in maintening the accelerators.

Experimental Procedure and Data Reduction

The experiment was done at the JAERI tandem accelerator. The protons were produced

from the in–terminal duo–plasmatron ion source. They were then chopped and bunched into a pulsed beam of 1 MHz repetition and 1 ns duration in FWHM in order to determine the neutron energy by Time–of–Flight (TOF) method. The average beam current was typically 100 nA at the target. The targets, C, Al, Fe, Ni, Cu, Ti and Pb, have chemical purity better than 99.2 %, and were fabricated into disks of 2 cm in diameter and 1 mm in thickness (thicker than the proton range). A target of SUS304 was also fabricated to a disk of 2 cm in dia. and 2mm in thickness. The neutrons were detected by a 12.5 cm dia. by 5.0 cm thick NE213 scintillator located about 3.7m from the target in the angular range from 0 to 140 deg. Bias of the detection system was set at approximately 300 keV proton equivalent. The data were recorded onto an optical magnetic disk through a PC–based data acquisition system.

Data reduction was done off line. Effects of the backgrounds, dead time (of TAC and ADC) and detection efficiency were corrected firstly. The detection efficiency was calculated by the code NEFF7[2]. The TOF spectra were converted to the energy spectra, and then effects of the in–scattering and attenuation in the target assembly were corrected. The correction factor was calculated by the MCNP program[3] considering the precise structure of the beam duct and target assembly and JENDL–3 based library. The corrected data were extrapolated below 1 MeV to obtain the total yield by assuming the evaporation spectrum, where the measured data became uncertain due to ambiguities in the detection efficiency. The data were finally compiled in an EXFOR–like format, with information on the random and correlated error components, in 50–keV interval.

The present results contain the following error components: statistics, flight path measurement (assumed to be 5 cm), dead time correction (assumed to be 10% of the correction), detection efficiency (statistics of the NEFF7 calculation), correction factor (statistics of the MCNP calculation), unknown common error (assumed to be 5 %). In the energy region below 1 MeV, an extra random error component was assumed for extrapolation procedure.

γ–ray activities from the irradiated targets were measured after approximately 60 hours from the irradiation by using a 100cc pure Ge detector. All of the distinct γ–rays were assigned to known radio activities.

Results and Discussion

In Figs. 1 and 2, results for carbon and aluminum at 0 deg. are shown. In these light elements, discrete level structures in the compound nuclei, especially of the isobaric–analog

state resonances, are prominent. The threshold of the ^{12}C(p,n) reaction is 1.8 MeV. Therefore, all the neutrons from the carbon sample come from ^{13}C, which is only 1% abundant. Because the beam dump of BTA will be made of carbon, use of isotopically enriched ^{12}C dump is preferred. The neutron spectra for heavier elements have only smooth shapes, as shown in Fig. 3 for Cu. The integrated neutron yields obtained from the present data were generally consistent with the data used in the shielding calculations.

No distinct γ—ray activities were obserbed from the carbon target. On the contrary, γ—rays coming from ^{56}Co and ^{48}V impurities were found from the Al target.

References

1) M. Mizumoto et al., "DEVELOPMENT PLAN OF BASIC TECHNOLOGY FOR A HIGH INTENSITY PROTON LINEAR ACCELERATOR", Proc. of the 2nd Int. Symp. on ADVANCED NUCLEAR ENERGY RESEARCH – Evolution by Accelerators –, Jan. 24 – 26, 1990, Mito, Ibaraki, Japan.

2) G. Dietze and H. Klein, "NEFF7", improved version of NEFF4, "NRESP4 and NEFF4", ISSN 0572-7170 (1982).

3) J.F. Briesmeister (Ed.) , "MCNP – A General Monte Carlo Code for Neutron and Photon Transport, Version 3A", LA-7396-M, Rev. 2 (1986).
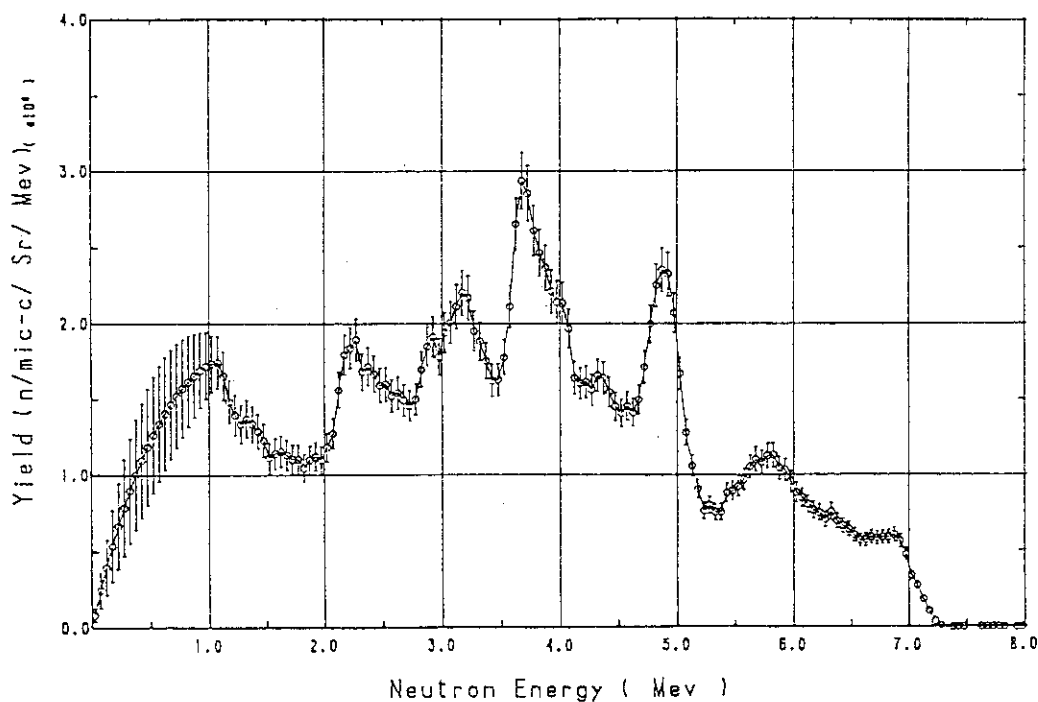
Fig. 1 Thick target (p,n) neutron spectrum from carbon measured at 0 deg. with 10-MeV protons.
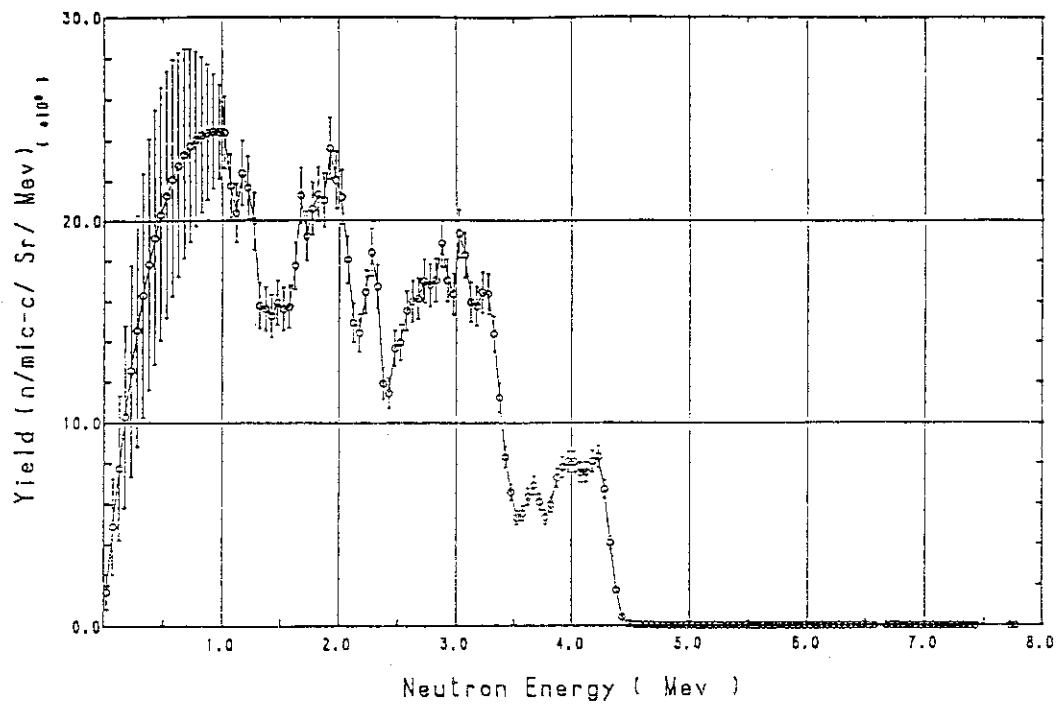
Fig. 2 Thick target (p,n) neutron spectrum from aluminum measured at 0 deg. with 10–MeV protons.
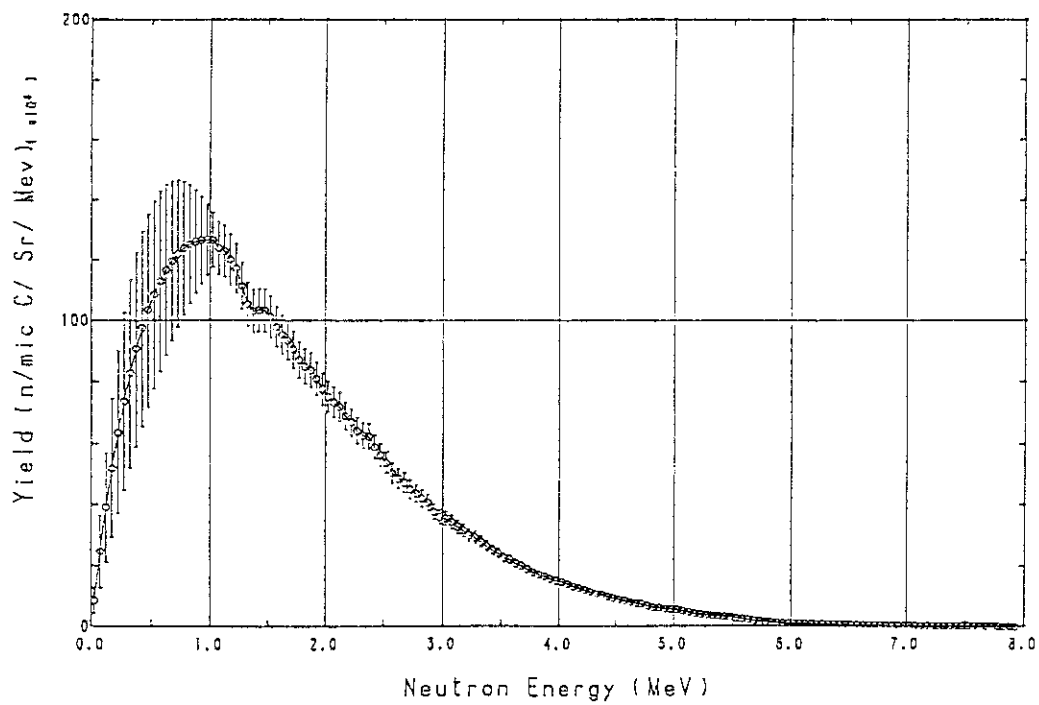
Fig. 3 Thick target (p,n) neutron spectrum from Cu measured at 0 deg. with 10–MeV protons.

4.3 Double-differential α-production Cross Section Measurements of Fe and Ni for 6.3, 7.1 and 9.7 MeV Neutrons

Mamoru BABA, Nobuo ITO, Shigeo MATSUYAMA and Naohiro

HIRAKAWA, Satoshi CHIBA*, Tokio FUKAHORI*, Motoharu

MIZUMOTO** and Kazuo HASEGAWA**

Faculty of Engineering, Tohoku University, *Department of

Physics, JAERI, **Department of Reactor Engineering, JAERI

1.Introduction

Energy-angular doubly-differential cross sections (DDX) for fast neutron induced α-production reactions are of prime importance for assessment of radiation damage and nuclear heating in fusion and accelerator-based reactors. However, very large discrepancies exist among the current evaluated data files because of difficulties in theoretical calculation and experiment for direct α-particle measurement.

In this study, α-production DDXs of Fe and Ni were measured using a high efficiency α-particle spectrometer[1-3] for 6.3, 7.1 and 9.7 MeV neutrons provided by JAERI tandem accelerator.

2. Experimental Procedure

Primary neutrons were produced by the D(d,n) reaction using a diatomic deuteron beam from the tandem accelerator and a deuterium gas target.

A specially designed gridded-ionization chamber (GIC)[1-3] was employed for α-particle detection. Figure 1 illustrates the schematic view of the present GIC: It was filled with $Kr-CO_2$ gas mixture to stop α-particles emitted from the sample between the cathode and Frisch grid. The energy and emission angle (relative to the incident beam) are determined simultaneously over $\sim 2\pi$ geometry by analyzing the set of anode and cathode signals. Therefore, owing to its large acceptance angle, GIC has much higher efficiency compared with conventional telescope-type devices. The present GIC consists of heavy-element (Ta, W) electrodes to suppress background production under fast neutron environment and has high stopping power required for fast neutron induced reactions. Neutrons incident on GIC were collimated within sample diameter to reduce backgrounds from structural materials.

Metallic foils of elemental Ni and Fe, 3 μ-m thick, were employed as

the samples and mounted on a sample changer. Backgrounds were measured by replacing the sample foils with a Ta plate.

A NE213 neutron detector placed behind GIC was employed to determine the fluence and energy of neutrons incident on GIC.

The signals from anode, cathode and ring electrodes were accumulated as three-parameter list data; the signal from the ring-electrode was used to reject background particles having longer range in anti-coincidence mode. An example of anode-cathode two-dimensional spectrum is shown in Fig.2; α-particle events are clearly observed between 0- and 90-deg lines.

The cross section was determined relative to hydrogen scattering cross section by measuring recoil protons by GIC.

This technique proved very effective even for neutrons around 10 MeV from the favorable signal to background ratio and the high count rate which enabled to get DDX within a few hours using beam current around 3 μA.

3. Results and Discussion

The results of DDX and angular distribution for Ni are shown, respectively, in Fig.3 and Fig.4 together with the corresponding values derived from ENDF/B-VI which uniquely provides charged-particle DDX. The present energy distributions show significant angle-dependence partly due to kinematical effect and differ markedly from ENDF/B-VI both in magnitude and shape. The experimental angular distributions are almost isotropic and suggest little contribution of non-equilibrium processes. It is noted that the present results are much lower than ENDF/B-VI.

The results for Fe are illustrated in Fig.5 and Fig.6. The spectra for Fe show angular dependence similar with Ni. The magnitudes of the present data are close to the ENDF/B-VI values. However, recent data by Saraf et al.[4] obtained by Ohio University E-TOF spectrometer are much lower than the present data. Further experiments should be done for other neutron energies as well as theoretical calculation to trace the problem.

References

1. M.Baba et al.: Proc.Int.Conf."Nuclear Data for Sci. Technol.," (May, 1991 Jeulich), to be published

2. N.Ito et al.: JAERI-M 92-027 (1992) pp.257

3. N.Ito et al.: JAERI-M 91-032 (1991) pp.302

4. S.K.Saraf et al.: Nucl.Sci.Eng., 107 365 (1991)
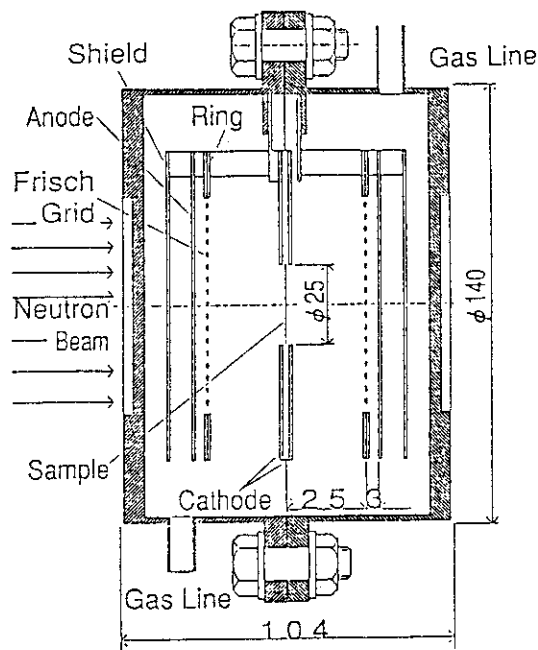
Fig.1: Schematic view of GIC
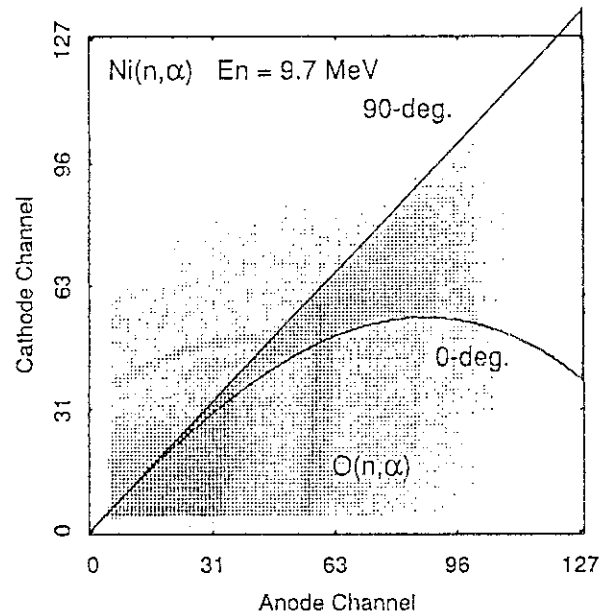
Fig.2: Two-dimensional spectrum
anode versus cathode signal
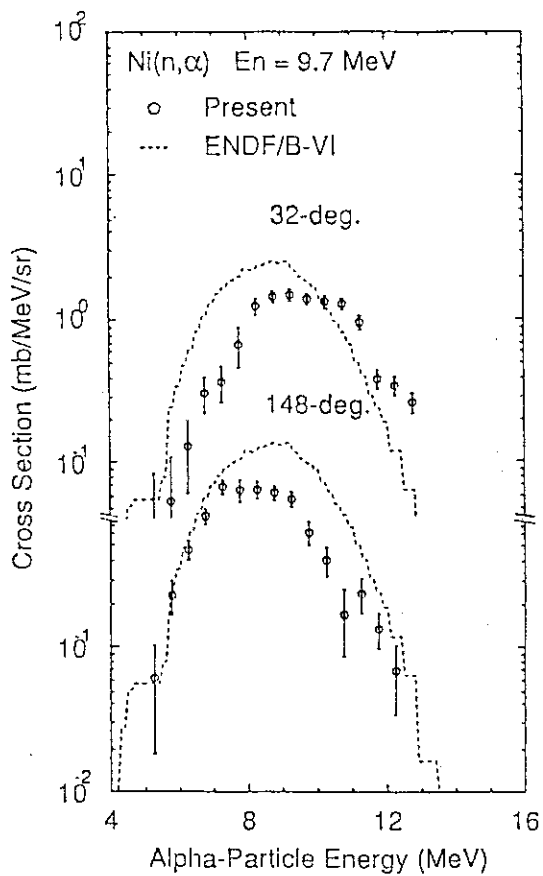
Fig.3: DDX for Ni(n,α) reaction
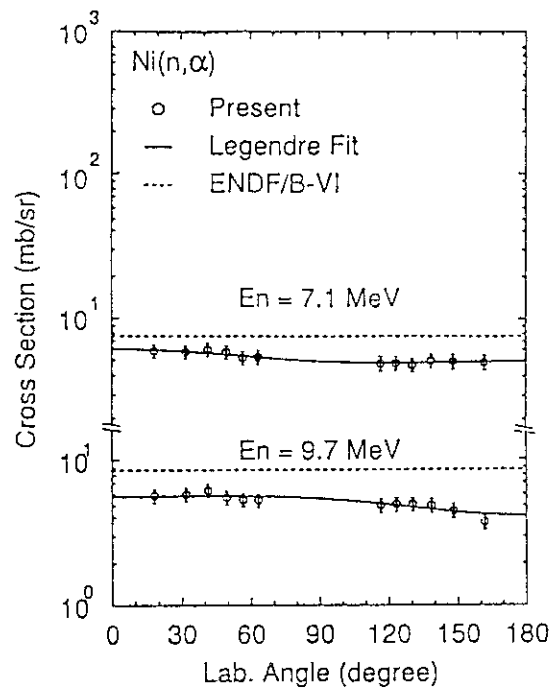
Fig.4: Angular distributions for
Ni(n,α) reaction
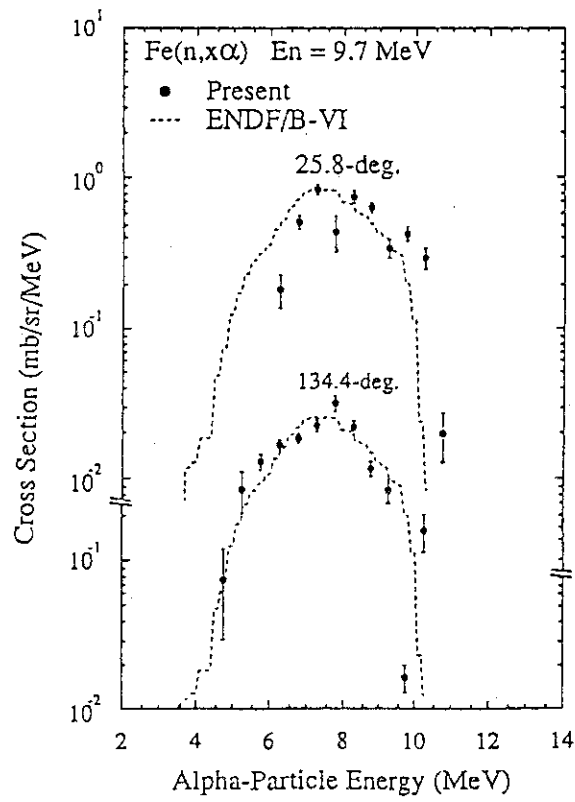
Fig.5: DDX for Fe(n,α) reaction
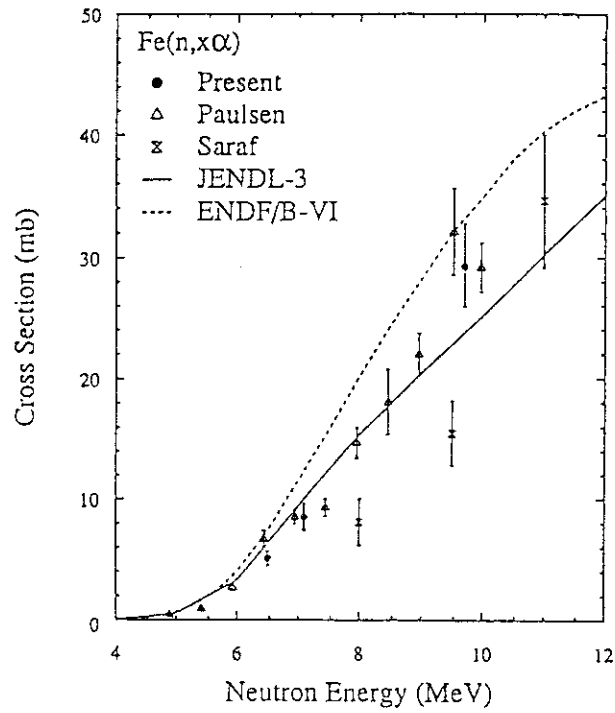
Fig.6: comparison of Fe(n,xα) reaction

− 141 −

V HEAVY ION NUCLEAR PHYSICS

5.1 In-beam Study of ^{107}Sn and ^{105}Sn

Tetsuro ISHII, Akiyasu MAKISHIMA[*], Kenichi KOGANEMARU[**],
Mituo NAKAJIMA[**], Masao OGAWA[**] and Mitsuhiko ISHII

Department of Physics, JAERI, [*]Center for Radioisotope Science,
National Defense Medical College, [**]Department of Energy Sciences,
Tokyo Institute of Technology

Excited states of the nucleus ^{107}Sn were populated by bombarding the target ^{54}Fe, 7 mg/cm², with a beam of 210 MeV ^{56}Fe from the tandem accelerator. In–beam γ–rays were sorted by charged–particle multiplicity with the Si box[1]. Under this condition we have made experiments of (1) γ–γ coincidences measured with four 30 % Ge detectors, (2) the angular distribution, and (3) the linear polarization with a Ge detector, 70 mm in diameter and 15mm thick. The lifetimes of some excited states were measured by the recoil–distance method with the target ^{56}Fe, 0.4 mg/cm², and a beam of 200 MeV ^{54}Fe. Level structure of the nucleus ^{105}Sn has been studied by use of the reaction
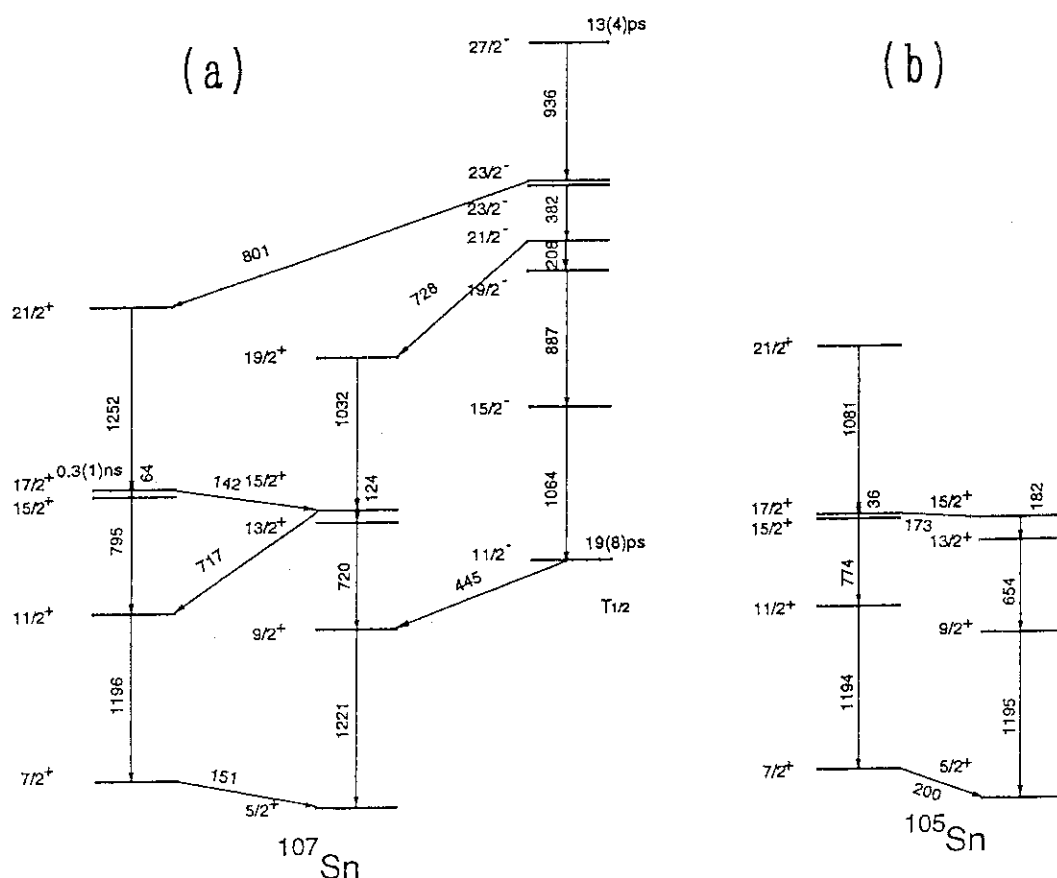
Fig.1 Level schemes of (a) ^{107}Sn and (b) ^{105}Sn. The transition energies are given in units of keV.

^{54}Fe(^{54}Fe, 2pn) ^{105}Sn with the bombarding energy of 210 MeV. Thus far experiments have been made on γ–γ coincidences and the anisotropy of the γ–ray. Based on these data, level schemes of ^{107}Sn and ^{105}Sn have been constructed as shown in figs. 1 (a) and (b), respectively.

We assigned the ground state as 5/2$^+$ and the first excited state as 7/2$^+$, which led the spin–assignments of higher excited states consistently with the experimental results. The ground and the first excited states can be interpreted in terms of a neutron in the orbit d$_{5/2}$ or g$_{7/2}$ coupling with the core nucleus ^{106}Sn in the ground state, because these neutron orbits lie near the Fermi surface. In the first–order approximation the Talmi binding energy formula[2] can explain the reason why ^{107}Sn possesses the spin 5/2$^+$ instead of 7/2$^+$ in the ground state. Excited states with even parity are thus attributed to excitation of ^{106}Sn. Besides, an odd–parity band is built on the 11/2$^-$ state coming from a neutron in the orbit h$_{11/2}$. The level scheme of ^{105}Sn has a similar structure to that of ^{107}Sn as can be seen in fig. 1 (b). By assuming that the ground state is 5/2$^+$, spins and parities of the excited states have been assigned. It is interesting that the transition energies are close to those in ^{107}Sn. No odd–parity states were observed.

References

1) M. Ishii et al.: in Nuclei off the line of Stability(ed. R. A. Meyer and D. S. Brenner, A.C.S., Washington D.C., 1986) p.350.
2) R.D. Lawson: Theory of the nuclear shell model(Clarendon press, Oxford, 1980) p80.

5.2 Search for a Double-γ Vibrational State in 168Er (II)

Masumi OSHIMA, Hideshige KUSAKARI[*], Masahiko
SUGAWARA[**], Yasuyuki GONO[***], Alan FERRAGUT[***], Yu Hu
ZHANG[***], Shin-ichi ICHIKAWA[****], and Takashi INAMURA[***]

Department of Physics, JAERI, [*]Faculty of Education, Chiba
University, Yayoi-cho, Chiba 260, [**]Chiba Institute of Technology,
Shibazono, Narashino, Chiba 275, [***]RIKEN, Wako-shi, Saitama
351-01, and [****]Department of Chemistry, JAERI

The multi-phonon vibrational excitations are known to be well established in near-spherical region. In deformed region, however, even two-phonon state has not been assined definitely. Their existence and collectivity is one of the central problem for elucidating the collective excitation of nuclei [1-4]. A candidate for the double-γ $K^{\pi}=4^{+}$ state was assigned at 2055 keV by W.F.Davidson et al. [5] and recently, while the experimental uncertainty is large, rather large B(E2) value was reported for the transition from this state to the one phonon γ-vibrational state at 821 keV by a lifetime measurement [6]. In order to derive the B(E2) value more accurately, we made a Coulomb-excitation experiment exclusively optimized for the observation of the known transitions from the 2055-keV level.

168Er was multiply Coulomb-excited with a 295-MeV 74Ge beam obtained from the tandem accelerator. The target 168Er was a self-supporting metallic foil of 1.8 mg/cm2 in thickness (95% isotopically enriched). Deexcitation γ rays were observed with ten Ge counters in coincidence with recoiled target atoms and scattered projectiles which were detected with four PPACs (Parallel Plate Avalanche Counter). The PPACs were placed symmetrically with respect to the beam, surrounding the target, so that they covered forward as well as backward angles. The size of PPAC was 10 cm × 10 cm, and the distance between the center of the PPAC window and the target was 7 cm. The PPACs provided the position signals of detected particles. The observed γ-ray spectra were corrected for Doppler shifts kinematically by using the position signals.
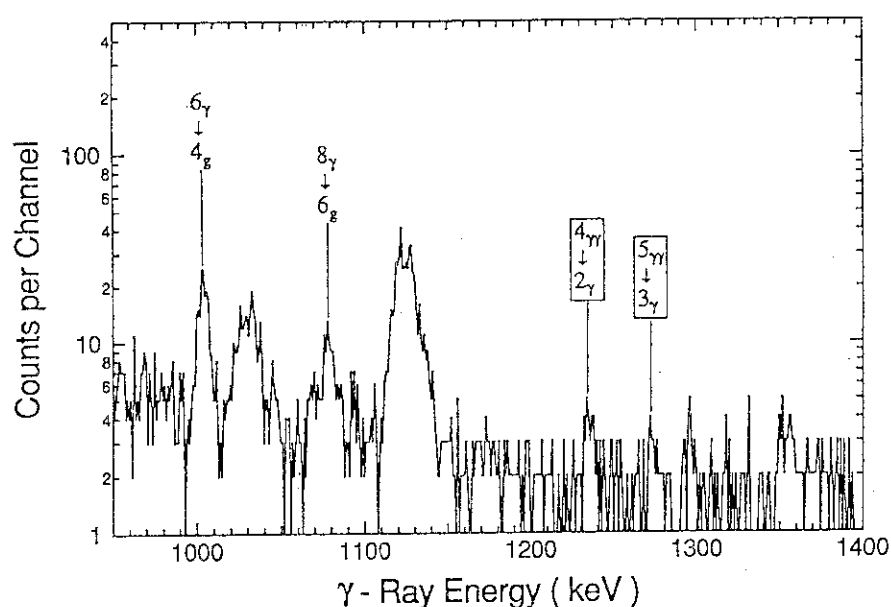
Fig. 1 Doppler corrected γ—ray spectrum following Coulomb excitation of [168]Er

We observed members of the ground—state rotational band up to 18^+ and of the γ band up to 10^+. Most importantly, the 1234—keV transition from the candidate of double—γ vibrational state to the one—phonon γ—vibrational state is observed for the first time in Coulomb excitation.

By comparing the experimental γ yield of this transition with that calculated by Coulomb excitation code GOSIA [7], we obtained tentatively the $B(E2;4_3{}^+ \to 2_2{}^+)$ value as 0.009 ± 0.006 e^2b^2. The present value agrees with the previously reported value of 0.028 ± 0.014 e^2b^2 within the experimental accuracy. The present value is significantly smaller than the general expectations from several theoretical models. A detailed analysis is still under way.

References:

[1] M.Matsuo and K.Matsuyanagi, Prog. Theor. Phys. **76**, 93 (1986); **78**, 591 (1987).

[2] N.Yoshinaga, Y.Akiyama, and A.Arima, Phys. Rev. Lett. **56**, 1116 (1986).

[3] V.G.Soloviev and N.Yu.Shirihova, Z. Phys. **A301**, 263 (1981).

[4] M.K.Jammari and R.Piepenbring, Nucl. Phys. **A487**, 77 (1988).

[5] W.F.Davidson et al., J. of Phys. **G7**, 455, 843 (1981).

[6] H.G.Borner et al., Phys. Rev. Lett. **66**, 691 (1991).

[7] D.Cline, Ann. Rev. Nucl. Part. Sci. **36**, 681 (1986); and references therein.

5.3 Electromagnetic Transition Probabilities in the Natural-parity Rotational Bands of ^{155,157}Gd

Masumi OSHIMA, Hideshige KUSAKARI[*], Akiko UCHIKURA[*],
Ariyoshi TOMOTANI[*], Masahiko SUGAWARA[**], Shin—ichi
ICHIKAWA[***], Hideki IIMURA[***], Tsuneyasu MORIKAWA[****],
Takashi INAMURA[****], and Masayuki MATSUZAKI[*****]

*Department of Physics, JAERI, *Chiba University, Yayoi—cho,
Inage—ku, Chiba 263, **Chiba Institute of Technology, Shibazono,
Narashino—shi, Chiba 275, ***Department of Chemistry, JAERI,
****RIKEN, Wako—shi, Saitama 351—01, *****Fukuoka University
of Education, Akama, Munakata—shi, Fukuoka 811—41*

We have previously reported signature dependence of M1 strength in the natural—parity rotational band of ^{163}Dy [1,2]. This has drawn considerable attention since the signature dependence is unexpectedly large and the phase of the zigzag pattern as a function of spin contradicts the selection rule [3] that is well established for unique—parity rotational bands based on high—j orbits [4—10]. This "inverted" signature dependence was shown in terms of the cranking model (previously referred to as "the rotating shell model") to originate from the characteristic coherence between the orbital and spin contributions in the spin—down ($\Omega = \Lambda - 1/2$) dominant one—quasiparticle states [2,11]; a particle—rotor—model calculation gave a similar result [12]. On the other hand, the counterpart, i.e., the spin—up ($\Omega = \Lambda + 9/2$) dominant configurations showed almost no signature dependence of B(M1) values, which is consistent with expectations given by the cranking model [13]. In order to clarify the general feature in this mass region, the intermediate situation in which the spin—down and spin—up configurations are strongly mixed should be studied. In this report we present the results of Coulomb—excitation experiments on ^{155} ^{157}Gd whose ground states contain comparable magnitudes of the spin—down and spin—up configurations. Part of this work has been published elsewhere [14].

The ground—state rotational bands of ^{155,157}Gd are commonly based on the natural—parity Nilsson state ν [521 3/2]. We have assigned levels up to $J^\pi = (25/2^-)$ in ^{155}Gd and $J^\pi = 25/2^-$ in ^{157}Gd and, by measuring γ—ray branchings, E2/M1 mixing ratios and nuclear lifetimes, the absolute intraband transition probabilities were

determined up to the 21/2⁻ state in ¹⁵⁵Gd and the 23/2⁻ state in ¹⁵⁷Gd .

Electromagnetic transition rates as well as quasiparticle energy splittings of ¹⁵⁵Gd and ¹⁵⁷Gd are shown in Figs. 1–4. The experimental signature splittings $\Delta e' = e'_{+i} - e'_{-i}$ are shown by solid lines in Fig. 1. Their sign is consistent with the dominant $h_{9/2}$ character. Their magnitudes in ¹⁵⁷Gd are about one half of those in ¹⁵⁵Gd. This difference can be understood, at least qualitatively, as due to the difference in the nuclear deformation. The B(M1) values are shown in Fig. 2. A distinct neutron–number dependence can be found in this quantity: (a) the averaged magnitudes are almost independent of spin in ¹⁵⁵Gd, while they increase gradually as a function of spin in ¹⁵⁷Gd; (b) the inverted signature dependence occurs in ¹⁵⁵Gd but it is not clearly seen in ¹⁵⁷Gd. The B(E2) values with $\Delta I = 1$ and 2 are shown in Figs. 3 and 4. They are rather smooth functions of spin. The uncertainties in the B(E2: I → I–1) values are, unfortunately, too large to allow any conclusions to be drawn from this data.

We performed cranking–model calculation for ¹⁵⁵Gd and ¹⁵⁷Gd based on the Nilsson potential. The formulation of the calculation is given in Ref.[16]. The results of theoretical calculations are also presented in Figs. 1–4. The signature splittings $\Delta e'$ in ¹⁵⁵Gd are reproduced excellently by the calculation using an axially symmetric shape deduced from the measured quadrupole moments of the adjacent even–even nuclei. In ¹⁵⁵Gd signature dependence of B(M1) is seen in the calculation as well as in the experiment although the measured absolute values are not well reproduced by the calculation.

In ¹⁵⁷Gd, the calculation gives a similar result to that of ¹⁵⁵Gd: the sign of the quasiparticle energy splittings is the same and the inverted signature dependence of B(M1) are seen. However, the energy splittings calculated in the same way as in ¹⁵⁵Gd are twice as small as the corresponding experimental values. The calculation for B(M1) deviates from the experimental values at high spins, giving smaller values. The origin of this difference is not clear.

B(E2:I → I–2) values are almost independent of the neutron number both in the experiment and calculation. The calculated values, however, are systematically smaller than the experiment. Since the quadrupole deformation is derived from the experimental quadrupole moments of adjacent even–even nuclei, the deviation may indicate that the deformation of ¹⁵⁵,¹⁵⁷Gd is larger than the even–even nuclei. This indication, however, contradicts the observation of quasiparticle energy splitting because the larger deformation causes smaller energy splitting and results in larger
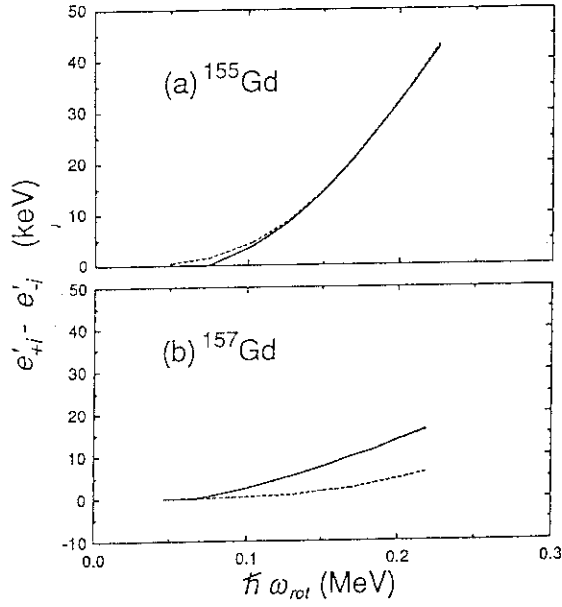
FIG. 1. Quasiparticle energy splittings of g—band in ^{155,157}Gd. The solid line connects the experimental values. The dashed line shows the calculation.
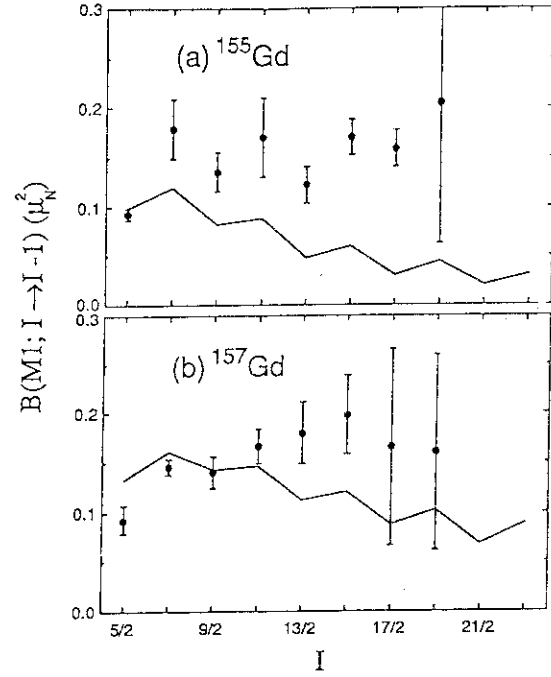
FIG. 2. B(M1;I → I—1) values of g—band in ^{155,157}Gd. The solid line shows the cranking—model calculation.
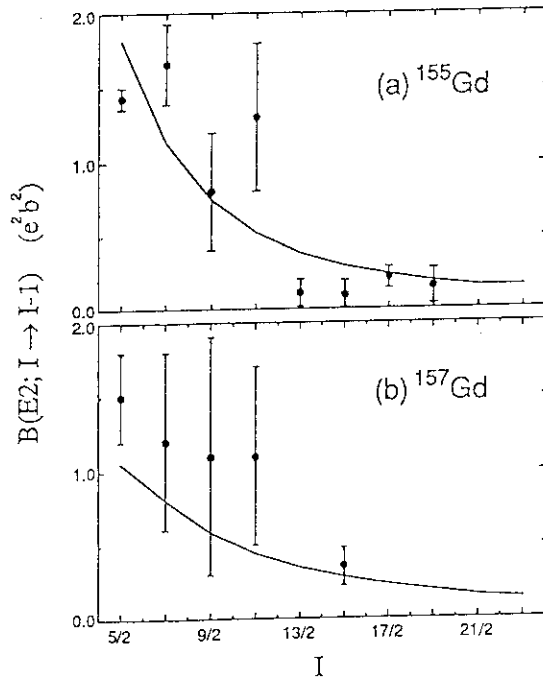
FIG. 3. B(E2;I → I—1) values of g—band in ^{155,157}Gd. The solid line denotes the present cranking—model calculation.
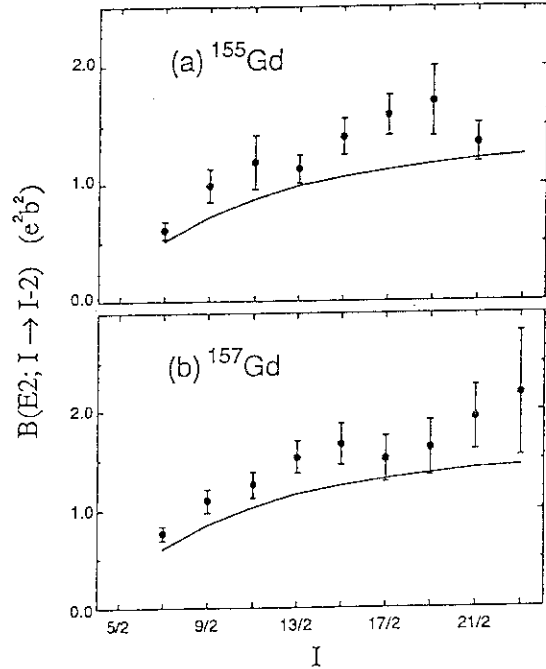
FIG. 4. B(E2;I → I—2) values of g—band in ^{155,157}Gd. The solid line denotes the present cranking—model calculation.

deviation from the experiment. B(E2: I → I–1) values in [155]Gd and [157]Gd are reproduced within the experimental accuracy.

References

[1] E.Minehara et al., Phys. Rev. C **35**, 858 (1987).

[2] M.Oshima et al., Phys. Rev. C **39**, 645 (1989).

[3] I.Hamamoto, Phys. Lett. **106B**, 281 (1981); in Proceedings of the Niels Bohr Centennial Conference on Nuclear Structure, Copenhagen 1985, ed. R.Broglia, G.B.Hagemann, and B.Herskind (North—Holland, Amsterdam—London, 1985) p.129.

[4] G.B.Hagemann et al., Nucl. Phys. **A424**, 365 (1984); D.C.Radford et al., in contribution to the workshop on Nuclear Structure, The Niels Bohr Institute, May, 1988.

[5] M.Ohshima et al., Nucl. Phys. **A436**, 518 (1985).

[6] K.Honkanen et al., in Proceedings of the American Chemical Society Meeting (1986).

[7] J.Gascon et al., Nucl. Phys. **A467**, 539 (1987).

[8] C.–H.Yu et al., Nucl. Phys. **A489**, 477 (1988).

[9] P.Frandsen et al., Nucl. Phys. **A489**, 508 (1988).

[10] M.Oshima et al., Phys. Rev. C **37**, 2578 (1988).

[11] M.Matsuzaki, Phys. Rev. C **39**, 691 (1989).

[12] A.Ikeda and T.Shimano, Prog. Theor. Phys. **85**, 547 (1991).

[13] M.Oshima et al., Phys. Rev. C **40**, 2084 (1989).

[14] H.Kusakari et al., Phys. Rev. C (1992) to be published.

5.4 Hyperfine Interactions of the 1.98MeV 2^+ State of ^{18}O in 7^+ Ion Measured by the γ-ray Recoil Method

Yasuharu SUGIYAMA, Yoshiaki TOMITA, Hiroshi IKEZOE, Yoshimaro

YAMANOUCHI, Kazumi IDENO, Daniel R. NAPOLI[*], Hee.J.KIM[**], Bujia

QI[***], Tsuyoshi SUGIMITSU[****] and Hiroshi FUJITA[*****]

Department of Physics, JAERI, [*]INFN,Laboratori Nazionali di Legnaro, Italy,

[**]Physics Devision, ORNL, U.S.A., [***]Beijing Tandem National Laboratory,

China Institute of Atomic Energy, China, [****]Department of Physics, Kyushu

University, [*****]Daiichi College of Pharmaceutical Sciences

It has been shown that information on nuclear spin alignment can be extracted from the precise measurement of a line shape of an outgoing excited nucleus in heavy-ion reactions[1]. The momentum of the outgoing excited nucleus is broadened by γ-rays emitted in flight. The line shape reflects the angular distribution of the γ-ray, which has a characteristic pattern for a different magnetic substate. So far we have obtained the m-substate populations from the line shape analysis where a quantization axis is taken along the center of mass scattering angle of the outgoing nucleus .

It is known that a hyperfine interaction in an isolated ion with a single-electon ionic ground-state perturbes the nuclear spin alignment and hence the γ-ray angular distributions. Following the paper by Glavish et al.[2] the angular distribution of γ-ray decaying from excited 2^+ state to the ground 0^+ in ^{18}O is expressed as,

$$W(\theta_\gamma) = \Sigma_k A_k G_k(q) P_k(\cos\theta_\gamma) ,$$
$$k=0,2,4, \qquad\qquad (1)$$

where the coefficients A_k are the Legendre expansion coefficients of the unperturbed angular distributions. The $G_k(q)$ account for attenuations due to HFI where q represents the charge state of ^{18}O. At the short nuclear lifetime of 2.0ps only the contact field associated with a single 1s electron is large enough to generate a measurable perturbation. The time–integral attenuation coefficients for static, randomly oriented HFI in the 7^+ charge state can be expressed as

$$G_k(7) = 1 - \alpha(7)\frac{k(k+1)}{(2I+1)^2}\frac{(\omega\tau)^2}{1+(\omega\tau)^2}.$$

The HFI frequency is given by $\omega = (2I+1)\mu_N g_I H(0)/\hbar$ where μ_N and g_I are the nuclear magneton and the nuclear g–factor, respectively. The magnetic field at oxygen nuclei is calculated to be H(0)=85.8MG. The quantity $\alpha(7)$ represents the ionic ground–state occupancy. There is no HFI in the 8^+ charge state and hence $G_k(8)=1$. The parameter A_k is extracted from the line shape of the outgoing nucleus in the 8^+ charge state. The γ–ray line shape in the 7^+ charge state gives us the parameters G_k which include nuclear g–factor g_I.

In the present experiment we measured momentum spectra of ^{18}O (2^+ 1.98MeV) in 7^+ and 8^+ charge states excited through the $^{18}O+^{58}Ni$ inelastic scattering. The ^{18}O beam obtained from the JAERI tandem at an energy of 60 MeV was bombarded on the ^{58}Ni target with a thickness of $67\mu g/cm^2$. The line shapes broadened by γ–ray recoil are measured precisely by using the heavy–ion magnetic spectrograph "ENMA"[3]. The broadened line shape in the 7^+ and 8^+ charge states of $^{18}O(2^+$ 1.98MeV) measured at $\theta_{lab}=32°$ are shown in Fig.1. Dashed lines in the figures are the results obtained through the χ^2 analysis of the date by using eq.(1). A preliminary value of $\alpha(7)(\omega\tau)^2/(1+(\omega\tau)^2)$ was obtained to be 0.61±0.02 which was about the same as the one obtained by the perturbed angular correlation method[2].

References

1) Y.Sugiyama et al., Z.Phys.A—Atoms and Nuclei 322(1985)579.

2) H.F.Glavish et al., Phys. Rev. Lett. 28(1972)763.

3) Y.Sugiyama et al., Nucl. Instr. and Meth. A281(1989)512.

$^{18}O+^{58}Ni$ inelastic scattering

$E_{lab}=60$ MeV, $\theta_{lab}=32^\circ$
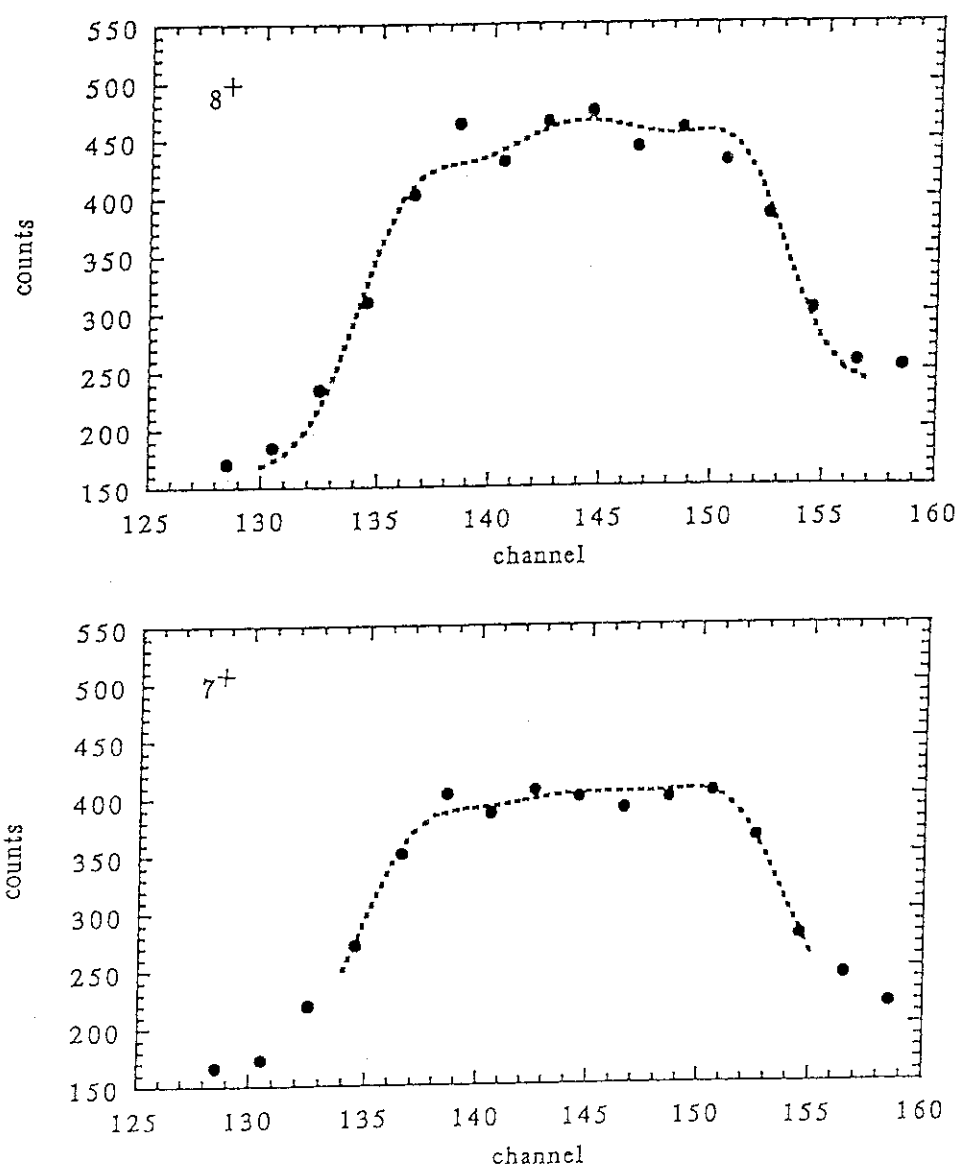
Fig.1 Measured line shapes of the 1—st excited 2^+ state of ^{18}O in 7^+ and 8^+ions
broadened by the γ—ray emission in flight. Dashed lines are results obtained through
the χ^2 analysis of the data by using eq.(1).

5.5 Measurement for $^{12}C(2^+)$ Spin Alignment Following the ^{12}C + ^{16}O Collision around E_{cm}=32MeV

Takashi MUKAE, Hiroshi FUJITA*, Takumi OKAMOTO, Shunji NIIYA, Makoto MATSUO, Shinichi MITSUOKA, Kenji UTSUNOMIYA, Yasuharu SUGIYAMA**, Yoshiaki TOMITA**, Kazumi IDENO**, Hiroshi IKEZOE**, Yoshimaro YAMANOUCHI**, Tsuyoshi SUGIMITSU, Norihisa KATO and Shunpei MORINOBU

Department of Physics, Kyushu University, *Daiichi College of Pharmaceutical Sciences, **Department of Physics, JAERI

Previous observation[1] of some resonance-like structure in the mutually excited $^{12}C(2^+)$ + $^{16}O(3^-)$ channel around E_{cm} = 32MeV in particular has stimulated us to study it in more detail by measuring the magnetic substate population of the outgoing $^{12}C(2^+)$ particles.

The present measurement is focussed on the $^{12}C(2^+)$ + $^{12}C(0^+gs)$ (single excitation) and $^{12}C(2^+)$ + $^{16}O(3^-)$ (mutual excitation) channels.

Excitation functions were taken at θ_{lab} = 7.0° from 72.2MeV to 79.0MeV in a step of 0.4MeV. Angular distributions were measured in the laboratory angle ranging from 4.0° to 15.0° in a step of 1° at the beam energies of 75.0MeV (on resonance) and 77.8MeV (off resonance).

The experiments were carried out at JAERI Tandem Van de Graaf accelerator by using the magnetic spectrograph ENMA. An $^{16}O^{6+}$ beam was used to bombard a ^{12}C target with 50 $\mu g/cm^2$ thickness. After the outgoing ^{12}C particle were momentum analyzed by the spectrograph, they were identified with a hybrid focal plane detector which allowed measurements of position, energy and δE of each particle. Typical momentum spectra are shown in Fig. 1. The broadened line shape for the $^{12}C(2^+)$ channels due to recoil by γ-ray emission is clearly observed as well as some sharp peaks for the $^{12}C(0^+gs)$ ones.

The obtained excitation functions are shown in Fig. 2. In the single excitation a resonant structure seems to exist at E_{cm} = 32.06MeV. In the mutual excitation a weakly correlated structure is also seen at the same energy. Because of this, we measured the angular distribution at two energies noted above.
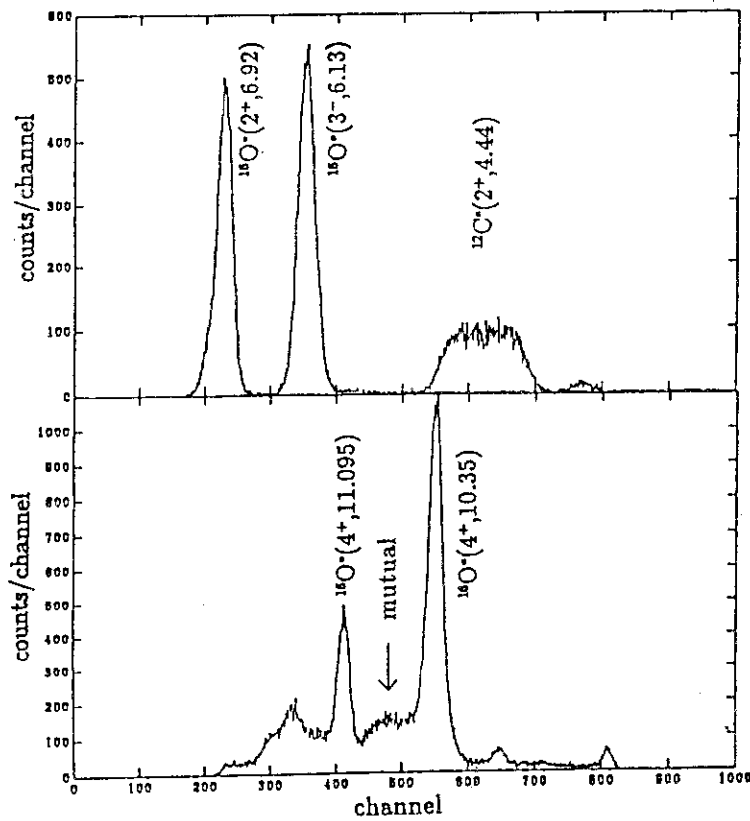
Fig. 1 Typical momentum spectra.

The relative differential cross sections are given in Fig. 3. In the single excitation an oscillatory amplitude for on resonance is smaller than the one for off resonance. In the mutual excitation the relative differential cross section for on resonance is out of phase with the one for off resonance.
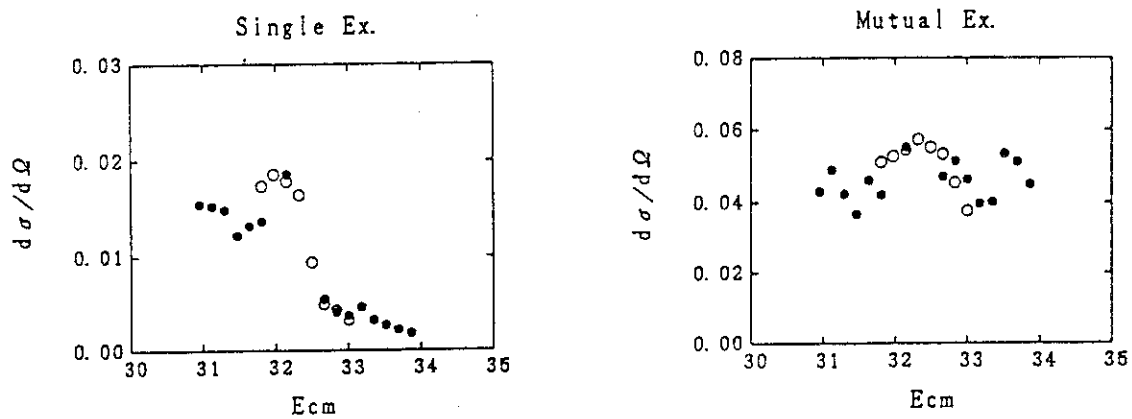
Fig. 2 Excitation function.

Single Ex.

Mutual Ex.
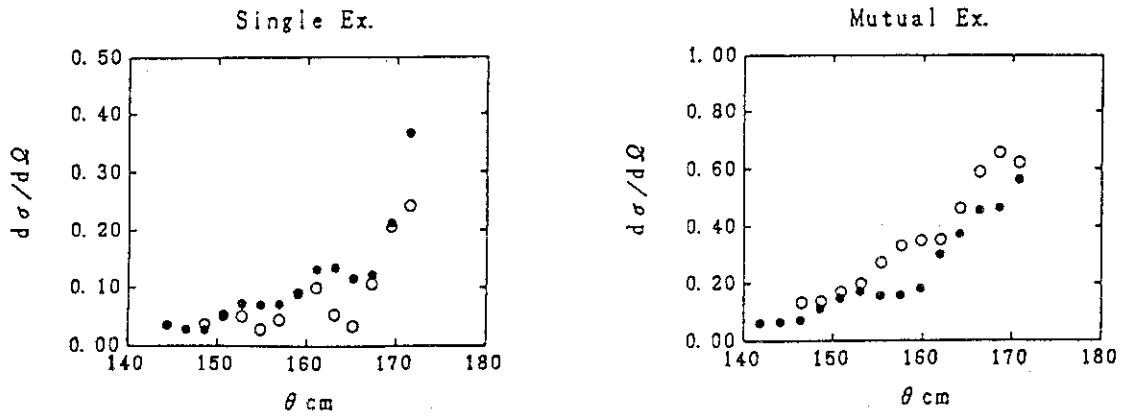
Fig. 3 Differential cross section.

The broadened line shape at each angle is analyzed in a similar procedure described in ref. 2. The magnetic substate population was determined through a least square fit to the measured line shape. Examples of the fitting are shown in Fig. 4 and the angular dependence of magnetic substate population is presented in Fig. 5.
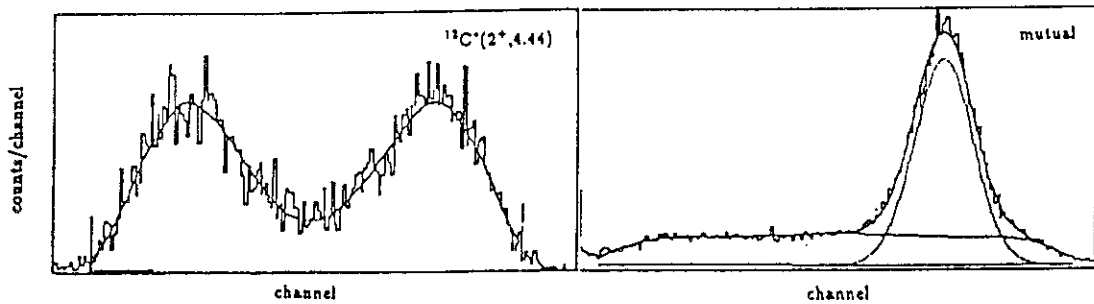
Fig. 4 Examples of line shape fitting.

Cross section for each magnetic substate[3] is predicted theoretically by the following equations: in single excitation

$$d\sigma_m(\theta) = |\sum_{\mu L'} a_{L'}(L'\,I-\mu\mu\,|\,L0)Y_L^{-\mu}(\theta,0)d_{\mu m}^I(\theta)|^2 \tag{1}$$

and in mutual excitation

$$d\sigma_m(\theta) = \sum_{S\mu'} |\sum_{L'} a_{L'}(II'\,\mu\mu'\,|\,SM)(L'\,S-MM\,|\,L0)Y_L^{-M}(\theta,0)d_{\mu m}^I(\theta)|^2. \tag{2}$$

If only one partial wave contributes on resonance ,we can estimate the substate population parameters. In Fig. 5 comparison between calculation and experiment is made for a (L, L') combination, where L and L' denote the initial and final angular momentum, respectively. Solid curve is the result of calculation. In the

single excitation calculation with L = J = 16, L′ = J − 2 = 14 or L = J = 17, L′ = J − 2 = 15 seem to be in better agreement with the experimental. Hence we conclude that the transition from L = J to L′ = J−2 is dominant and that spin of the resonance may be 16 or 17ħ. In the mutual excitation, however, the calculation any (L, L′) combination failed to reproduce the experiment and further consideration is necessary.
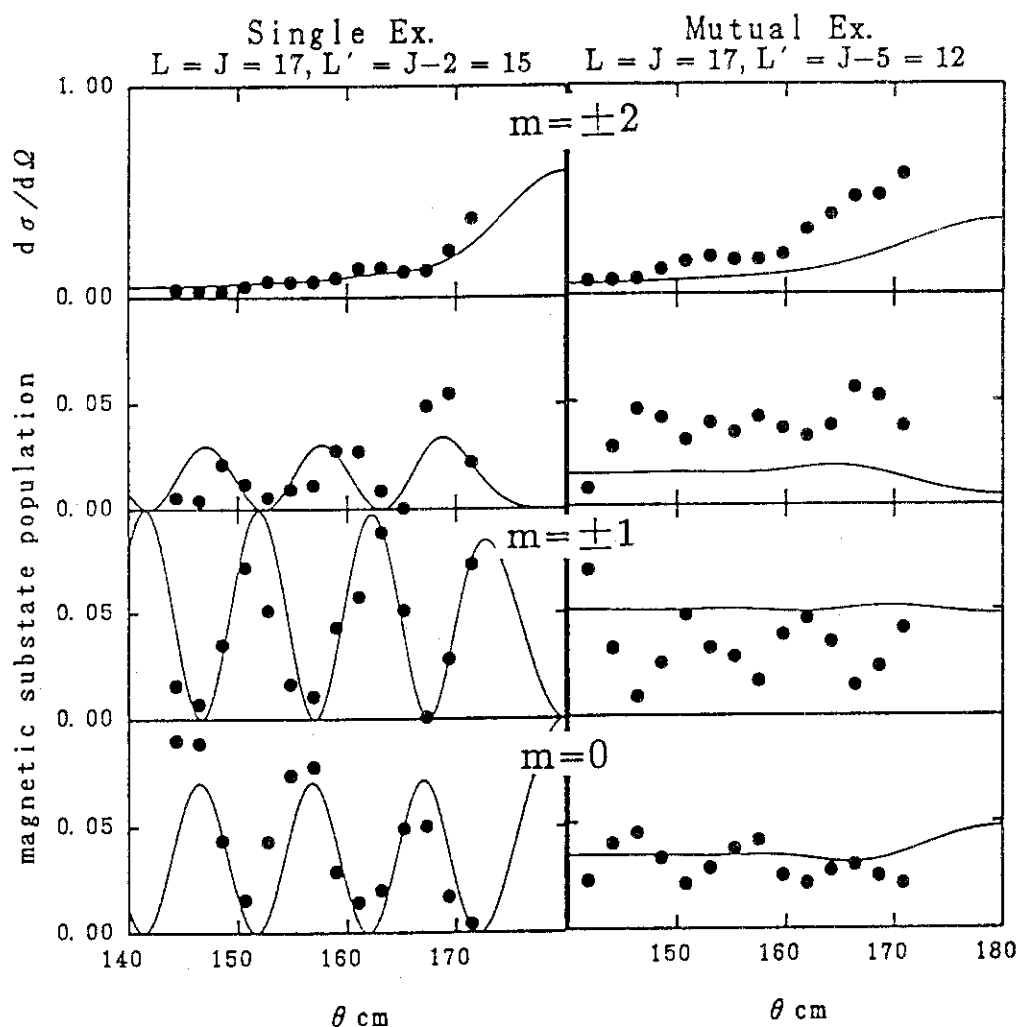
Fig. 5 Magnetic substate population.

References

1) N. Kato et al., Kyushu University Tandem Accelerator Laboratory Report (1980−1984) p.106.

2) Y. Sugiyama, Y. Tomita, H. Ikezoe, and N. Shikazono, Z. Phys. A - Atoms and Nuclei 322 (1985) 579.

3) A. H. Wuosmaa, et al., Phys. Rev. C41 (1990) 2666.

5.6 Charged Particle Emissions in Fission Process

Hiroshi IKEZOE, Naomoto SHIKAZONO, Yuichiro NAGAME,
Tsutomu OHTSUKI, Yasuharu SUGIYAMA, Yosiaki TOMITA,
Kazumi IDENO, Ikuo KANNO, H.J. KIM[*], B.J. QI[**] and
Akira IWAMOTO

Department of Physics, JAERI, [*]ORNL, Oak Ridge, TN 37831, U.S.A.,
[**]Institute of Atomic Energy, Beijing 102413, China

Neutron mltiplicity measurements in the fission process provide information on the time scale of the fission process. From these it has been inferred that the fission process is a relatively slow process (few 10^{-20} sec to 10^{-19} sec[1]). On the other hand, we have reported that the observed pre—scission proton and α particle multiplicities are fairly consistent with standard statistical model calculations[2], and it seemed that such a long fission time scale does not influence the pre—scission proton and α particle emissions.

In order to study the problem, we measured and analyzed the post—scission proton and α particle multiplicities for the $^{16}O + ^{197}Au$, $^{19}F + ^{181}Ta$, ^{197}Au and ^{208}Pb, and $^{28}Si + ^{197}Au$, and ^{208}Pb systems at a number of incident energies. Since the post—scission charged particle multiplicities give us information on excitation energies of fission fragments, it is possible to check the experimental consistency of pre—scission neutron data and post—scission charged particle data.

The observed multiplicities of post—scission protons and α particles are shown in Fig.1 and Fig.2, respectively, as a function of the compound nucleus excitation energies U. In the present analysis, excitation energies of fission fragments were estimated by subtracting the energies removed by emitting pre—scission neutrons from the compound nucleus before fission. Then the particle evaporations from two fission fragments were calculated by using the statistical model code PACE2[3]. The shaded areas in the figures represent the calculated results where the fission fragment excitation energies are estimated by taking into account the pre—scission neutron multiplicities ν_n^{obs} observed by Hinde et al.[1]. The overall trends of the experimental data as a function of U are consistent with the calculations. The dashed lines represent the calculated results by using ν_n^{cal} predicted by PACE2 instead of ν_n^{obs}. It is noted that the ν_n^{cal} considerably underestimates the pre—scission neutron multiplicity at U $\geq$ 60 MeV[1], while the PACE2 calculations reproduce the measured pre—scission charged particle data[2] rather well. The dashed lines overestimate the post—scission charged particle multiplicities for all reaction systems studied here. The present result indicates that more energies than predicted by the statistical model calculation are in fact lost from the compound nucleus before fission by

emitting pre—scission neutrons and the present data are consistent with the pre—scission neutron data measured by Hinde et al..

The fission time scale is generally believed to consist of the transient time for the initial configuration to reach stationary outgoing flux at the saddle point and the descent time from saddle to scission. If the pre—scission charged particles, especially α particles, are mainly emitted from a very early stage of the compound nucleus decay as predicted by the statistical model calculation, the present results suggest that the transient time is seemed to be short and the major part of the excess pre—scission neutron over the statistical model calculations may be emitted during the saddle—to—scission region in the fission process. The detailed analysis is still underway.

References

1) D.J. Hinde, et al., Nucl. Phys. A452 (1986) 550.
2) H. Ikezoe, et al., Proceedings of Fourth International Conference on Nucleus—Nucleus Collisions, Kanazawa, Japan, June 10—14, 1991, Nucl. Phys. A538 (1992) 299c
3) A. Gavron, Phys. Rev. C21 (1980) 230.
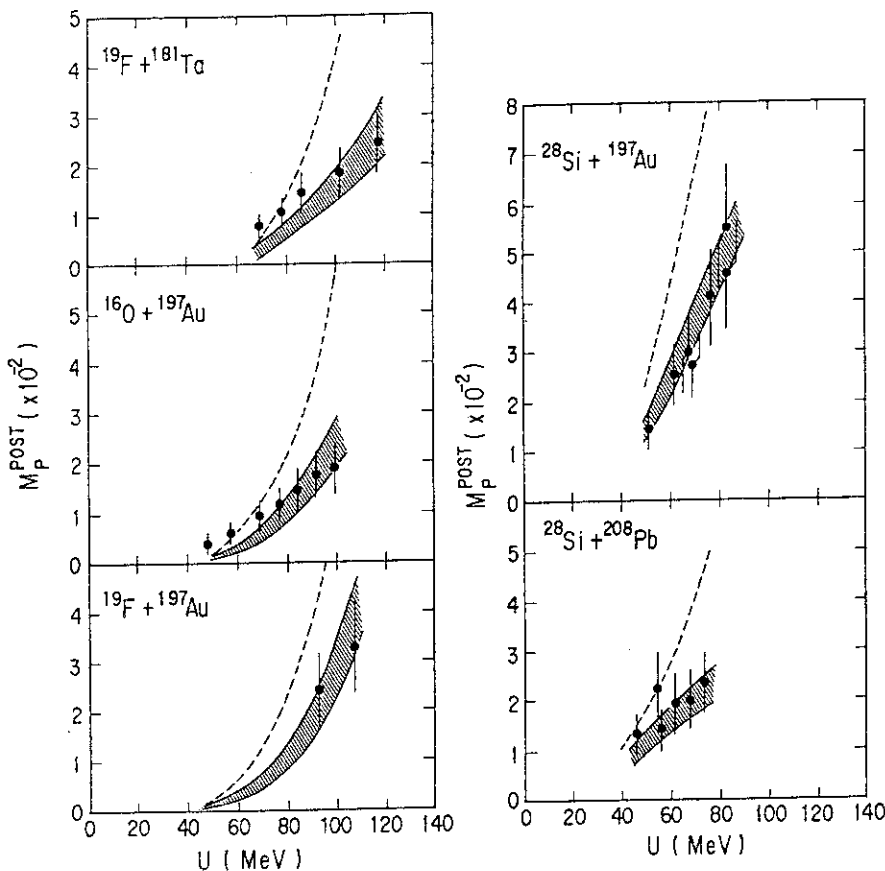
Fig.1 Post—scission proton multiplicities as a function of the compound nucleus excitation energy U. The reaction types and the fissility X of the compound nuclei are shown in the figure. The shaded areas and dashed lines are the two types of statistical model calculations (see text).
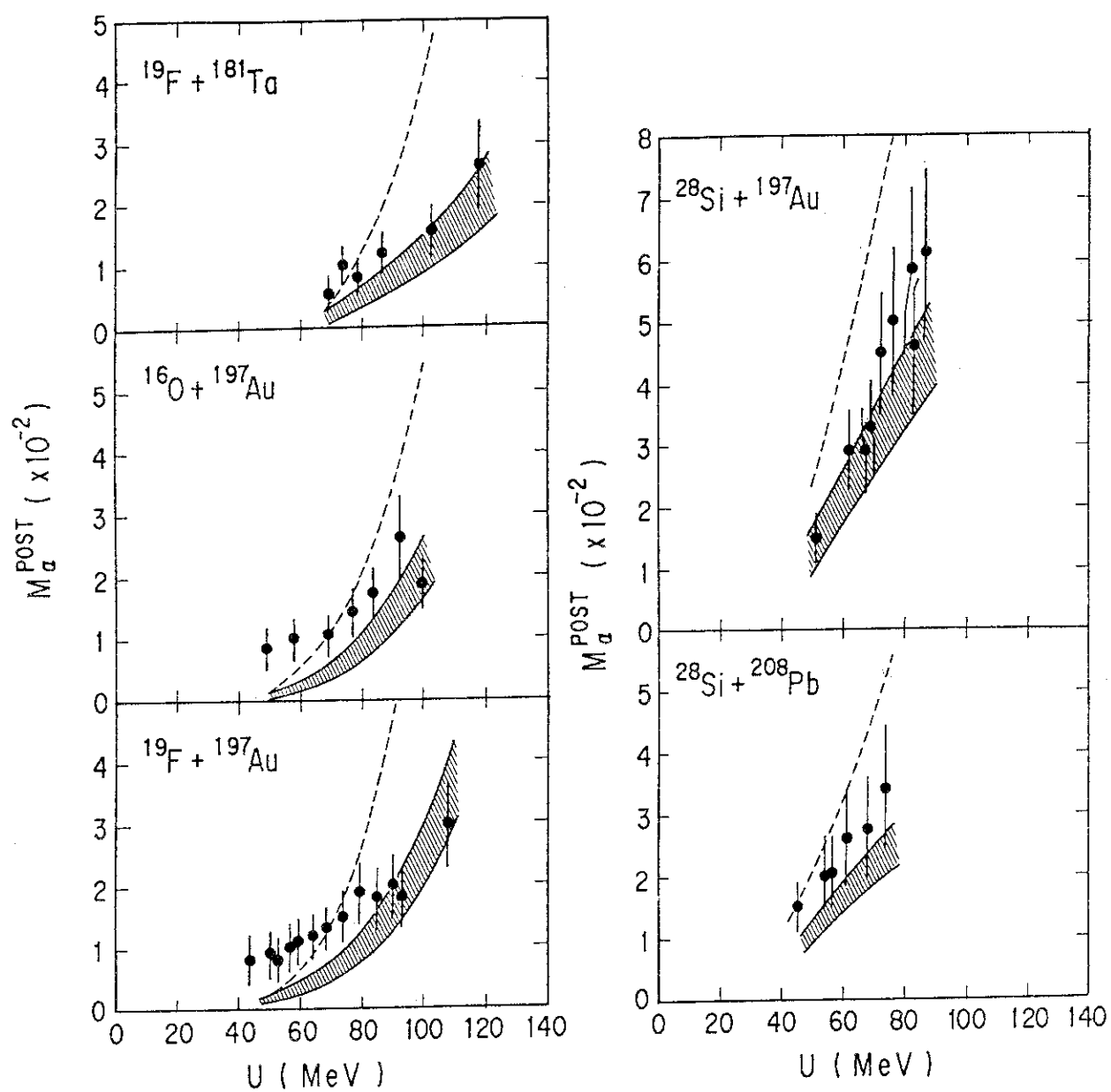
Fig.2 Same as Fig.1, but for the post—scission α particle multiplicities as a function of the compound excitation energy U.

5.7 Triaxial Deformation and the IBM

Michiaki SUGITA

Department of Physics, JAERI

There exists one–to–one correspondence between the states of the Davydov–Filippov (DF) model and the states belonging to the $\nu_\Delta = 0$ representation of the Wilets–Jean (WJ) model. The following relation gives this correspondence between the two models:

$$\tau(K) = I + \mod(I, 2) - \frac{K}{2}, \tag{1}$$

where I the angular momentum, τ the seniority quantum number of the WJ model, K the x-component of intrinsic I in the DF model. For given I, the WJ and DF states are related by eq. (1) in energy order. The $E2$ selection rules of the two models are given by $|\tau_i - \tau_f| = 1$ for the WJ model and $|K_i - K_f| = 2$ for the DF model. If these rules are satisfied, $E2$ transitions between i and f states occur for WJ and DF, respectively.

Differences in $E2$ between the two models can be found from eq. (1) as follows: Case (A) $E2$ transitions are allowed in DF but forbidden in WJ, when $|K_i - K_f| = 2$ and $|\tau_i - \tau_f| = 3$. An example is given by $E2(I = 4_1 \rightarrow 5_2)$; $K_i = 4, K_f = 2, \tau_i = 2, \tau_f = 5$. Case (B) $E2$ transitions are allowed in WJ but forbidden in DF, when $|K_i - K_f| = 6$ and $|\tau_i - \tau_f| = 1$. An example is given by $E2(I = 6_1 \rightarrow 4_3)$; $K_i = 6, K_f = 0, \tau_i = 3, \tau_f = 4$. In ref. 1 we have shown, based on the IBM, that, for a realistic N value, the γ–fixed and the γ–unstable wavefunctions overlap largely. Only when N is unrealistically large, these two wavefunctions differ significantly. Using the same procedure as in ref. 1, differences in $E2$ between γ–unstable and γ–rigid wavefunctions are investigated for the realistic situation. In table 1, the $E2$ values are compared between the O(6), $\gamma = 30°$, and the DF model for $E2(I = 4_1 \rightarrow 5_2)$ and $E2(I = 6_1 \rightarrow 4_3)$ at $N = 5$. This shows that the $E2$ transition for $\gamma = 30°$ is closer to that of the O(6) rather than to the DF result at realistic N.

Table 1 : Differences in $E2$ transition between the three models.

$E2$ transition	O(6)	$\gamma = 30°$	DF
$E2(I = 4_1 \rightarrow 5_2)$	0.000	0.001	1.581
$E2(I = 6_1 \rightarrow 4_3)$	0.920	0.917	0.000

Reference

1) M. Sugita, T. Otsuka and A. Gelberg, Nucl. Phys. **A498**(1989)350

5.8 Adiabatic Approximation in Multi-dimensional Tunneling Problem

Akira IWAMOTO and Yoshiaki TOMITA

Department of Physics, JAERI

1. Introduction

Calculation of the penetrability through a multi—dimensional potential barrier is not only an attractive problem in itself but also is a necessity to understand several quantum phenomena. A typical example is the nuclear fission in which we need several shape parameters to specify the potential energy surface. In Ref.1, we showed that the adiabatic path deviates little from the minimum action path and two action integrals are nearly the same. In this report, we will investigate why this happens and show that the adiabatic approximation is useful in fission study. The details of this report will be published in Ref.2.

2. Standard Coordinate System

In Ref.1, the adiabatic path is defined with the help of the equation,

$$M \frac{d\vec{q}}{ds} \mathbin{/\!/} \nabla V, \tag{1}$$

where M is mass tensor and s is an arbitrary parameter. This equation means that the path is determined from the condition that the momentum vector is directed to the gradient of the potential. To understand the characteristics of the adiabatic approximation, we first perform the coordinate transformation to a standard coordinate system. In a 2—dimensional case, where the essential part of the problem is seen clearly, we can prove the following theorem.

Theorem: By a local coordinate transformation, a region in (q^1, q^2)—space which does not contain the extreme point in potential $V(q^1, q^2)$, can be mapped onto a region in the (x^1, x^2)—space where

$$M_{12} = 0 \quad \text{and} \quad \frac{\partial V}{\partial x^2} = 0. \tag{2}$$

The proof is given in Ref.2. In a higher dimensional case, the theorem is partially generalized, in which potential is flat except for x^1 direction and mass tensors are diagonal along one solution of (1).

The definition of adiabatic path is as follows: Let the potential have a simple geometry
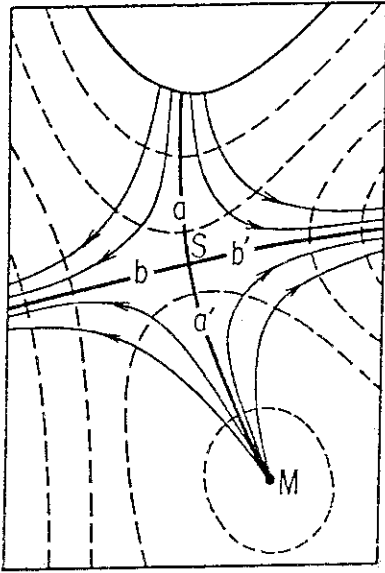
as llustrated in Fig.1., where one minimum (ground state) and one saddle point exist. The solution of (1) is given by the solid lines and there appear two separatrices which divide the whole space into 4 regions. According to the definition given in Ref.1, the adiabatic path is one of the separatrices a—a'.

Fig.1. Definition of the adiabatic path as one of the separatrices of the solution of (1). M is the minimum point and S is the saddle point of the potential. Separatrix a—a' is defined as the adiabatic path.

3. General Condition for the Application of the Adiabatic Approximation

We denote the unit of potential gradient field by $\vec{t}$,

$$\vec{t} = \frac{\nabla V}{|\nabla V|}.$$

(3)

The motion along this path is written as

$$\vec{p} = p\vec{t}$$

(4)

where $\vec{p}$ is the momentum in the inverted potential problem and p is its absolute value. We will consider the artificial motion of an object with the constraint that the object moves smoothly along the adiabatic path. We assume the eikonal equation which is obtained in the semiclassical treatment of the wave function[3],

$$\frac{1}{2} (\vec{p}, M^{-1}\vec{p}) = E + V.$$

(5)

Taking the derivative of eq.(4), we get the expression

$$\frac{d\vec{p}}{d\tau} = \nabla V + p \frac{1}{\sqrt{m}} \frac{d}{d\tau}(\sqrt{m}\,\vec{t}),$$

(6)

where we introduced an effective mass m by

$$\frac{1}{m} = (\vec{t}, M^{-1}\vec{t}) , \tag{7}$$

Changing the coordinate system to the standard coordinate, we can prove that a sufficient condition for the validity of the adiabatic approximation in this coordinate system is given by

$$M_{ii} = M_{ii}(q^1) , \tag{8}$$

which means that the diagonal masses in the standard coordinate depend only on the coordinate q^1 as is the same as the potential V. In the case of constant mass $(M = M_0)$, (6) can be rewritten as

$$\frac{d\vec{p}}{d\tau} = \nabla V + \frac{M_0 v^2}{R} \vec{n} . \tag{9}$$

where $\vec{n}$ is the principal normal of the path. The the second term of (9), which is the centrifugal force, stands for the additional force.

4. Plausibility of Adiabatic Approximation in Fission Decay

As was shown in Ref.1, determination of the path which gives the minimum action in multi-dimensional barrier penetration is reduced to finding a solution of classical Hamilton equation for the inverted potential with suitable boundary conditions. Adiabatic path approximates it under the conditions discussed in the previous section. Because of the complex coordinate dependence of the mass tensors in fission problem, general discussions alone are not sufficient and we will discuss the validity of the adiabatic approximation in the specific fission process in the followings.

First, we can show that near two end points of the minimum action path, the adiabatic approximation is good. For the end point, the discussion is simple because p become zero from the eikonal equation (5). For the initial point, the discussion is more complicated but if we assume the smooth behavior of mass tensor as a function of coordinate, we can prove that adiabatic path becomes good.

The major contribution to the action integral comes from the region near the saddle point. In this region the discussion given in Ref.4 is applicable for our purpose. If we can assume that the mass tensors do not change rapidly near the saddle point, which is the case if we calculate the mass classically, we can show that two separatrices are solutions of Euler equation near the saddle point. If we choose the adiabatic path (one of the separatrices) and follow it to inner and outer saddle directions until the value of the potential becomes sufficiently small, it satisfies again the Euler equation. It satisfies the correct boundary conditions as well. Between the saddle and two end points, no definite discussion is possible. We can expect, however, that the adiabatic path we defined will approximately satisfy the minimum action requirement.

5. Summary

We examined the validity of the adiabatic approximation for describing the spontaneous fission. The basic equation (1) of the method was found to be closely related to a special coordinate system in which mass tensors are diagonal and potential perpendicular to the adiabatic path is flat. The validity condition of the adiabatic approximation takes a simple form if one use the standard coordinate system.

Next, we investigated the minimum action path and path of the adiabatic approximation in fission life—time calculation. When the potential and mass tensors are assumed to be smoothly changing, we could show that the adiabatic path is a good approximation of the minimum action path. Since the numerical calculation of the adiabatic path is much easier than the determination of the minimum action path, this will be a good starting point for the search of the minimum action path.

In realistic calculations of spontaneous fission, the potential energy changes rather rapidly due to the shell effect. The mass tensors might show very complex structure. Thus the plausibility of the adiabatic approximation should be checked numerically in realistic cases. To this end, however, we must have a good method to calculate the mass tensor. Usual cranking model has a problem that the mass diverges at the single—particle level crossing. Even if we include the pairing correlation, we cannot eliminate all the divergence. Thus it is an urgent problem in this field to develop a reliable method to calculate the mass tensors by taking the nuclear structure effect into account.

REFERENCES
1) T. Kindo and A. Iwamoto, Phys.Lett.B225 (1989) 203.
2) A. Iwamoto and Y. Tomita, Prog. Theor. Phys. in press
3) A. Schmid, Ann. Phys. 170 (1986) 333.
4) M. Brack et al., Rev.Mod.Phys.44 (1972) 320.

5.9 Antiproton Production in p+A and A+A Collisions

Koji NIITA

Department of Physics, JAERI

The production of particles at energies below the free nucleon–nucleon threshold ("subthreshold production") constitutes potentially one of the most promising source of information about the properties of nuclear matter at high densities since the particles are produced predominantly during the compressed stage[1]. However, poor knowledge of the relevant elementary production vertices near the threshold energy and the complicated phase–space evolution of a high–energy nucleus–nucleus system have so far hindered a reliable interpretation of the data. It is, therefore, useful to study these in–medium processes also in proton–nucleus reactions where the nuclear phase–space distribution does not alter so drastically during the collision and nuclear density stays close to ρ_0.

Antiproton production at energies of a few GeV/u is the most extreme subthreshold process of all particle production processes. Recently, experiments performed at JINR[2] and at BEVALAC[3] have reported the first measurements of subthreshold antiproton production in nucleus–nucleus collisions. Varius descriptions of these data have been proposed. Based on thermal models it has been suggested that the antiproton yield contains large contributions from ΔN, $\Delta\Delta$ and $\rho\rho$ channels[4,5]. On the other hand, Shor et al. have shown in a first chance collision model[6] that the experimental antiproton spectra for p+A reactions can be described when using high momentum tail of the target distribution in line with data on backward proton scattering. However, the nucleus–nucleus data are underestimated by more than three orders of magnitude in this model.

We have reanalyzed this problem whithin a nonequilibrium transport approach that explicitly propagates nucleons (N), nucleon resonances (Δ, $N^*(1440)$) and pions with their isospin degrees of freedom[7]. The production of antiproton is treated perturbatively as described in[8] by including all baryon–baryon production channnels. As input for the elementary cross section we adopt the parametrization

$$\sigma_{pp\to\bar{p}+x}(\sqrt{s}) \approx 0.01 \ (\sqrt{s}-3.7532 \ \text{GeV})^{1.846} \ [\text{mb}] \tag{1}$$

that describes the available data ($\sqrt{s}$–4m > 1 GeV, where m denotes the nucleon mass) for this process very well. Since the extrapolation to threshold is rather arbitrary we have performed additional calculations involving upper and lower limits for the process (1) at $\sqrt{s}$–4m < 1 GeV [8]. Furthermore, due to lack of experimental data, we assumed the baryon–baryon production channels to give the same antiproton cross section (1) as a function of the invariant energy $\sqrt{s}$.

Our calculated results for p + ^{63}Cu are shown in Fig.1 in comparison to the data of Dorfan et al.[9] at $\theta = 0^O$ in the lab. frame for bombarding energies of 4.0, 4.55 and 6.1 GeV. We have indicated in the figure separetely the contributions of nucleon–nucleon collisions (dashed lines) and those of collisions involving also resonances (solid lines) at each bombarding energy. The relative contributions of nucleon resonances becomes more important with decreasing bombarding energy. Since we have only considered Δ and N^*(1440) resonances explicitly, the present results have to be taken as a lower limit. In order to demonstrate the sensibility of the antiproton yield to different extrapolations of the elementary cross section (1) to threshold, we show the results for 6.1 GeV by dotted lines in Fig. 1 which correspond to the lower and upper limits of the extrapolations adopted[8]. We note, that this uncertainty is about one order of magnitude at 6.1 GeV and become even larger at lower energy. Therefore, we have included only overall attenuation factor of 0.1 in the calculations which accounts for 90% antiproton reabsorption.

The calculated antiproton invariant cross section for the reaction ^{28}Si + ^{28}Si at 2.1 GeV/u is shown in Fig. 2 in comparison to the experimental data[3]. We again observe that the contribution due to collisions involving resonances (solid line) is a factor 10 larger than those involving only nucleons (dashed line) thus confirming one of the main results of ref. 4). The uncetainty for the total cross section due to upper and lower extrapolations of (1) to threshold is again indicated by the dotted lines in Fig. 2. Since its variation is about one order of magnitude, we do not attempt to include any direct estimate for reabsorption.

Whereas in p+A reactions the dominant yield of antiproton arises from first and secondary baryon collisions[8], these primary collisions play a negligible role for ^{28}Si + ^{28}Si at 2.1 GeV/u where the dominant contribution arises from resonance–resonance production, i.e. both baryons have at least scattered once before producing an antiproton in a mutual collision. Essential for this result is the presence of multiple–collision events.

However, it is very difficult to draw any definite conclusions from this case since the calculations neglected antiproton annihilation as well as other possibly important production channels such as $\rho\rho \rightarrow p\bar{p}$ or further cooperative phenomena.

Also, because of the very low bombarding energy in this experiment, the calculated results are extremely sensitive to the extraporation of the elementary production cross section (1) to threshold energies.

In order to draw more definite conclusion experimentally, Chiba et al. have started to measured antiproton cross section from p+A, d+A and α+A at 3 GeV/u to 5 GeV/u in KEK/PS[10]. By taking the ratios of antiproton yield from p+A, d+A and α+A reactions and comparing them with theoretical prediction, one can reduce the ambiguity of the elementary production cross section near threshold and also that of the reabsorption factor, since the nuclear phase—space distributions and nuclear density do not differ so drastically in these systems. In Fig. 3 we show our predictions of antiproton cross section at 4 and 5 GeV/u in these reactions. At 5 GeV/u, the momentum distributions of produced antiproton in these reactions have almost the same shape and the ratios of the yield are roughly proportional to that of projectile mass. This means that the dominant yield of antiproton arises from first baryon collisions since the bombarding energy is near to the free threshold. On the other hand, for the 4 GeV/u case, the shapes of the momentum distribution are quite different from each other and the yiels in the α induced reaction is very much enhanced compared with that of proton induced case. The antiproton yield from α+^{12}C at 1GeV/c is a factor 60 larger than that from p+^{12}C, and this huge enhancement is coming from the energy boost due to the baryon multiple collisions in our description. If our prediction could explain the newly coming data, one can discuss the effects of multiple scattering more qualitatively and if not, the experimental data might suggest unknown production mechanism, i.e. a coherent or cooperative production mechanism.

References

1) W. Cassing, V. Metag, U. Mosel and K. Niita: Phys. Rep. 188 (1990) 363

2) A.A. Baldin et al.: JETP Lett. 47 (1988) 137

3) J.B. Carrol et al.: Phys. Rev. Lett. 62 (1989) 1829

4) P. Koch and C.B. Dover: Phys. Rev. C40 (1989) 145

5) C.M. Ko and X. Ge: Phys. Lett. B205 (1988) 195

6) A. Shor et al.: Phys. Rev. Lett. 63 (1089) 2192

7) Gy. Wolf, G. Batko, W. Cassing, U. Mosel, K. Niita and M. Schaefer: Nucl. Phys. A517 (1990) 615

8) G. Batko, W. Cassing, U. Mosel, K. Niita and Gy. Wolf:
   Phys. Lett. B256 (1991) 331

9) D. Dorfan et al.: Phys. Rev. Lett. 14 (1965) 995

10) J. Chiba: private communication
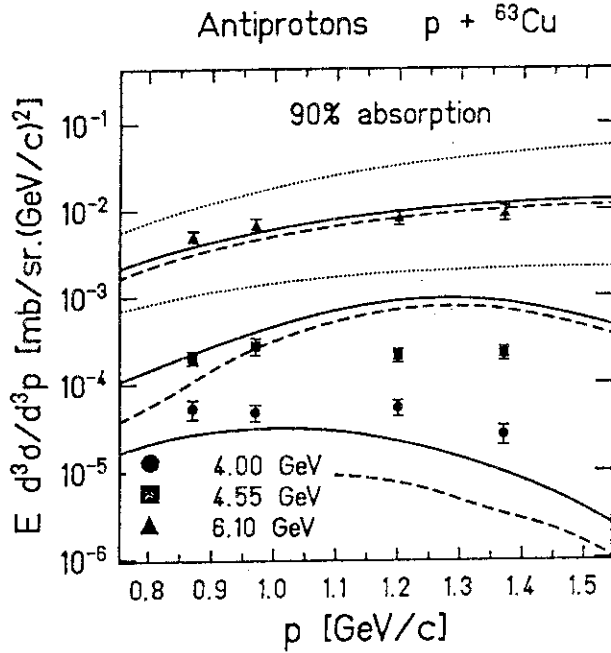
Fig. 1: Invariant $\bar{p}$ cross section for $p+{}^{63}Cu$ at 4.0, 4.55 and 6.1 GeV at $\theta=0°$ in comparison to the experimental data[9]. The dashed lines indicate the contribution from NN collisons only, while the solid lines include the contribution from collisions involving resonances. The dotted lines give the upper and lower limit of the cross sections due to different extrapolations of the elementary cross section (1) to threshold at 6.1 GeV incident eneergy.
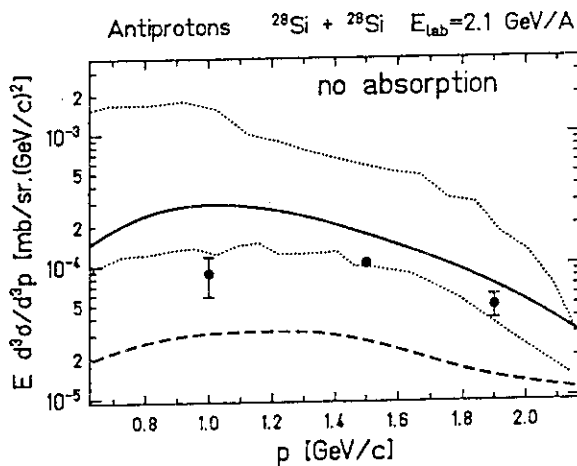
Fig. 2: Same as Fig. 1 for the reaction ${}^{28}Si+{}^{28}Si$ at 2.1 GeV/u in comparison to the data of ref. 3)

no reabsorption
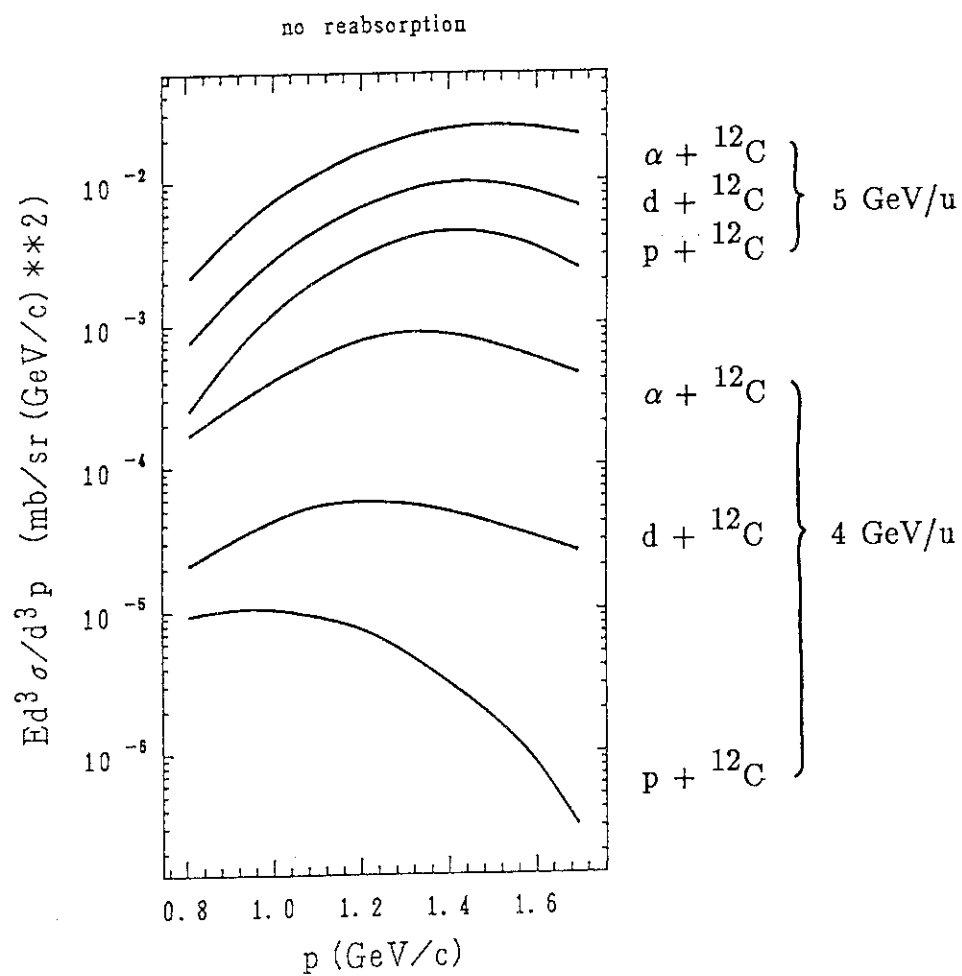
Fig. 3: Our predictions of invariant $\bar{p}$ cross section for p, d, α + ^{12}C reactions at 4.0 and 5.0 GeV/u at $\theta=0^{\circ}$.

VI PUBLICATION IN JOURNALS AND PROCEEDINGS

Publication in Journals and Proceedings

1. Aoto, A., Watanabe, Y., Hane, H., Kashimoto, H., Koyama, Y., Sakai,
   H., Yamanouti, Y., Sugimoto, M., Chiba, S. and Koori, N.
   Measurement of Double Differential Charged—Particle Emission Cross
   Sections for Reactions Induced by 20-40 MeV Protons
   Proc. of the 1991 Seminar on Nuclear Data, Nov. 28-29, 1991, Tokai,
   Japan

2. Batko, G., Cassing, W., Mosel, U., Niita, K. and Wolf, Gy.
   Antiproton Production in p—Nucleus and Nucleus—Nucleus Collisions
   Phys. Lett. B256 (1991) 331

3. Chiba, S., Guenther, P.T., Smith, A.B., Sugimoto, M. and Lawson, R.D.
   Fast—neutron Interaction with Elemental Zirconium and the Dispersive
   Optical Model
   Phys. Rev. C45 (1992) 1260

4. Chiba, S. and Smith, D.L.
   A Suggested Procedure for Resolving an Anomaly in Least—Squares Data
   Analysis Known as "Peele's Pertinent Puzzle" and the General Impli-
   cations for Nuclear Data Evaluation
   ANL/NDM-121, Sept. 1991.

5. Chiba, S., Yu, B. and Fukahori, T.
   Evaluation of JENDL Fusion File
   JAERI-M 92-027, (1992) p.35

6. Corradi, L., Napoli, D.R., Stefanini, A.M., Signorini, C., Sugiyama,
   Y., Ikezoe, H., Tomita, Y., Ideno, K., Kim, H.J., Nagashima, Y.,
   Masuda, T., Fujiwara, H., Pu, Y.H., Tagishi, Y., Sugimitsu, T. and
   Qi, B.
   A Study of Elastic Scattering and Inelastic Scattering Collisions of
   $^{58}Ni+^{90,94}Zr$ at Two Near-barrier Energies
   AIP Conference Proceedings 250 on Towards a Unified Picture of Nu-
   clear Dynamics, Nikko (1991) p.17

7. Ferragut, A., Murakami, T., Gono, Y., Nakajima, M., Seki, H., Ogawa,
   M., Min, B.J., Oshima, M., Morikawa, T., Kusakari, H., Morita, K.,
   Yoshida, A., Kumagai, H. and Zhang, Y.H.
   Coulomb Excitation of Unstable Nucleus Beam
   RIKEN Accel. Progr. Rep. Vol.25 (1991) p.50

8. Hannuscke, S., Cassing, W., Mosel, U. and Niita, K.
   Microscopic Analysis of Deeply Inelastic Heavy-ion Collisions
   Nucl. Phys. A535 (1991) 120

9. Hvelplund, P., Tawara, H., Komaki, K., Yamazaki, Y., Kuroki, K., Watanabe, H., Kawatsura, K., Sataka, M., Imai, M., Kanai, Y., Kambara, T. and Awaya, Y.
   Binary Encounter Peaks for 0° Electrons in Collisions between 2MeV/amu Si^{q+} and He, J. Phys. Soc. Jpn., 60 (1991) 3675

10. Iimura, H., Shibata, M., Ichikawa, S., Sekine, T., Oshima, M., Shinohara, N., Miyachi, M., Osa, A., Yamamoto, H. and Kawade, K.
    Level Scheme of ^{123}Ba Fed by the ^{123}La Decay
    J. Phys. Soc. Japan 60 (1991) 3585

11. Ikezoe, H., Shikazono, N., Nagame, Y., Ohtsuki, T., Sugiyama, Y., Tomita, Y., Ideno, K., Kanno, I., Kim, H.J., Qi, B.J., and Iwamoto, A.
    Nucl. Phys. A538 (1992) 299c

12. Ishii, T. and Booster Group
    The JAERI Tandem Booster Project
    JAERI-M 91-115 (1981) 1

13. Y. Ito et al.
    Brightness Enhanced Intense Slow Positron Beam Produced using an Electron Linac
    Nucl. Instrum. & Methods A305 (1991) 269

14. Iwamoto, A. and Herrmann, R.
    Evaporation of Charged Particles from Highly Deformed Nucleus
    Z. Phys. A338 (1991) 303

15. Iwamoto, A.
    Nuclear Physics with High Flux Proton Accelerator
    JAERI-M 91-095 (1991) 78

16. Iwamoto, A.
    Cold Fission, Bimodal Fission
    Hohshasen 17 (1991) 2

17. Iwamoto, A.
    High Energy Fission
    JAERI-M 92-039 (1992) 172

18. Iwamoto, A.
    Report on Tours International Symposium on Nucleus-Nucleus Collision
    KURRI-TR-360 (1992) 1

19. Iwamoto, A.
    Multi-Dimensional Tunneling and Nuclear Fission
    New Trends in Nuclear Collective Dynamics (Springer 1992, p125)

20. Iwase, A., Iwata, T., Nihira, T. and Sasaki, S.
Defect Recovery and Radiation Annealing in FCC Metals Irradiated
with High Energy Ions
Rad. Eff. and Defects in Solids 124 (1992) 117

21. Iwase, A., Masaki, N. Iwata, T. and Nihira, T.
Effect of 120 MeV Oxygen Ion Irradiation on I—V Characteristics in
YBaCuO
Mat. Res. Soc. Symp. Proc. 209 (1991) 847

22. Iwase, A., Iwata, T., Nihira, T. and Sasaki, S.
Defect Recovery in FCC Metals Irradiated with 0.5–126 MeV Energetic
Ions
Materials Science Forum 97–99 (1992) 605

23. Iwata, T. and Iwase, A.
Radiation Annealing in Ni and Cu by Heavy Ion Irradiation
Nucl. Instrum. Meth. B61 (1991) 436

24. Kadar, I., Altevogt, H., Kohrbruck, R., Montemayor, V., Mattis, A.,
Schiwietz, G., Skogvall, B., Sommer, K., Stolterfoht, N., Kawatsura,
K., Sataka, M., Nakai, Y., Naramoto, H., Kanai, Y., Kambara, T.,
Awaya, Y., Komaki, K. and Yamazaki, Y.
High Resolution Auger Spectroscopy of Na–like Argon and Sulfur Ions
Singly Excited in High Energy Collisions with Light Target Atoms,
Phys. Rev. A44 (1991) 2900

25. Kanno, I.
Incident Angle Dependence of Residual Defect in Silicon Surface
Barrier Detector
J. Nucl. Sci. & Technol. 28 (1991) 582

26. Kanno, I.
Feasibility Stydy of Silicon Surface Barrier Detector as Charged
Particle Identifier
J. Nucl. Sci. & Technol. 28 (1991) 1061

27. Kanno, I.
Heavy Ion Induced Phenomena in Silicon Surface Barrier Detector and
Single Event Phenomena
Hoshasen, 17 (1991) 66

28. Kawatsura, K., Sataka, M., Naramoto, H., Imai, M., Komaki, K.,
Yamazaki, Y., Kuroki, K., Kanai, Y., Kambara, T., Awaya, Y., Hansen,
J.E., Kadar, I. and Stolterfoht, N.
High–Rydberg and Auger Electrons from Fast Projectile Ions Studied

by Zero-degree Electron Spectroscopy

Nucl. Instrum. & Methods B53 (1991) 421

29. Komaki, Y. and Ishikawa, N.

    Pattern Formation on Polyimide using Irradiation by Heavy Ion and
    the Subsequent Etching

    JAERI-M 92-036, Department of Chemistry Progress Report, 284-288,
    Mar. (1992)

30. Mashiko, K., Shoji, T., Ishizaki, N., Tayama, H. and Yokomizo, H.

    States of JAERI Linac

    Proceedings of the 16th Linear Accelerator Meeting in Japan (1991) 4

31. Matsumoto, Y., Matsuura, Y., Hibino, Y., Iwata, K., Komaki, Y.,
    Ishikawa, N., Sakurai, T. and Tachikawa, E.

    Ion Beam Radiation Effects on Polyimide Films

    Proc. Int. Conf. on Evolution by Beam Applications, Takasaki, Nov. 5
    (1991)

32. McGowan, F.K., Johnson, N.R., Lee, I.Y., Baktash, C., McConnel, J.W.,
    Rao, M.N., Oshima, M., Wells, J.C., Larabee, A., Riedinger, L.L.,
    Bengtsson, R. and Xing, Z.

    Nucl. Phys. A530 (1991) 490

33. Mizusaki, T., Otsuka, T. and Sugita, M.

    M1 Excitation in Sm Isotopes and Proton and Neutron sdg Interacting
    Boson Model

    Phys. Rev. C44 (1991) R1277

34. Murakami, T., Gono, Y., Ferragut, A., Zhang, Y.H., Nakajima, M.,
    Seki, H., Ogawa, M., Min, B.J., Oshima, M., Morikawa, T., Kusakari,
    H., Morita, K., Yoshida, A. and Kumagai, H.

    High Spin Isomers in ^{144}Pm Observed in the ^{14}N(^{136}Xe,6n) Reaction

    RIKEN Accel. Progr. Rep. Vol.25 (1991) p.48

35. Niita, K.

    Heavy-Ion Reaction at Intermediate Energy

    JAERI-M 91-115 (1991) 59

36. Niita, K.

    Present Status of Intermediate Heavy-Ion Collisions

    Proc. Riken Symp. on Heavy-Ion Reaction (1991) 8

37. Niita, K.

    High and Intermediate Heavy-Ion Collisions: Present State and Problems

    Soryuushiron Kenkyuu 84 (1992) 224

38. Niita, K.

Simulations for Heavy-Ion Collisions

Genshikaku Kenkyuu $\underline{36}$ (1992) 43

39. Niita, K.

Dynamical Simulation of Heavy-Ion Collisions, VUU and QMD Method

JAERI-M 92-039 (1992) 189

40. Noda, K.

Studies of Irradiation Effects on Lithium and Tritium Transport in

Ceramic Breeder by Ionic Conductivity Measurements

Proc. Int. Workshop on Ceramic Breeder Blanket Interactions (Clear-

water, October 22-23, 1991) p.30-36

41. Noda, K., Ishii, Y., Matsui, H., Ohno, H. and Watanabe, H.

Electrical Conductivity of Li_2O under and after Irradiation

J. Nucl. Mater., $\underline{179-181}$ (1991) 835

42. Noda, K.

Radiation Damage and Irradiation Effects in Solid Breeders

J. Nucl. Mater., $\underline{179-181}$ (1991) 37

43. Noda, K., Ishii, Y., Nakazawa, T., Matsui, H., Vollath, D. and

Watanabe, H.

Model Experiments for Tritium Behavior in Pure and Al-doped Lithium

Orthosilicate by Using Ionic Conductivity Measurements

Fusion Engrg. Des. $\underline{17}$ (1991) 55

44. Ohtsuki, T., Nagame, Y., Tsukada, K., Shinohara, N., Baba, S.,

Hashimoto, K., Nishinaka, I., Sueki, K., Hatsukawa, Y., Hata, K.,

Sekine, T., Kanno, I., Ikezoe, H. and Nakahara, H.

Mass Yield Curves in Low-energy Proton-induced Fission of ^{233}U, ^{235}U,

^{236}U, ^{237}Np, ^{239}Pu, ^{242}Pu, ^{244}Pu, ^{241}Am, ^{243}Am

Phys. Rev. C44 (1991) 1405

45. Ohtsuki, T., Ikezoe, H., Nagame, Y., Tsukada, K. and Nakahara H.

Proceedings of the International Workshop on Dynamical Aspects of

Nuclear Fission, Chechoslovakia, June (1991)

46. Ono, F., Lu Bang, Matsumoto, N., Maeta, H., Haruna, K. and Shen, Q.Y.

Irradiation Effects in High Permeability Amorphous Materials

Proc. International Colloquium on Magnetic Films and Surfaces

(Glasgow, 26-30, 1991 p.74-75)

47. Oshima, M., Gono, Y., Murakami, T., Kusakari, H., Sugawara, M.,

Morita, K., Yoshida, A. and Kumagai, H.

Observation of Coulomb Excitation of Unstable Nucleus - Utilization

of a Secondary Beam —

Nucl. Instrum. & Methods A312 (1992) 425

48. Roux, N., Johnson, C.E. and Noda, K.

Properties and Performance of Tritium Breeding Ceramics

J. Nucl. Mater., 191-194 (1992), in press.

49. Sugiyama, Y.

Recent Topics on Heavy-ion Nuclear Reactions in Tandem Energy Region

Proceedings of the Specialists' Meeting on High Energy Nuclear Data,

JAERI-M 92-039 (1992) 82

50. Yamanouti, Y.

Experimental Work and Facilities in Japan

Proc. of the NEANDC Specialists' Meeting on Neutron Cross Section

Standards for Energy Region above 20 MeV, May 21-23, 1991, Uppsala,

Sweden

Contributions to Scientific and Technical Meetings

1. Aoto, A., Watanabe, Y., Hane, H., Kashimoto, H., Koyama, Y., Sakaki,
   Y., Yamanouti, Y., Sugimoto, M., Chiba, S. and Koori, N.
   Measurement of Double Differential Charged-Particle Emission Cross
   Sections for Reactions Induced by 20-40 MeV Protons
   The 1991 Seminar on Nuclear Data in JAERI (Nov. 28-29, 1991)

2. Aruga, T., Takamura, S., Nakata, K., Itoh, Y. and Hirose, M.
   Defect Distribution in Ion-Irradiated Stainless Steel by Positron
   Beam
   Fall Meeting of Japan Institute of Metals in Hiroshima (Oct. 1-3,
   1991)

3. Lu Bang, Matumoto, N., Maeta, H., Jakubovics, J.P., Haruna, K. and
   Ono, F.
   High Energy Ion Irradiations in Fe-B-Si-C Amorphous Alloys
   Spring Meeting of the Physical Society of Japan in Yokohama (Mar.
   27-30, 1992)

4. Chiba, S., Takahashi, A., Klein, H. and Smith, A.B.
   Neutron Scattering: Technological Achievements and Illustrative
   Results
   Int. Conf. on Nuclear Data for Science and Technology in Jülich,
   Germany (May 13-17, 1991)

5. Chiba, S., Sugimoto, M., Ikeda, Y. and Yamanouti, Y.
   Study of Fast Neutron Cross Sections at JAERI Tandem Accelerator
   Beijing International Symposium on Fast Neutron Physics, Beijing
   (Sept. 9-13, 1991)

6. Chiba, S., Yu, B. and Fukahori, T.
   Evaluation of the Double-differential Cross Sections for JENDL
   Fusion File
   IAEA Research Co-ordination Meeting on "Measurement and Analysis of
   14 MeV Neutron-Induced Double-Differential Neutron Emission Cross
   Sections Needed for Fission and Fusion Reactor Technology, Chiang
   Mai (March 31 - April 2, 1992)

7. Chiba, S., Guenther, P.T., Smith, A.B., Sugimoto, M. and Lawson, R.D.
   Neutron Scattering Cross Sections of Zr and the Optical Model
   Potential
   Fall Meeting of Atomic Energy Society of Japan in Fukuoka
   (Oct. 15-18, 1991)

8. Chiba, S., Yu, B. and Fukahori, T.
Evaluation of JENDL Fusion File and its Status
Spring Meeting of Atomic Energy Society of Japan in Hiratsuka
(March 28-30, 1992)

9. Fujita, H., Kato, N., Sugimitsu, T., Funatsu, Y. Okamoto, T., Niiya,
S., Sugiyama, Y., Ikezoe, H., Tomita, Y., Ideno, K., Tanaka, M.H.
and Kubono, S.
Inelastic Scattering of ^{19}F on ^{28}Si at 120 and 155 MeV
4-th Int. Comf. on Nucleus-Nucleus Collisions, Kanazawa (1991)

10. Hatsukawa, Y., Hoffman, D.C. and Nakahara, H.
Alpha Decay Systematics
Spring Meeting of American Chemical Society in Atlanta (April 19,
1991)

11. Ikezoe, H., Shikazono, N., Nagame, Y., Ohtsuki, T., Sugiyama, Y.,
Tomita, Y., Ideno, K., Kanno, I., Kim, H.J., Qi, B.J. and Iwamoto, A.
Charged Particle Emissions in Fission Process
Riken Symposium in Wako (Jan. 28-29, 1992)

12. Ikezoe, H.
Tandem-Booster Project in Genken
Riken Symposium in Wako (Jan. 28-29, 1992)

13. Ishii, T., Ichii, M., Saito, Y., Nakajima, M. and Ogawa, M.
Nuclear Structure of ^{107}Sn
Autumn Meeting of Physical Society of Japan in Sapporo (Oct., 1991)

14. Ishii, T.
In-beam γ-ray Experiments at JAERI
Symposium on In-beam γ-ray Spectroscopy with Heavy-ions at RIKEN
(Aug. 6, 1991)

15. Ishikawa, N., Iwase, A., Iwata, T. and Yoshizaki, R.
Ion Irradiation Effects in Y-Ba-Cu-O High-T_c Superconductor
Spring Meeting of the Physical Society of Japan in Yokohama
(Mar. 27-30, 1992)

16. Ito, Y. et al.
Intense Brightness Enhanced Positron Beam from an Electron Linac and
its Applications
9th Intern. Conf. Positron Annihilation (Aug. 1991)

17. Iwamoto, A. and Niita, K.
Subbarrier Fusion and Renormalization of Optical Potential
4-th International Conference on Nucleus-Nucleus Collision
in Kanazawa (June 10-14, 1991)

18. Iwamoto, A. and Herrmann, R.

    Evaporation of Charged Particles Accompanying Fission

    4-th International Conference on Nucleus-Nucleus Collision

    in Kanazawa (June 10-14, 1991)

19. Iwamoto, A.

    Charged-Particle Evaporation in Fission Process

    Tours International Symposium on Nuclear Physics in Tours

    (Aug. 29-31, 1991)

20. Iwamoto, A.

    Subbarrier Fusion and Renormalization of Optical Potential

    Scientific Meeting on Nucleon-Nucleon Correlation in Nuclei in Tokyo

    (Sep. 13-14, 1991)

21. Iwamoto, A. and Niita, K.

    Subbarrier Fusion and Optical Potential

    Fall Meeting of Physical Society of Japan in Sapporo (Sep. 27-30,

    1991)

22. Iwamoto, A.

    Multi-Dimensional Tunneling and Nuclear Fission

    Scientific Meeting ISQM-Tokyo '92 in Tokyo (Nov. 21-22, 1991)

23. Iwamoto, A.

    Calculation of Fission Life-Time

    Scientific Meeting on Halo Nucleus in Kyoto (Nov. 28-30, 1991)

24. Iwamoto, A.

    On Fission Path

    RIKEN Symposium on Reaction and Structure of Unstable Nuclei in Wako

    (Jan. 27-29, 1992)

25. Iwamoto, A.

    Adiabatic Base and Adiabatic Approximation

    Scientific Meeting on Halo Nucleus in Sendai (Feb. 3-4, 1992)

26. Iwase, A., Iwata, T. and Nihira, T.

    Dependence of Irradiation Damage on Specimen Thickness in Ion-

    Irradiated Cu and Ni

    Fall Meeting of Physical Society of Japan in Sapporo (Sep. 27, 1991)

27. Iwase, A.

    Irradiation Damage by High Energy Ions in Metals and Effect of

    Electron Excitation

    Fall Meeting of Physical Society of Japan in Sappro (Sep. 27, 1991)

28. Iwase, A., Iwata, T. and Nihira, T.
Defect Production Rate in Ion-Irradiated FCC Metals
Spring Meeting of Physical Society of Japan in Hiyoshi
(March 30, 1992)

29. Izumo, M., Shigeta, N., Hashimoto, K., Kobayashi, K., Hatsukawa, Y.,
Matsuoka, H. and Sekine, T.
Production of ^{139}Ce with the ^{139}La(p,n) Reaction
The 35th Symposium on Radiochemistry in Osaka (Oct. 2, 1991)

30. Izumo, M., Sekine, T., Motoishi, S., Matsuoka, H., Kobayashi, K.,
Hashimoto, K., Hatsukawa, Y., Shigeta, N., Miura, F., Sorita, T.,
Moriya, T., Kudo, H. and Umezawa, H.
Radioisotope Production Facilities Utilizing Ion Beams from AVF
Cyclotron
Int. Conf. on Evolution in Beam Applications in Takasaki
(Nov. 5-8, 1991)

31. Kanno, I.
Feasibility Study of Particle Identification with Si Surface Barrier
Detector
1991 Fall Meeting of the Atomic Energy Society of Japan
(Oct. 15-18, 1991)

32. Kanno, I.
Single Event Phenomena in View of Detector Physics
International Workshop on Radiation Effects of Semiconductor Devices
for Space Application, Takasaki Radiation Chemistry Research
Establishment, JAERI (Feb. 25-26, 1992)

33. Kanno, I., Kanazawa, S. and Kimura, I.
Measurements of Plasma Delay in Si Surface Barrier Detector
1992 Annual Meeting of the Atomic Energy Society of Japan
(Mar. 28-30, 1992)

34. Kazumata, Y. and Okayasu, S.
Ion Irradiation Effects of High Tc Materials
Spring Meeting of Physical Society of Japan (Hiroshi, April 30, 1992)

35. Kazumata, Y.
What is the Effective Pinning Defects Induced by Irradiation?
New Superconductive Material Forum: 14th Symposium (Tokyo, January
28, 1992)

36. Kim, H.J., Sugiyama, Y., Ideno, K., Ikezoe, H., Qi, B., Tomita, Y.,
Fujita, H., Nagashima, Y. and Sugimitsu, T.

Evolution of Reaction Mechanism between the $^{74}Ge+^{45}Sc$ and ^{51}V Systems near the Barrier

4-th Int. Conf. on Nucleus-Nucleus Collisions, Kanazawa

(June 10-14, 1991)

37. Kumakura, H., Kitaguchi, H., Togano, K., Maeda, H., Kase, J., Morimoto, T., Okayasu, S. and Kazumata, Y.

Effect of Cu and Br Ion Irradiation on Textured $Bi_2Sr_2CaCu_2O_8$

Fall Meetings of Japan Institute of Metals in Hiroshima

(Oct. 1-3, 1991)

38. Kumakura, H., Ikeda, S., Kitaguchi, H. Togano, K., Maeda, H., Kase, J., Morimoto, T., Okayasu, S. and Kazumata, Y.

Effect of Ion Irradiation on Textured Bi(2212)

Fall Meetings of Cryogenic Society of Japan in Kobe (Nov. 25-27, 1991)

39. Kumakura, H., Chenevier, B., Ikeda, S., Kitaguchi, H., Togano, K., Maeda, H., Kase, J., Morimoto, T., Okayasu, S. and Kazumata, Y.

Ion and Electron Irradiation on Bi(2212) Oxide Superconductor

Spring Meeting of the Japan Society of Applied Physics in Narashino

(March 28-31, 1992)

40. Maeta, H., Lu, B., Haruna, K. and Ono, F.

Radiation Effects of Heavy Ion-irradiated Synthetic Diamond by X-ray Measurements

Spring Meeting of the Physical Society of Japan in Yokohama

(Mar. 27-30, 1992)

41. Mizusaki, T., Otsuka, T. and Sugita, M.

M1 Excitation of the 1+ States in Sm and sdg IBM-2

Autumn Meeting of the Physical Society of Japan in Sapporo

(Sep. 27, 1991)

42. Mukae, T., Fujita, H., Okamoto, T., Niiya, S., Matsuo, M., Mitsuoka, S., Utsunomiya, K., Sugiyama, Y., Tomita, Y., Ideno, K., Ikezoe, H., Yamanouchi, Y., Sugimitsu, T., Kato, N. and Morinobu, S.

Measurement for Spin Alignment of $^{12}C(2^+)$ for O + C System around $E_{cm}=32MeV$

The 47th Annual Meeting of the Physical Society of Japan

(Mar. 27-30, 1992)

43. Niita, K.

Subthreshold Meson Production in Heavy-Ion Collisions

Fourth International Conference on "Nucleus-Nucleus Collisions",

in Kanazawa (June 10-14, 1991)

44. Niita, K.

    Effective Interaction in VUU

    Riken Molecule on "Microscopic Approach to Heavy-Ion Collisions"

    in Kyoto (Oct. 2-3, 1991)

45. Niita, K.

    Dynamical Simulation of Heavy-Ion Collisions; VUU and QMD Method

    Specialists' Meeting on High Energy Nuclear Data

    in JAERI (Oct. 3-4, 1991)

46. Niita, K.

    Simulations for Heavy-Ion Collisions

    INS Meeting on Nuclear Reaction Models from Technological Viewpoints

    in INS (Dec. 17-18, 1991)

47. Niita, K.

    Event Simulators for Medium and High Energies

    Riken Symposium on High Energy Heavy-Ion Collisions

    in RIKEN (Jan. 23, 1992)

48. Niita, K.

    Subthreshold Particle Production in Heavy-Ion Collisions

    Riken Meeting on New Results of Riken Accelerator Facilities

    in RIKEN (Jan. 27, 1992)

49. Niita, K.

    Review on Subthreshold Particle Production

    RCNP Workshop on Critical Review of Particle Production

    in RCNP (March 6-7, 1992)

50. Niita, K.

    Antiproton Production in p+A, d+A and α+A at 4, 5 GeV/u

    Spring Meeting of Physical Society of Japan

    in Yokohama (March 27-30, 1992)

51. Nitani, Y., Yano, D., Takahashi, N., Baba, H. and Shinohara, N.

    Fission of the ^{238}U + p System in the Giant Dipole Resonance Region

    The 35th Symposium on Radiochemistry in Osaka (Nov. 1-3, 1991)

52. Nitani, N., Yamaguchi, T., Yano, D., Takahashi, N., Baba, H. and

    Shinohara, N.

    Fission of the ^{238}U + p System in the Giant Dipole Resonance Region

    The 63th Spring Annual Meeting of the Chemical Society of Japan in

    Osaka (March 28-31, 1992)

53. Noda, K., Ishii, Y., Nakazawa, T., Matsui, H., Vollath, D. and

    Watanabe, H.

Model Experiments for Tritium Behavior in Pure and Al-doped Lithium
Orthosilicate by Using Ionic Conductivity Measurements
2nd Int. Symposium on Fusion Nuclear Technology in Karlsruhe,
Germany (June 2-7, 1991)

54. Noda, K., Nakazawa, T., Ishii, Y., Matsui, H., Watanabe, H. and
Vollath, D.
Radiation Damage in Li_4SiO_4 and Al-doped Li_4SiO_4
Fall Meeting of Atomic Energy Society of Japan in Fukuoka
(Oct. 15-17, 1991)

55. Noda, K., Ishii, Y., Nakazawa, T., Matsui, H., Igawa, N., Vollath,
D., Ohno, H. and Watanabe, H.
Radiation Damage in Pure and Al-doped Li_4SiO_4
5th Int. Conf. on Fusion Reactor Materials in Clearwater, USA
(Oct. 17-22, 1991)

56. Noda, K.
Studies of Irradiation Effects on Lithium and Tritium Transport in
Ceramic Breeder by Ionic Conductivity Measurements
Proc. Int. Workshop on Ceramic Breeder Blanket Interactions in
Clearwater, USA (Oct. 22-23, 1991)

57. Ohtsuki, T., Nagame, Y., Ikezoe, H., Tsukada, K., Nishinaka, I.,
Sekine, T., Nakahara, H.
Structure for Kinetic Energy Distribution with Fission of Light
Actinides
The 35th Symposium on Radiochemistry in Osaka (Nov. 1-3, 1991)

58. Oshima, M., Sekine, T., Ichikawa, S., Hatsukawa, Y., Nishinaka, I.,
Morikawa, T. and Iimura, H.
Development of a Laser-Enhanced Ion-Guide Ion Source
The 12th International Conference on Electromagnetic Isotope
Separators and Techniques Related to Their Applications
(Sendai, Sept. 2-6, 1991)

59. Oshima, M.
Development of a Laser-Enhanced Ion-Guide Ion Source
International Symposium on Lasers in Nuclear Physics (Saitama,
Sept. 9-10, 1991)

60. Roux, N., Johnson, C.E. and Noda, K.
Properties and Performance of Tritium Breeding Ceramics
5th Int. Conf. on Fusion Reactor Materials in Cleawater, USA
(Oct. 17-22, 1991)

61. Sekine, T., Ichikawa, S., Morikawa, T., Oshima, M., Osa, A., Hatsukawa, Y., Iimura, H. and Shinohara, N.
   Decay of ^{122}La: Structure of the ^{122}Ba Nucleus
   The 35th Symposium on Radiochemistry in Osaka (Oct. 2, 1991)

62. Sekine, T., Ichikawa, S., Oshima, M., Iimura, H., Morikawa, T., Osa, A., Chung, W.H. and Hatsukawa, Y.
   Decay Spectroscopy of ^{122,124,126}La Isotopes by Means of Heavy-Ion Reaction and Isotope Separator On-Line
   Int. Conf. on Evolution in Beam Applications in Takasaki (Nov. 5-8, 1991)

63. Sekine, T., Ichikawa, S., Oshima, M., Iimura, H., Morikawa, T., Osa, A., Chung, W.H. and Hatsukawa, Y.
   Measurement of Beta-Ray Maximum Energy for Short-Lived Nuclei with an HPGe Detector
   Int. Conf. on Evolution in Beam Applications in Takasaki (Nov. 5-8, 1991)

64. Shinohara, N., Ichikawa, S., Magara, M., Tsukada, K. and Ohtsuki, T.
   Gamma-Ray Measurement of Short-Lived Ruthenium Isotopes Separated by SISAK
   The 35th Symposium on Radiochemistry in Osaka (Nov. 1-3, 1991)

65. Stefanini, A.M., Napoli, D.R., Corradi, L., Signorini, C., Sugiyama, Y., Ikezoe, H., Tomita, Y., Ideno, K., Kim, H.J., Masuda, T., Fujiwara, H., Pu, Y.H., Tagishi, Y., Sugimitsu, T. and Qi, B.
   Elastic and Inelastic Scattering of ^{58}Ni+^{90,94}ZR near the Coulomb Barrier
   4th Int. Conf. on Nucleus-Nucleus Collisions, Kanazawa (June 10-14, 1991)

66. Sugita, M., Gelberg, A. and Otsuka, T.
   Triaxial Deformation and the IBM
   RIFP Meeting in Kyoto (Jan. 9, 1992)

67. Sugita, M., Gelberg, A. and Otsuka, T.
   Triaxial Deformation and the IBM
   Spring Meeting of the Physical Society of Japan in Yokohama (Mar. 28, 1992)

68. Sugiyama, Y., Tomita, Y., Ikezoe, H., Ideno, K., Kato, N., Sugimitsu, T., Okamoto, T., Niiya, S., Funatsu, Y., Matsuo, M., Mitsuoka, S., Mukae, T. and Fujita, H.
   Spin Alignment of ^{12}C(2^+ 4.44MeV) State in ^{16}O+^{12}C Inelastic

Scattering

4-th Int. Conf. on Nucleus—Nucleus Collisions, Kanazawa

(June 10-14, 1991)

69. Sugiyama, Y., Tomita, Y., Ikezoe, H., Ideno, K., Kato, N., Sugimitsu, T. and Fujita, H.

Transfer Reactions for $^{16}O+^{144,152}Sm$ near the Coulomb Barrier

4-th Int. Conf. on Nucleus—Nucleus Collisions, Kanazawa

(June 10-14, 1991)

70. Sugiyama, Y.

Spin Alignment of the Single and Mutual Excitations in Inelastic Scattering

INS Sympsoium (Dec. 24, 1991

71. Sugiyama, Y.

Heavy—Ion Reactions with JAERI Tandem Accelerator

Seminar at China Institute of Atomic Energy, Beijing, China

(Aug. 19, 1991)

72. Sugiyama, Y.

High Resolution Works on Heavy—Ion Reactions

Seminar at Institute of Modern Physics, Lanzhou, China (Aug. 29, 1991)

73. Sugiyama, Y.

Heavy—Ion Reactions with JAERI Tandem Accelerator

Seminar at Shanghai Institute of Nuclear Research, Shanghai, China

(Aug. 29, 1991)

74. Sugiyama, Y., Tomita, Y., Ikezoe, H., Ideno, K., Corradi, L., Napoli, D.R., Stefanini, A.M., Signorini, C., Kim, H.J. Nagashima, Y., Masuda, T., Fujiwara, H. Pu, Y.H., Tagishi, Y., Sugimitsu, T. and Qi, B.

A Study of Elastic Scattering and Inelastic Scattering Collisions

of $^{58}Ni+^{90}Zr$ near the Coulomb Barrier

Fall Meeting of the Physical Society of Japan in Sapporo

(Sep. 27-29, 1991)

75. Takeuchi, S.

Superconducting FF Activities at JAERI

The 5th Workshop on RF Superconductivity, Hamburg (Aug. 19-23, 1991)

76. Takeuchi, S., Ishii, T., Min, B.J. and Shibata, M.

Superconducting Resonators for Heavy Ion Acceleration at JAERI

The 5th Workshop on RF Superconductivity, Hamburg (Aug. 19-23, 1991)

77. Tsukada, K., Sueki, K., Nishinaka, I., Tanikawa, M., Nakahara, H., Shinohara, N., Ichikawa, S. and Hoshi, M.

Extremely Mass Division Produced on Proton-Induced Fission of Actinides

The 35th Symposium on Radiochemistry in Osaka (Nov. 1-3, 1991)

78. Watanabe, Y., Aoto, A., Hane, H., Yamanouti, Y., Sugimoto, M. and Chiba, S.

^{98}Mo(p,xp) and (p,xd) Reactions at E_p=25.6 MeV

Fall Meeting of Atomic Energy Society of Japan in Fukuoka (Oct. 15, 1991)

79. Watanabe, Y., Aoto, A., Hane, H., Yamanouti, Y., Sugimoto, M. and Chiba, S.

Measurements of Charged-Particle Nuclear Data Using JAERI Tandem(I)

Autumn Meeting of the Atomic Energy Society of Japan in Fukuoka (Oct. 15-18, 1991)

80. Yamanouti, Y., Sugimoto, M., Chiba, S., Mizumoto, M., Hasegawa, K. and Watanabe, Y.

Scattering of 28.2 MeV Neutrons from ^{12}C and 18.5 MeV Neutrons from ^{52}Cr and ^{60}Ni

Int. Conf. on Nuclear Data for Science and Technology in Jülich, Germany (May 13-17, 1991)

81. Yamanouti, Y.

Experimental Work and Facilities in Japan

NEANDC Specialists' Meeting on Neutron Cross Section Standards for Energy Region above 20 MeV in Uppsala, Sweden (May 21-23, 1991)

82. Yamanouti, Y., Sugimoto, M., Mizumoto, M., Watanabe, Y. and Hasegawa, K.

Inelastic Scattering of 18.5 MeV Neutrons from ^{52}Cr and ^{60}Ni

Fall Meeting of Atomic Energy Society of Japan in Fukuoka (Oct. 15, 1991)

Ⅶ PERSONNEL AND COMMITTEES
(April 1991— March 1992)

(1) Personnel

Department of Physics

Mitsuhiko	Ishii	Deputy Director
Fujiyasu	Nomura	Administrative Manager
Yuuki	Kawarazaki	Principle Scientist

Accelerators Division

Scientific Staff	Chiaki	Kobayashi*
	Shiro	Kikuchi
	Suehiro	Takeuchi
	Susumu	Hanashima
Technical Staff	Tadashi	Yoshida**
(Tandem, V.D.G)	Susumu	Kanda
	Katsuzo	Horie
	Yoshihiro	Tsukihashi
	Shinichi	Abe
	Shuhei	Kanazawa
	Norikio	Ohgoshi
Technical Staff	Katuo	Mashiko**
(Linac)	Tokio	Shoji
	Nobuhiro	Ishizaki
	Hidekazu	Tayama

Nuclear Physics Laboratory

Scientific Staff	Akira	Iwamoto*
	Yasuharu	Sugiyama
	Yoshiaki	Tomita
	Hiroshi	Ikezoe
	Masumi	Ohshima
	Kazumi	Ideno
	Yoshimaro	Yamanouchi
	Tetsuro	Ishii
	Michiaki	Sugita
	Koji	Niita

* Head

** Leader, Technical Staff

Linac Laboratory
  Scientific Staff   Yasuo   Suzuki*
                        Makio   Ohkubo
                        Eisuke   Minehara
                        Yoshimaro Yamanouchi
                        Masayoshi Sugimoto
                        Satoshi   Chiba
                        Ryoji   Nagai
                        Masayuki Takabe
                        Jyun   Sasabe
                        Masaru   Sawamura

Solid State Physics Laboratory I
  Scientific Staff   Yukio   Kazumata*
                        Hiroshi   Naramoto
                        Hiroshi   Tomimitsu
                        Satoru   Okayasu
                        Kazunari Aizawa

Solid State Physics Laboratory II
  Scientific Staff   Tadao   Iwata*
                        Saburo   Takamura
                        Akihiro   Iwase

Nuclear Data Center
                        Yasuyuki Kikuchi*
                        Satoshi   Chiba

Atomic and Molecular Physics Laboratory
  Scientific Staff   Hiroshi   Maeta
                        Masao   Sataka
                        Makoto   Imai

* Head

Department of Chemistry

Nuclear Chemistry Laboratory 2
Scientific Staff   Michio   Hoshi*
                      Shin-ichi   Ichikawa
                      Nobuo   Shinohara
                      Hidenori   Iimura

Physical Chemistry Laboratory
Scientific Staff   Mutsuhide   Komaki
                      Jiro   Ishikawa

Laser Chemistry Laboratory
Scientific Staff   Shin-ichi   Ohno*
                      Katsutoshi   Furukawa

Department of Radioisotopes

Isotope Research and Development Division
Scientific Staff   Hiromitsu   Matsuoka
                      Kentaro   Hata
                      Toshiaki   Sekine
                      Yuichiro   Nagame
                      Takami   Sorita
                      Mishiroku   Izumo
                      Hiroyuki   Sugai

Department of Fuels and Materials Research

Radiation Effects and Analysis Laboratory
Scientific Staff   Akimichi   Hishinuma*
                      Takeo   Aruga
                      Shozo   Hamada
                      Tomotsugu   Sawai
                      Katsumaro   Fukai

* Head

Material Processing and Qualification Laboratory
  Scientific Staff   Hitoshi   Watanabe*

                       Kenji   Noda

                       Yoshinobu   Ishii

                       Tetsuya   Nakazawa

Department of Reactor Engineering

Thermal Reactor Physics Laboratory
  Scientific Staff   Ikuo   Kanno

Department of Health Physics

Radiation Control Division II
  Technical Staff   Shoji   Izawa**

                       Kenji   Yamane

                       Masamitsu   Kikuchi

* Head
** Chief

(2) Tandem Steering Committee

(Chairman)	Naomoto Shikazono	(Deputy Director General, Tokai Research Establishment since October 1, 1991 Director General, Naka Establishment)
(Chairman)	Masashi Iizumi	(Deputy Director General, Tokai Research Establishment since October 1, 1991)
	Toru Hiraoka	(Director, Department of Reactor Engineering)
	Tatuo Kondo	(Director, Department of Fuels and Materials Research)
	Mitsuhiko Ishii	(Deputy Director, Department of Physics)
	Enzo Tachikawa	(Director, Department of Chemistry)
	Hirokazu Umezawa	(Director, Department of Radioisotopes)
(Secretary)	Chiaki Kobayashi	(Head, Accelerators Division)
(Secretary)	Fujiyasu Nomura	(Administrative Manager, Department of Physics)

(3) Tandem Consultative Committee

(Chairman)	Takumi	Asaoka	(Director General, Tokai Research Establishment)
(Vice Chairman)	Naomoto	Shikazono	(Deputy Director General, Tokai Research Establishment since October 1, 1991 Director General Naka Establishment)
(Vice Chairman)	Masashi	Iizumi	(Deputy Director General, Tokai Research Establishment since October 1, 1991)
(Vice Chairman)	Mitsuhiko	Ishii	(Deputy Director, Department of Physics)
	Hiromichi	Kamitsubo	(Principal Scientist, Institute of Physical and Chemical Research)
	Koji	Nakai	(Professor, National Laboratory for High Energy Physics)
	Hiroyasu	Ejiri	(Professor, Osaka University)
	Shiori	Ishino	(Professor, University of Tokyo)
	Hiroyuki	Tawara	(Associate Professor, Institute of Plasma Physics, Nagoya University)
	Kohzoh	Masuda	(Professor, University of Tsukuba)
	Nobutsugu	Imanishi	(Professor, Kyoto University)
	Ichiro	Fujiwara	(Professor, Otemon Gakuin University)
	Kenji	Sumita	(Professor, Osaka University)
	Naohiro	Hirakawa	(Professor, Tohoku University)
	Hirosuke	Yagi	(Professor, University of Tsukuba)
	Syunpei	Morinobu	(Associate Professor, Research Center for Nuclear Physics Osaka University)
	Hiromichi	Nakahara	(Professor, Tokyo Metropolitan University)
	Sadaei	Yamaguchi	(Professor, The Research Institute for Iron, Steel and Other Metals, Tohoku University)

(Vice Chairman)	Nobutsugu	Imanishi	(Associate Professor, Kyoto University)
	Mamoru	Akiyama	(Professor, University of Tokyo)
	Yasuo	Ito	(Associate Professor, University of Tokyo)
(Secretary)	Chiaki	Kobayashi	(Head, Accelerators Division)
(Secretary)	Fujiyasu	Nomura	(Administrative Manager, Department of Physics)
(Secretary)	Hirokazu	Umezawa	(Director, Department of Radioisotopes)
(Secretary)	Tadao	Iwata	(Head, Solid State Physics Laboratory II)
(Secretary)	Hitoshi	Watanabe	(Head, Material Processing and Qualification, Department of Fuels and Materials Research)
(Secretary)	Hiroshi	Maeta	(Head, Atomic and Molecular Physics Labotatory)

(4)   Tandem Program Advisory Committee

(Chairman)	Mitsuhiko	Ishii	(Deputy Director, Department of Physics)
	Shoji	Izawa	(Chief, Radiation Control Group, Department of Health Physics)
	Hitoshi	Watanabe	(Head, Material Processing and Qualification Laboratory)
	Yuuki	Kawarasaki	(Principal Scientist, Department of Physics)
	Akira	Iwamoto	(Head, Nuclear Physics Laboratory)
	Yukio	Kazumata	(Head, Solid State Physics Laboratory I)
	Toshiaki	Sekine	(Department of Radioisotopes)
(Secretary)	Chiaki	Kobayashi	(Head, Accelerators Division, Department of Physics)
(Secretary)	Shiro	Kikuchi	(Accelerators Division, Department of Physics)
(Secretary)	Tadashi	Yoshida	(Accelerators Division, Department of Physics)

Ⅷ CO-OPERATIVE RESEARCHES

Title	Contact person Organization
1. Gamma-Ray Spectroscopy in the Neighbour Nuclei of ^{100}Sn	Masao OGAWA Tokyo Institute of Technology
2. Mass Division Processes in Fissions of Actinide Elements	Hiromichi NAKAHARA Faculty of Science, Tokyo Metropolitan University
3. Study of Nuclear Interactions in Heavy-Ion Reaction	Takao NAKAJIMA Department of Physics, Kyushu University
. Atomic Collision Research Using Highly Charged Ions	Ken-ichiro KOMAKI Institute of Physics, College of Arts and Sciences, University of Tokyo
5. Effect of Electron Excitation on Radiation Damage of Heavy Ion-Irradiated FCC Metals	Takeshi NIHIRA Faculty of Engineering, Ibaraki University
6. Study of Formularlism for Radiation Damage by Heavy Ion-Irradiation	Shiori ISHINO Faculty of Engineering, University of Tokyo
7. Study of Single Event Phenomenon on High Energy Heavy Ion-Irradiation	Takeo GOKA National Space Development Agency of Japan
8. Study of Higher-Order Effect in Nuclear Collective Motion through Coulomb Excitation	Hideshige KUSAKARI Faculty of Education, Chiba University
9. Response of Semiconductor Detectors on Heavy Ions	Itsurou KIMURA Faculty of Engineering, Kyoto University

10. A Research for the Production
    of Transuranium Elements

    Ichiro FUJIWARA
    Faculty of Economy,
    Otemon Gakuin University

11. A Study of Irradiation Behavior
    of Ceramic Breeders

    Hisayuki MATSUI
    Faculty of Engineering,
    Nagoya University

12. Radiation Damage of Materials
    for Environment Resistance
    Devices

    Kazutoshi OHASHI
    Faculty of Engineering,
    Tamagawa University

13. Irradiation Effect on Electrical
    Property of LiAl with Li and
    Other Heavy Ions

    Kazuo KURIYAMA
    Research Center of Ion Beam
    Technology, Hosei University

14. Study of Phase Transition on
    Nuclear Fission Phenomenon

    Hiroshi BABA
    Faculty of Science,
    Osaka University

15. Radiation Effects of High T_c
    Materials

    Hiroaki KUMAKURA
    National Research Institute
    for Metals

16. Study on Continuous Spectra
    of Emitted Particles Induced
    by 20-40 MeV Protons

    Yukinori KANDA
    Department of Energy Conversion
    Engineering, Kyushu University